NASA Technical Memorandum 78125

# Space Processing Applications Rocket Project

## SPAR II - Final Report

(NASA-TM-78125) SPACE PROCESSING APPLICATIONS ROCKET PROJECT, SPAR 2 Final Report (NASA) 276 p HC A13/MF A01 CSCL 22A

N78-15145

Unclas
G3/15 01859

NOVEMBER 1977

NASA

SPACE PROCESSING APPLICATIONS

ROCKET PROJECT

SPAR II

FINAL REPORT

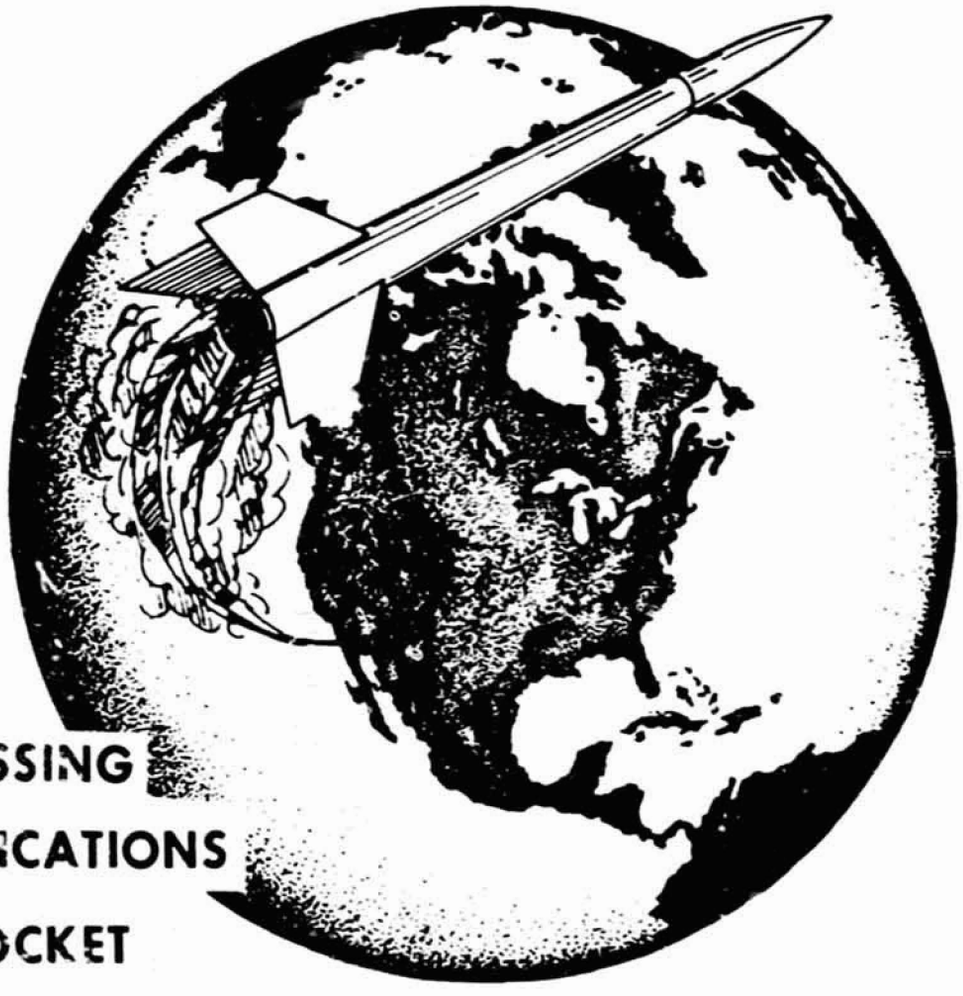

**SPACE PROCESSING APPLICATIONS ROCKET**

NASA Technical Memorandum 78125

# Space Processing Applications Rocket Project

## SPAR II - Final Report

George C. Marshall Space Flight Center
Marshall Space Flight Center, Alabama

National Aeronautics
and Space Administration

**Scientific and Technical Information Office**

1977

# CONTENTS


| Chapter | | Page |
|---|---|---|
| | INTRODUCTION | iii |
| I. | SPAR II ENGINEERING REPORT | I-1 |
| II. | SCIENCE PAYLOAD II (Test Report) | II-1 |
| III. | SPACE SOLIDIFICATION OF Pb-Sb EUTECTIC (Experiment 74-5) | III-1 |
| IV. | FEASIBILITY OF PRODUCING CLOSED-CELL METAL FOAMS IN A ZERO GRAVITY ENVIRONMENT FROM SPUTTER-DEPOSITED INERT GAS-BEARING METALS AND ALLOYS (Experiment 74-10) | IV-1 |
| V. | THE DIRECT OBSERVATION OF DENDRITE REMELTING AND MACROSEGREGATION IN CASTING (Experiment 74-21) | V-1 |
| VI. | AGGLOMERATION IN IMMISCIBLE LIQUIDS (Experiment 74-30) | VI-1 |
| VII. | CASTING DISPERSION-STRENGTHENED COMPOSITES AT ZERO GRAVITY (Experiment 74-34) | VII-1 |
| VIII. | SOLIDIFICATION BEHAVIOR OF Al-In ALLOYS UNDER ZERO GRAVITY CONDITIONS — Preliminary (Experiment 74-62) | VIII-1 |

# SPACE PROCESSING APPLICATIONS ROCKET PROJECT

# SPAR II

## Final Report

## INTRODUCTION

Space materials processing, a new technology derived from the experiment era of Skylab and Apollo-Soyuz, is defined as using the unique aspects of space environment to process materials. Space flights, such as those of Skylab, Apollo-Soyuz, and now the Space Processing Applications Rocket (SPAR) Project provide the facilities of a launch vehicle and the experiment apparatus to continue to explore the unique materials processing environment of space.

Presently, the primary reason for exploring the potentials of space processed materials is to learn how to take advantage of the effects of very low gravity in modifying the properties of materials. Significant reductions in thermal convection, sedimentation of heavier particles, and bouyancy of lighter particles or bubbles in a fluid have been shown to occur during low-gravity space flights.

Building on these known advantages of a low-g environment for materials processing, NASA has recognized a continuing need for space flight research such as SPAR, as a prelude to the Space Shuttle and Spacelab flights, to further develop and to continue to bring to fruition this new era in materials technology. Presented in this SPAR II Final Report are the experimental results of six materials experiments flown on the SPAR Black Brant VC Sounding Rocket May 17, 1976. Information concerning each of the SPAR experiment results is contained in separate experiment report sections furnished by the Principal Investigators (PI). Limited editing was performed by NASA/ MSFC to provide consistency in presentation, where necessary.

The materials experiments conducted on the SPAR II mission cover a wide range of scientific interest. NASA obtained the participation of the government agencies and domestic and foreign industrial and academic organizations in planning the experiments and studying the results.

# CHAPTER I

# SPAR II

# ENGINEERING REPORT

By

A. Boese

Marshall Space Flight Center

PRECEDING PAGE BLANK NOT FILMED

## CONFIGURATION

The total rocket configuration is shown in Figure 1, and the SPAR II science payload is shown in Figure 2.

## PERFORMANCE

### Low Gravity

The payload performance is shown in Figure 3. The low-g ($10^{-4}$ or less) duration was 267 sec, starting at 89 sec and ending at 356 sec.

### Events

Figure 4 shows the predicted and actual experiment timelines. All functions occurred well within the acceptable limits of each experiment. The largest variation occurred in Experiments 74-21/2 and /3. This known variation was compensated for with liberal time programmed for completion of the experiments. With the exception of the measurement module and the telemetry system in the support module, the science payload was shut off at 660 sec. However, loss of telemetry signal occurred at 780 sec, which precluded getting any environmental data beyond this point. [1]

### Power Distribution

The battery specification is $28^{+15}_{-2}$ V. Figure 5 shows the battery performance. Power was transferred from ground support equipment to the onboard battery at T-3 min; in approximately 24 sec, with part of the payload on line, the voltage dropped to 35 V. At T+75 sec, when all the systems were on line, the voltage dropped to 29 1/4 V. Recovery back to approximately 35 V occurred as less demand was being placed on the battery.

1. S-band (2200-2300 MHz) telemetry signals travel in essentially a straight line, and the payload was on the down leg of the flight and below the horizon at 780 sec, hence, the loss of signal.

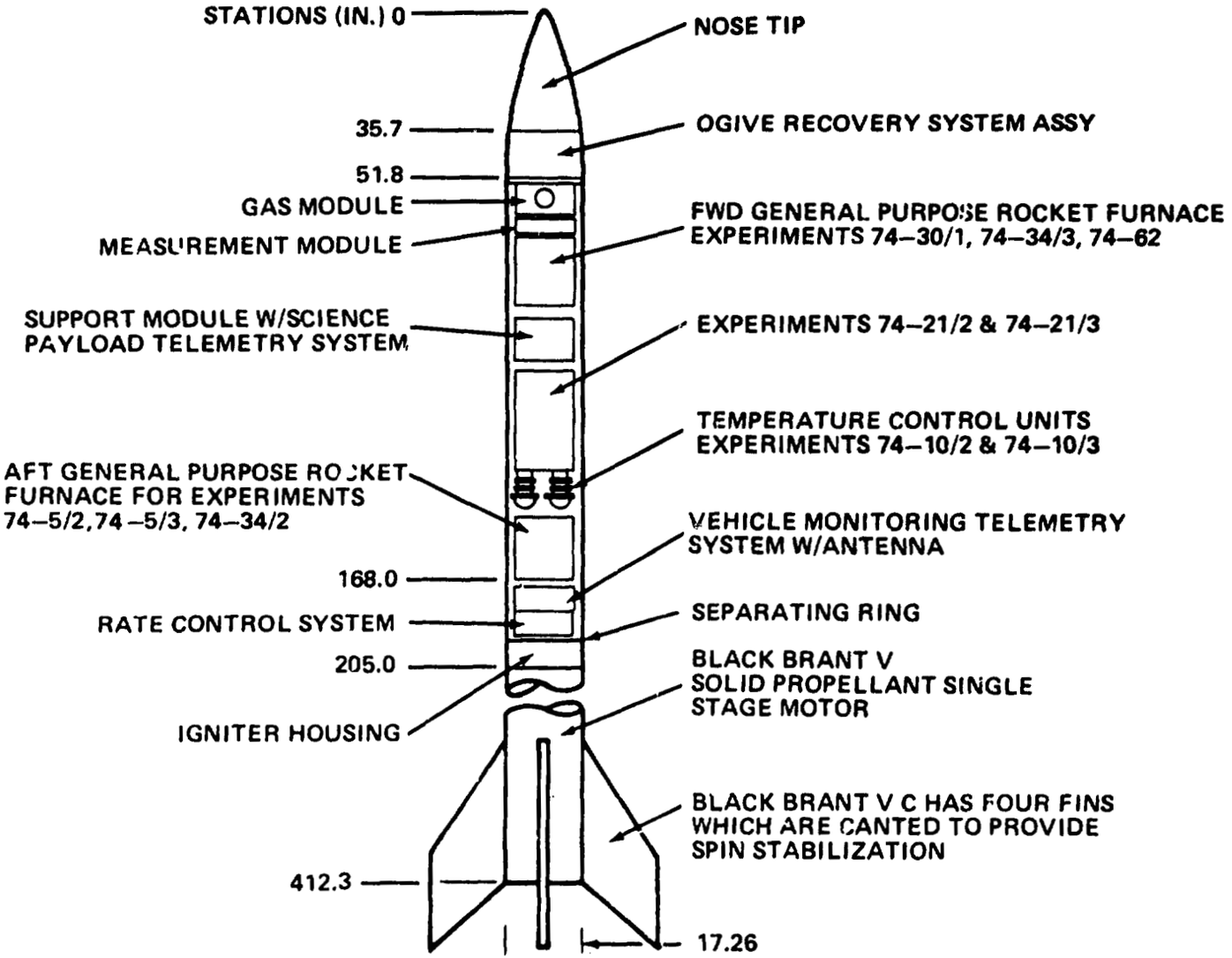


Figure 1. SPAR II.

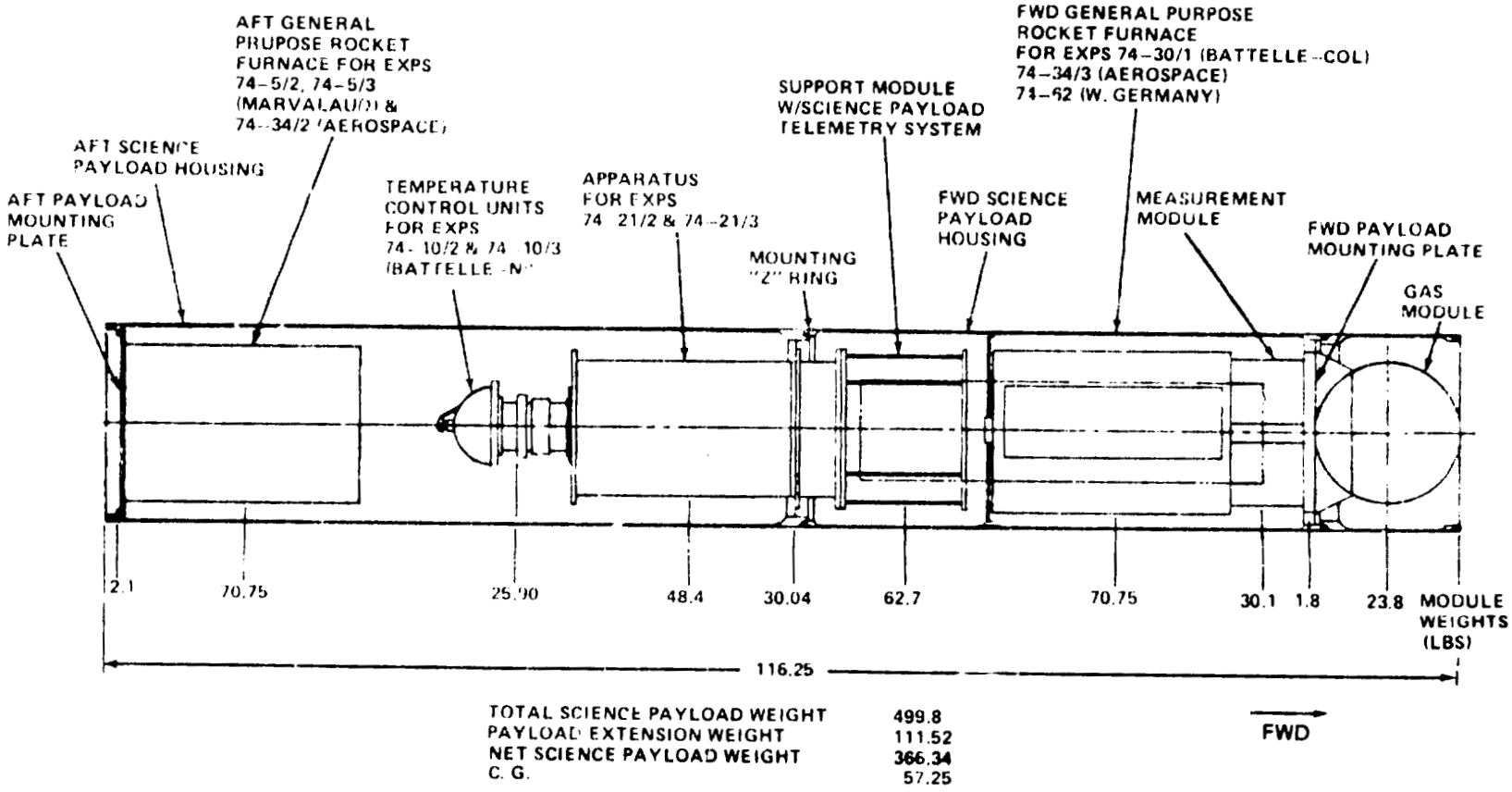


Figure 2. SPAR payload II.

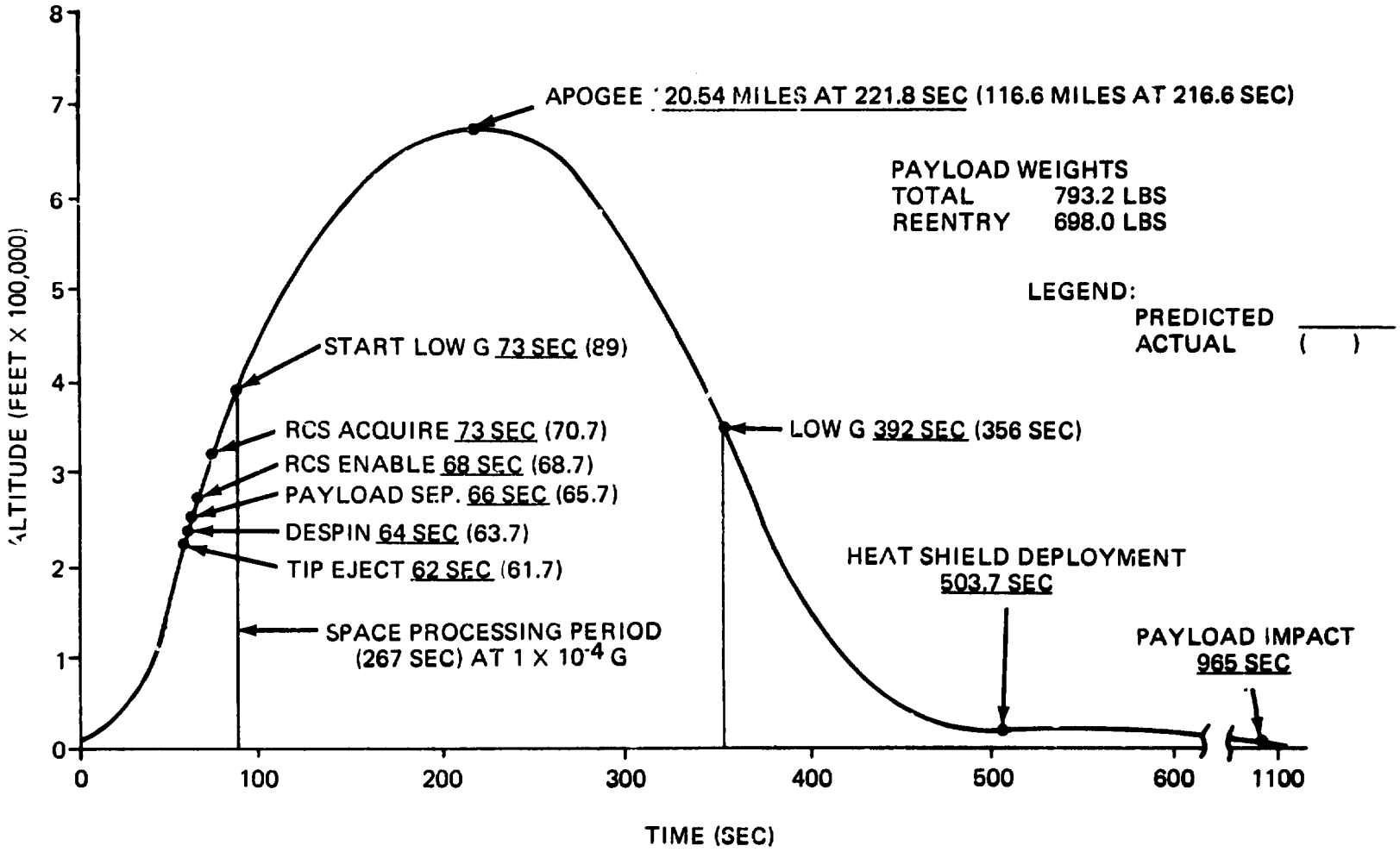


Figure 3. SPAR II flight profile and events/conditions May 17, 1976, at 1000 MDT predicted and actual.

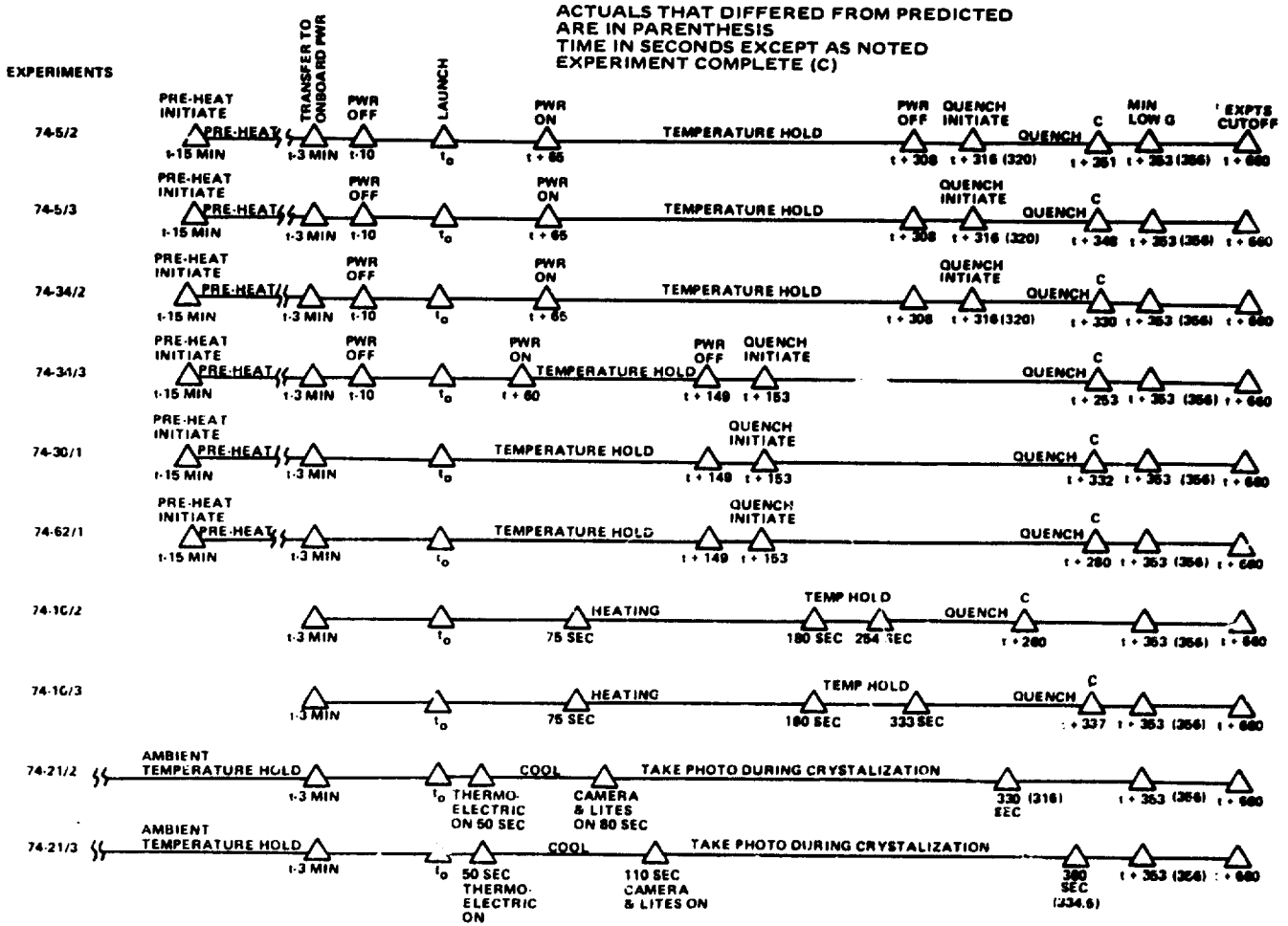


Figure 4. SPAR payload II experiment timeline.



ORIGINAL PAGE IS
OF POOR QUALITY

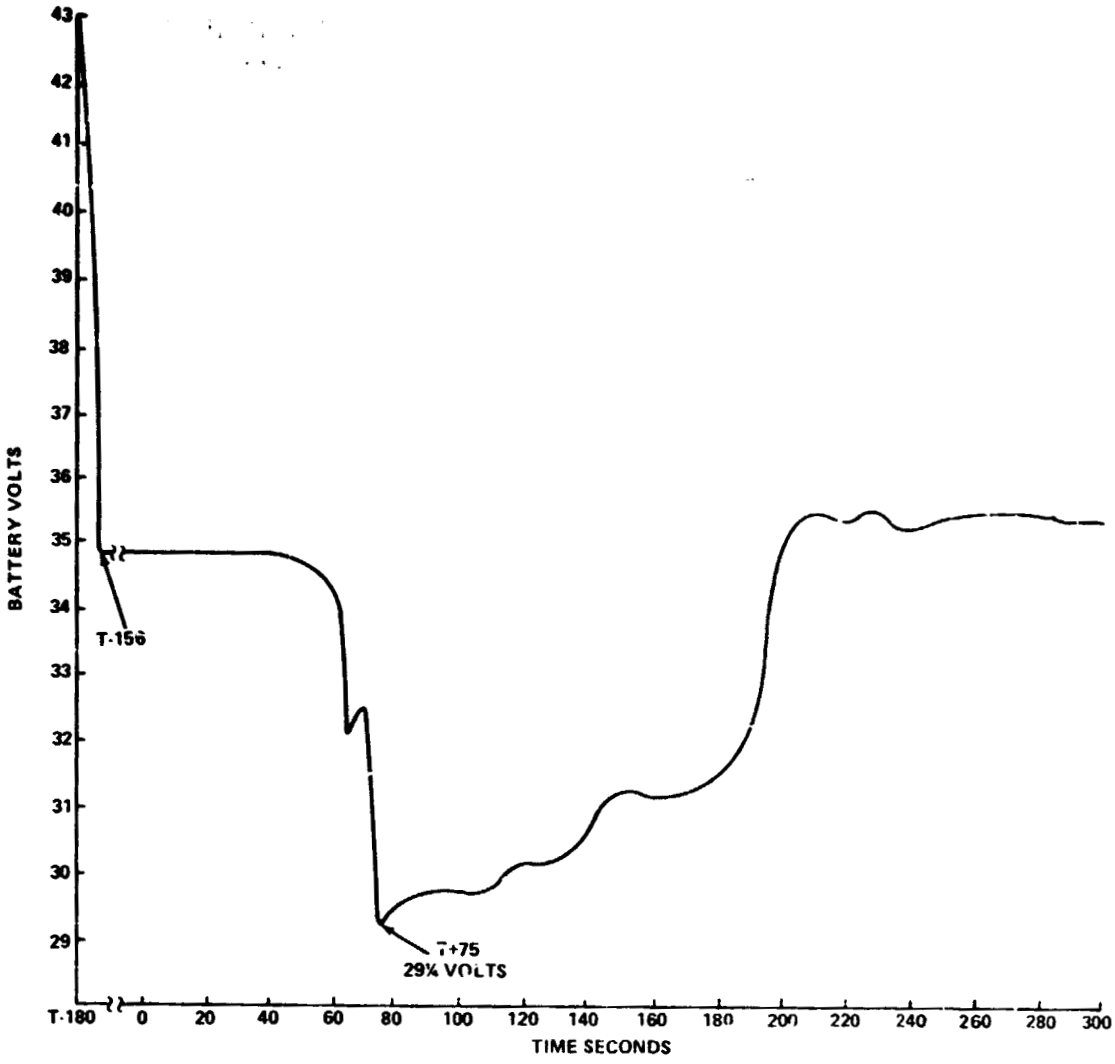


Figure 5. SPAR II battery voltage.

## INSTRUMENTATION — TELEMETRY

### Temperatures

The measurement locations on SPAR II were the same for each module as on SPAR-I except for the addition of C28-SM on the transmitter plate in the support module and the relocation of C39-MM to the measurement module base plate next to the forward General Purpose Rocket Furnace (GPRF) (Fig. 6).

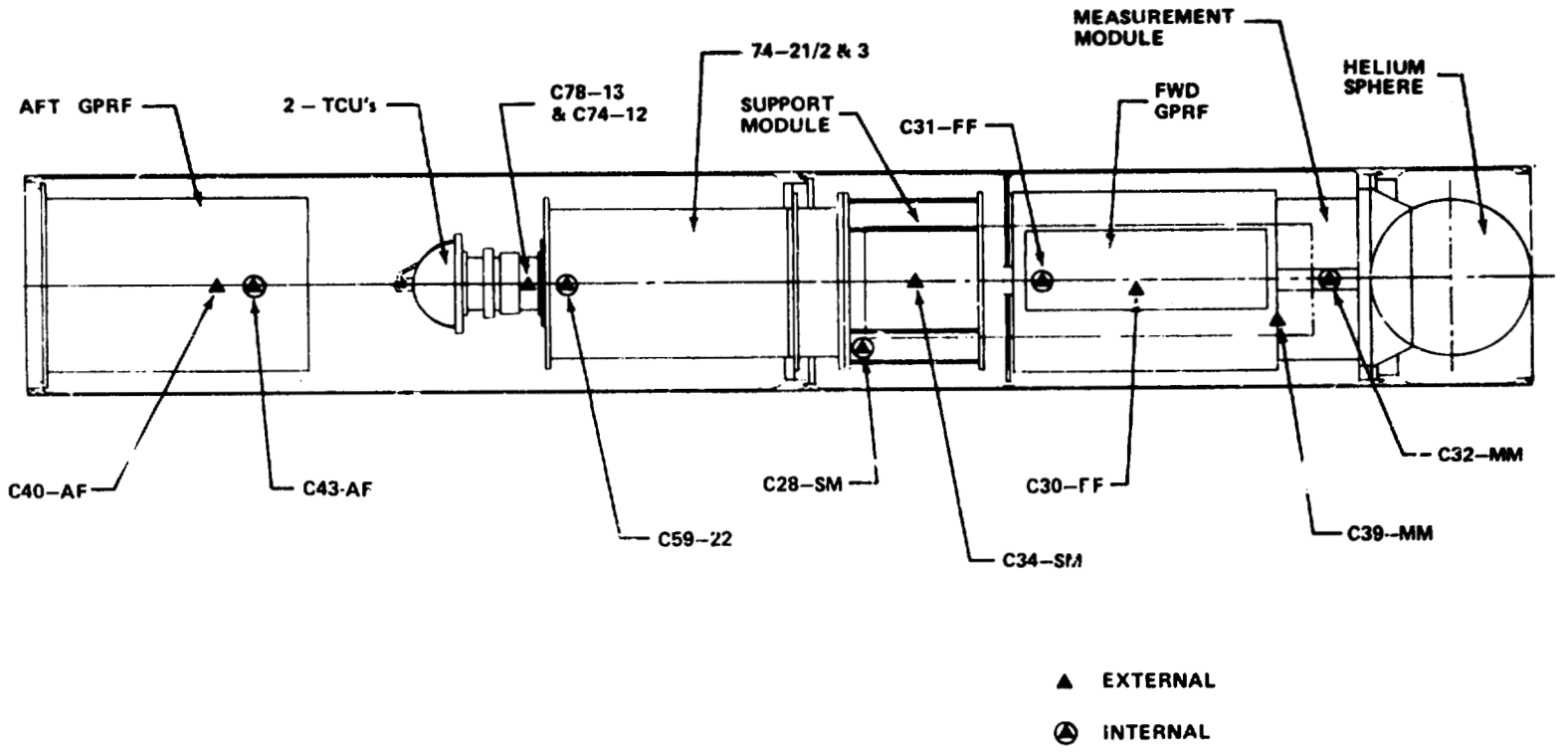


Figure 6. SPAR II engineering measurement locations.

ORIGINAL PAGE IS
OF POOR QUALITY

Figure 7 presents the temperature profile of each engineering temperature measurement. The data indicate that some aerodynamic heating influence occurred during boost and reentry. However, in both cases, the aerodynamic heating is of short duration and has little apparent effect on the total payload heating. The experiments in the aft experiment bay had the same rate of temperature increase during flight as the aft experiments on SPAR I. The experiments in the forward experiment bay were consistently hotter than in the aft bay due to the influence of the high temperature GPRF and higher aerodynamic heating at the forward end of the payload. The transient seen on C74-12 is due to sample processing and cooldown of Experiment 74-10/2. The conclusion drawn from this evaluation is that all engineering temperatures were within their expected ranges, and no anomalies were noted.

## Pressure

Pressure in the forward end of the science payload dropped from 13.7 psia to 0.8[2] by T+61 sec and stabilized until it started up at T+400 sec to 10.5 psia at T+660 sec.

## Acoustics

Figure 8 presents the SPAR II sound pressure levels.

## Vibration and Shock

The vibration accelerometers in the x- and z-axes did not generate good data. It appears that the calibration of ±25 g on these instruments was too low. Data from the y-axis and the shock accelerometer, which is in the z-axis and set at ±100 g, is plotted in Figure 9 versus the qualification specification requirements. These data show that protoflight qualification requirements in the z-axis are accurate, but data in the y-axis show the vibration levels to be well below the requirements. The landing shock load was not recorded because telemetry was lost before impact.

2. This gage does not measure accurately below 1 psia. On future flights, measurements between 30 and $10^{-4}$ torr are planned.

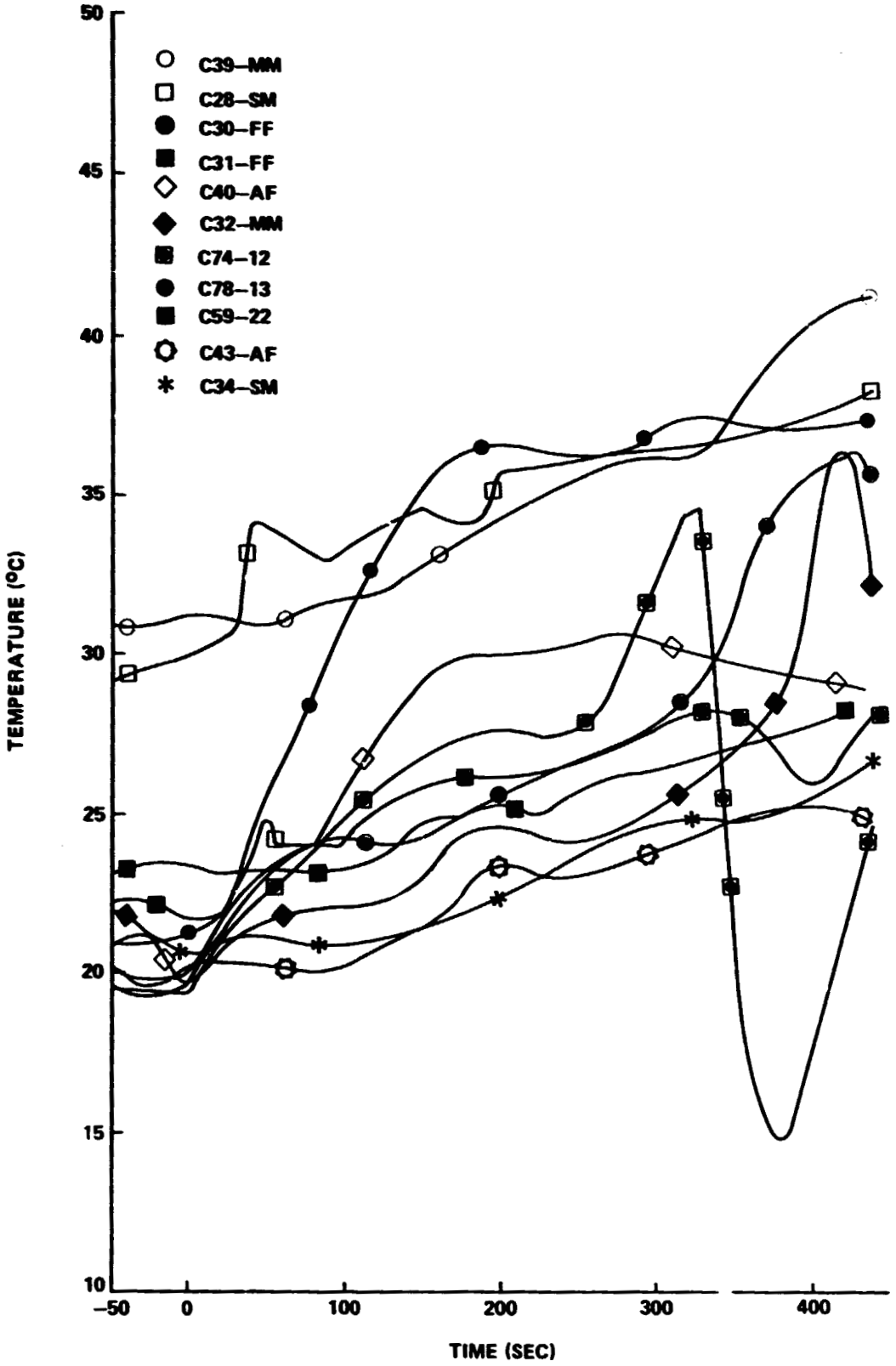


Figure 7. Engineering measurements SPAR II.

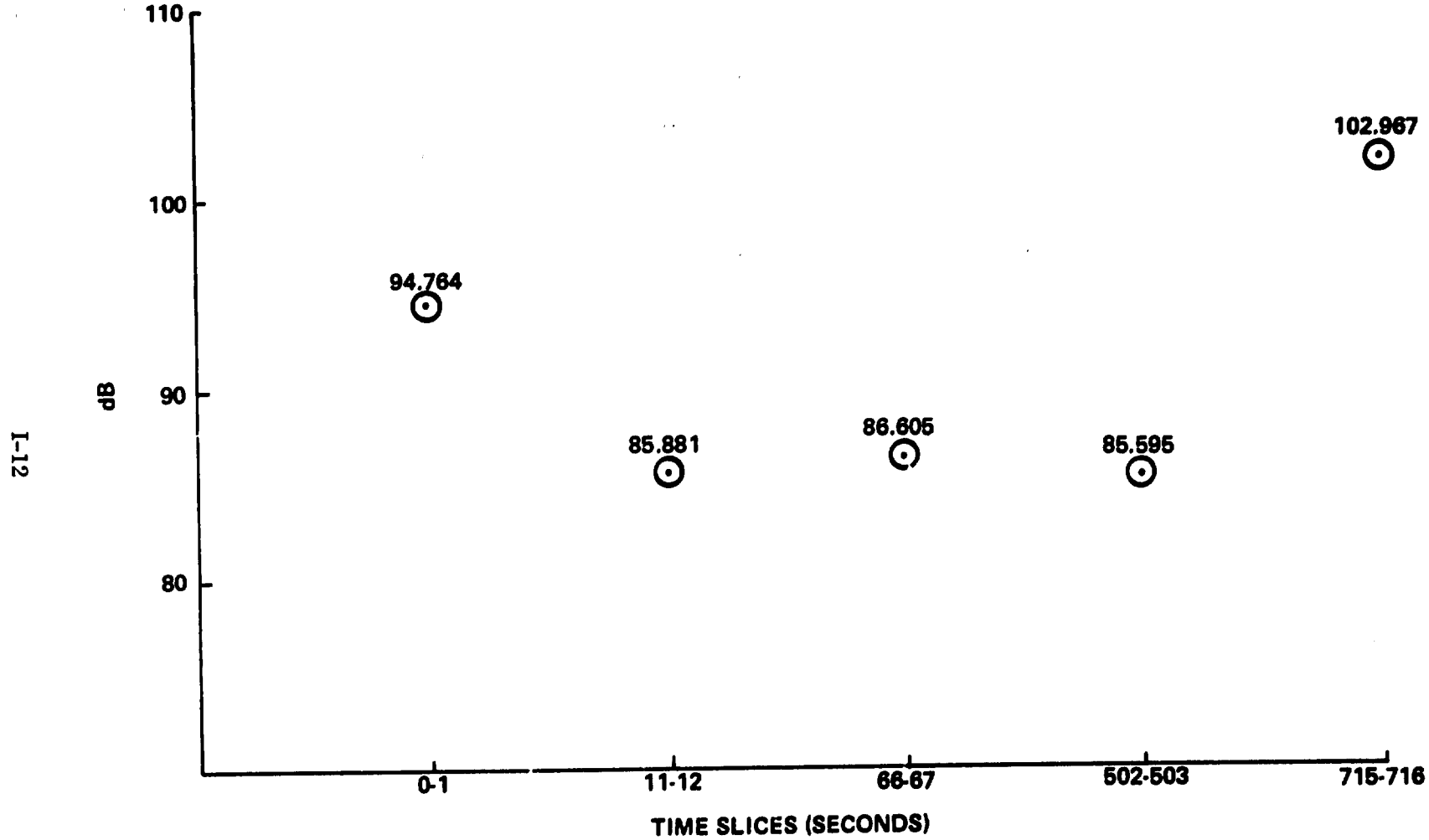


Figure 8. SPAR II sound pressure levels.

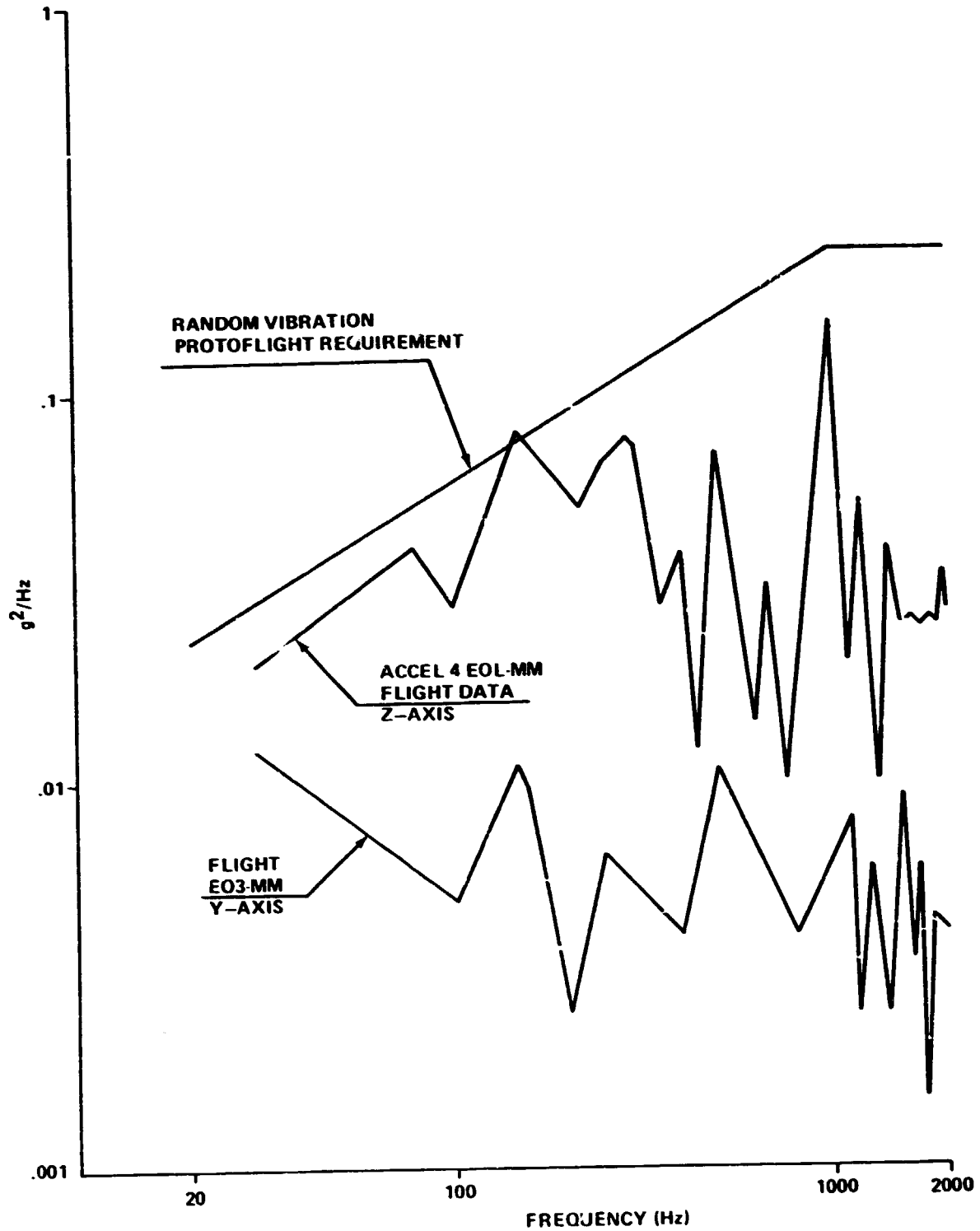


Figure 9. Time slice 0-1 sec — SPAR II.

## General Purpose Rocket Furnace Experiments

### General

The GBT were performed at 4.8 V higher than the lowest voltage experienced during flight. The effect of this lower voltage is reflected on the thermal profiles of each of the experiments (Figs. 10 through 15). The thermal profiles were satisfactory on all experiments except 74-34/3. Regarding the unanticipated extrusion of experiment material into the 74-5 cartridge vent tube (Ref. Observation and Data paragraph in Chapter III), MSFC low-g accelerometer data from the SPAR II flight do not reveal acceleration levels high enough to have caused the extrusion.

### 74-34/3

To accommodate an early quench on Experiments 74-62 and 74-30, the final heatup and soak for 74-34/3 was shortened to 149 sec. Consequently, with the reduced voltage experienced during flight, not enough energy was supplied to melt the sample completely. Figure 15 shows the difference between flight and GBT thermal profiles.

## Thermal Control Units (TCU) 74-10/2/3

These systems performed satisfactorily.

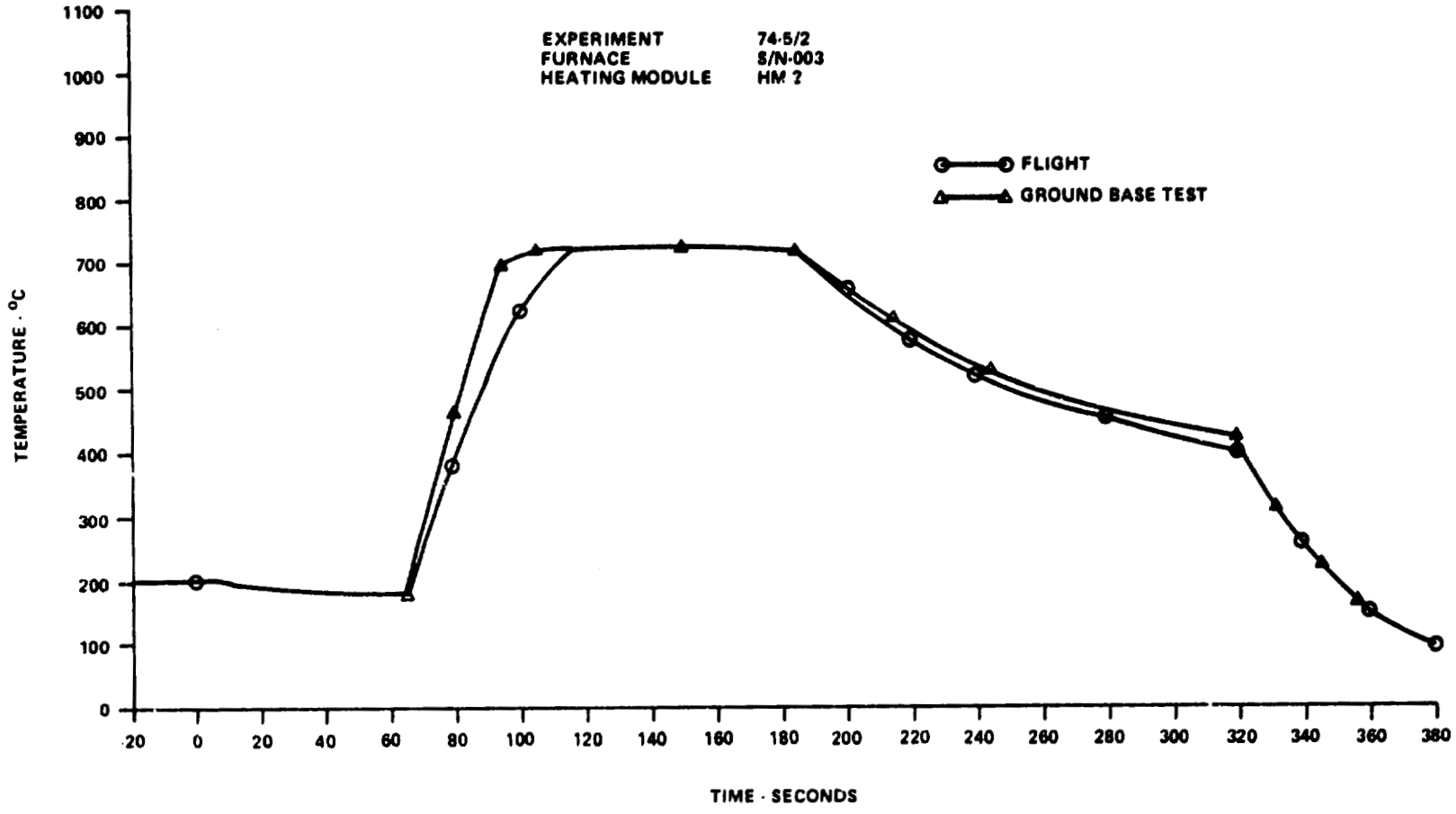


Figure 10. SPAR II furnace experiment.

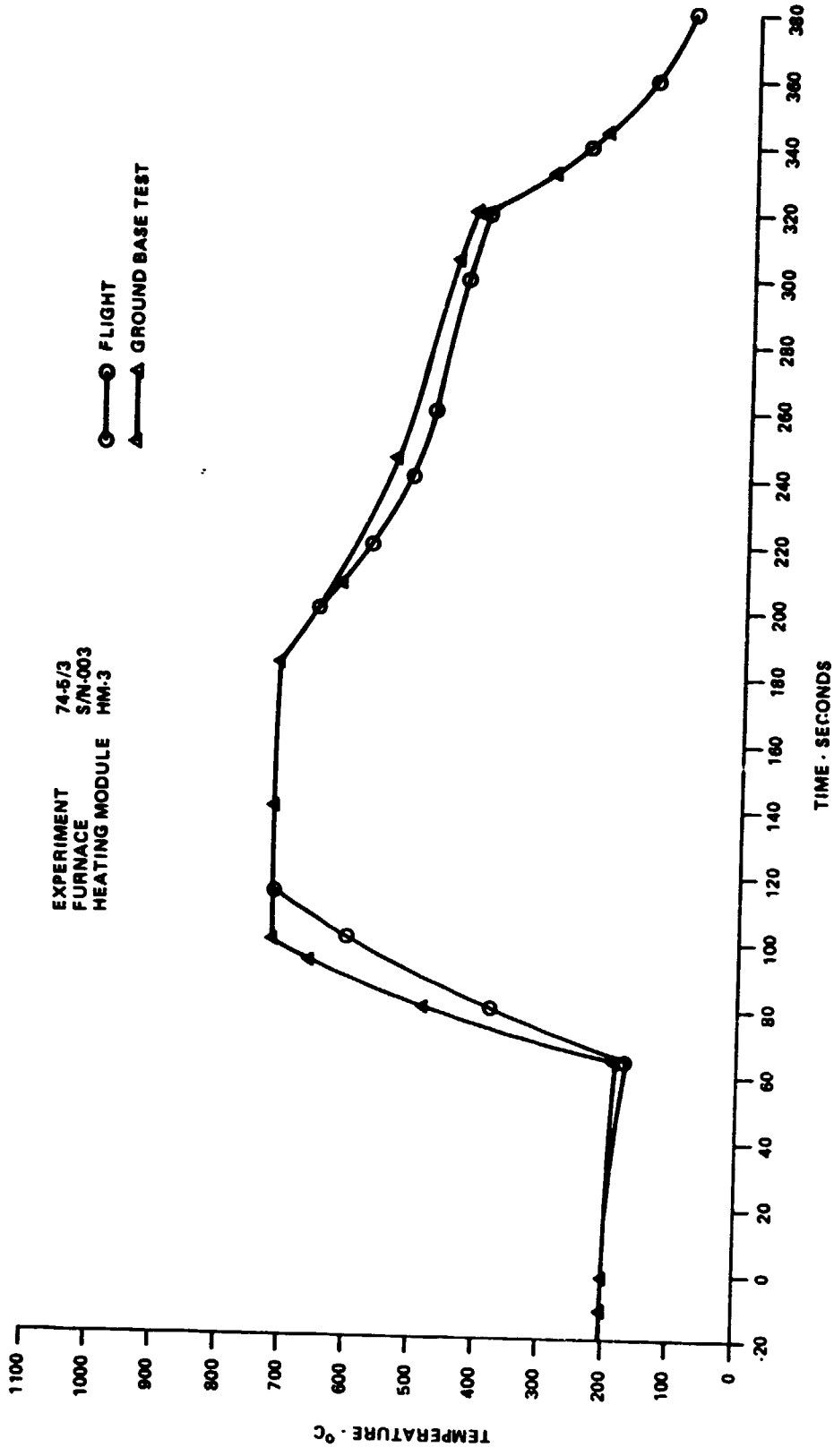


Figure 11. SPAR II furnace experiment.

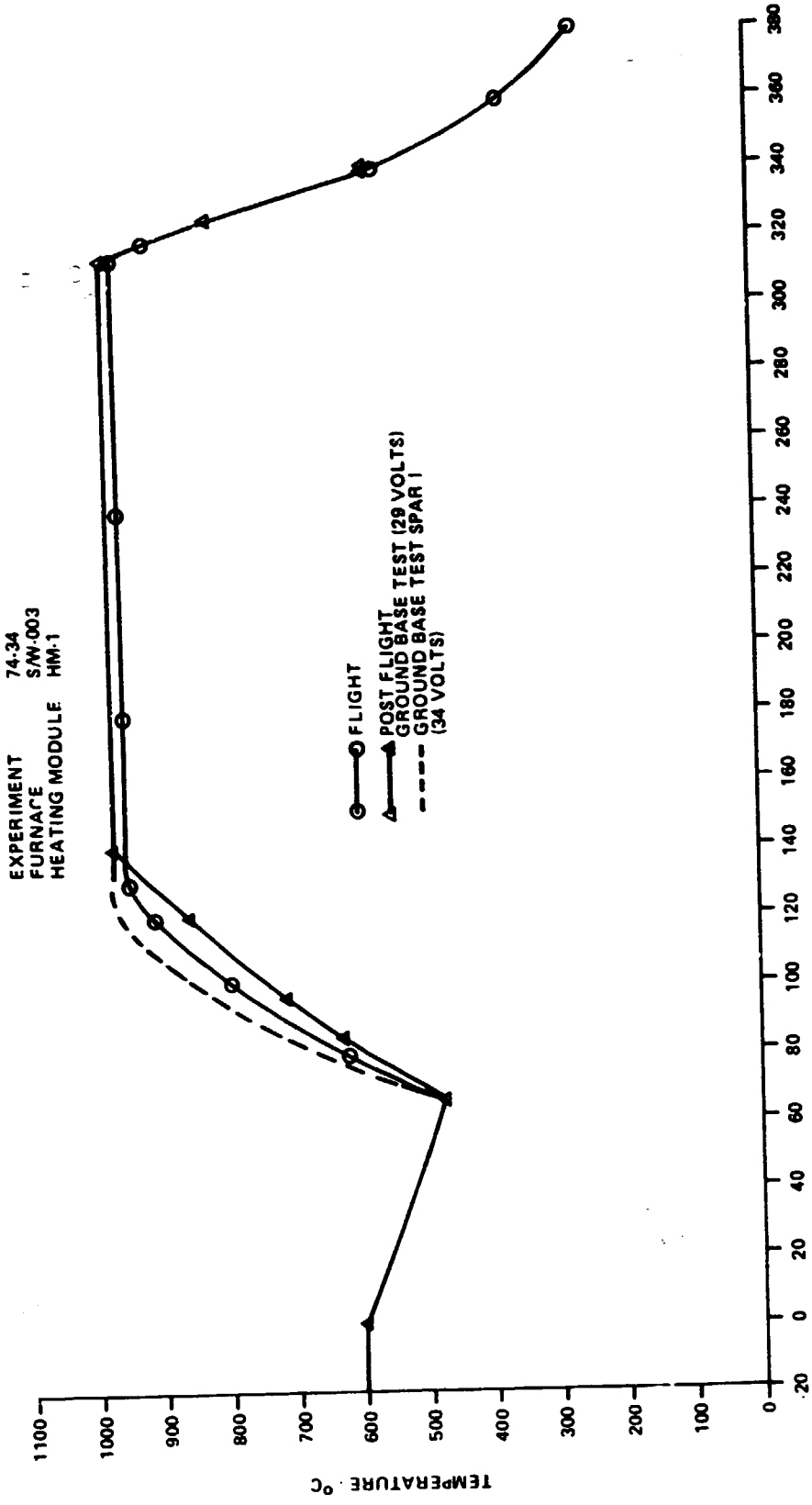


Figure 12. SPAR II furnace experiment.

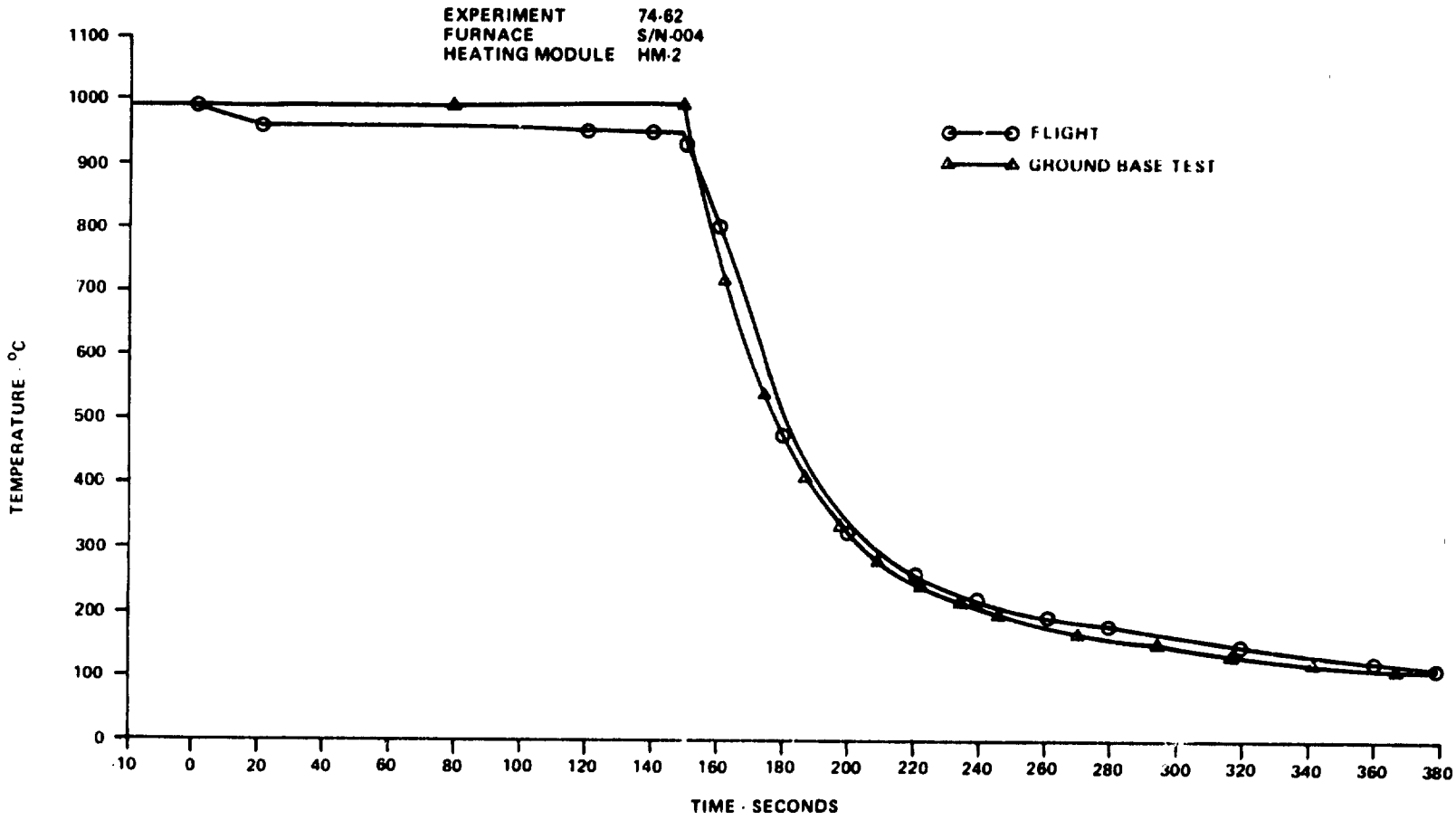


Figure 13. SPAR II furnace experiment.

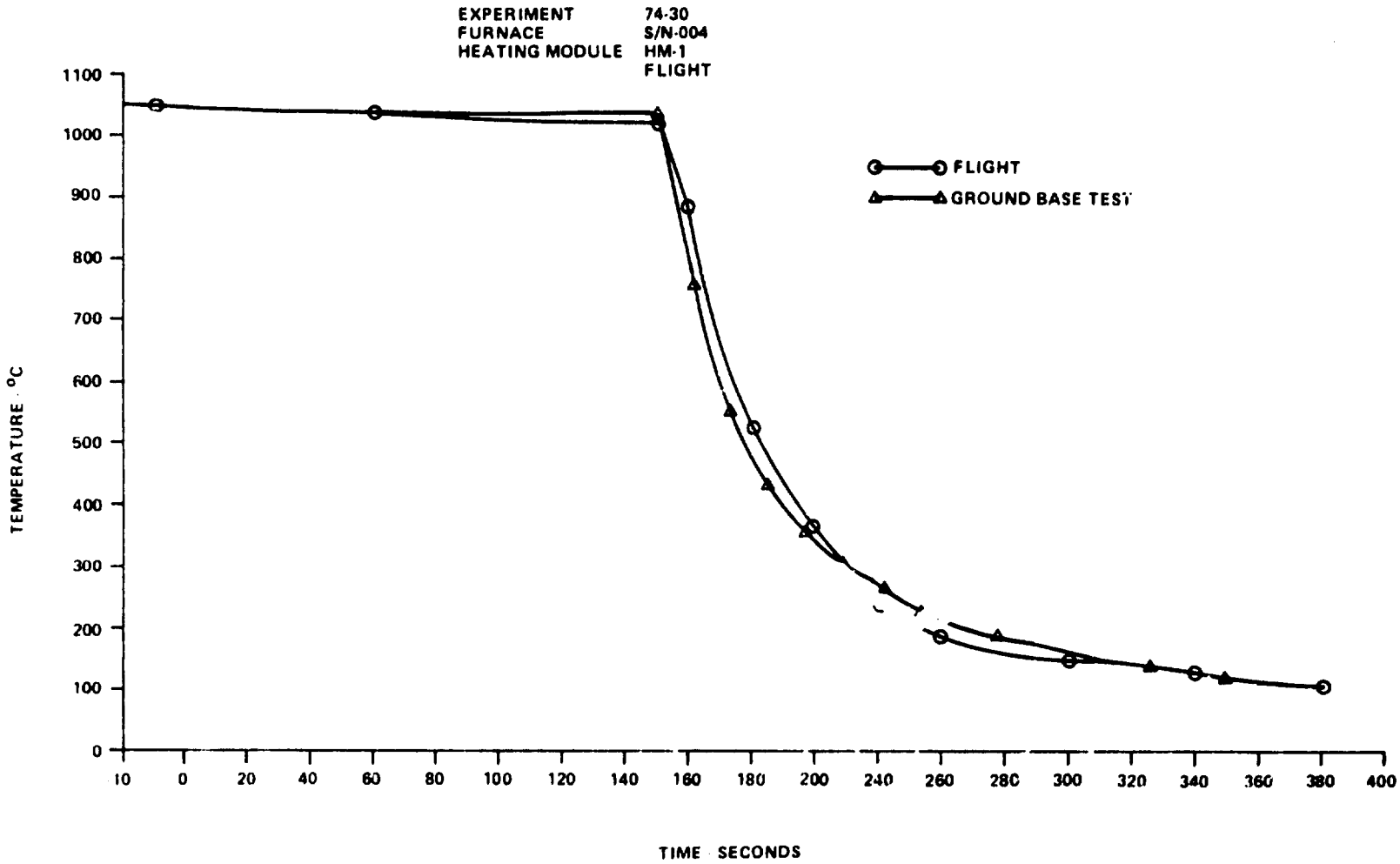


Figure 14. SPAR II furnace experiment.

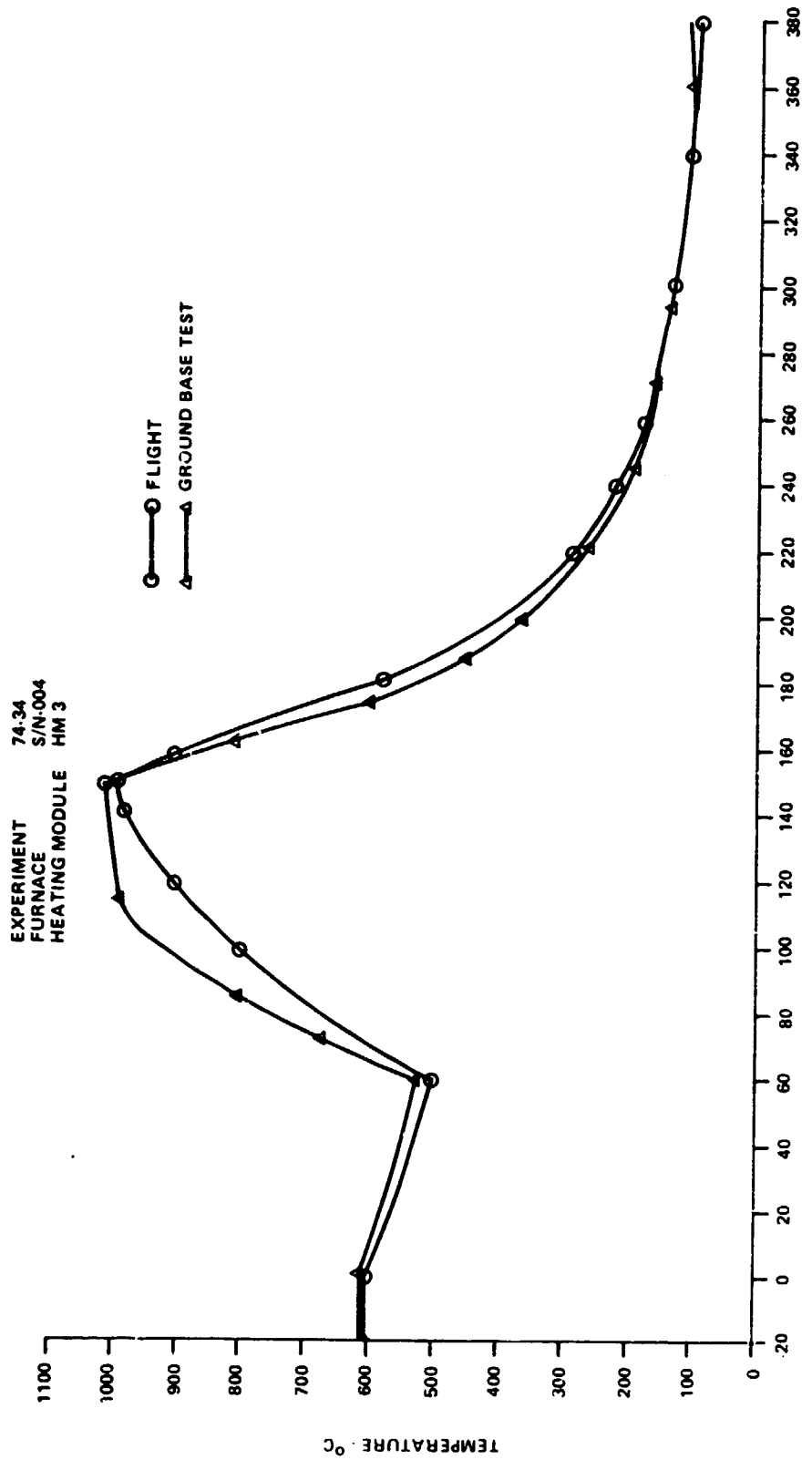


Figure 15. SPAR II furnace experiment.

# CHAPTER II

# SCIENCE PAYLOAD II

## Test Report

Marshall Space Flight Center

# INTRODUCTION

## Purpose

This report documents the testing and related activities during Post-Manufacturing Checkout (PMC), Integration, Pre-Launch and Launch of Space Processing Applications Rocket (SPAR) Project Payload II.

## Scope

All significant testing and operations are presented from the arrival of SPAR Project Science Payload II at MSFC, Building 4619, for post-manufacturing checkout, through launch operations at the White Sands Missile Range. Post-manufacturing checkout, integration activities at Goddard Space Flight Center (GSFC), and pre-launch/launch activities are presented in this chapter. Tests are listed individually in sequence of performance and include procedure number, test title, objective(s), and test performance. A summary of Discrepancy Reports (DR's) and Test Discrepancy Reports (TDR's) written during post-manufacturing checkout at MSFC is presented in Appendix A and TDR's written during integration testing at GSFC and during pre-launch and launch activities at WSMR are listed in Appendix B. Payload II actual test schedule is shown in Figure 1.

PRECEDING PAGE BLANK NOT FILMED

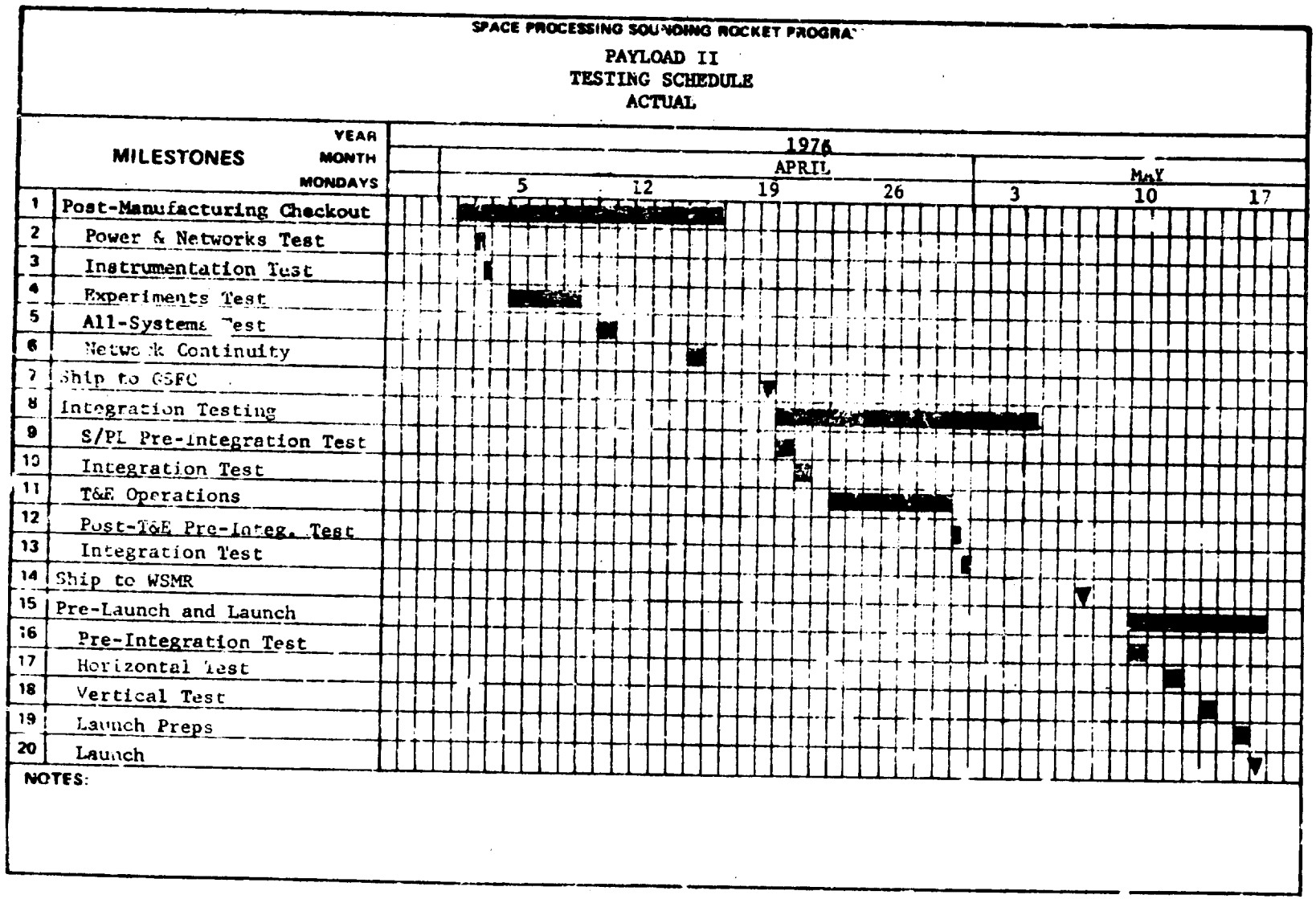


Figure 1. Payload II testing schedule, actual.



ORIGINAL PAGE IS
OF POOR QUALITY

## POST-MANUFACTURING CHECKOUT

**Test Title:** Single Point Ground Isolation, Electrical Power and Networks Subsystem

**Procedure Number:** MTCP-FS-SPAR-2-608

**Test Objective:** To verify single point ground isolation, proper power transfer between modules, and that the support module network circuitry conforms to systems design.

**Test Performance:** The power and network subsystem was verified to conform to systems design. Anomalies occurring during the test and corrective actions were:

a. Experiment 74-21/2 and -21/3 cameras were shorted to payload chassis. Isolation tape and washers were placed between cameras and payload structure. Reference TDR M-SPAR-2-608-1.

b. Resistance between forward GPRF module I element and payload chassis was 500 ohms and should have been greater than 50K ohms. The furnace module was replaced. Reference TDR M-SPAR-2-608-2 and DR 1368.

---

**Test Title:** Instrumentation Subsystem Test

**Procedure Number:** MTCP-FS-SPAR-2-610

**Test Objective:** The objectives of this test were to verify:

a. Proper transmitter deviation.

b. Subcarrier and commutated data channels.

c. Proper operation of telemetry calibrator.

**Test Performance:** The objectives of this test were met successfully. One anomaly occurred during the test. Calibrations, when operated manually, were erratic. The manual step relay in the GSE control panel was defective and replaced. Reference TDR M-SPAR-2-610-1.

---

Test Title: GPRF Subsystem Test, Aft and Forward Modules Operational Test

Procedure Number: MTCP-FS-SPAR-2-605

Test Objectives: To verify operation of individual modules at low temperatures, response to GSE commands, and proper responses through telemetry.

Test Performance: The objectives of the test were met successfully. No anomalies occurred during the test.

---

Test Title: Subsystem Test Procedure, AO 74-21/2 and 3

Procedure Number: MTCP-FS-SPAR-2-612

Test Objective: To verify proper operation of the experiments and to demonstrate experiment-GSE compatibility.

Test Performance: Operation of the experiments and compatibility of the experiments and GSE were verified. No anomalies occurred during the test.

---

Test Title: Subsystem Test Procedure, Experiment 74-10/2

Procedure Number: MTCP-FS-SPAR-2-613

Test Objective: To operate the experiment in a payload configuration and to verify event timer operation.

Test Performance: The objectives of the test were met successfully. No anomalies occurred during the test.

---

Test Title: Subsystem Test Procedure, Experiment 74-10/3

Procedure Number: MTCP-FS-SPAR-2-614

Test Objective: To operate the experiment in a payload configuration and to verify event timer operation.

Test Performance: The objectives of the test were met successfully. One anomaly was detected during the test. The voltage level of the support module event timer output pulses at the multiplexer input was approximately 11.0 V, causing crosstalk on telemetry channels adjacent to the channels displaying the event timer output pulses. The support module signal conditioner board A2 was corrected per E.O. 001-030 to limit the voltage to telemetry to 5.6 V. Reference TDR M-SPAR-2-614-1.

---

Test Title: All Systems Test

Procedure Number: MTCP-FS-SPAR-2-615

Test Objective: To functionally verify systems operational compatibility and to detect nonconformances to test requirements and specifications.

Test Performance: The objectives of this test were met successfully. All systems were verified to be operational and compatible. Anomalies occurring during the test were:

a. The camera for Experiment 74-21/3 did not cut off prior to experiment power off at plus 660 sec. Forty frames remained on the camera frame counter when film ran out preventing cut-off. Camera cut-off during retest was as expected. Reference TDR M-SPAR-2-615-1.

b. Transients were generated by support module and Experiment 74-21 event timers randomly when power was applied to the event timers. System configuration changes due to the transients were corrected by procedure. Reference DR 1319.

c. Measurement C15-31, Temperature, 74-30/1 sample, telemetry channel F1-15-A14, read zero (0) volt during test. The sample for Experiment 74-30/1 had no sensor attached. The sensor was installed with the flight sample. Reference DR 1370.

d. Measurement C40-AF, Temperature, AFT GPRF External Case, telemetry channel F1-15-A17, read zero (0) volt during test. A wiring error existed in the AFT GPRF internal connector J21. The mating connector to J21, P21, was rewired to be compatible with J21 connector wiring. Reference DR 1327 and Waiver ET 76-42.

e. Measurement C43-AF, Temperature, AFT GPRF Z-Wing, telemetry channel F1-15-A17, read zero (0) volt during test. A wiring error existed in the AFT GPRF internal connector J20. The mating connector to J20, P20, was rewired to be compatible with J20 connector wiring. Reference DR 1369 and Waiver ET 76-43.

f. Measurement C18-23, Temperature, 74-21/3 location 6, telemetry channel F1-15-A23, read zero (0) volt during test. The thermistor was open. The cuvette assembly was replaced prior to launch for flight. Reference DR 1372.

g. Experiment 74-10/3 Reference Junction Temperature, Measurement C26-13, telemetry output dropped to zero (0) volt at plus 253 sec during the test. The TCU was removed after the test, refurbished and retested satisfactorily. Reference DR 1326.

h. Measurement B01-MM, Sound Pressure Level, telemetry channel F1-21, read zero (0) volt during test. The acoustic sensor and amplifier were replaced. Reference DR 1316.

---

Test Title: Network Continuity Test

Procedure Number: MTCP-FS-SPAR-2-636

Test Objectives:

a. To verify that systems operation remains acceptable and that network cabling remains unchanged after installation in the Payload housing.

b. To verify that the helium system leakage rate does not exceed the maximum rate allowable to maintain minimum launch pressure.

Test Performance: The objectives of this test were met successfully. The initial leakage rate of the helium system was approximately 100 lb/hr. Rework of the helium system connections reduced the leakage rate to 30 lb/hr. Reference TDR M-SPAR-2-636-1.

---

## NONSCHEDULED TESTING

Testing of the helium system pressure transducer was made per Test Preparation Sheet (TPS) — II-1. The pressure transducer was not receiving excitation voltage. Circuitry on support module signal conditioner board A2 to provide the excitation voltage was corrected by E.O.'s 1 and 2 to drawing 95M32118. Reference TDR TPS-II-1-1.

## INTEGRATION TESTING

Test Title: Science Payload Pre-Integration Test

Procedure Number: GTCP-FS-SPAR-2-618

Test Objective: To functionally verify that no damage occurred to science payload systems during transporting operations.

Test Performance: Science payload systems were verified to be functional. One anomaly occurred during testing. Measurement K27-SM, Timer Output SPL Power, telemetry channel F1-16-B24, read 2.0 V, with variations, during test instead of ground reference (0) voltage. This condition existed when SPL power relay K13 was open and no output from the support module event timer. The telemetry multiplexer channel was open allowing the multiplexer to build a voltage. Valid information of event timer operation would be present on the telemetry channel. Reference TDR G-SPAR-2-618-1.

---

Test Title: Integration Test

Procedure Number: GTCP-FS-SPAR-2-619, 21.033NP Integration Test

Test Objective: To verify that the science payload and rocket systems perform as designed when mated.

Test Performance: The objective of this test was met successfully. All systems were operated through a simulated flight sequence. Anomalies occurring during the test were:

a. The camera for Experiment 74-21/2 did not cutoff prior to 660 sec after simulated liftoff. The frame count indicator registered four frames at end of film preventing camera cut-off. The camera is cut-off when the frame count indicator reaches zero. Cut-off of the camera occurred during retest. Reference TDR G-SPAR-2-619-1.

b. Power to the telemetry and measurement module systems was not interrupted at plus 1088 sec as programmed. Wires to pins 17, 18, and 19 of support module event timer mating connector P9 were found loose. The wires were resoldered. Reference TDR G-SPAR-2-619-2.

The event timer output pulses for SPL power off at plus 660 sec, measurement K27-SM, did not appear on telemetry channel F1-16-B24. The measurement is output on pin 18 of event timer connector. Reference TDR-G-SPAR-2-619-3. Four runs were made of the event timer after resolder of the wires with all timer output pulses and telemetry indications occurring as programmed.

## BALANCE AND VIBRATION

### Balance

The balance of the total payload, not including nose cone, was made at a rotation of 150 rpm on a spin-balance table. The lower plane for weights was in the rocket systems and the upper plane at 3.75 in. below the top of the science payload forward extension section. The balance weight mounted in the science payload at the upper plane was 2448 grams centered at 116° from 0 centerline.

### Vibration

Procedure Number: GTCP-FS-SPAR-2-627

The total payload was vibrated in x, y, and z axes and vibrations of sine sweep, sine spec, and random in each axis. The vibration levels during test were:

Sine Sweep — 10-20 Hz at 0.25 g peak; 20-2000 Hz at 1 g peak.

Sine Spec. — 110-800 Hz at 3.5 g; 800-2000 Hz at 10 g.

Random Spec. — 20-1000 Hz, 0.01-0.10 $g^2$/Hz; 1000-2000, 0.10 $g^2$/Hz.

The science payload telemetry system and measurement module were active during vibration and data transmission was monitored. No experiments were active. Review of telemetry data indicated one anomaly. Visual inspection of the payload showed no structural damage. Vibration testing was performed with water installed in the reservoirs of 74-10/2 and 74-10/3 and a flight type battery installed. The anomaly detected during review of telemetry data was two indications on measurement K12-22, 74-21/2 Camera Exposure Monitor, that the camera had attempted to operate. This occurred during random vibration. The camera would not operate during test after vibration. The camera (No. F2 7667247) was replaced with camera No. F2 7669996. Test of the replacement camera was satisfactory. Reference TDR G-SPAR-2-627-1.

---

Test Title: Science Payload Post-T& E Pre-Integration Test

Procedure Number: GTCP-FS-SPAR-2-620

Test Objective: To verify that systems operation was not degraded when subjected to a vibration environment.

Test Performance: The objective of this test was met, and all systems were verified to be operational. No anomalies occurred during the test.

---

Test Title: Post-T& E Integrated Test

Procedure Number: GTCP-FS-SPAR-2-621, 21.033 NP Post-T& E Integrated Test

Test Objective: To verify that the science payload and rocket systems perform as designed when mated.

Test Performance: The objectives of this test were met successfully. The General Purpose Rocket Furnaces (GPRF) were operated through use of a load in series with the furnace heater elements. A flight type payload battery was used for payload power. One anomaly occurred during the test. The support module event timer was reset at plus 660 sec when relay K13 was opened to interrupt experiment power. This systems malfunction would delay cut-off of power to the telemetry system and measurement module by 660 sec. During retest of the support module event timer all times occurred as programmed. The system was used "as is" because experiments system performance would not be degraded by an additional telemetry systems operation of 660 sec if the event timer reset occurred during flight. Reference TDR G-SPAR-2-621-1.

## PRE-LAUNCH TESTING AND LAUNCH

**Test Title:** Science Payload Pre-Integration Test

**Procedure Number:** WTCP-FS-SPAR-2-623

**Test Objective:** To functionally verify that no damage occurred to science payload systems during transporting operations.

**Test Performance:** All systems were verified to be functionally operational, and no damage had occurred. No anomalies occurred during the test.

---

**Test Title:** Rocket 21.033 Horizontal Test

**Procedure Number:** WTCP-FS-SPAR-2-625, 21.033 Horizontal Test

**Test Objectives:** To verify the science payload and rocket systems operate as designed and that ground support systems are ready to support a launch.

**Test Performance:** The objectives of this test were met successfully. All systems were operated through a simulated mission. The GPRF were operated through use of a load in series with the furnace heater elements. Both temperature control units (TCU's) were operated with water quench. No anomalies occurred during the test.

---

**Test Title:** Rocket 21.033 Vertical Test

**Procedure Number:** WTCP-FS-SPAR-2-626, 21.033 Vertical Test

**Test Objective:** To verify the launch readiness of the rocket systems.

**Test Performance:** All systems except experiments 74-10/2 and 74-10/3, which were previously readied for launch, were operated through a simulated flight sequence. The GPRF were operated through use of test boxes. One anomaly occurred during the test. The telemetry output of measurement K23-SM, Timer Output 74-34/2 Power on, telemetry channel F1-16-B19, was varying between 2.0 and 3.0 V, indicating the telemetry multiplexer channel was open. Valid information of event timer operation would be present on the telemetry channel. Reference TDR W-SPAR-2-626-1.

---

Test Title: 21.033 NP Science Payload Countdown and Launch Procedure

Procedure Number: WTCP-FS-SPAR-2-628

Procedure Objective: To perform close-out preparations of systems and to establish the systems configuration and necessary conditions of experiments for launch.

Test Performance: The objectives of the countdown and launch procedure were met successfully. Flight cuvettes for Experiments 74-21/2 and 74-21/3 installed were S/N's 4/2 and 4/3, respectively. Fligh. payload battery S/N 05 was installed. The internal temperature of the payload at the cuvettes for Experiments 74-21/2 and 74-21/3 was maintained at 71° F prior to launch through use of a tower environmental control system. The helium system, to be at approximately 2000 psia at launch, was pressurized to 2230 psia to allow for leakage. No anomalies occurred during countdown and launch.

## Weight and Center of Gravity Measurement

Measurements of weight and center of gravity were made of the science payload and rocket systems prior to mating to the rocket motor. Measurements taken of the payload, minus the igniter housing and nose cone, were 700 lb and 76.203 in. from aft end of RCS unit for center of gravity.

## Landline Verification

Landlines between the blockhouse and launch tower were verified to be operational prior to science payload testing on the launch tower.

## APPENDIX A

## DISCREPANCY REPORT AND TEST DISCREPANCY REPORT SUMMARY

### POST-MANUFACTURING CHECKOUT

| DR/TDR Number | Date Written/Closed | Description/Disposition |
|---|---|---|
| 1368 | 4/7/76 | Low resistance reading between forward GPRF module 1 heater and payload chassis. |
| | 4/9/76 | Closed — Forward GPRF module 1 replaced and verified. |
| 1319 | 4/10/76 | Support module and Experiment 74-21 event timers produced transients when power was applied to timers. |
| | 4/16/76 | Closed — System configuration changes due to transients corrected by procedure. Use as is. |
| 1370 | 4/10/76 | Thermistor for measurement C15-31 not installed. |
| | 4/16/76 | Closed — Thermistor installed on sample and verified. |
| 1327 | 4/10/76 | Aft furnace connector J21 not wired per drawing. |
| | 4/16/76 | Closed — Mating connector P21 rewired to correct measurement C40-AF circuitry. Waiver ET 76-42. Circuitry verified. |
| 1369 | 4/10/76 | Aft furnace connector J20 not wired per drawing. |

| DR/TDR Number | Date Written/Closed | Description/Disposition |
|---|---|---|
| 1369 | 4/16/76 | Closed — Mating connector P20 rewired to correct measurement C43-AF circuitry. Waiver ET 76-42. Circuitry verified. |
| 1372 | 4/10/76 | Thermistor for measurement C18-23 open. |
| | 4/16/76 | Closed — Cuvette assembly replaced prior to payload launch and measurement verified. |
| 1326 | 4/10/76 | Experiment 74-10/2 reference temperature, Measurement C26-13, telemetry output dropped to zero (0) volts during all-systems test. |
| | 4/16/76 | Closed — Experiment 74-10/3 TCU refurbished and retested satisfactorily. |
| 1316 | 4/10/76 | Defective amplifier for acoustic measurement B01-MM. |
| | 4/13/76 | Closed — Sensor and amplifier replaced and verified. |
| 1175 | 4/16/76 | Tubing connecting upper and lower housing of experiment 74-10/3 TCU interferred with closing payload housing door. |
| | 4/16/76 | Closed — Tubing replaced with tubing of different configuration. |
| M-SPAR-2-608-1 | 4/3/76 | Short between Experiment 74-21 cameras and payload chassis. |
| | 4/7/76 | Closed — Cameras isolated with isolation tape and washers. |

| DR/TDR Number | Date Written/Closed | Description/Disposition |
|---|---|---|
| M-SPAR-2-608-2 | 4/7/76 | Reference DR 1368 |
| | 4/9/76 | Closed |
| M-SPAR-2-610-1 | 4/3/76 | Erratic calibration operation in manual mode. |
| | 4/5/76 | Closed — Replaced manual step relay in GSE. |
| M-TPS-II-1-1 | 4/6/76 | No excitation voltage to helium system pressure transducer. |
| | 4/7/76 | Closed — Support module signal conditioner board A2 circuitry corrected to provide excitation voltage. Circuitry verified. |
| M-SPAR-2-614-1 | 4/8/76 | Crosstalk on telemetry channels adjacent to channels with event timer output pulse information. |
| | 4/9/76 | Closed — Support module signal conditioner board A2 corrected to limit voltage to telemetry to proper amplitude. |
| M-SPAR-2-615-1 | 4/10/76 | Experiment 74-21/3 camera did not cut off during All-Systems Test prior to 660 sec. |
| | 4/10/76 | Closed — Film too short to drive frame counter to zero to turn camera off. Use as is. Retested satisfactorily. |
| M-SPAR-2-615-2 | 4/10/76 | Reference DR 1319 |
| | 4/16/76 | Closed |

| DR/TDR Number | Date Written/Closed | Description/Disposition |
|---|---|---|
| M-SPAR-2-615-3 | 4/10/76 | Reference DR 137[illegible] |
| | 4/12/76 | Closed |
| M-SPAR-2-615-4 | 4/10/76 | Reference DR 1327 |
| | 4/12/76 | Closed |
| M-SPAR-2-615-5 | 4/10/76 | Reference DR 1369 |
| | 4/12/76 | Closed |
| M-SPAR-2-615-6 | 4/10/76 | Reference DR 137[illegible] |
| | 4/12/76 | Closed |
| M-SPAR-2-615 7 | 4/10/76 | Reference DR 1316 |
| | 4/13/76 | Closed |
| M-SPAR-2-636-1 | 4/15/76 | Helium system leakage rate was approximately 100 lb/hr. should be no greater than 20 lb/hr. |
| | 4/16/76 | Closed — Tubing realigned. Leakage rate reduced to 30 lb/hr. Use system as is. |

## APPENDIX B

## TEST DISCREPANCY REPORT SUMMARY
## INTEGRATION AND PRE-LAUNCH TESTING

| TDR Number | Date Written/Closed | Description/Disposition |
|---|---|---|
| G-SPAR-2-618-1 | 4/20/76 | Telemetry output of measurement K27-SM, telemetry channel F1-16-B24, was biased at 2.0 V, should be zero (0) volt. |
| | 4/21/76 | Closed — Voltage due to charge in multiplexer when channel open. Use as is. |
| G-SPAR-2-619-1 | 4/21/76 | Experiment 74-21/2 camera did not cut off prior to 660 sec. |
| | 4/21/76 | Closed — Film too short to drive frame counter to zero to cut off camera. Retest satisfactory. Use as is. |
| G-SPAR-2-619-2 | 4/21/76 | Power to telemetry system was not interrupted prior to 1200 sec after simulated liftoff. |
| | 4/22/76 | Closed — Loose wires on mating connector to event timer output connector resoldered. Retest satisfactory. |
| G-SPAR-2-619-3 | 4/21/76 | Timer output pulse, measurement K27-SM, did not appear on telemetry channel F1-16-B24. |
| | 4/22/76 | Closed — Loose wires on mating connector to event timer output connector resoldered. Retest satisfactory. |

| TDR Number | Date Written/Closed | Description/Disposition |
|---|---|---|
| G-SPAR-2-619-4 | 4/21/76 | Experiment 74-21/3 lamp assembly lens cracked. |
| | 5/3/76 | Closed — Lens replaced. |
| G-SPAR-2-627-1 | 4/29/76 | Experiment 74-21/2 camera failed during vibration test. |
| | 4/29/76 | Closed — Camera replaced and verified. |
| G-SPAR-2-621-1 | 4/30/76 | Support module event timer reset to zero when experiment power was cut off. |
| | 5/3/76 | Closed — Use system as is. |
| W-SPAR-2-626-1 | 5/14/76 | Telemetry output of measurement K23-SM varied between 2.0 and 3.0 V, should be zero (0) volt. |
| | 5/17/76 | Closed — Open circuit presented to multiplexer. Data valid. Use as is. |

# CHAPTER III

# SPACE SOLIDIFICATION OF Pb-Sb EUTECTIC

## Experiment 74-5

By

Robert B. Pond, Sr., John M. Winter, Jr.,
Stephen L. Van Doren, and David A. Shifler

Marvalaud, Inc.

PRECEDING PAGE BLANK NOT FILMED

## SUMMARY

A three part experiment was undertaken to try to produce a eutectic structure of Pb–Sb free of primary crystallization products by using microgravity to eliminate gravitational segregation problems. The eutectic alloy was flown on SPAR I, and a hypoeutectic alloy and a hypereutectic alloy were flown on SPAR II. A large number of various types of ground based samples were prepared at 1 g and compared mechanically and microstructurally with the flight specimens (over 1000 photomicrographs were taken). In addition a number of specimens were prepared under high g conditions (ranging from 2 to 1000 g), and compared microstructurally with the 1 g and microgravity specimens (80 photomicrographs).

It was found that the ground based specimens have bracketed the SPAR flight specimens with respect to mechanical properties and that there is no classification with respect to these properties that sets the SPAR flight specimens apart from the ground based ones. The eutectic composition in both has apparently been shifted due to supercooling at the solidification rates involved, but this shift is not clearly defined because of the presence of dual primary crystallization product. This dual primary crystallization product is the result of thermal supercooling. High gravitational fields tend to sweep the nuclei responsible for primary crystallization from the melt, resulting in radical segregation. In the microgravity solidification environment, the primary crystallization products were homogeneously dispersed. All other gravity fields produced more erratic dispersion of the lead dendrites.

## STATEMENT OF THE PROBLEM

### Background Information

There has been a great interest in superplasticity during the past 15 years. A search for materials which behave superplastically was instituted for two reasons. The first of these reasons was to allow a deeper understanding of this phenomenon whereby metallic materials can undergo enormous tensile strains (of the order of 100 percent) before rupturing. The second of these was to allow operations and manufacturing procedures which heretofore had not been

possible. One of these heralded operations is the deep drawing of cases and containers. A second area which has been little publicized is the use of superplastic material in shaped charge liners to enhance the penetrating power of the jet formed when the shaped charge is properly detonated. Besides having use as devices for tapping furnaces and opening up oil sands, the liners are used in warfare.

One of the materials the U.S. Army has been interested in is the eutectic of Pb-Sb. This material in the eutectic structure should be superplastic and should possess the proper average density to be an effective liner. One of the principal problems with the material is that its eutectic composition is not precise. The alloy composition for this structure should be 88.8 Pb, and although portions of a heat will solidify into a lamellar or chinese script structure of this composition there always seems to be some segregation of the primary crystallization type. Blumenthal [1] concludes that it is because of the tendency of the eutectic to supercool that this imprecision occurs.

It should be noted that the density of Pb is 11.34 and the density of Sb is 6.62 [2]. If during the solidification process, nucleation of either of these phases occurs homogeneously (or unattached to a wall or substrate) the density difference could cause a tendency to separate because of gravity. If this solidification experiment was carried out at near zero gravity then the material should not have a tendency to segregate and the imprecision problem should disappear, thereby allowing a true measurement of the superplastic properties of this material.

## Objective of the Experiment

The prime purpose of this investigation was to ascertain whether it is possible to get a faithful and complete eutectic structure in 88.8 Pb- 11.2 Sb in microgravity. With relatively high solidification rates, it is recognized that the material does supercool [1] and that because of this nonequilibrium condition, the eutectic composition will shift. It would be difficult to predict which way the eutectic point would shift, but it is certainly possible to start with the accepted eutectic composition (88.8 Pb- 11.2 Sb) and to get an off-eutectic structure because of the high rate.

It is interesting to note from the work of Varich and Yakunin [3], Borromee-Gautier et al. [4], and Ramachandrarao et al. [5] that if the solidification rate of Pb-Sb alloys is maximized and the solid solubility of Pb in Sb and Sb in Pb are extended or increased, new metastable crystalline solids can be developed and amorphous solid constituents can be identified. Certainly the solidification rate is not maximized in the rocket experiments, but because rate is increased, it was necessary to establish the extent to which these identified shifts occur.

## Approach

The experiment was carried out using three different alloys: (a) a hypoeutectic alloy (7.0 weight percent Sb), (b) a eutectic alloy (11.2 weight percent Sb), and (c) a hypereutectic alloy (18.0 weight percent Sb). As can be seen from the binary phase diagram, if supercooling to the 200°C level is experienced, then it is expected that either the 7.0 percent Sb or the 18.0 percent Sb alloy could become the eutectic composition. Supercooling to the 117°C level has been reported for pure Sb [6]. The extent to which these alloys can supercool as a function of quench rate is not known; however, such hypo- and hypereutectic alloys will allow an evaluation of the shift in the eutectic composition as a function of solidification rate.

In the rocket experiments, the abbreviated time during which microgravity is effective necessitated the use of every precaution to make sure the melt was devoid of any segregation and was absolutely homogeneous. This condition was met by mechanically mixing small particles of wrought eutectic and then consolidating the mass and not remelting again until microgravity was achieved. The abbreviated time has also necessitated the rapid solidification of the alloy which in turn required prior knowledge of the effect of such rapid solidification on the microstructure at 1 g. Such a requirement demanded a ground based study of structure as a function of solidification rate.

## SCHEDULE

Only the eutectic alloy was carried in SPAR I. The other two alloys were carried in cartridges on SPAR II.

The three alloys were prepared by the same technique (described in the next sections), and each of the alloys was sealed in stainless steel cartridges. A decision had to be made as to the integrity of the Pb-Sb in the 321 stainless cartridge when operating at the anticipated temperatures during flight. A series of experiments was therefore scheduled to investigate the corrosion of the cartridge by the alloy as a function of temperature. After it was ascertained that the welded cartridge was satisfactory, 17 loaded cartridges were delivered to MSFC and several of them used in evaluating the flight furnaces, and the balance was either flight specimens or back-up specimens.

The eutectic alloy was melted and solidified at varying rates at Marvalaud to determine the effect of the quench rate on the microstructure as well as on the mechanical properties of the alloy.

After the flights, the recovered samples were examined to determine their solidification rate (by comparison with the ground based rate studies) as well as their microstructure and their mechanical properties. Because the microstructural observations showed primary crystallization products of both Pb and Sb, additional ground based studies were carried out. In these studies, the effect of gravity constants as high as 1000 on the solidification of the three alloys was observed.

## PROCEDURE

### Cartridge Compatibility

An initial survey of the literature including appropriate binary phase diagrams raised some doubt as to the compatibility between the 321 stainless furnace cartridge and the Pb-Sb alloys. The use of a graphite liner, although considered, has the disadvantage that for a reasonable design, the flight sample would be considerably smaller (40 percent of the volume without a liner). Direct experiment showed that a TIG welded cartridge would contain the eutectic alloy satisfactorily at temperatures as high as 1000°C as long as the supply of air to the surface of the melt was restricted. The latter was accomplished experimentally by covering the top of the open cartridge with a plate of graphite. The flight specimens were sealed into the stainless furnace cartridge under vacuum to ensure that this condition was met.

## Alloy Preparation

The Sb and Pb used were Asarco Grade B-58 (99.99 + percent) from lots A-75 and 2-73, respectively. The major impurities in the Sb are 50 ppm of As and 10 ppm of Pb and Bi. The major impurities in the Pb are 7 ppm of Bi and 3 ppm of Cu. In preparing the alloys, the weighing accuracy is more than adequate to insure that the given composition will be achieved within the implied accuracy. Melts were prepared by first melting the Pb in a stainless steel crucible at approximately 400°C, deoxidizing it thoroughly, adding the Sb and immersing it to coat it with Pb, then covering the crucible with graphite and rapidly heating it to approximately 600°C. At this point the balance of the Sb can be quickly dissolved by stirring with a stainless steel rod, and the resulting alloy is quickly quenched by casting it into appropriate molds. This casting is then remelted and recast as required, but these operations can now be conducted at low temperatures, since the alloy melts at 252°C.

## Flight Sample Preparation

The flight samples were prepared by remelting at approximately 260°C and recasting the alloy into a bar approximately 1 by 3/8 by 6 in. This bar was then rolled to approximately 90 percent reduction in thickness. In the process, the alloy becomes extremely ductile. The resulting strip is cut into small pieces, and these are hydrostatically compressed to form a cylindrical briquette. This in turn was extruded with a 4.5:1 extrusion ratio to form a cylinder (with a 0.471 in. diameter) which was approximately 1 ft. Segments were then sawed from the cylinder to become specimens after the ends were machined in a lathe. Lengths ranged from 0.825 to 0.830 in. Weights and densities were measured and recorded. The specimens were then inserted into the stainless cartridges, the lids were TIG welded into place, the cartridges evacuated to approximately $1 \times 10^{-4}$ torr, and the cartridges were sealed off. Upon receipt of the flight specimen from SPAR I, the cartridge was carefully sawed open and the specimen weighed and its density measured.

## Ground Based Sample Preparation

Ground based samples were prepared using a number of different quench methods on specimens of the same size and shape as the flight specimens, except these specimens were instrumented with thermocouples. The methods are listed and described as follows:

Quench Method 1 — The melt is contained in a stainless furnace cartridge and is allowed to solidify while totally surrounded with insulating refractory brick.

Quench Method 2 — The melt is contained in a stainless furnace cartridge and is allowed to solidify while resting in quiescent air on top of a refractory brick.

Quench Method 3 — The melt is contained in a small graphite crucible and is allowed to solidify as water is poured into a bowl containing the crucible.

Quench Method 4 and 5 — The melt is contained in a small graphite crucible and is allowed to solidify as high pressure air is blown around the crucible.

Two additional quench methods were employed to prepare ground based specimens which were not instrumented with thermocouples and not used in mechanical testing, but were used as a source of microstructures for comparison. These final two are listed as follows:

Quench Method 6 — The melt is contained in a very thin walled graphite crucible and is allowed to solidify as the crucible is quickly thrust into a bowl of water.

Quench Method 7 — The melt is not contained in a crucible, but droplets of the alloy are permitted to fall into a bowl of water.

Each of the quench methods which employed a thermocouple can be characterized by some quench rate information as follows:

Quench Method 1 — 220 sec thermal arrest, approximately 0.5°C/ sec drop before and after arrest.

Quench Method 2 — 150 sec thermal arrest, approximately 1.0°C/ sec drop before and after arrest.

Quench Method 3 — No discernible arrest, average rate of approximately 20°C/ sec.

Quench Method 4 and 5 — No discernible arrest, average rate of approximately 3°C/ sec.

Finally, it can be assumed that the quench rates corresponding to quench methods 6 and 7 are much higher.

## Specimen Sectioning and Metallography

After removing the stainless steel can, a longitudinal plank was sliced off the Pb-Sb cylinder with a thin (0.018 in.) slotting saw. The cut was defined by a chord 0.100 in. from the cylinder exterior, resulting in a 0.080 in. maximum thickness plank (Fig. 1). To define the tensile specimen gage section, two longitudinal slots, 180° apart, were machined with a 3/16 in. diameter end mill which had rounded corners (Fig. 2). Transverse slices with the thin slotting saw then produced the tensile specimen wafers, approximately 0.070 in. thick. The final test specimen is shown in Figure 3. The gage length of the wafer specimens, as defined by the straignt portion of the machined opening, was 0.120 in. The gage width varied from 0.115 to 0.143 in. among all the test specimens.

Figure 1. Final test specimen.

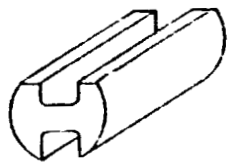

Figure 2. Machining gage section.

A gage width
B gage thickness
C gage length
D gage opening

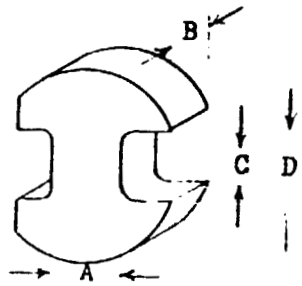


Figure 3. Final test specimen.

The machining procedure for the ground based specimens was the same as for the flight specimens. All but one of the ground based specimens (F2) were different in that the upper half of each cylinder (containing thermocouple wires) was cut off as the first step. Identification of the wafers from each cylinder was achieved using a numbering system as shown in Figure 4. The wafers were numbered consecutively, beginning with 1, from the uppermost (relative to gravity) slice from the ground based cylinders and from an assigned end of the flight cylinders. It should be noted that at the ends of each cylinder typically a very thin wafer is cut to provide an initial parallel surface. Hence, for example, wafer 2 is the first flight tensile wafer.

The faces of each wafer were then ground by hand on silicon carbide papers, finishing with a 600 grit paper. One face of each specimen was then polished for metallographic inspection. A coarse polish was achieved on wet Buehler microcloth which was covered with a thick paste of levigated (15 $\mu$) alumina and water. Using one fingertip to hold the specimen with moderate pressure on the stationary polishing cloth, the specimen was rotated in 2 in. circles for approximately 3 to 5 min. Following a water rinse, the specimen was ready for final polishing on wet microcloth on top of flat glass with a thick paste of Linde B alumina (0.5 $\mu$) and water. Approximately 5 ml of fresh etchant (1 part ammonium hydroxide; 2 parts 3 percent hydrogen peroxide; and 3 parts water) were added to the paste before the actual polishing of each specimen. Polishing was achieved as with the coarse polishing for approximately 2 to 5 min. Immediately after rinsing the specimen with water, the specimen was dried with a blast of nitrogen gas.

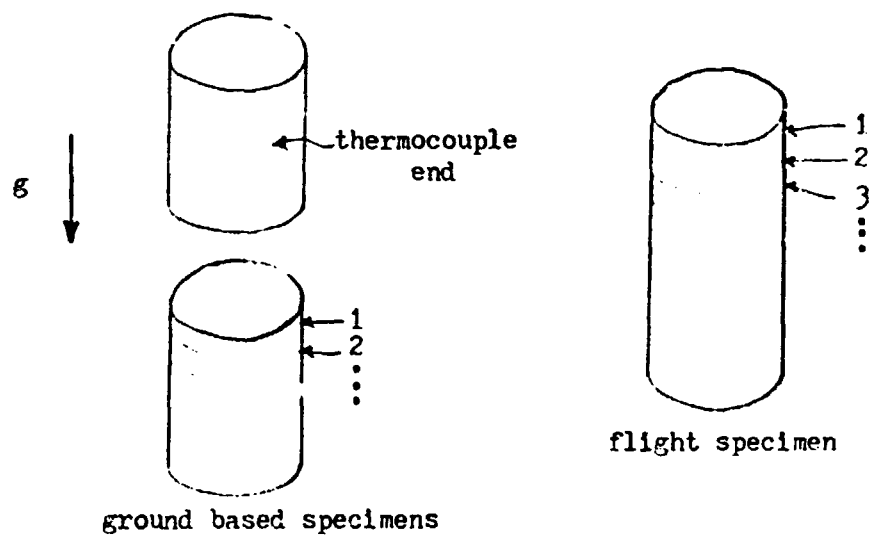


Figure 4. Identification of tensile wafers.

## Mechanical Testing

To justify the assertion that tensile tests of specimens with these unorthodox dimensions would produce meaningful data, preliminary testing was made of Pb-Sn eutectic alloy. Two mechanical states of Pb-Sn were tested: 40 percent rolled reduction in thickness, and greater than 88 percent reduction in thickness by rolling. The latter material exhibits superplasticity at crosshead rates of near 0.01 cm/ min. The tensile specimens were approximately the same size and shape as those tested later in the Pb-Sb study, and the specimen grips, testing machine, and crosshead rate were also the same. In the Pb-Sn tests, the greater than 88 percent rolled material produced elongations from 1200 to 1800 percent while the 40 percent rolled material elongated no more than 500 percent. This demonstrates the sensitivity of the mechanical test to material properties.

The tensile tests were performed on a two screw testing machine with a constant crosshead rate. All tests were completed at a crosshead rate of 0.009 cm/ min. Eighty-two specimens were tested in all. Testing temperature was room temperature.

The specimen grips utilized sliding, tapered clamps, producing a wedge effect to hold the thin, soft specimens (Fig. 5). Loads were determined by a bending beam load cell connected in series with the grip system. Output of the beam strain gages was monitored at timed intervals on a Vishay/ Ellis 10 Portable Strain Indicator. Dead weight loading was used to calibrate the system to within 1/ 4 lb. In addition to load-time information, a specimen total elongation was measured after rupture. The two pieces were fitted back together and the gage opening, previously defined by the milling operation, was measured at both sides with a vernier caliper while viewing at 7X through a stereo microscope. Elongation values could not be taken from crosshead displacements, because the wedge grips operate with varying amounts of movement before positively gripping each specimen.

## OBSERVATIONS AND DATA

The eutectic flight specimen from the SPAR I flight had rounded edges on both ends indicating that it had been solidified in a microgravity environment. However, the hypoeutectic and hypereutectic specimens from the SPAR II flight

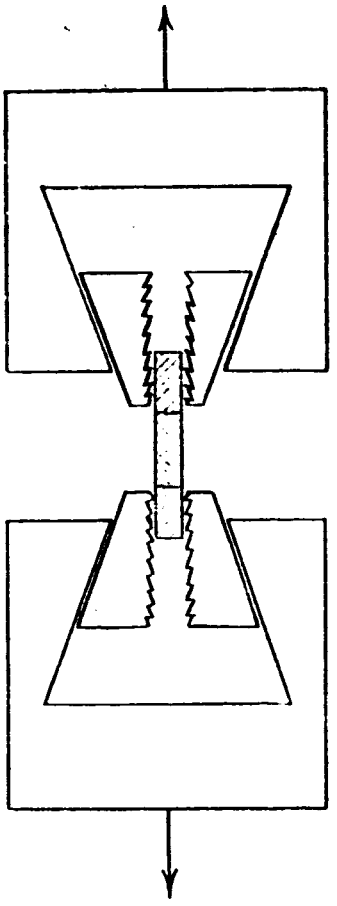

Figure 5. Specimen wedge grips.

showed sharp corners on the vent tube end and extrusion of the alloy for a short distance into the vent tube. Upon sectioning these specimens, it was found that a cavity (or cavities) existed in the approximate center of these specimens or the end nearest the vent tube. An acceptable explanation of these cavities has not been determined. However the presence of the cavities and their location in the specimens severely limited the mechanical test evaluation for these two alloys.

## Mechanical Testing Data

Eighty-two tensile tests were conducted in all, 27 of which were specimens from the flight samples. Some of the resulting data for each test are listed in the Appendix. Figure 6 shows peak stress versus strain at fracture for all the eutectic tests. It is to be noted that the peak stress is essentially constant regardless of the elongation (or strain) exhibited at fracture. This means the modulus of toughness (or the area under an individual stress-strain curve) is essentially directly and linearly proportional to the ductility for all tests. It is also true that almost all the eutectic ground based specimens from quench methods 3, 4, and 5 are more ductile than ground based specimens from quench methods 1 and 2. This can be seen from the data in the Appendix. It should also be noted that the mechanical properties of the eutectic flight specimens are well bracketed by the eutectic ground based specimens. Figure 7 shows peak stress versus strain at fracture for the hypoeutectic and hypereutectic tests.

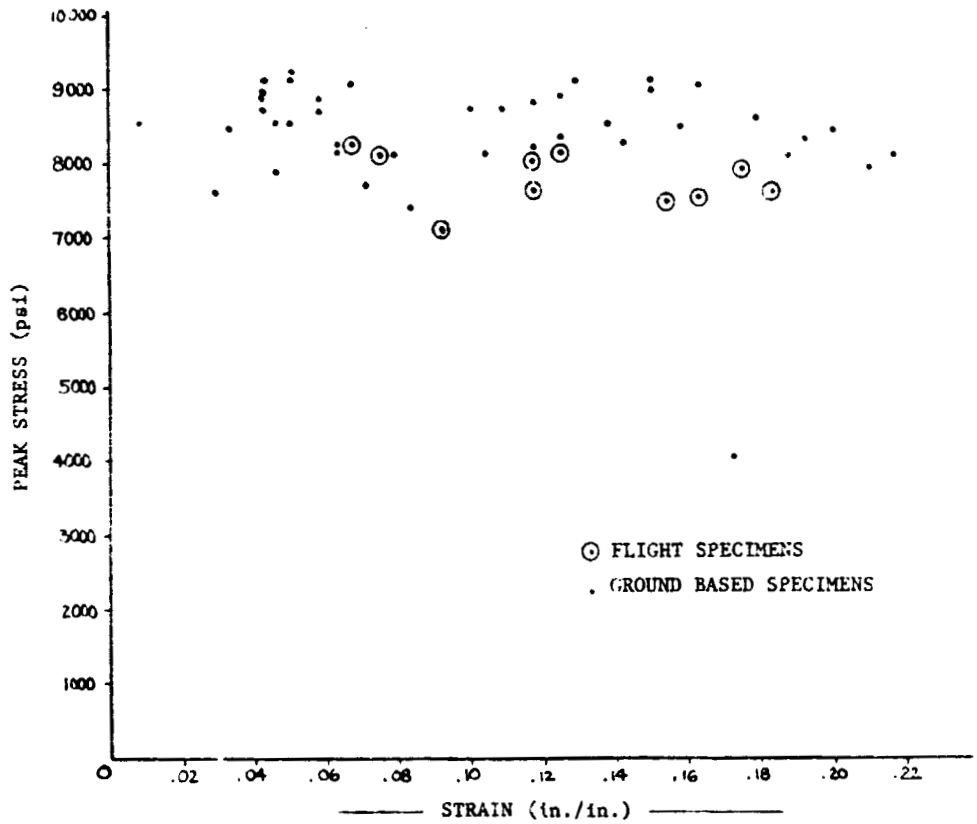


Figure 6. Peak stress versus strain at fracture for eutectic specimens.

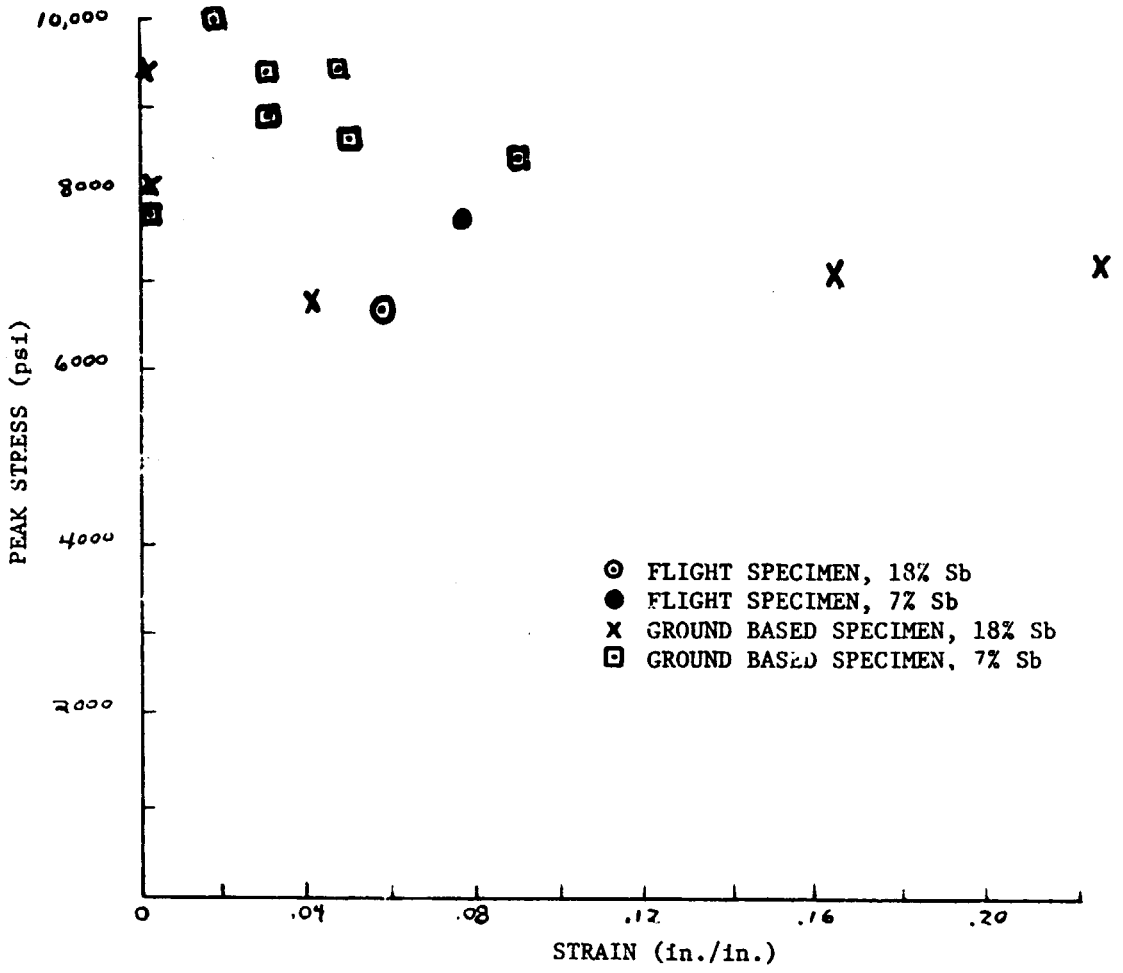


Figure 7. Peak stress versus strain at fracture for hypoeutectic and hypereutectic specimens.

## Microstructural Observations

Approximately 1040 photomicrographs were taken of ground based and flight specimens. In these photomicrographs, the lead phases are dark and the antimony phases are light, as a result of the etching procedure used.

Figures 8, 9, and 10 illustrate the microstructures from the flight specimens. The black areas in Figures 8 and 10 are voids.

ORIGINAL PAGE IS
OF POOR QUALITY

Figure 8. Typical microstructure for hypoeutectic flight specimen (255X).

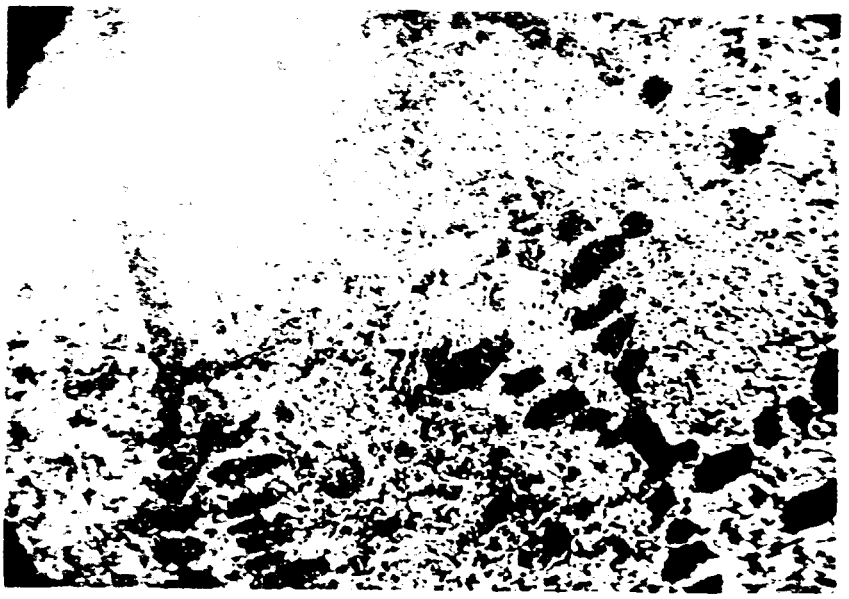

Figure 9. Typical microstructure for eutectic flight specimen (255X).

Figure 10. Typical microstructure for hypereutectic flight specimen (255X).

## DISCUSSION OF OBSERVATIONS

Approximately 700 of the photomicrographs of the tensile specimens were closely examined using standard methods of quantitative mellography (255X and 64X). The average dendritic arm spacing was determined for the lead dendrites in each specimen. The results are listed in the Appendix and are shown in Figures 11 and 12 in which the arm spacing is plotted versus ductility. There is a correlation between the two, although there is a lot of scatter in the data. It is to be noted that the flight specimens do not stand apart in the plots.

Additionally, a characteristic eutectic lamellar spacing was determined for a number of specimens (but not all) using statistically valid methods quantitative metallography. The results are listed in the Appendix and are shown in Figures 13 and 14 as plots of lamellar spacing versus ductility. Here again a correlation exists although the data show scatter, and the flight specimens do not stand apart from the ground based specimens.

Figures 11 through 14 show parameters proportional to solidification rate plotted versus ductility.

ORIGINAL PAGE IS
OF POOR QUALITY

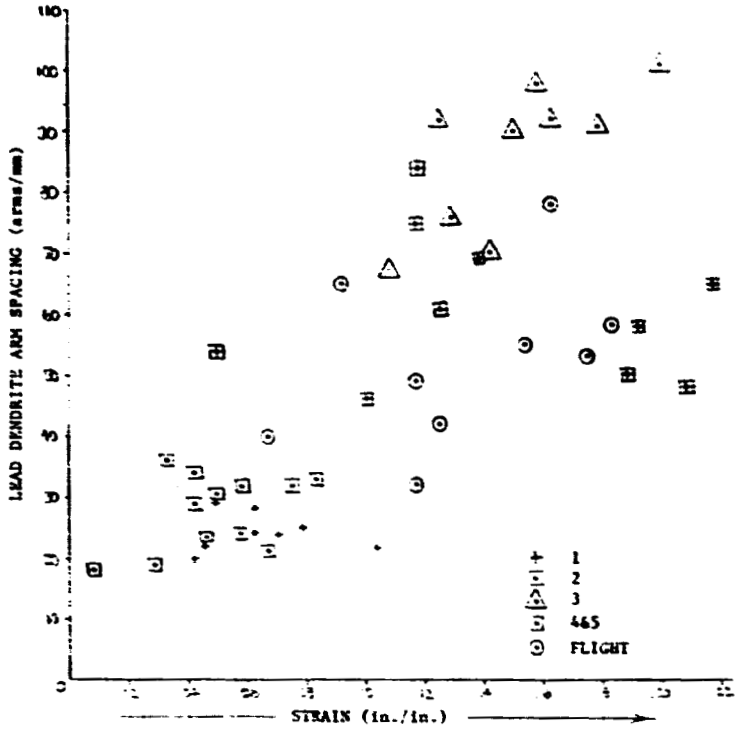


**Figure 11. Lead dendrite arm spacing versus ductility for eutectic specimens.**

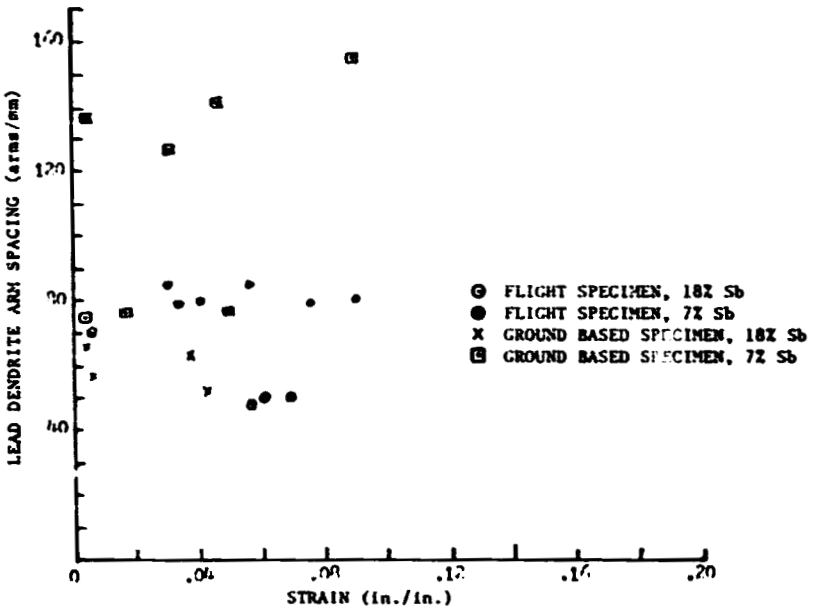


**Figure 12. Lead dendrite arm spacing versus ductility for hypoeutectic and hypereutectic specimens.**

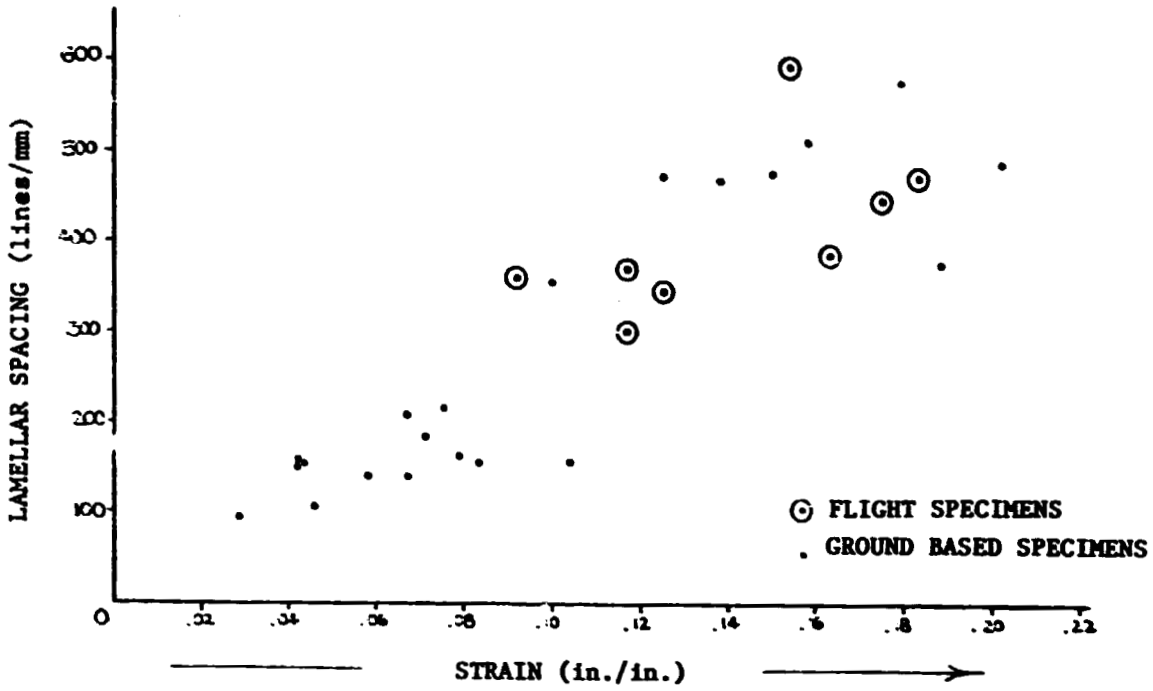


**Figure 13. Eutectic lamellar spacing versus ductility for eutectic specimens.**

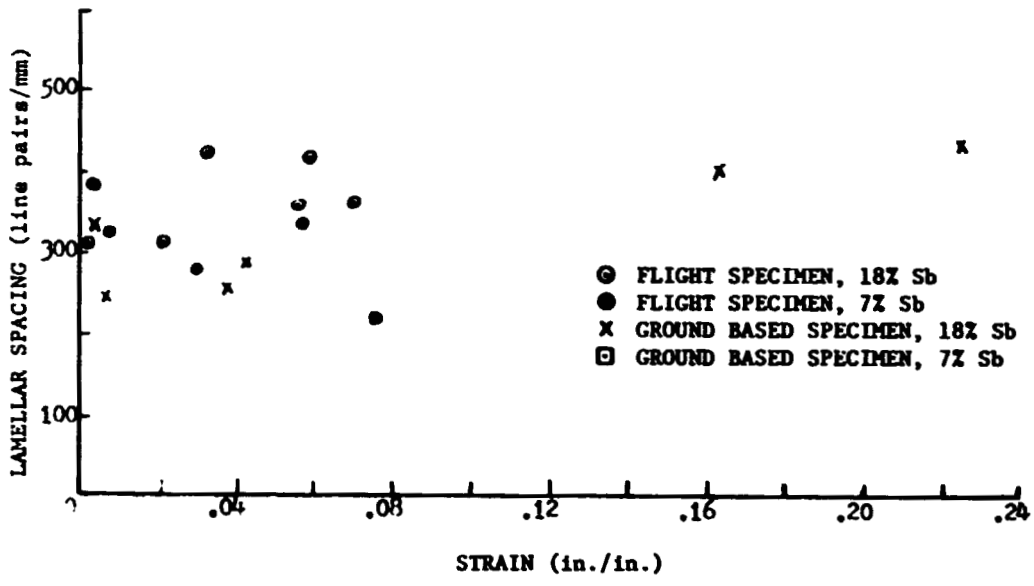


**Figure 14. Lamellar spacing versus ductility for hypoeutectic and hypereutectic specimens.**

Figure 9 shows blocky white Sb primary crystallization product either adjacent to or within primary Pb crystallization product. This mixed primary product seems to be characteristic of these alloys solidified at these rates. If one is to believe that the solidification process is governed by the equilibrium diagram for Pb-Sb, such a complimentary product is not reasonable. The phenomenon occurs in flight and ground based specimens.

It was observed that primary Sb dendrites occur at very high quench rates indicating that as quench rate is increased the microstructure changes from one with primary Pb dendrites to primary Sb dendrites.

## HIGH g EXPERIMENTS

In an endeavor to explain the anomalous dual primary crystallization products witnessed in the ground and flight specimens, a series of alloys was centrifuged for varying times and at various g levels and the subsequent microstructures examined.

The specimens in these tests were melted in steel cavities 1/4 by 5/8 in. The plane of rotation of these specimens was perpendicular to the Earth's gravity direction.

Preliminary experiments were conducted wherein hypoeutectic, hypereutectic, and eutectic alloys were held at approximately 1000 g level during heating to temperatures slightly above the liquidus temperature for various times after which they were solidified while still under the influence of the high g field. Figure 15 is a macrograph of a eutectic composition showing the segregation typically witnessed in such solidifications. In all cases (hypoeutectic, eutectic, or hypereutectic) considerable segregation was inidicated. Such a segregation of antimony at the low g end and lead at the high g end is not too surprising when one considers that (presuming no viscosity effects) the separation time over the specimen length is of the order of 1 msec at 1 g and the solidification time is of the order of 1 sec. The solidification time at 1000 g is still approximately 1 sec, but the separation time is of the order of microseconds.

Because of this radical segregation, the high g experiments were conducted in the following way. For each alloy the specimen was heated slightly above the liquidus, the selected rotational gravity field imposed for the selected time, the rotational gravity field returned to zero, and then the specimen solidified. Using this recipe an alloy of each of the compositions (7, 11.2, and 17 percent Sb) was rotationally accelerated to 1, 25, 280, and 1000 g for times of 0.1, 1, 10, 100, and 1000 min.

Figure 15. Macrograph of sectioned capsule showing segregation in eutectic solidified at 1000 g (10X).

Following solidification each specimen was longitudinally sectioned and metallographically examined. It was observed that, although dual primary crystals were observed in every case, the size of the Pb particles increased with time and with an increase in g. This is illustrated in Figure 16 which shows the diameter of the Pb particle as a function of product of time at high g and g. Figures 17, 18, and 19 show the microstructural appearance of the hypoeutectic alloy solidified after being at 25 g for 0.1, 10 and 100 min. It should be noted that 1 g for 1000 min is not exactly equivalent to 1000 g for 1 min and that the Earth' s gravity field effect on the 1.0 g rotational field is less effective than the Earth' s gravity field on a 1000 g rotational field. It is felt that this difference is indicated in the data of Figure 16 and in the microstructures.

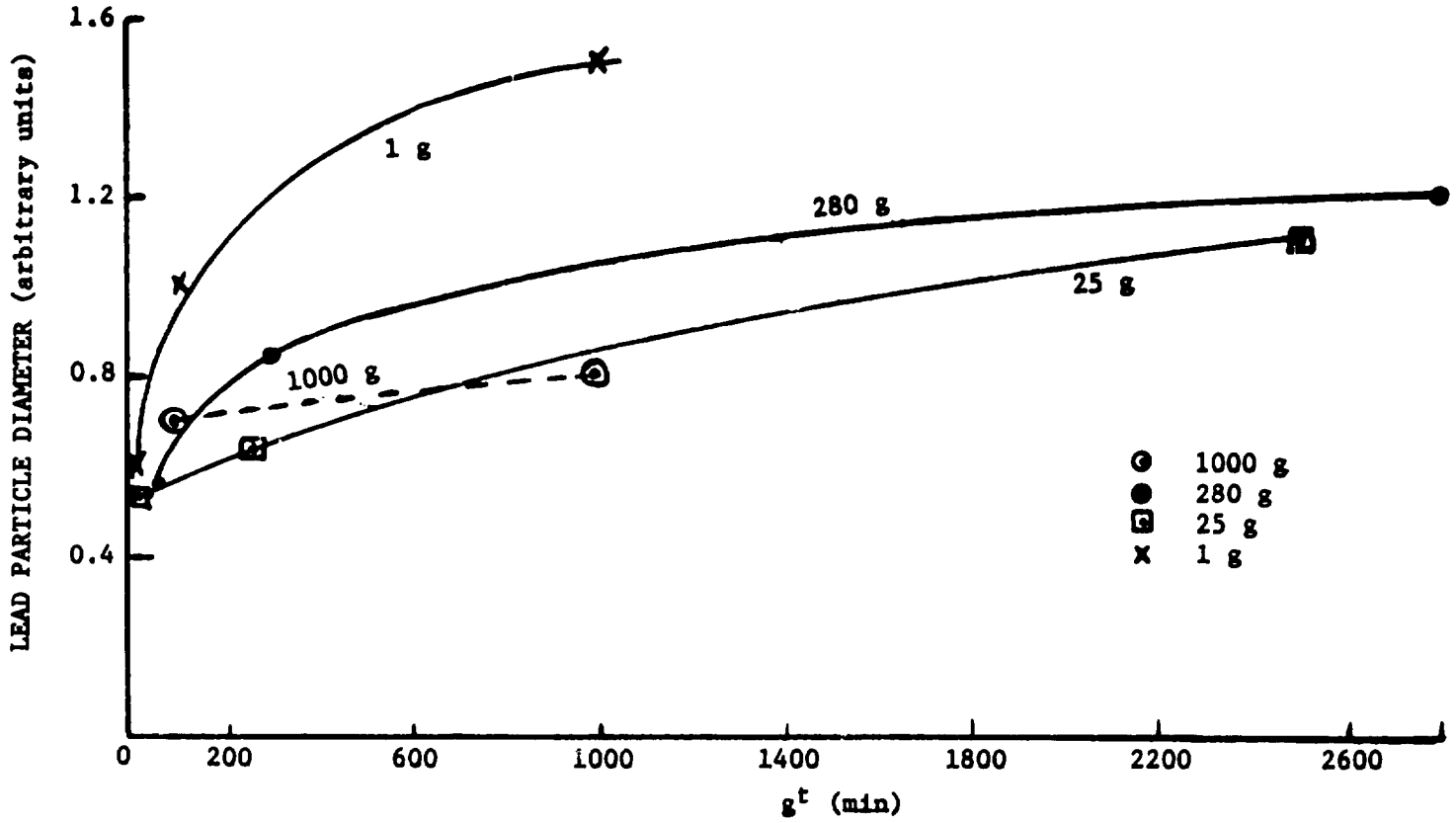


Figure 16. Lead particle diameter versus $g^t$ for hypoeutectic Pb-Sb (7.0 weight percent Sb).

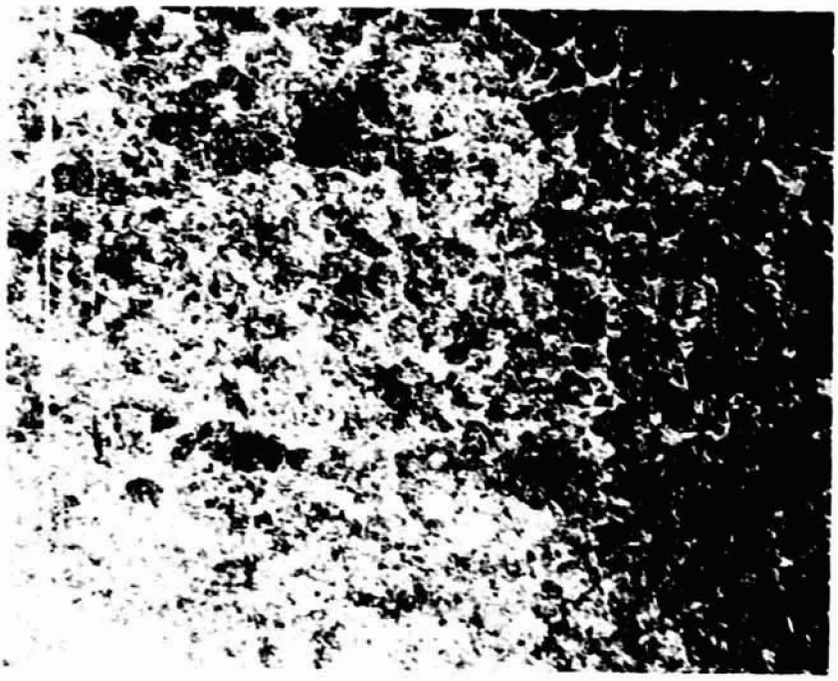

Figure 17. Typical microstructure of hypoeutectic after 0.1 min at 25 g (137X).

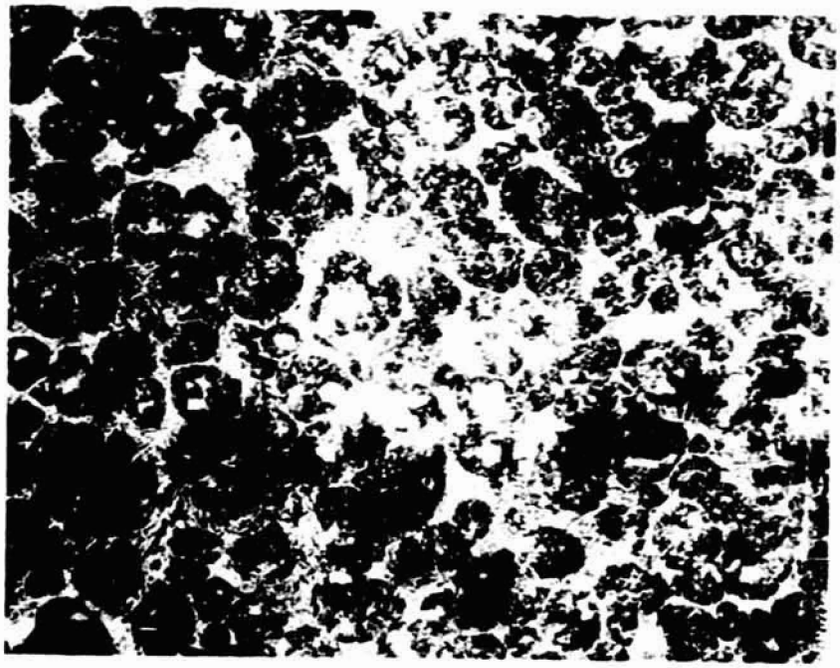

Figure 18. Typical microstructure of hypoeutectic after 10 min at 25 g (137X).

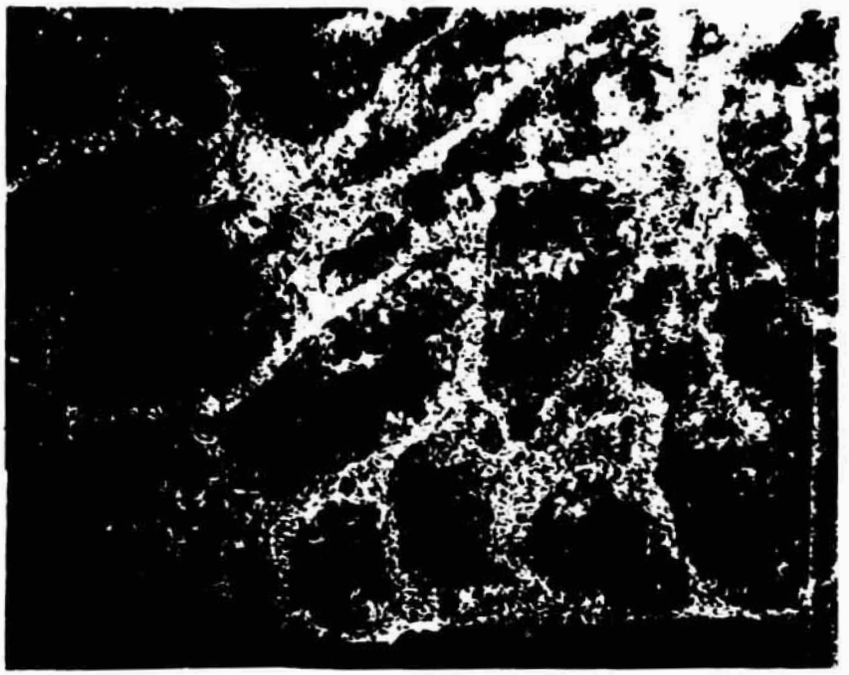

Figure 19. Typical microstructure of hypoeutectic after 100 min at 25 g (137X).

It would be expected that if the primary lead particle size increases with the $g^t$ product and if the volume of primary lead remains constant for each alloy, the number of lead particles (or dendrites) would decrease with increasing $g^t$ product. Although there is considerable scatter in the data, this seems to be as in Figure 20.

Study of the microstructures indicates that Sb is the nucleating phase in the eutectic reaction and does most often nucleate the Pb dendrites. The size increases of the Pb particle and the number of particles decreases can be interpreted as evidence that the number of Sb rich nuclei are decreasing as a function of the $g^t$ product. If this effect is extrapolated to micro-g, one would expect to find many dendrites very homogeneously distributed. This is in fact what is observed in all flight specimens.

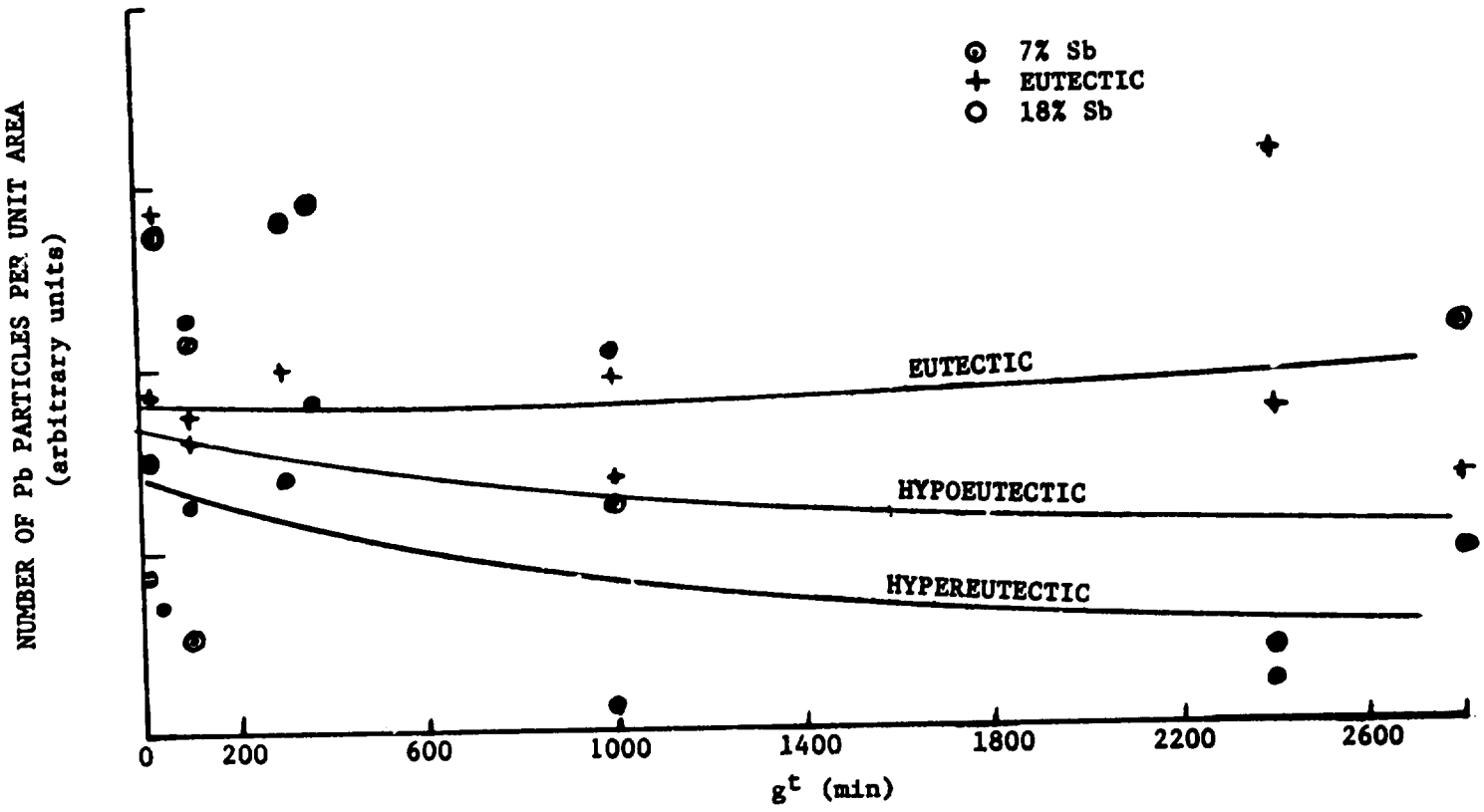


Figure 20. Number of lead particles versus $g^t$.

## CONCLUSIONS

1. It has been found that the ground based specimens have bracketed the SPAR flight specimens with respect to mechanical properties and that there is no classification with respect to these properties that sets the SPAR flight specimens apart from the ground based ones. There is no discernable difference between them. Due to the cavities found in the SPAR II specimens only a minimum number of mechanical tests were possible; however, the microstructural portrayal overrode this deficiency.

2. The eutectic composition in the flight specimens and ground based specimens has apparently been shifted due to supercooling at the solidification rates involved, but this shift is not clearly defined due to the presence of dual primary crystallization product.

3. The dual primary crystallization product is the result of thermal supercooling in the Pb-Sb alloys.

4. The radical segregation of the anomalous primary crystallization products is gravity driven.

5. High gravitation fields tend to sweep the nuclei responsible for primary crystallization from the melt. This sweeping action however results in radical segregation.

6. Due to the microgravity field experienced during solidification of the SPAR specimens, the primary crystallization products were homogeneously dispersed. All other gravity fields produced more eratic dispersion of the Pb dendrites.

## REFERENCES


1. Blumenthal, B.: Trans. AIME, 156, 240 (1944).

2. Metals Handbook, 8th Ed., 1, 53, Am. Soc. for Metals, Metals Park, Ohio (1961).

3. Varich, N. I. and Yakunin, A. A.: The Solubility of Cd, Mg, Sb, & Sn in Pb on Quenching the Alloys Form the Liquid State. Russian J. Phys. Chem. 41, 437 (1967) (From Zhur. Fiz. Khim.), 41, 844 (1967).

4. Borromee-Gautier, C., Giessen, B. C., and Grant, N. J.: Metastable Phases in the Pb-Sb and Pb-Bi Systems. J. Chem. Phys., 48, 1905 (1968).

5. Ramachandrarao, P., Garg, P. K., and Anantharaman, T. R.: Rapid Quenching of Liquid Pb-Sb Alloys. Indian J. Technol., 8, 263 (1970).

6. Hollomon, J. H. and Turnbull, D.: Progress in Metal Physics, 4, 356, Bruce Chalmers, ed., Pergamon Press, London (1953).

## APPENDIX

## MECHANICAL AND MICROSTRUCTURAL DATA

### Eutectic Specimens

Specimen No. Code: XYZ X = melt; Y = quench method; Z = wafer number (Fig. 4)

Melts A, C, and F all ground based; U, flight samples

| Specimen Number | Peak Stress (psi) | Elongation (Δ1)(in.) | Strain (in./in.) | Dendrite (arms/mm) | Lamellar Spacing (lines/mm) |
|---|---|---|---|---|---|
| C23 | 8560 | .001 | .008 | 18 | |
| C22 | 7610 | .0035 | .029 | 19 | 98 |
| A24 | 8470 | .004 | .033 | 36 | |
| C15 | 8970 | .005 | .042 | 20 | 152 |
| A25 | 9130 | .005 | .042 | 29 | 154 |
| F29 | 8730 | .005 | .042 | 34 | 153 |
| F27 | 8930 | .005 | .042 | | |
| A15 | 8540 | .0055 | .046 | 22 | 106 |
| F28 | 7920 | .0055 | .046 | 23 | |
| A53 | 9120 | .006 | .050 | 54 | |
| A13 | 8540 | .006 | .050 | 29 | |
| F23 | 9240 | .006 | .050 | 30 | |
| C24 | 8880 | .007 | .058 | 24 | |
| A23 | 8710 | .007 | .058 | 32 | 140 |
| A14 | 8270 | .0075 | .063 | 28 | |
| C14 | 8160 | .0075 | .063 | 24 | |
| C25 | 9070 | .008 | .067 | 21 | 140 |
| U8 | 8270 | .008 | .067 | 40 | 209 |
| C12 | 7720 | .0085 | .071 | 24 | 183 |
| F21 | 8130 | .009 | .075 | 32 | 215 |
| A12 | 8120 | .0095 | .079 | 25 | 162 |
| F22 | 7420 | .010 | .083 | 33 | 155 |
| U3 | 7130 | .011 | .092 | 65 | 360 |
| A52* | 8750 | .012 | .100 | 46 | 356 |
| C13 | 8150 | .0125 | .104 | 22 | 158 |
| A33 | 8760 | .013 | .108 | 67 | |
| A54* | 8830 | .014 | .117 | 75 | |
| A44 | 8240 | .014 | .117 | 84 | |
| U10 | 8050 | .014 | .117 | 32 | 300 |
| U4 | 7650 | .014 | .117 | 49 | 370 |
| C31* | 8920 | .015 | .125 | 92 | 471 |

| Specimen Number | Peak Stress (psi) | Elongation ($\Delta l$)(in.) | Strain (in./in.) | Dendrite (arms/mm) | Lamellar Spacing (lines/mm) |
|---|---|---|---|---|---|
| A43 | 8360 | .015 | .125 | 61 | |
| U9 | 8160 | .015 | .125 | 42 | 346 |
| A32* | 9140 | .0155 | .129 | 76 | ? |
| A55* | 8560 | .0165 | .138 | 69 | 468 |
| C34* | 8510 | .017 | .142 | 70 | |
| C32 | 9150 | .018 | .150 | | |
| A34* | 9020 | .018 | .150 | 90 | 475 |
| U5 | 7510 | .0185 | .154 | 55 | 593 |
| C35* | 8530 | .019 | .158 | 98 | 510 |
| C33 | 9080 | .0195 | .163 | 92 | |
| U2 | 7590 | .0195 | .163 | 78 | 384 |
| U7 | 7960 | .021 | .175 | 53 | 443 |
| A36* | 8630 | .0215 | .179 | 91 | 575 |
| U6 | 7660 | .022 | .183 | 58 | 470 |
| C42 | 8130 | .0225 | .188 | 50 | 376 |
| C43 | 8360 | .023 | .192 | 56 | |
| A35* | 8500 | .024 | .200 | 101 | |
| C45 | 7960 | .025 | .208 | 48 | 485 |
| C44 | 8130 | .026 | .217 | 65 | |

*"Fine" dendrites, category (c), see section on Observation and Data

## Hypereutectic and Hypoeutectic Specimens

| Specimen No. Code: | Quench Method | Specimen Code |
|---|---|---|
| P = 7 percent Sb hypoeutectic ground based specimen | 3 | P2X, S2X |
| S = 18 percent Sb hypereutectic ground based specimen | 4, 5 | P1X. S1X |
| L = 7 percent Sb hypoeutectic flight specimen | | |
| R = 18 percent Sb hypereutectic flight specimen | | |
| 1, 2, 3 etc. as given in Figure 4. | | |

| Specimen Number | Peak Stress (psi) | Strain (in./in.) | Dendrite (arms/mm) | Lamellar Spacing (line pairs/mm) |
|---|---|---|---|---|
| P12 | 8680 | .0481 | 77 | -- -- |
| P13 | 10000 | .0160 | 76 | -- -- |
| P14* | 4690 | -.0027 | 82 | -- -- |
| P15 | 9410 | .0294 | 74 | -- -- |
| P22 | 8480 | .0882 | 155 | -- -- |
| P23 | 7830 | .0027 | 136 | -- -- |
| P24 | 9400 | .0455 | 142 | -- -- |
| P25 | 8920 | .0294 | 127 | -- -- |
| S12 | 9470 | .0027 | 66 | 338 |
| S13 | 7930 | .0053 | 56 | 245 |
| S14* | 5710 | .0374 | 63 | 256 |
| S15 | 6830 | .0428 | 52 | 288 |
| S22 | 7170 | .1631 | -- | 404 |
| S23 | 7250 | .2246 | -- | 437 |
| L1* | 5430 | .0588 | No photos taken | |
| L2 | -- | -.0134 | 76 | 240 |
| L3 | -- | -- | 91 | 260 |
| L4* | 3850 | .0294 | 85 | 280 |
| L5* | 5810 | .0561 | 85 | 340 |
| L6* | 5920 | .0882 | 81 | -- -- |
| L7* | 5170 | .0321 | 79 | -- -- |
| L8* | 5560 | .0401 | 80 | -- -- |
| L9 | 7770 | .0749 | 79 | 220 |
| R1* | -- | -- | -- | -- -- |
| R2 | 6 :0 | .0588 | 50 | 420 |
| R3* | 5630 | .0688 | 50 | 363 |
| R4* | 6030 | .0321 | -- | 426 |
| R5* | 6150 | .0214 | -- | 314 |
| R6 | 6680 | .0561 | 48 | 361 |
| R7* | 1370<br>2160 | .0053 | 70 | 335 |
| R8* | -- | .0027 | -- | 393 |
| R9* | -- | 0 | -- | 314 |

*All mechanical tests with asterisks had voids within the gauge length and are therefore not considered valid.

# CHAPTER IV

# FEASIBILITY OF PRODUCING CLOSED-CELL METAL FOAMS IN A ZERO GRAVITY ENVIRONMENT FROM SPUTTER-DEPOSITED INERT GAS-BEARING METALS AND ALLOYS

## Experiment 74-10

By

J. W. Patten and E. N. Greenwell

Battelle-Northwest Laboratories

## ABSTRACT

This report describes technical results obtained on SPAR II flight from Experiment 74-10. These results are considered together with results of related experiments obtained on the SPAR I flight and conclusions are presented.

## SUMMARY

This report describes technical results obtained on the second SPAR flight from Experiment 74-10. These results are considered together with results of related experiments obtained on the first SPAR flight [1] and conclusions are presented. The experiments from both SPAR flights represent a 1 year feasibility study. They were critical experiments because development and operation of a new furnace design with an associated fully automatic electronic control package were required in addition to demonstration of the metal foam formation concept.

The process of metal foam formation from sputtered deposits was demonstrated in 1 g and zero g environments. Very uniform cell size foams were produced in 1 g in one series of experiments, possibly because a very thick oxide scale was allowed to form, thus providing uniform constraints to the samples. Bubble coarsening was observed in these samples with increasing time above the melting point. In other 1 g experiments and in all zero g experiments, the oxide scales fractured during expansion of the foam, providing nonuniform sample constraint. In the thickest samples foamed in zero g, much more bubble coarsening and a larger void volume fraction were observed with increasing time above the melting point. However, the effects of the oxide scale were still quite pronounced and kinetic information on foam formation behavior was not obtained. It is also believed that much more difference would be noted between ground-based and zero g foam behavior without mechanical restriction from oxide scale. Mechanical constriction should be examined independently by providing a closed container for the foaming material since there may be an effect on bubble coalescence. Also the sample section should remain large or be increased relative to expected bubble size to minimize the effects of sample surfaces on bubble movement in the molten sample.

It is believed that the zero g environment will be essential to prevent density driven bubble segregation and retain preformed shapes in anything but the simplest geometries and smallest sizes of useful engineering materials, particularly since large cross-sections will require slower heating and cooling. The current experiments were restricted to Al because of furnace temperature limitations and the desire to examine a commercially important material. However, since future experiments should be conducted with a metal which does not form a strong and adherent oxide, maximum furnace temperature should be extended to at least 1080°C to allow experimentation with copper.

# INTRODUCTION

## Foam Formation Concept

Experiments to examine the possibility of manufacturing controlled density metals (metal foams) in space were first initiated by General Dynamics/ Convair [2]. Manufacture of these foams was regarded as desirable because of their unique characteristics such as high stiffness-to-density ratio, high damping capability, high impact resistance, and low thermal conductivity. Such foams, unlike similar ceramic materials, are expected to be electrically conducting and to lend themselves to fabrication by conventional metal forming, welding, brazing, etc., techniques.

Potential applications for these metal foams include:

1. Hydride formers such as the Fe-Ti system for hydrogen storage cells.

2. Fusion reactor fuel cells.

3. Fissile fuel element material.

4. Structural materials with requirements for one or more of the following properties:

   a. High structural modulus.

   b. Low density.

   c. High resistance to environmental effects.

   d. Conductivity.

   e. Easy fabrication.

   f. High damping coefficients.

5. Deep sea components, armor.

6. Tip seals for gas turbine blade protection.

Closed-cell foams would be particularly attractive in many of these applications due to isolation of each cell from its neighbors and the environment. If similar foam structures could be fabricated from nonmetallic crystalline materials and glasses, they should find application in areas requiring low density, very low conductivity, good corrosion resistance and resistance to other environmental effects, retention of properties to high temperature, and very good thermal shock resistance.

The methods first proposed for producing these foams, however, are complicated, require equipment that has not been fully developed, and are restrictive as to the gas-metal combinations that may be examined.

## Battelle-Northwest Experiments to Produce Metal Foams in Space

An alternative method with none of these shortcomings was applied by Battelle-Northwest (BNW) to produce metal foam materials on flights conducted by the SPAR I project in a Phase I feasibility investigation.

Briefly, the technique consists of high-rate sputter depositing, in a 1 g environment, the pure metal or alloy to be foamed under such conditions that a controlled quantity of the inert sputtering gas is trapped uniformly throughout the deposit. Next this metallic deposit is melted in a zero g environment, allowing the inert gas atoms to coalesce, produce bubbles, and expand to provide a closed cell foam structure. On cooling, the foam solidifies and the atmosphere within each bubble is high-purity, low-pressure inert gas, effectively a high quality vacuum.

Experiments preliminary to the first proposal were conducted in a 1 g environment. Trapped inert gas contents of 0 to 2200 ppm were reproducibly achieved during sputter deposition. When samples of these materials were very rapidly heated by discharge of a capacitor bank and immediately cooled, a metal foam was obtained. However, this technique of rapidly heating and cooling is only applicable to thin specimens, primarily due to RF skin effects. Slower heating necessitates longer times at temperature above the melting point. Here the inertia of the molten metal is overcome, relative density differences causes separation of molten metal and gas, bubbles coalesce, and a general effect similar in outward appearance to boiling is observed. When this occurs, a uniform metal foam does not result.

It was expected that similar experiments in a zero g environment would produce quite different results. Specifically, it was expected that there would no longer be a density difference driving force to induce separation of the gas bubbles from the metal matrix. Relative surface energies, the ideal gas laws, and viscosity of the molten metal would be expected to govern behavior. It should therefore be possible to control bubble size, bubble frequency, bubble wall thickness, and the resulting foam density over a wide range by varying trapped gas content, melt temperatures, and time at temperature.

The fundamental distinctions between the Battelle series of experiments and the experiments previously conducted arise from the method of incorporating the gas in the metal. Gas trapping during sputter deposition is a well documented phenomenon, although trapping mechanisms are poorly understood [3-8]. This gas trapping allows a very wide range of metals and alloys to be considered, permits a great simplification of in-flight experimental apparatus (only radiant heating, quenching, and temperature sensing equipment are required) and makes use of an extensive sputtering technology that is already well established.

## OBJECTIVE

The long-range objective of the program initiated by this Phase I feasibility study is to produce metal foam materials from sputtered metal deposits. It is anticipated that these foams will be produced with a wide range of preselected and reproducible densities and uniform, isolated, evacuated cells. It is further anticipated that the foams will be produced from a wide range of metallic materials and in complex shapes usable in engineering applications.

The work required to achieve this long range objective was divided into three phases. As originally proposed, Phase I was to be completed in the first 2 years. However, Phase I was rescheduled to be completed in the first year to aid NASA/MSFC in attaining their flight scheduling objectives. The results of the Phase I experiments will be used to direct the experiments in Phases II and III.

### Phase I — Feasibility

1. Produce inert gas-bearing metal sputtered deposits and melt small samples of these deposits in a zero g environment to produce a foam. Evaluate

the effects of gas concentration, melt temperature, and time at melt temperature on foam structure and foaming kinetics. Correlate results with data from similar experiments conducted in a 1 g environment. Formulate a model describing the effects of gravitational fields on the behavior of gases in molten metals. Measure basic physical and mechanical properties of foam samples to predict suitability for engineering applications.

2. Produce hollow right-circular cylinders of inert gas-bearing metal by sputter deposition and melt samples of these deposits in a zero g environment to produce foamed shapes. Evaluate the feasibility of accurately predicting the shape and dimensions of complex parts formed in this manner.

### Phase II — Experimental Scale-Up

1. Investigate zero g production of more massive foam products from large sections of thick sputtered deposits.

2. Investigate additional metal (or alloy) inert gas systems.

3. Investigate reproducible production of more complex shapes, including complex curvatures.

4. Investigate forming, cutting, welding, and brazing of metal foams.

### Phase III — Fabrication of Prototypic Configurations for a Specific Application

## APPROACH

### Phase I — Feasibility

The experimental approach to this phase, the subject of this report, may be outlined as follows:

- Make sputtered deposits containing inert gas.
- Obtain facility for melting in space (and on ground).

- Test deposited materials and melting facility.
- Conduct space experiment.
- Evaluate the results.

Details of this approach were separated by SPAR II flight as follows:

1. The first experiments (sputtering) in Phase I were to be conducted in a 1 g environment with the objective of identifying a suitable pure metal and gas combination for further examination. Suitable sputtered deposits from this pure metal and gas system (Al and Ar) were then to be produced for the first series of tests conducted in space. Six of the 1 by 0.10 by 0.05 cm samples were to be mounted in a quartz fixture with spot-welded thermocouple leads. This fixture was to be mounted in a Temperature Control Unit (TCU) furnace, as provided by NASA/MSFC and modified by BNW, and flown in Flight No. 1. In flight, the samples were to be radiantly heated to a temperature above their melting point, held at this temperature for a time less than 2 min, and water quenched. Time and temperature were to be recorded for each sample. The metal foam samples were to be recovered for metallographic examination and measurements of density, cell size and distribution, cell wall thickness, electrical and thermal conductivity, compressive strength, and other properties. It was anticipated that only one metal-gas combination would be used for this first phase. Three gas concentrations were to be investigated. Since duplicate samples were to be exposed to each test condition, a total of six samples would be foamed in the zero g environment and examined for each furnace run.

2. The second series of tests (Flight No. 2) to be conducted in space was to use two TCU furnaces similar to the one used in Flight No. 1. These furnaces were to contain flat specimens (as in Flight No. 1) and specimens sectioned from sputter-deposited hollow cylinders. Foam density was to be varied by the amount of gas trapped during sputter deposition and the length of time above the sample melting point. The two furnaces in this flight were to provide different times above the melting point to supplement data obtained in Flight No. 1. Evaluation was to be similar to that conducted on samples from the first flight. The three different times above the melting point were to allow an approximate Arrhenius determination of activation energies involved in the foaming process and, perhaps, speculation on the mechanism(s) involved. In addition, changes in sample dimensions and shape were to be recorded. Concurrent experiments on similar samples were to be conducted in a 1 g environment, and results were to be compared with results of the zero g experiments. A model describing

the behavior of these metal foams during formation was to be formulated. The Phase I experiments were to be considered successful if uniform closed-cell metal foams with predictable densities were produced.

### Phase II and Phase III — Experimental Scale-Up and Fabrication of Prototypic Configurations for a Specific Application

If the results of Phase I were sufficiently encouraging, specific Phase II and Phase III experiments were to be designed to achieve the results outlined in the Objective section above. Since the size and capabilities of the rockets available in 2 to 3 years are in question at this time, it was not possible to specify the extent of the experiments. It was hoped, however, that they would be considerably more ambitious in sample size and complexity than the Phase I experiments.

## REQUIREMENTS

Four requirements to be satisfied for experimental success in any phase were identified as follows:

1. Samples must contain appropriate amount of inert gas.

2. Furnace and controls must function properly, i.e., heat and cool at the the right time and provide accurate time-temperature data.

3. Metals must foam.

4. Foams must be recovered and identified for examination.

## EXPECTED RESULTS

It was expected that a new class of engineering materials would be produced by these investigations. These materials were expected to be pure metal or alloy closed-cell foams with uniform cell size and wall thickness, and evacuated cell or cells. Good control of foam density and cell size was expected.

In addition, it was expected to be possible to accurately foam-produce complex engineering shapes to final dimensions. These foams were expected to be useful in a wide range of structural applications. Additional applications such as hydrogen storage batteries and reactor fuels are also possible.

## MATERIALS AND PROCEDURES

### Constraints on Experiment Design

Time constraints imposed by the NASA/MSFC request to fly on SPAR Flight No. 1 and the availability of the TCU equipment flown on previous space flights dictated that the initial metal foam experiment be based on the TCU design. This design had several drawbacks, however. It was not equipped to process more than one sample capsule, to measure sample temperature directly, or to heat samples above approximately 300°C. It was determined that all of these limitations could be overcome by using only the TCU outer container and water quench apparatus and redesigning all heating elements, heat shields, sample capsules, sample geometry, temperature measurement provisions, and furnace controls. Preliminary calculations indicated that design would be much simplified if the maximum sample temperature sought was less than 1000°C.

### Furnace Design

As mentioned earlier, the available TCU furnaces were modified for this project. The modifications resulted from several iterations of building and testing, and included provisions to rapidly heat six individually thermocoupled samples to near 1000°C and cool them with a water quench. The resulting design proved to be very reliable. An assembly and testing procedure was developed and was included in the previous technical report [1]. Photographs taken at various stages during assembly are also included in this report.

Details of the design modifications are included in Battelle Drawings R-2160, Sheet 1, Rev. 2 and Sheet 2, Rev. 0, together with a description and drawings of the Furnace Control Electronics for SPAR Flight No. 1 [1].

## Furnace Control Electronics — SPAR Flight No. 2

### Requirements

The control requirements for SPAR Flight No. 2 were:

1. Turn on furnace heating elements in both TCU's 75 sec after launch (approximately 25 amp load each).

2. Maintain temperature (for 1 min above 700°C in one furnace and for 2 min above 700°C in the other furnace).

3. Turn off power to heating elements.

4. Open water quench solenoid valves at the same time as heating element power is shut off.

5. Provide appropriately conditioned signals to the rocket telemetry system from the sample thermocouples, temperature reference, and input power voltage.

6. Physically, the control unit had to mount in a small space beside the TCU and wi hstand the 25 g vibration testing.

### Circuit Description

The sample and furnace temperatures are monitored by chromel-alumel thermocouples. Seven amplifiers change these millivolt signals to the 0 to 5 V signals required by the rocket telemetry system. A compensated thermocouple amplifier is used to measure the cold-junction temperature and provides compensation to the other amplifier. A regulated 25 V supply powers all the amplifiers.

An EXAR 2240 M IC timer provides the delay between launch and applying power to the furnace element. A "G" switch activated by the launch acceleration triggers the timer, which closes the N219 furnace power relay 75 sec later. A single thermocouple in the furnace center monitors the overall furnace temperature. An LM311 voltage comparator detects the moment this signal is equal to a pre-set voltage equivalent to 700°C and cycles the power relay to maintain this temperature. The quench solenoid is activated by another 2240 M timer releasing the water into the sample chamber and simultaneously the furnace power relay is turned off, preventing any further heating.

A regulated 5 V output powers the timer and provides reference bias to the amplifier and comparator.

Design and construction details are included in Battelle Drawings R-2198, Sheet 1, Rev. 1 and R-2173, Sheet 2, Rev. 0. Reproductions of these two drawings are included in Appendix A.

Sample Preparation by Sputter Deposition

The pure metal-inert gas system chosen for initial experimentation was Al-Ar. This choice was based on the melting point of Al (660°C, well below the 1000°C equipment maximum temperature), the ready availability of pure Al target material, previously published data on Ar trapping in Al during sputtering [3,6] and the commercial importance of Al.

Four sputter-deposition experiments (NASA 1-4) were conducted with each experiment producing a 12.7 cm (5 in.) diameter disc of sputtered Al.

A fifth sputter deposition experiment produced a hollow cylindrical deposit of sputtered Al 1.9 cm (0.75 in.) in diameter, 0.1 to 0.2 cm (0.040 to 0.080 in.) thick, and 13 cm (5 in.) long.

The nominal chemical composition of all deposits is indicated in Table 1. Sputter-deposition parameters, deposit thickness, and Ar content are indicated in Table 2.

The sputtering apparatus and sputtering procedures have been described previously [1] and no changes other than use of a Cu tube substrate rotated over the Al target were incorporated in the most recent work.

Ground Based Testing Prior to SPAR Flight No. 1

Ground based testing at BNW included sufficient furnace and electronics testing to assure satisfactory operation through at least five repeated heating cycles. The water quench was not operated, however, as MSFC personnel intended to replace the solenoid activating the water quench in the TCU because of a mechanical problem encountered in a similar solenoid at MSFC. In addition, sputtered aluminum samples from the same material to be flown in the zero g

TABLE 1. NOMINAL DEPOSIT COMPOSITION

| Element | Concentration (wt%) |
|---|---|
| Cr | 0.01 to 0.1 |
| Cu | 0.01 to 0.1 |
| Fe | 0.1 |
| Mg | 0.001 to 0.01 |
| Mn | 0.001 to 0.01 |
| Ni | 0.01 to 0.1 |
| Si | 0.01 to 0.1 |
| Ti | 0.01 to 0.1 |
| V | 0.01 to 0.1 |
| Ca | < 0.001 |

Not Detected

B, Cd, Co, Pb, Mo, Sn, W, Zr, Nb, Ta and Zn

Note: Chemical composition of the deposits was determined by standard analytical techniques and by x-ray fluorescence.

experiments were heated above their melting point in the preliminary laboratory furnace models and in the flight furnace assembly. These samples were air cooled. Metallographic examination indicated that the samples did foam and thus gave a preliminary indication that the furnace design and the materials concepts were sound.

Modification of the TCU was completed, the associated control electronics were completed, dummy samples appropriate for the NASA testing plan were installed in the TCU, and the TCU with electronics was shipped via courier to NASA/MSFC on August 14, 1975 with delivery on Aug 15.

TABLE 2. SPUTTER DEPOSITION PARAMETERS AND RESULTS

| Experiment Number | Target Potential (volts) | Target Current (amps) | Substrate Bias (volts) | Substrate Current (amps) | Argon Pressure (x 10⁻³ torr) | Substrate Temperature (°C) | Deposit Thickness (mm) | Argon Content* (ppm) |
|---|---|---|---|---|---|---|---|---|
| NASA #1 | 2000 | 1.5 | Floating | 0 | 6.2 | 21 | 0.2 | 30 |
| NASA #2 | 2000 | 1.75 | -100 | 1.9 | 6.2 | 21 | 0.9 | 231 |
| NASA #3 | 2000 | 1.75 | - 60 | 1.75 | 6.2 | 21 | 0.6 | 23 |
| NASA #4 | 2000 | 1.75 | -150 | 1.75 | 6.2 | 21 | 0.6 | 272 |
| NASA #5 | 2000 | 1.75 | -100 | 1.3 | 5.0 | 21 | 1-2 | 24 |

*Argon content was measured by vacuum fusion techniques with gas composition measured with a quadropole mass spectrometer.



ORIGINAL PAGE IS
OF POOR QUALITY

The following drawings were also completed and delivered to NASA/MSFC at this time:

| Drawing Title | BNW Drawing Number |
|---|---|
| TCU Furnace Modification | R-2160 (2 sheets) |
| Specimen Metallic Foam Experiment | R-2170 |
| Rocket Furnace Electronics | R-2173 (sheet 1 of 2) |
| Rocket Furnace Electronics Details | R-2173 (sheet 2 of 2) |
| Block Diagram Furnace Electronics | R-2183 |

In addition, the assembly procedure used to install samples in the TCU and prepare the TCU for testing was recorded and several photographs were taken during the assembly process. These drawings and the assembly procedure were included in the earlier technical report [1].

The TCU was further modified at NASA (after delivery from BNW) in areas relating to gas purge fittings, water input lines, and provision for pressure equilization between the water reservoir and the furnace chamber. No drawings or written description of these modifications were prepared by NASA/MSFC.

The TCU and associated electronics withstood the first MSFC vibration testing in September 1975. One crack was observed in the quartz heater support, but this crack was not expected to affect the experiment in any way. Several assembly screws used in the heat shield assembly worked loose, none of which would affect the experiment. However, the assembly procedure was modified and now includes RTV coating of the screws to prevent loosening during future tests and experiments. Some failures in sample thermocouple solder joints (cold junction) were also encountered and procedures were modified to provide better joint reliability.

The MSFC-provided water quench solenoid valve leaked during vibration testing. MSFC indicated that they would change valves to prevent future problems in this area.

ORIGINAL PAGE IS
OF POOR QUALITY

MSFC personnel indicated that ground-based tests would be conducted on or about October 10 and that presence of the PI or his representative would be required for installation of test samples and for furnace refurbishment.

The TCU was partially disassembled at MSFC in early October 1975, and the water quench solenoid valve was replaced. After reassembly, a short was noted in the control thermocouple, so the TCU was immediately shipped back to Battelle. The control thermocouple was replaced with a design that was expected to be more resistant to damage. All solder joints to thermocouples were examined and some were resoldered. The TCU was shipped back to MSFC the same day it had been received.

MSFC tested the TCU through its complete temperature cycle more than one time, and after one of these cycles noted that the heating element was shorted to the TCU outer wall. The TCU was shipped back to BNW, where it was refurbished including installation of all new thermocouples, quartz sample tubes, quartz heater support, a heating element wound in such a way as to avoid the shorting problem, and new dummy test samples. The TCU was then shipped to MSFC where it again underwent testing through the complete temperature cycle, with no difficulties being encountered.

On Monday, October 20, 1975, MSFC telephoned and requested the presence of the PI and Eric Greenwell at MSFC on Wednesday, October 22, for ground-based tests. On October 22 the TCU was completely refurbished as above but including new radiation shielding and ground-based test samples. Testing difficulties associated with NASA control functions and with other experiments produced delays in the test schedule such that the first ground-based test (GB 1) was conducted on October 28. A second set of ground-based test samples was then installed in the furnace, and a second ground-based test (GB 2) was conducted. On October 30 the refurbished TCU, complete with a new set of dummy samples, was made available to MSFC for installation in the science payload and shipment to GSFC.

The ground-based tests previously described provided 12 specimens for evaluation and use as a basis of comparison for the zero g processed specimens. Four samples were much larger than originally planned in this group (four times as wide) (Table 3). External appearances seemed to indicate that foaming had occurred, and the effects of gravity were clearly evident in sample "sagging" or flowing (Table 4). These samples were evaluated metallographically. In addition, a computer program designed to analyze metallography of indicated reactor fuel cell materials was modified to suit the foam material and used to provide statistical analysis of the microstructure.

## TABLE 3. QUANTITATIVE OBSERVATIONS ON FOAM SPECIMENS ASSOCIATED WITH SPAR FLIGHT NO. 1

| Processing | Specimen Number | Mean Cell Size (μ) | Median Cell Size (μ) Volume | Cell Count/cm$^3$ | Cell Volume Fraction (%) | Cell Specific Surface Area (cm$^2$/cm$^3$) | Content (ppm) | Width* (mm) | Thickness* (mm) | Melting Point (sec) | Cooling Rate through Melting Point (°C/sec) |
|---|---|---|---|---|---|---|---|---|---|---|---|
| Space | 1-D-1 | 2.66 | $5.00\times10^{1}$ | $2.87\times10^{8}$ | 1.15 | $1.07\times10^{2}$ | 30 | 1.1 | 0.2 | 31.0 | 1310 |
| | 1-D-2 | 5.05 | $3.99\times10^{1}$ | $1.32\times10^{8}$ | 3.34 | $1.87\times10^{2}$ | | | | | |
| | 1-D-3 | 6.39 | $6.27\times10^{1}$ | $7.10\times10^{7}$ | 3.26 | $1.57\times10^{2}$ | | | | | |
| Space | 1-J-1 | 4.09 | 9.10 | $2.91\times10^{8}$ | 1.69 | $2.33\times10^{2}$ | 30 | 4.2 | 0.2 | 25.0 | 220 |
| | 1-J-2 | 4.90 | $2.84\times10^{1}$ | $1.35\times10^{8}$ | 3.80 | $1.97\times10^{2}$ | | | | | |
| | 1-J-3 | 4.49 | $2.53\times10^{1}$ | $2.02\times10^{8}$ | 4.00 | $2.54\times10^{2}$ | | | | | |
| Space | 2-C-1 | 7.61 | $4.46\times10^{1}$ | $1.61\times10^{7}$ | 2.10 | $7.34\times10^{1}$ | 231 | 1.2 | 0.9 | 31.0 | 170 |
| | 2-C-2 | 5.45 | | $4.31\times10^{7}$ | 12.79 | $1.18\times10^{2}$ | | | | | |
| | 2-C-3 | 5.71 | $3.18\times10^{1}$ | $5.10\times10^{7}$ | 2.80 | $1.34\times10^{2}$ | | | | | |
| Space | 3-C-1 | 4.51 | $2.02\times10^{1}$ | $6.86\times10^{7}$ | 1.52 | $9.59\times10^{1}$ | 23 | 1.2 | 0.6 | 29.0 | 1370 |
| | 3-C-2 | 7.42 | | $1.59\times10^{7}$ | 32.82 | $1.24\times10^{2}$ | | | | | |
| | 3-C-3 | 3.97 | $8.81\times10^{1}$ | $4.20\times10^{7}$ | 3.76 | $9.07\times10^{1}$ | | | | | |
| Space | 4-C-1 | 3.97 | 8.15 | $5.91\times10^{7}$ | 0.25 | $3.98\times10^{1}$ | 272 | 1.2 | 0.6 | 22.0 | 1310 |
| | 4-C-2 | $1.01\times10^{1}$ | $4.46\times10^{1}$ | $2.22\times10^{7}$ | 6.13 | $1.81\times10^{2}$ | | | | | |
| | 4-C-3 | 5.83 | $3.99\times10^{1}$ | $4.68\times10^{7}$ | 4.17 | $1.35\times10^{2}$ | | | | | |
| Space | 4-J-2 | 5.21 | $4.46\times10^{1}$ | $3.07\times10^{7}$ | 2.35 | $8.55\times10^{1}$ | 272 | 4.1 | 0.5 | 26.0 | 1250 |
| | 4-J-3 | 4.29 | $4.46\times10^{1}$ | $5.33\times10^{7}$ | 4.52 | $1.33\times10^{2}$ | | | | | |
| GB 1 | 1-A-1 | 4.04 | 4.65 | $2.65\times10^{8}$ | 0.60 | $1.48\times10^{2}$ | 30 | 1.1 | 0.2 | 42 | |
| | 1-A-2 | 3.56 | 3.70 | $2.24\times10^{8}$ | 0.60 | $1.90\times10^{2}$ | | | | | |
| | 1-A-3 | 2.91 | 2.95 | $3.75\times10^{8}$ | 0.28 | $1.05\times10^{2}$ | | | | | |
| GB 1 | 1-G-1 | 4.45 | 9.10 | $2.07\times10^{8}$ | 1.29 | $1.81\times10^{2}$ | 30 | 4.2 | 0.2 | 21 | |
| | 1-G-2 | 4.25 | $1.02\times10^{1}$ | $2.19\times10^{8}$ | 1.33 | $1.75\times10^{2}$ | | | | | |
| | 1-G-3 | 4.05 | 8.15 | $1.57\times10^{8}$ | 0.66 | $1.09\times10^{2}$ | | | | | |
| GB 1 | 2-A-1 | 3.58 | 5.20 | $1.48\times10^{8}$ | 0.31 | $7.23\times10^{1}$ | 231 | 1.1 | 0.9 | 14 | |
| | 2-A-2 | 4.41 | $1.29\times10^{1}$ | $6.30\times10^{7}$ | 0.60 | $6.24\times10^{1}$ | | | | | |
| | 2-A-3 | 4.70 | 8.15 | $8.80\times10^{7}$ | 0.51 | $8.01\times10^{1}$ | | | | | |

*All specimens were 1-cm long.



ORIGINAL PAGE IS OF POOR QUALITY

TABLE 3. (Concluded)

| Processing | Specimen Number | Mean Cell Size (μ) | Median Ce Size (μ) Volume | Cell Count/cm³ | Cell Volume Fraction (%) | Cell Specific Surface Area ($cm^2/cm^3$) | Content (ppm) | Width* (mm) | Thickness* (mm) | Melting Point (sec) | Cooling Rate through Melting Point (°C/sec) |
|---|---|---|---|---|---|---|---|---|---|---|---|
| GB 1 | 3-A-1 | 5.65 | $2.53x10^{1}$ | $8.92x10^{7}$ | 3.62 | $1.93x10^{2}$ | | | | | |
| | 3-A-2 | 5.80 | $3.18x10^{1}$ | $9.90x10^{7}$ | 1.42 | $2.15x10^{2}$ | 23 | 1.1 | 0.6 | 8 | |
| | 3-A-3 | 3.77 | $1.15x10^{1}$ | $7.00x10^{7}$ | 0.32 | $4.37x10^{1}$ | | | | | |
| GB 1 | 4-A-1 | 3.88 | $3.56x10^{1}$ | $6.77x10^{8}$ | 6.77 | $5.03x10^{2}$ | | | | | |
| | 4-A-2 | 4.30 | $7.87x10^{1}$ | $5.20x10^{8}$ | 16.37 | $5.89x10^{2}$ | 272 | 1.1 | 0.6 | 24 | |
| | 4-A-3 | 2.95 | 3.70 | $1.16x10^{8}$ | 0.11 | $3.51x10^{1}$ | | | | | |
| GB 1 | 4-G-1 | 5.82 | $2.02x1^{1}$ | $2.12x10^{8}$ | 5.18 | $3.83x10^{2}$ | | | | | |
| | 4-G-2 | 5.68 | 9.10 | $2.29x10^{8}$ | 2.11 | $2.96x10^{2}$ | 272 | 4.0 | 0.6 | 21 | |
| | 4-G-3 | 6.41 | $1.44x10^{1}$ | $2.54x10^{8}$ | 4.51 | $4.23x10^{2}$ | | | | | |
| GB 2 | 1-B-1 | 4.44 | 7.30 | $2.55x10^{8}$ | 1.15 | $1.99x10^{2}$ | | | | | |
| | 1-B-2 | 3.19 | 4.15 | $2.30x10^{8}$ | 0.32 | $8.45x10^{1}$ | 30 | 1.1 | 0.2 | | |
| | 1-B-3 | 3.67 | 4.65 | $2.27x10^{8}$ | 0.44 | $1.11x10^{2}$ | | | | | |
| GB 2 | 1-H-1 | 3.52 | 4.65 | $1.40x10^{8}$ | 0.24 | $6.28x10^{1}$ | | | | | |
| | 1-H-2 | 3.46 | 4.65 | $2.17x10^{8}$ | 0.41 | $9.58x10^{1}$ | 30 | 4.2 | 0.2 | | |
| | 1-H-3 | 5.34 | $1.02x10^{1}$ | $1.36x10^{8}$ | 1.38 | $1.73x10^{2}$ | | | | | |
| GB 2 | 2-B-1 | 5.38 | $7.87x10^{1}$ | $2.25x10^{8}$ | 17.28 | $4.50x10^{2}$ | | | | | |
| | 2-B-2 | 4.46 | $6.27x10^{1}$ | $5.75x10^{8}$ | 8.93 | $5.53x10^{2}$ | 231 | 1.1 | 0.9 | | |
| | 2-B-3 | 3.98 | $2.02x10^{1}$ | $1.05x10^{9}$ | 6.67 | $7.29x10^{2}$ | | | | | |
| GB 2 | 3-B-1 | 5.48 | 9.10 | $4.11x10^{8}$ | 3.54 | $1.95x10^{2}$ | | | | | |
| | 3-B-2 | 5.15 | 7.30 | $3.61x10^{8}$ | 2.26 | $3.69x10^{2}$ | 23 | 1.2 | 0.6 | | |
| | 3-B-3 | 4.24 | 5.20 | $2.51x10^{8}$ | 0.66 | $1.56x10^{2}$ | | | | | |
| GB 2 | 4-B-1 | 3.67 | 5.80 | $1.56x10^{8}$ | 0.37 | $7.96x10^{1}$ | | | | | |
| | 4-B-2 | 4.46 | 9.10 | $1.31x10^{8}$ | 0.74 | $1.08x10^{2}$ | 272 | 1.1 | 0.6 | | |
| | 4-B-3 | 4.14 | $1.02x10^{1}$ | $1.13x10^{8}$ | 0.65 | $8.41x10^{1}$ | | | | | |
| GB 2 | 4-H-1 | 5.08 | $1.29x10^{1}$ | $2.66x10^{8}$ | 2.81 | $3.12x10^{2}$ | | | | | |
| | 4-H-2 | 5.03 | $3.18x10^{1}$ | $1.85x10^{8}$ | 4.84 | $2.84x10^{2}$ | 272 | 4.0 | 0.6 | | |
| | 4-H-3 | 4.87 | $3.99x10^{1}$ | $1.69x10^{8}$ | 4.88 | $2.49x10^{2}$ | | | | | |

*All specimens were 1-cm long.

## TABLE 4. QUALITATIVE OBSERVATIONS ON FOAM SPECIMENS

### Space Processed Specimens

| Specimen No. | Cell Volume | Deformation | TC Contact Maintained? |
|---|---|---|---|
| 1-D | Sampling apparently very good except for 2 large coalescence areas. | Very little sample deformation observed. | No |
| 1-J | Sampling did not count area with highest density of large cells (rt of 1-J-2) or large tear or coalescence areas (resulting from deformation?) | Sample elongation and resulting tearing, possibly due to mechanical recovery in the supporting TC wires. | Yes |
| 2-C | Sampling did not count area with highest density of large cells (left of 2-C-2) or large coalescence areas. Overall sample cell volume fraction probably 20-25%. | Very little deformation. Sample bending possibly occurred during quench as sample was detached from support and TC wires. | No |
| 3-C | Sampling did not count areas of highest cell density. Areas with about 5 times more porosity were present. Only 1 large coalescence area was present and it was counted. | Very little sample deformation evident. | Yes |
| 4-C | All typical areas sampled well. Sample very uniform with no large coalescence areas. | Very little sample deformation evident. | No |
| 4-J | Sampling fairly good but did not count large coalescence areas. Overall sample cell volume fraction probably 15-20%. | Sample elongation and thickening to one end, probably due to quench. | No |



ORIGINAL PAGE IS
OF POOR QUALITY

TABLE 4. (Continued)

GB 1 Specimens

| Specimen No. | Cell Volume | Deformation | TC Contact Maintained? |
|---|---|---|---|
| 1-A | Sampling apparently very good. | Extensive elongation apparent. | Yes |
| 1-G | Sampling very good. No large coalescence areas were present. | Very extensive sample elongation, appearance of "running" or fluid flow. | No |
| 2-A | Sampling good but one very large coalescence area (cell) formed as did several smaller ones. These were not counted. Overall sample cell volume fraction was probably 20-25%. | Very little plastic flow was evident but a very extensive oxide or corrosion product film was observed on the sample. This film probably limited fluid flow. | Yes |
| 3-A | Sampling was good but did not count the many large coalescence areas. Sample cell volume fraction was probably 15-20%. | Very little sample elongation was observed. | Yes |
| 4-A | Sampling was good but the sample had only melted on one end. | Sample flow was extensive on the end that melted. Breakup (mechanical) of the heavy corrosion product film was evident. | Yes |
| 4-G | Sampling was very good with no large coalescence areas observed. | Flow was very extensive with nearly all of the sample material accumulating at the bottom support wire. | Yes |



ORIGINAL PAGE IS
OF POOR QUALITY

TABLE 4. (Concluded)

GB 2 Specimens

| Specimen No. | Cell Volume | Deformation | TC Contact Maintained? |
|---|---|---|---|
| 1-B | Sampling good but did not count large coalescence areas. Overall sample cell volume fraction probably 20-25%. | Extensive elongation apparent. | Yes |
| 1-H | Sampling very good but one very large coalescence area (cell) formed so that overall sample cell volume was probably 60-70%. | Extensive fluid flow bordering on droplet formation. | No |
| 2-B | Sampling was very good. No large coalescence areas were observed. | Very little plastic flow was evident, again probably a result of the very heavy corrosion product film. | Yes |
| 3-B | Sampling was very good. No large coalescence areas were observed. | Sample bent and sagged severely. | Yes |
| 4-B | Sampling was good except that a large coalescence area (cell) was not counted. This cell was 20-25% of the sample volume. | The center of the sample formed a droplet and fell off the support wires. The large cell was formed in this piece. | No |
| 4-H | Sampling was very good with only one large coalescence area forming (not counted). | Flow was similar to that observed in 4-G. However, the sample separated in the middle (tearing) during the quench. | Yes |



ORIGINAL PAGE IS
OF POOR QUALITY

The ground-based testing was conducted without any difficulties related to the TCU or its associated electronics. Experiment performance was satisfactory as was the collection of in-test time and temperature data.

However, time-temperature detailed data on these tests were not received until June 28, 1976, so that analysis of the ground-based test results could not be completed until long after SPAR flight No. 1 and, in fact, more than a month after SPAR Flight No. 2.

SPAR Flight No. 1

On December 2, the flight samples and flight furnace components were delivered to White Sands Missile Range, New Mexico. Due to delays in the White Sands testing schedule, the TCU was made available for refurbishment on December 5. At this time the furnace was refurbished and the flight samples were installed.

The flight experiment was flown on December 11. The TCU and electronic packages were shipped by MSFC personnel and arrived at BNW on December 16. The TCU was immediately disassembled and examined. The water quench had operated, heating element operation seemed to have been normal, all samples remained in their quartz capsules and appeared to have melted and foamed, and the thermocouples appeared to have remained intact throughout the experiment. It was tentatively concluded that the experiment was a success, provided that suitable time-temperature data had been transmitted to the ground facility and recorded.

The flight samples were analyzed in the same manner as the ground-based tested samples, and preliminary results were presented during a review meeting at MSFC on January 5 and 6. Statistical and metallographic data were left with project personnel at MSFC to aid in demonstration of the success of the SPAR I experiment and to indicate feasibility of metal foam production.

An informal Post-Flight Preliminary Report in the form of a letter to Roger Chassay was written on January 21, 1976. This report briefly documented the results presented at the January 5-6 MSFC meeting and was reproduced in the previous report.

Note that although the raw thermocouple voltage data from SPAR Flight No. 1 were available to examine at the January 5-6 MSFC meeting, detailed time-temperature and time-voltage data were not available for examination

until February 20, 1976, seven days before the scheduled Comprehensive Review Meeting at MSFC on March 5, 1976, and more than two months after the flight. Furthermore, these data revealed that drift had occurred in the thermocouple amplifiers before the flight; therefore, a new zero-point had to be determined for each thermocouple system and all data received from MSFC had to be adjusted to compensate for these values. Corrections to the time-temperature data from the flight were completed on March 8, permitting final analysis of flight data to begin.

## Ground-Based Testing Prior to SPAR Flight No. 2

Modification of the second TCU furnace was completed in January 1976. During February 1976, modifications to both TCU's were completed, construction of control electronics was completed, and all components were trial assembled (including components for the flight experiments on SPAR 2), and satisfactory functioning was verified. Both TCU's were assembled with dummy samples, packaged, and shipped along with their control electronics to MSFC for systems tests.

Also during February, a set of Test Specifications and Requirements for SPAR Payload II, Experiment 74-10, was prepared and sent to B. T. Ondrak and R. Ruff, MSFC. These specifications and the attendant cover letter are included in Appendix B.

A procedure for refurbishing the TCU's was prepared and sent to R. Ruff, MSFC, who provided support at MSFC by following all equipment tests and repairing/ refurbishing as required. This procedure is included in Appendix C.

NASA functional testing and verification of TCU-electronics system operation was completed at MSFC with the following problems being encountered:

1. Low readings from the thermocouple amplifier outputs resulting from too low impedance of NASA chart recorder.

2. Power relay cycling after the quench resulting from NASA substituting a solenoid with too high resistance.

3. Power relay cycling immediately after application of power resulting from NASA g-switch not being connected.

4. Observed time-at-temperature too long on 74-10/3 resulting from Battelle changing time-at-temperature setting and not informing NASA.

The TCU electronics control packages were then returned to BNW by NASA MSFC. The soak temperature set-points were adjusted in both units, and triggering of the water quench solenoid was set. All thermocouple amplifiers were calibrated.

Ground-based testing preliminary to SPAR II was completed at NASA/MSFC with R. Ruff accomplishing all associated TCU refurbishment, specimen installation, etc. No specimens or time-temperature results were immediately sent to BNW; therefore, adequate information concerning equipment performance was acquired prior to SPAR Flight No. 2 but no information as to material (experiment sample) behavior was available.

## SPAR Flight No. 2

On May 11 and 12, the PI and R. Ruff (MSFC) refurbished both TCU's at White Sands Missile Range, New Mexico. Also at this time flight components and experiment samples were installed in the TCU's, and resistance tests were conducted to assure correct experiment assembly.

On May 18, R. Ruff delivered the two TCU's (after SPAR Flight No. 2) and related ground-based test specimens to the PI at Richland, Washington.

On May 19, the PI removed the flight samples and heater components from the two TCU's, returned the TCU's and electronic control packages to R. Ruff for transport to MSFC, and initiated evaluation of the SPAR Flight No. 2 specimens.

## ANALYSIS OF RESULTS AND DISCUSSION — SPAR I

### Ground-Based Tests

Metallography from 12 ground-based tested samples was included in the Post-Flight Technical Report, SPAR Flight No. 1. Table 3 summarizes data recorded during analysis of these specimens, and Table 4 contains qualitative observations on the foamed specimens.

Approximate times above the melting point for GB-1 samples were estimated from recording pen traces and thermal arrests. Computer-processed data were not received from NASA/ MSFC until June 28, 1976. However, these data did not differ significantly from the estimates and therefore is not included here.

No times above the melting point for GB-2 samples are included in Table 4 because no data were recorded at NASA/ MSFC for this test.

In general, results of GB-1 and GB-2 testing showed gross sample flow and separation from thermocouples during testing because of the effects of gravity. It was concluded from these tests that ground based testing prior to SPAR Flight No. 2 would serve to verify satisfactory experiment operations from an equipment standpoint, but little insight into foam behavior could be expected. That is, it was concluded that all kinetic information would have to be provided by zero g processed samples.

## SPAR Flight No. 1

Metallography from the six SPAR Flight No. 1 samples was also included in the Post Flight Technical Report, SPAR Flight No. 1. Table 3 summarizes sample sizes, processing methods, time above the melting point (if available), cooling rate through the melting point, trapped argon content, and cell size and distribution statistics.

Table 4 contains qualitative observations on the foamed specimens.

Note that times at which melting occurred on heating for space processed samples were taken as the beginning of thermal arrests observed in the time-temperature data. Each of these thermal arrests occurred within a few degrees of the published 660°C melting point of aluminum. Times at which solidification occurred were taken as the times when the samples cooled through 660°C. Cooling rates here were very rapid; therefore, very little time error was involved with this measurement. Cooling rates from each sample (temperature was measured each 0.1 sec) are listed in Table 3. Accuracy in the estimated times above the melting point (Table 3) for space-processed samples was judged to be ±1 sec. Heating rate was approximately 10°C/ sec.

It was concluded that gas content variations up to 250 ppm were not as strongly influential on foaming behavior as expected. This may have been clouded by the difficulty in counting large pores in the quantitative analysis, by the very strong (positive) influence on cell volume fraction of a few large cells, and by the weak (negative) influence on pore specific surface area of a few large cells. It was further concluded that these effects could be more effectively treated in samples of much greater sample thickness so that thicker samples were scheduled for experiments on SPAR Flight No. 2.

Trends were observed toward fewer cells/unit volume, less scatter in the number of cells/unit volume, and a larger median cell size in space processed samples than in ground-based samples. No trends were observed in mean cell size or scatter in mean cell size. More speculation concerning these data, however, was deferred pending availability of reliable time-temperature data for the ground-based tested samples.

As previously mentioned, the accurate time-temperature data for GB-1 samples did not significantly alter estimates of the time-temperature data and therefore did not provide additional information on foam behavior. It was also concluded that formation of a corrosion product scale (in spite of a flushed nitrogen atmosphere) on the samples and the resulting non-uniform constraints on sample movement during foam development, combined with the small sample thickness (on the order of bubble dimensions), presented the most significant obstacles to analysis of results. Largely because of these effects, each sample was used completely for metallographic examinations and no mechanical testing was conducted. However, it was believed that this information, particularly that included in Table 3, provided very good characterization of SPAR Flight No. 1 samples for comparison with SPAR Flight No. 2 samples (processed for two longer times above the melting point) to obtain kinetic data. Further, it was believed that larger samples on SPAR Flight No. 2 would reduce the effects of surface area, oxide scale, and dominance by a few large cells.

## ANALYSIS OF RESULTS AND DISCUSSION — SPAR II

### Ground-Based Tests

Representative metallography from Experiments 74-10/2 and 74-10/3 is included in Figures 1 and 2. All specimens in these ground-based tests experienced much more surface oxidation than did the specimens tested prior

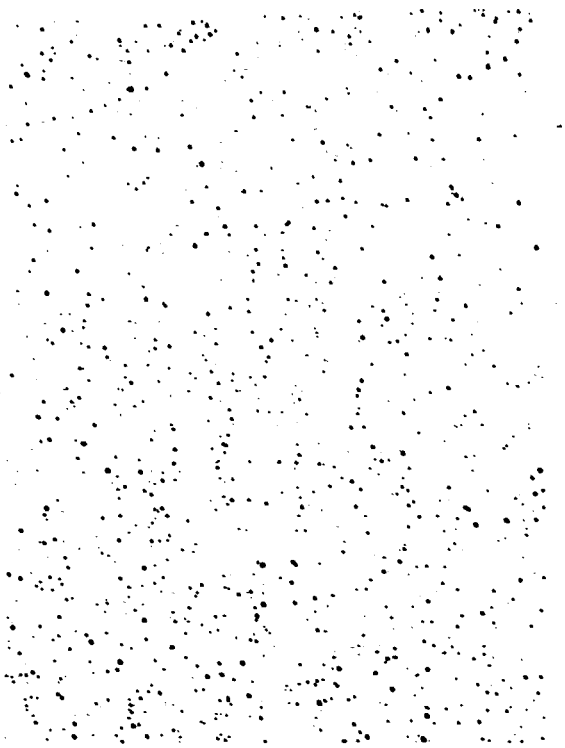

Deposit NASA #2

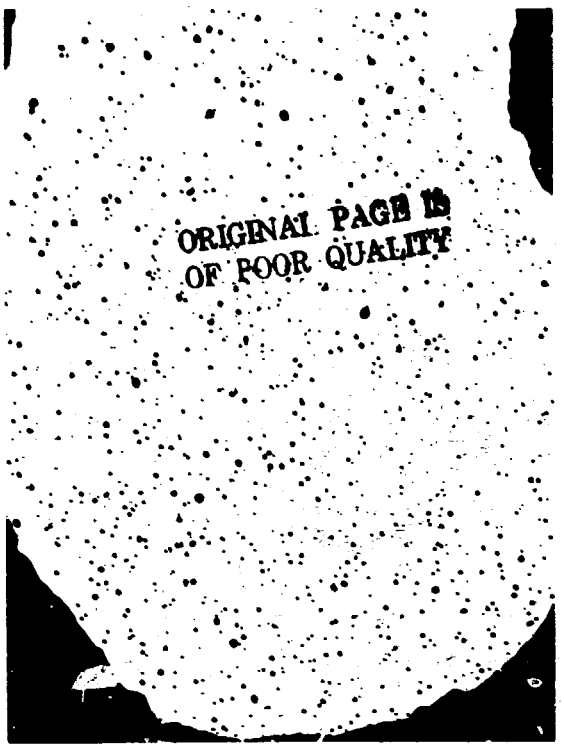
ORIGINAL PAGE IS
OF POOR QUALITY

Deposit NASA #4

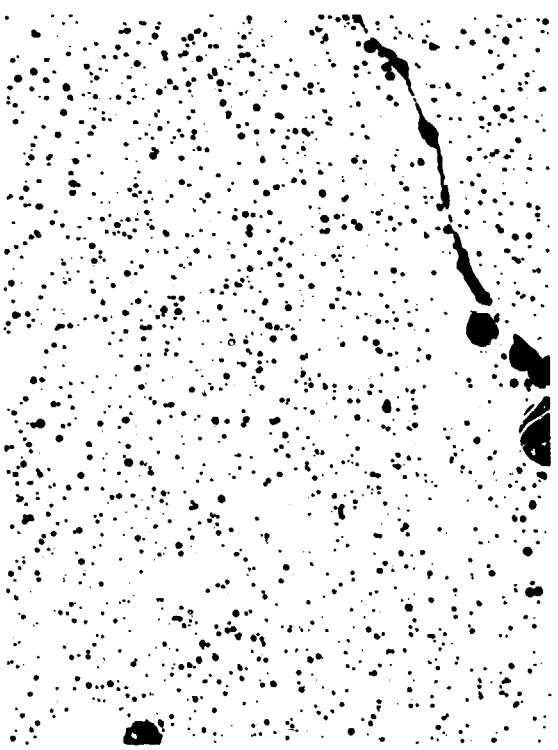

Deposit NASA #5

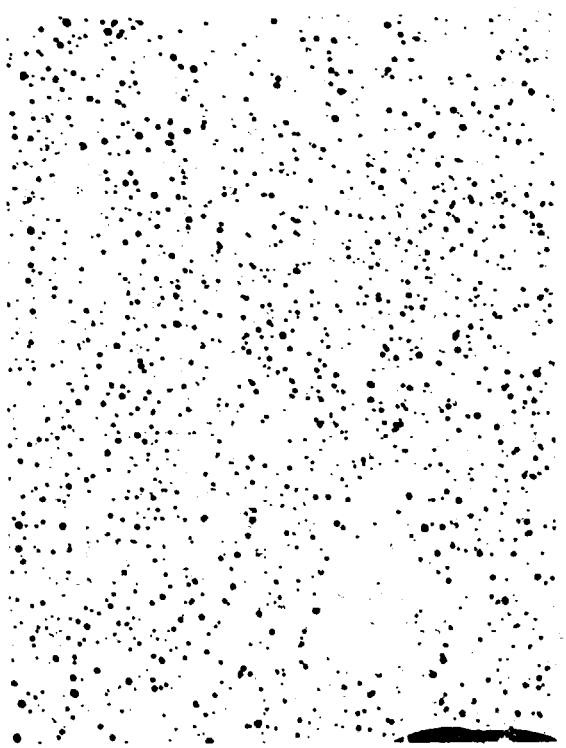

Deposit NASA #5

Figure 1. Specimens from Experiment 74-10/2. Samples of deposit NASA No. 1 and deposit NASA No. 3 were fragmented too badly to examine As-polished, 50X.

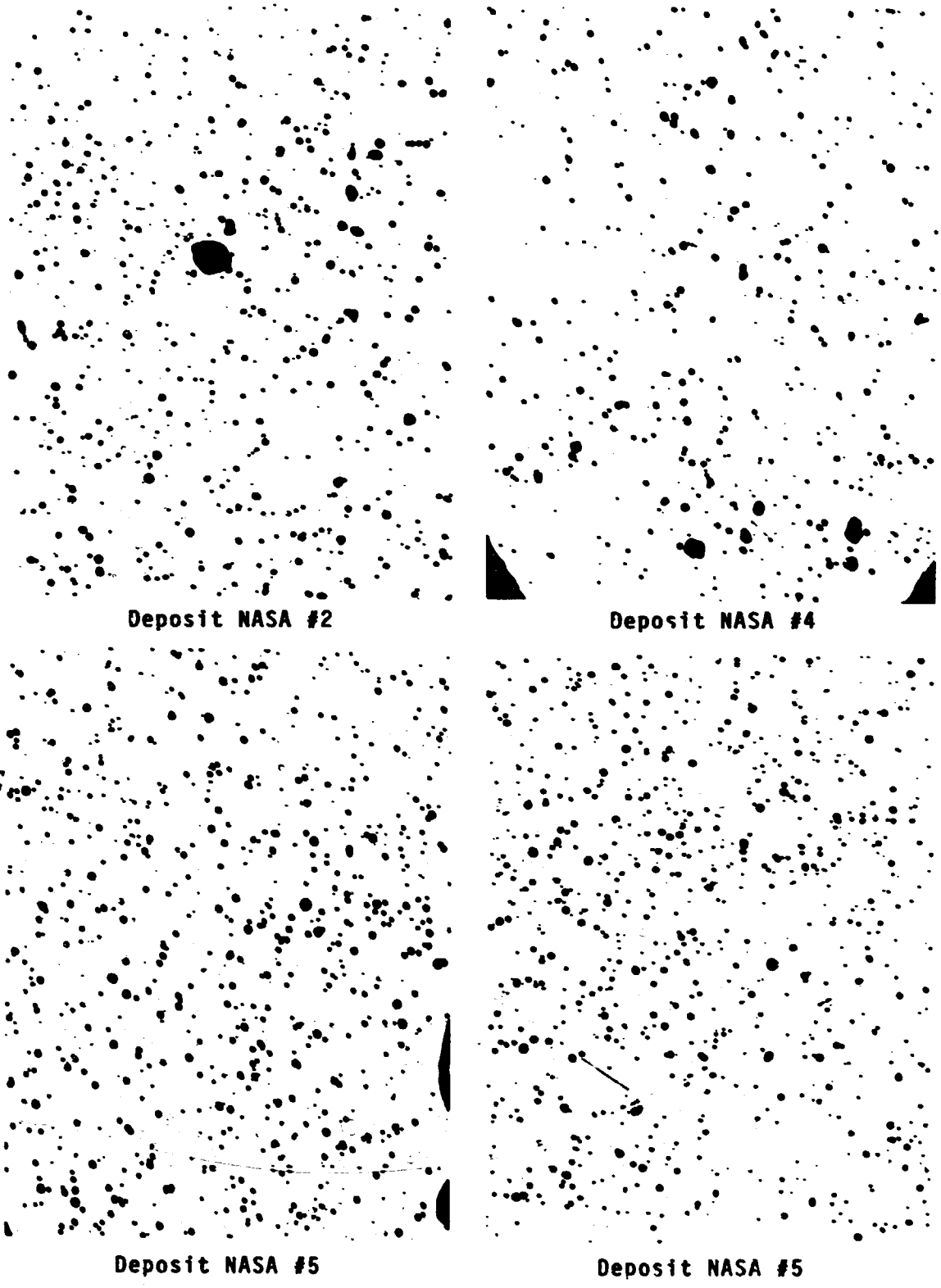


ORIGINAL PAGE IS
OF POOR QUALITY

Figure 2. Specimens from Experiment 74-10/3. Samples of deposit NASA No. 1 and deposit NASA No. 3 were fragmented too badly to examine. As-polished, 50X.



C-2

to SPAR I; therefore, there was much less metal flow in the samples while they were molten. The restraining forces may also have been the cause of the complete absence of large bubbles. The resulting microstructures typically showed very uniform distribution of small bubbles. The specimens in Experiment 74-10/2 were above the melting point for approximately 85 sec and the specimens in Experiment 74-10/3 were above the melting point for approximately 160 sec, as in the actual flight experiments (Table 5). The effect of the increased time above the melting point is clearly evident in the bubble distribution in Figures 1 and 2 with longer time producing larger and fewer bubbles. Further investigation might, in fact, demonstrate that foam formation with uniform mechanical constraint (to prevent large void formation) and a zero g environment (to prevent "boiling," or a density driven bubble segregation, in large sections) is the most effective way to fabricate metallic foam shapes. Because of this strong (and poorly understood) restraint of the oxide scale, no detailed analysis of the foam structure was attempted.

## SPAR Flight No. 2

Results for the two experiments conducted on SPAR Flight No. 2 are included in Table 5. Specimens in Experiment 74-10/2 were molten (above 660°C) for approximately 85 sec, and specimens in Experiment 74-10/3 were molten for approximately 160 sec.

No metallographic examinations were conducted on specimens 1-F, 4-E, and 4-D because sufficient specimen material was not recovered after the experiment. Metallography on the remaining nine specimens is included in Figures 3 through 7. Note that the curved "T" samples usually did not maintain their curved shape well (Fig. 6). This was attributed to the irregular mechanical restraint provided to the expanding foam by an adherent fracturing oxide film. Evidence of this may be observed in the low magnification macrographs included in the figures and in the irregular surfaces of the metallographic cross-section.

There is extensive literature [9-31] concerning the mechanisms and kinetics of inert gas bubble formation, movement, and growth in metals, particularly in the solid state near the melting point. It was intended that this information be applied to the analysis of the Ar-Al foams; however, it is believed that the restraining effects of the oxide film would invalidate any conclusions of such an analysis.

## TABLE 5. OBSERVATIONS FROM SPAR FLIGHT NO. 2

Experiment 74-10/2

| Specimen No. | Comments | Time After Launch (sec to heat to 660°C) | Time After Launch (sec to cool to 660°C) | Time Above 660°C Δt (sec) | Ar Content (ppm) |
|---|---|---|---|---|---|
| 1(1-F) | No metallography, specimen detached from thermocouple and support wires and lost. | 158.9 | 253.8 | 94.9 | 30 |
| 2(2-H) | Specimen fragmented, only a small part attached to the support wire was recovered. | 174.4 | 254.1 | 79.7 | 231 |
| 3(3-H) | Specimen detached from thermocouple and support wires, two pieces recovered. | 173.1 | 254.6 | 81.5 | 23 |
| 4(4-E) | No metallography, specimen detached from thermocouple and support wires and lost. | 173.7 | 254.5 | 80.8 | 272 |
| 5(T-C)* | Specimen remained attached to thermocouple and support wires. | 165.4 | 254.9 | 89.5 | 24 |
| 6(T-D)* | Specimen detached from thermocouple and support wires, flowed out through a water hole in one end plate while still molten. | 172.3 | 254.4 | 82.1 | 24 |
| 7 (Furnace) | | 183.2 | ~257.5 | 74.3 | |

Experiment 74-10/3

| | | | | | |
|---|---|---|---|---|---|
| 1(1-E) | Detached thermocouple wire, specimen remained in sample tube. | 178.5 | 333.8 | 155.3 | 30 |
| 2(2-G) | Detached thermocouple wire, specimen remained in sample tube. | 175.6 | 333.9 | 158.3 | 231 |
| 3(3-G) | Specimen remained attached to thermocouple and support wires. | 175.9 | 333.7 | 157.8 | 23 |
| 4(4-D) | No metallography, specimen fragmented, two pieces were recovered. | 167.5 | 333.9 | 166.4 | 272 |
| 5(T-A)* | Specimen remained attached to thermocouple and support wires. | 156.3 | 334.1 | 177.8 | 24 |
| 6(T-B)* | Specimen remained attached to thermocouple and support wires. | No reading - large pulse @ 198 sec. | | | 24 |
| 7 (Furnace) | | 191.3 | ~336.0 | 144.7 | |

*All "T" specimens were sectioned from Experiment NASA #5, see Table II.



ORIGINAL PAGE IS OF POOR QUALITY

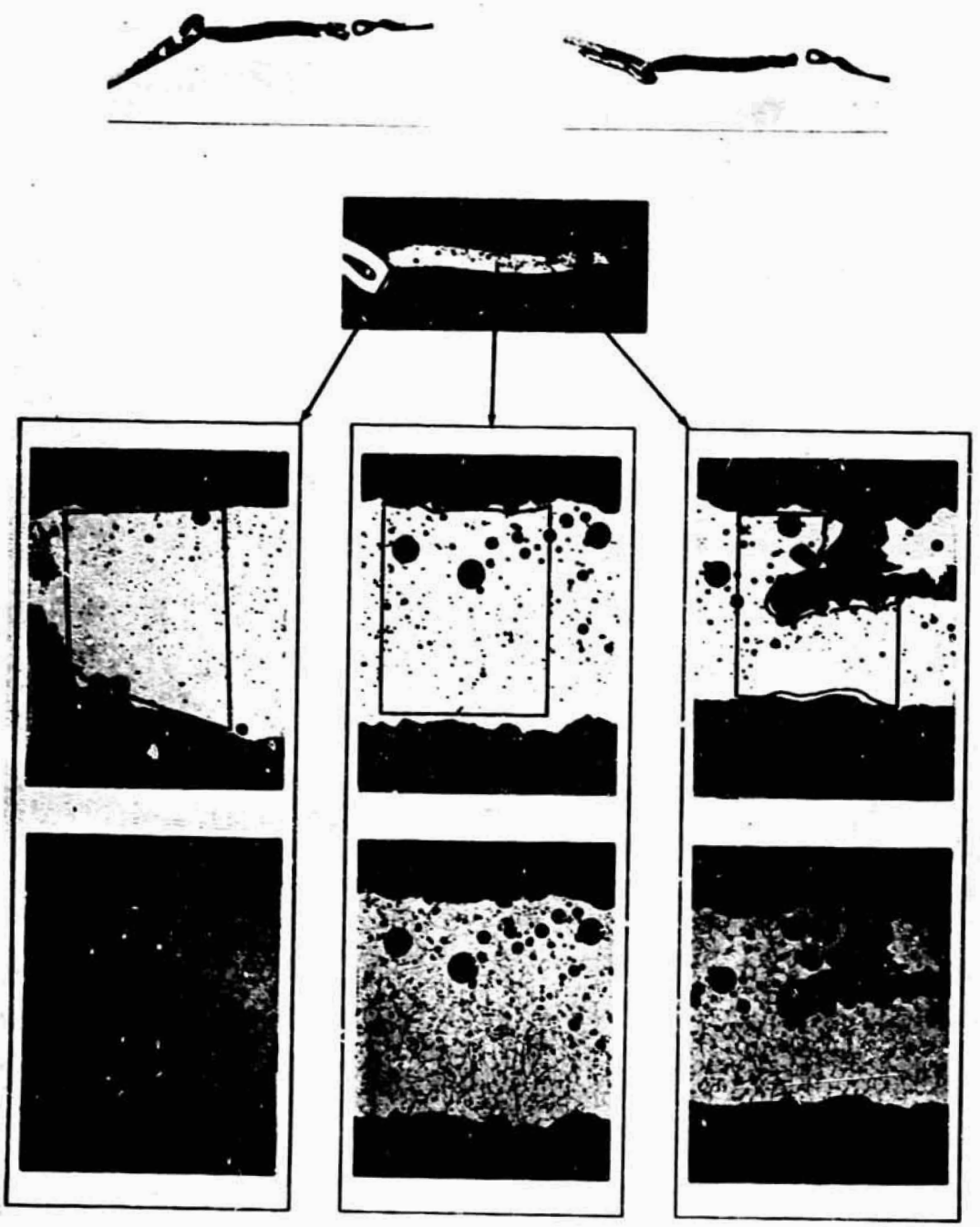

Figure 3a. Specimen 1-D, SPAR 1, ~30 sec above 660°C. The top two photos are 3X magnification and show two views of the specimen with support wires at the left and thermocouple wires at the right. The next lower photo is 5X magnification and shows a cross-section of the specimen. The bottom six photos are 50X magnification and show as-polished (top 3) and etched (bottom 3) microstructures.



ORIGINAL PAGE IS
OF POOR QUALITY

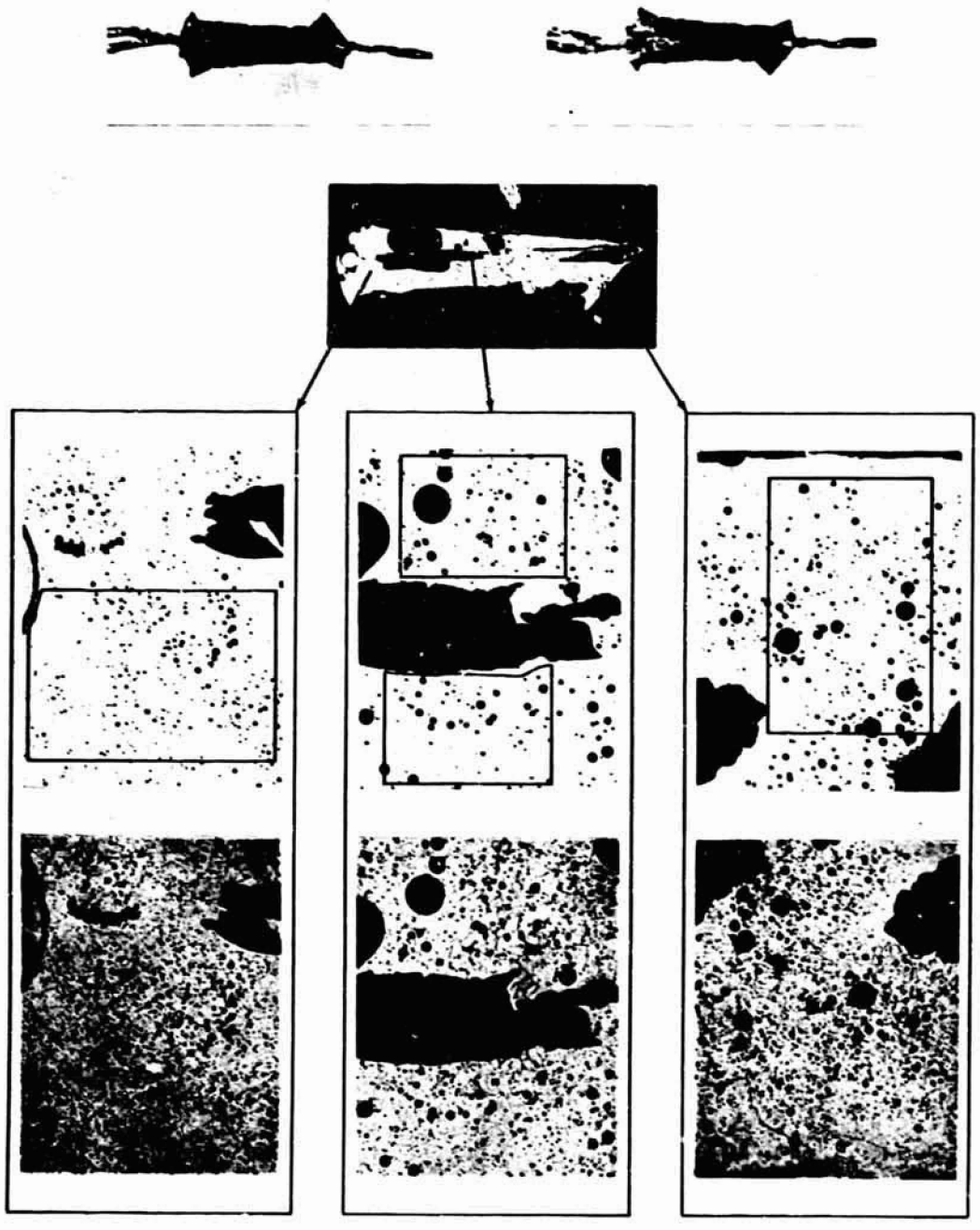

Figure 3b. Specimen 1-J, SPAR 1, ~30 sec above 660°C. The top two photos are 3X magnification and show two views of the specimen with support wires at the left and thermocouple wires at the right. The next lower photo is 5X magnification and shows a cross-section of the specimen. The bottom six photos are 50X magnification and show as-polished (top 3) and etched (bottom 3) microstructures.

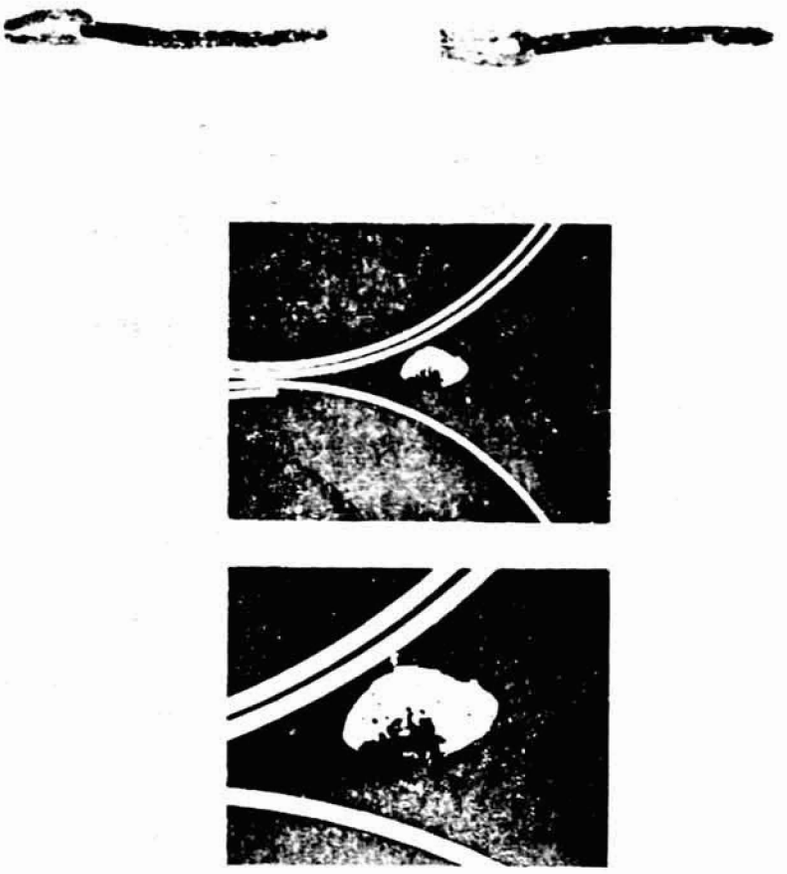

Figure 3c. Specimen 1-E, SPAR 2, 74-1/3, ~85 sec above 660°C. The top two photos are 3.5X magnification and show the specimen and its support wire (left). The center and bottom photos are 10X and 25X magnification (as-polished cross-section), respectively. The curved clips are used to hold specimens in place for metallographic mounting.

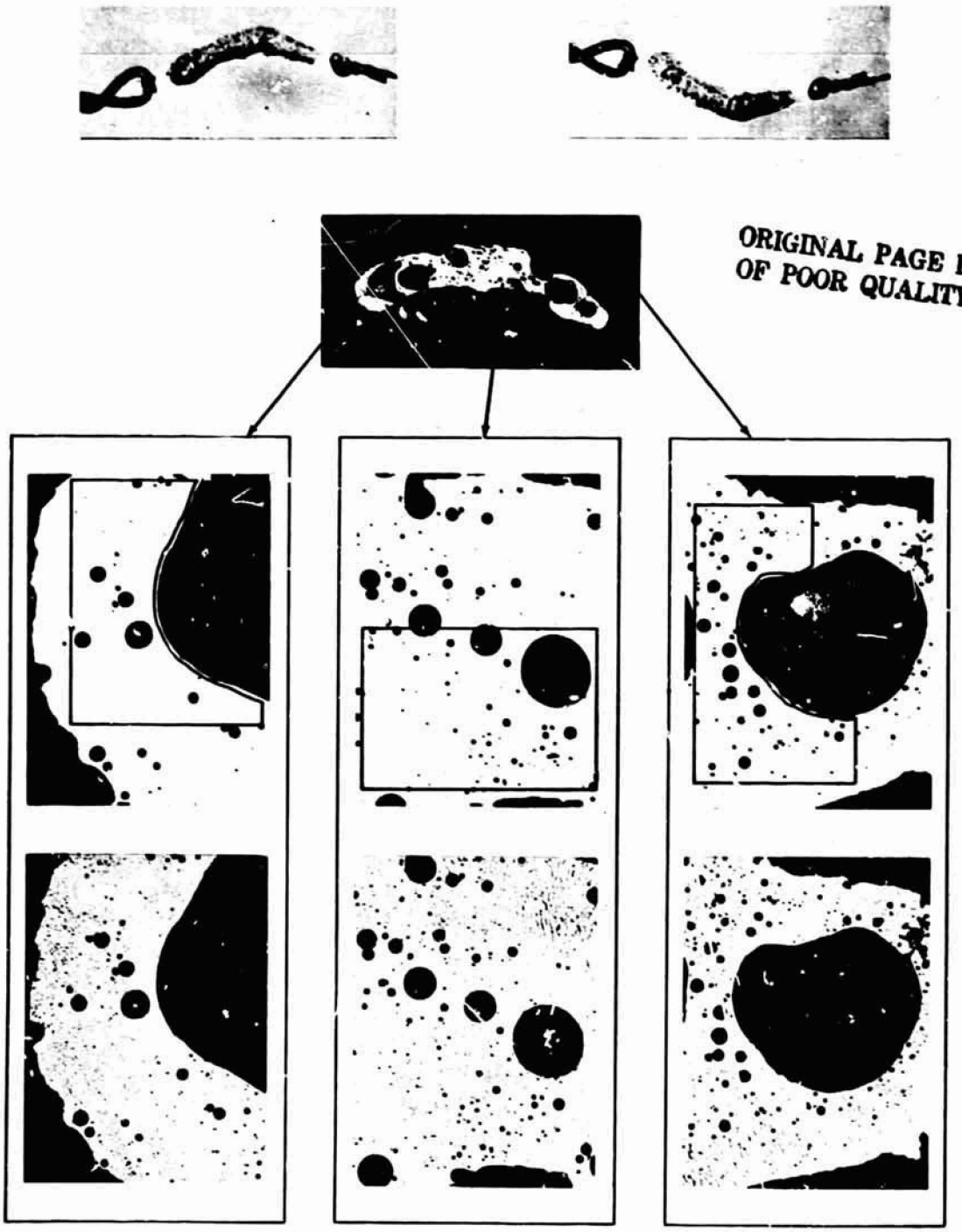

ORIGINAL PAGE IS
OF POOR QUALITY

Figure 4a. Specimen 2-C, SPAR 1, ~30 sec above 660°C. The top two photos are 3X magnification and show two views of the specimen with support wires at the left and thermocouple wires at the right. The next lower photo is 5X magnification and shows a cross-section of the specimen. The bottom six photos are 50X magnification and show as-polished (top 3) and etched (bottom 3) microstructures.

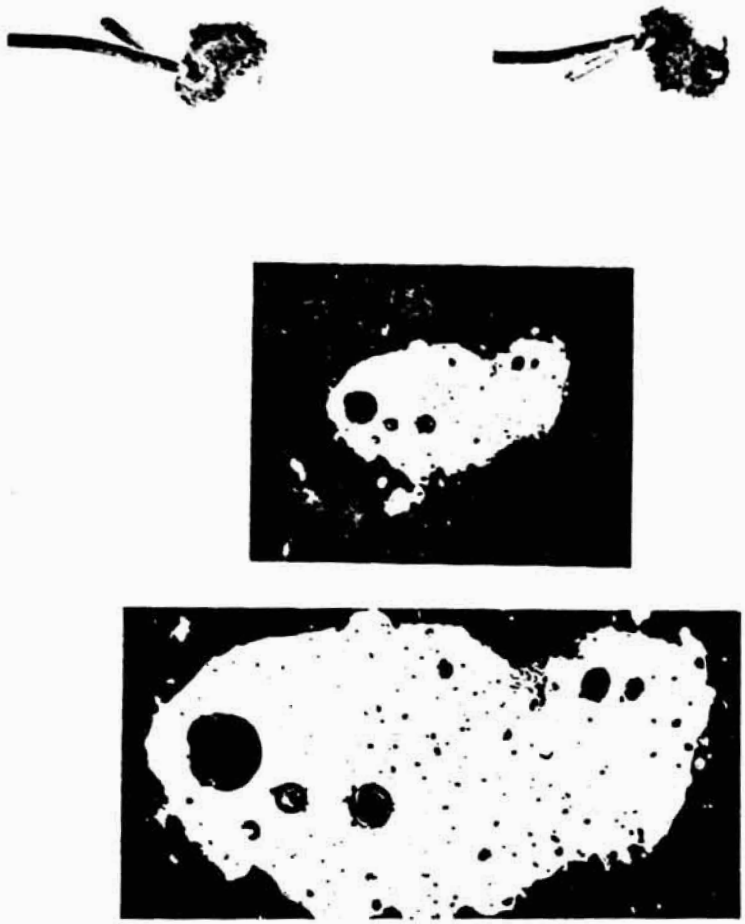

Figure 4b. Specimen 2-H, SPAR 2, 74-10/2, ~85 sec above 660°C. The top two photos are 3.5X magnification and show the specimen and its support wire (left). The center and bottom photos are 10X and 25X magnification (as-polished cross-section), respectively.

ORIGINAL PAGE IS
OF POOR QUALITY

Figure 4c. Specimen 2-G, SPAR 2, 74-10/3, ~160 sec above 660°C. The top two photos are 3.5X magnification and show the specimen and its support wire (left). The center and bottom photos are 10X and 25X magnification (as-polished cross-section,, respectively.

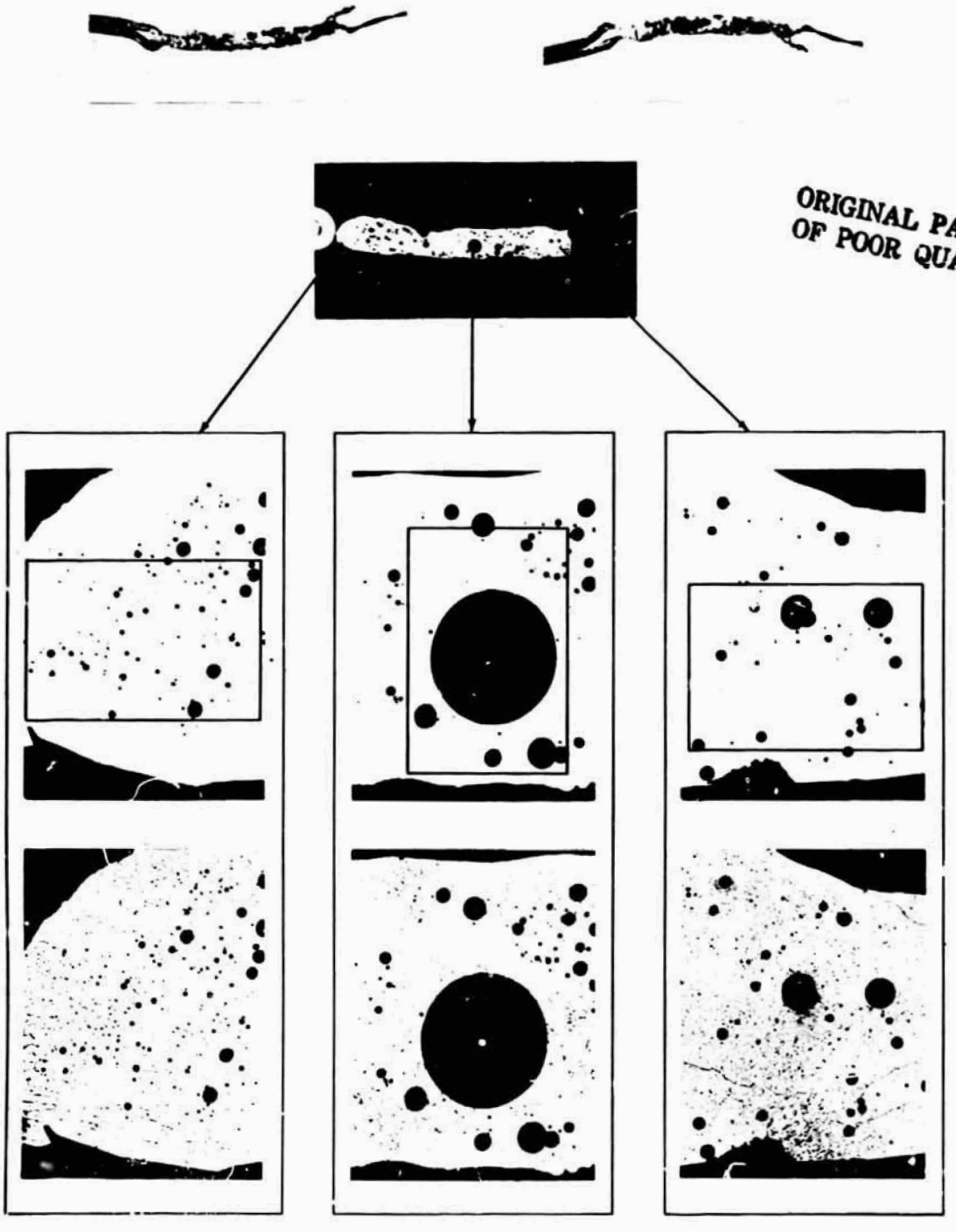

ORIGINAL PAGE IS
OF POOR QUALITY

Figure 5a. Specimen 3-C, SPAR 1, ~30 sec above 660°C. The top two photos are 3X magnification and show two views of the specimen with support wires at the left and thermocouple wires at the right. The next lower photo is 5X magnification and shows a cross-section of the specimen. The bottom six photos are 50X magnification and show as-polished (top 3) and etched (bottom 3) microstructures.

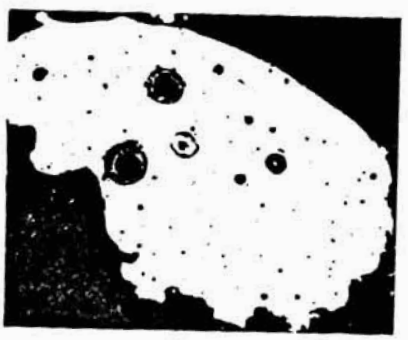

Figure 5b. Specimen 3-H, SPAR 2, 74-10/2, ~85 sec above 660°C. The top two photos are 3.5X magnification and show the specimen and its support wire (left). The center and bottom photos are 10X and 25X magnification (as-polished cross-section), respectively.

ORIGINAL PAGE IS
OF POOR QUALITY

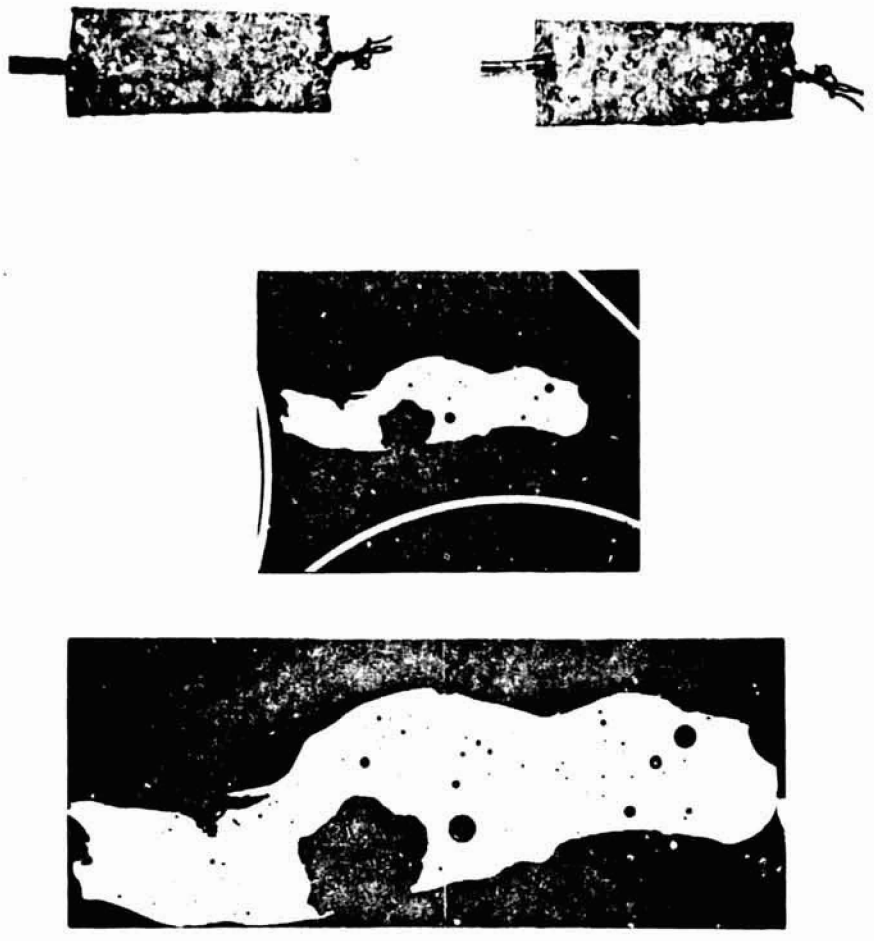

Figure 5c. Specimen 3-G, SPAR 2, 74-10/ 3, ~160 sec above 660°C. The top two photos are 3.5X magnification and show the specimen, its support wire (left), and the thermocouple (right). The center and bottom photos are 10X and 25X magnification (as-polished cross-section), respectively. The curved clips are used to hold specimens in place for metallographic mounting.

ORIGINAL PAGE IS
OF POOR QUALITY

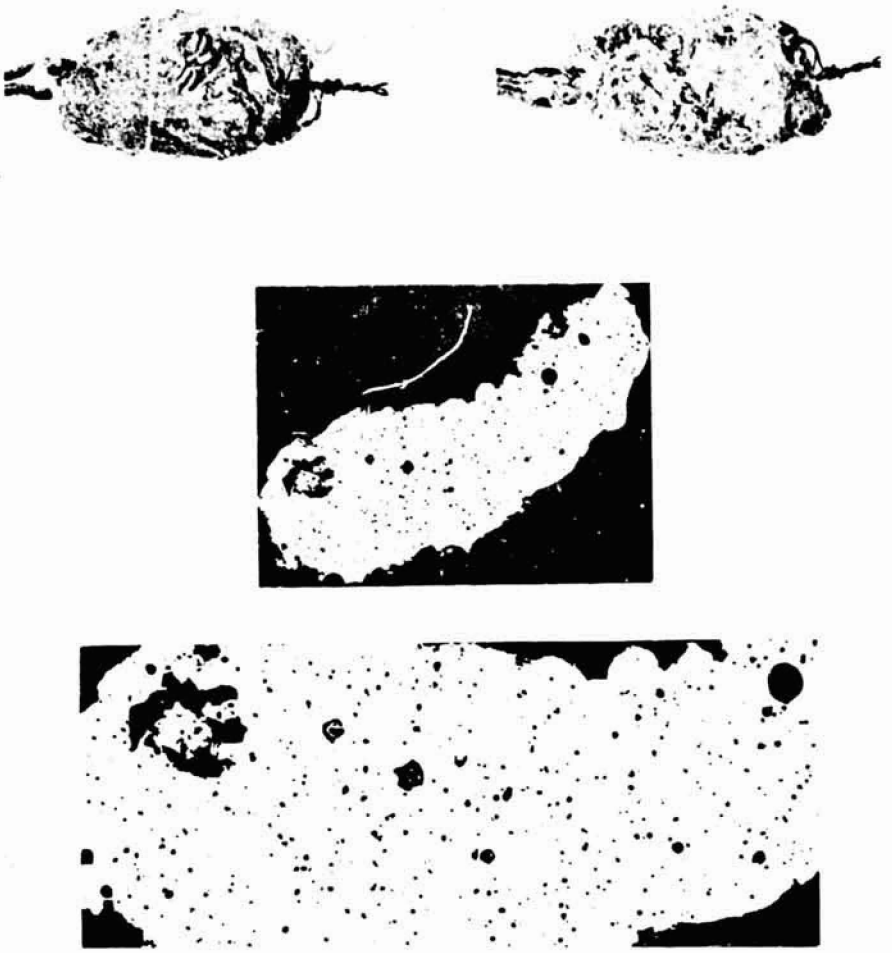

Figure 6a. Specimen T-C, SPAR 2, 74-10/2, ~85 sec above 660°C, deposit NASA No. 5. The top four photos are 3.5X magnification and show the specimen, its support wire (left), and the thermocouple (right). The center and bottom photos are 10X and 25X magnification (as-polished cross-section), respectively.

ORIGINAL PAGE IS
OF POOR QUALITY

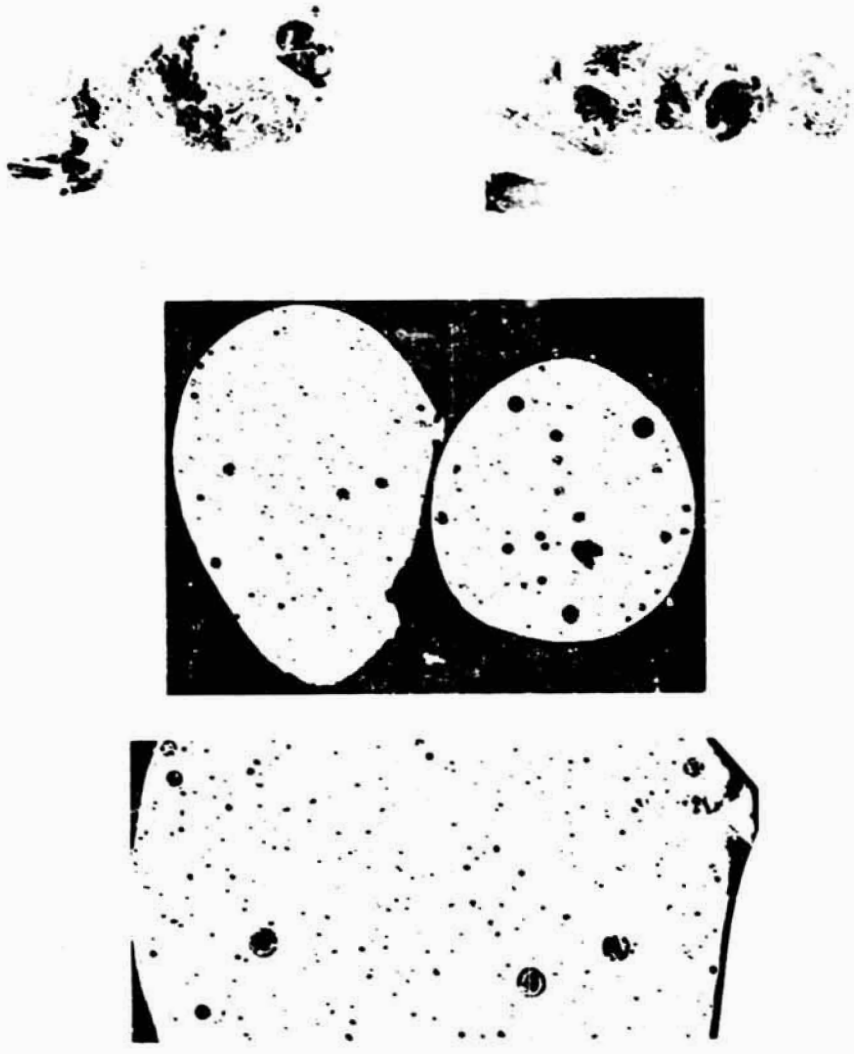

Figure 6b. Specimen T-D, SPAR 2, 74-10/2, ~85 sec above 660°C, deposit NASA No. 5. The top four photos are 3.5X magnification and show the specimen, its support wire (left), and the thermocouple (right). The center and bottom photos are 10X and 25X magnification (as-polished cross-section), respectively.

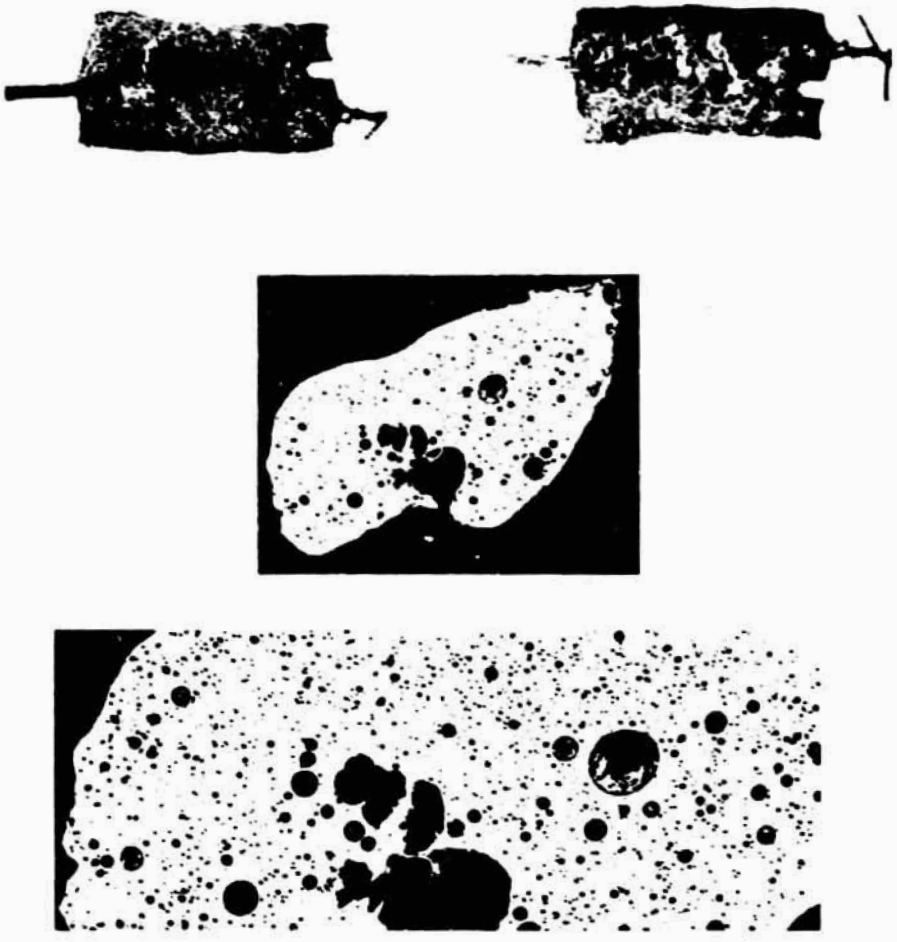

Figure 6c. Specimen T-A, SPAR 2, 74-10/3, ~160 sec above 660°C, deposit NASA No. 5. The top two photos are 3.5X magnification and show the specimen, its support wire (left), and the thermocouple (right). The center and bottom photos are 10X and 25X magnification (as-polished cross-section), respectively.

ORIGINAL PAGE IS
OF POOR QUALITY

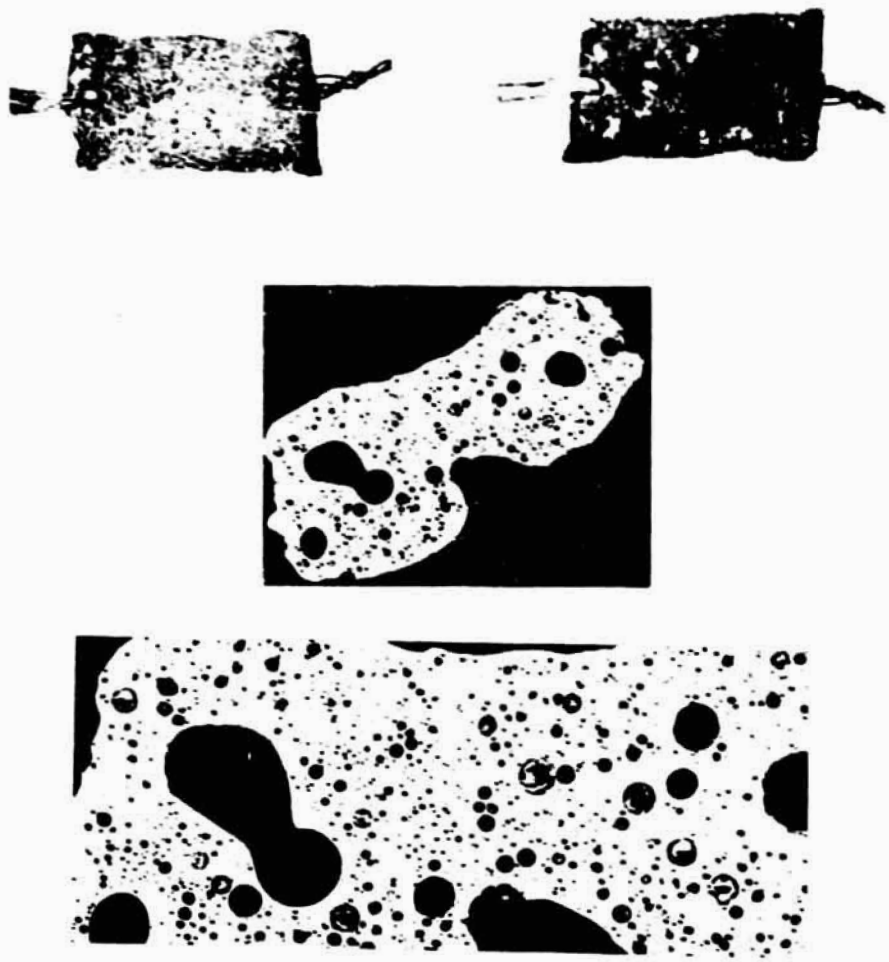

Figure 6d. Specimen T-B, SPAR 2, 74-10/3, ~160 sec above 660°C, deposit NASA No. 5. The top two photos are 3.5X magnification and show the specimen, its support wire (left), and the thermocouple (right). The center and bottom photos are 10X and 25X magnification (as-polished cross-section), respectively.

ORIGINAL PAGE IS
OF POOR QUALITY

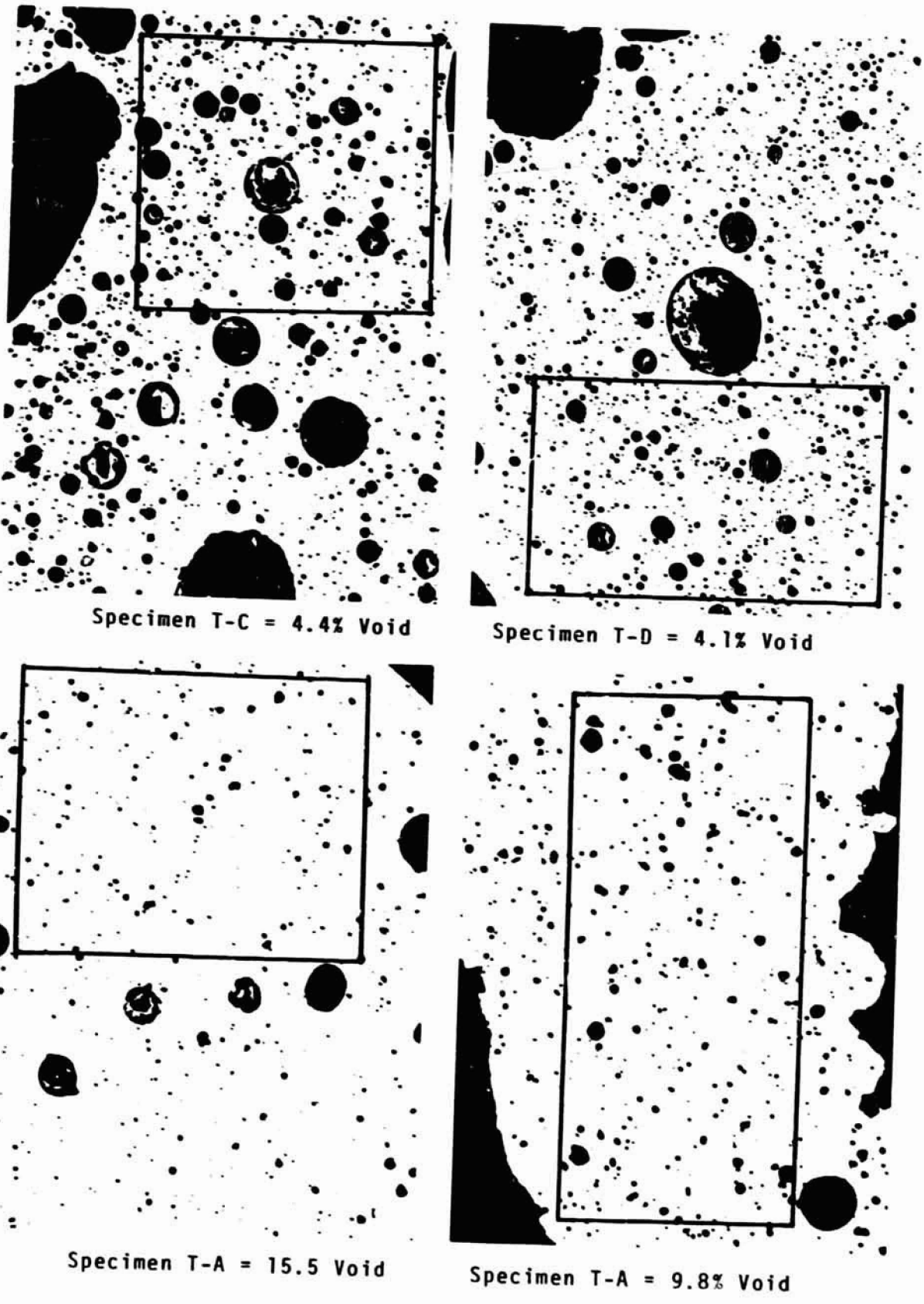


Figure 7. Void volume fractions were measured in the areas enclosed with black lines. SPAR 2, 50X magnification.

If analysis of the ground-based tests results had been possible before SPAR II, the extent of this oxide layer effect would have been better understood and samples of sufficient thickness would have been used exclusively for the SPAR III experiments so that more useful data would have been accumulated and a better understanding of the effects of gas content and time above the melting point (2 times) would have been gained.

There was no large systematic difference in microstructure resulting from increased time at temperature for thin specimens. This may be seen by comparing specimens 1-D and 1-J (SPAR 1, ~30 sec above 660°C) with specimen 1-E (SPAR 2, 74-10/3, ~160 sec above 660°C), see Figure 3, or specimen 2-C (SPAR 1, ~30 sec above 660°C) with specimen 2-H (SPAR 2, 74-10/2, ~85 sec above 660°C) and specimen 2-G (SPAR 2, 74-10/3, ~160 sec above 660°C), see Figure 4, or Specimen 3-C (SPAR 1, ~30 sec above 660°C) with specimen 3-H (SPAR 2, 74-10/2, ~85 sec above 660°C) and specimen 3-G (SPAR 2, 74-10/3, ~160 sec above 660°C), see Figure 5. However, when sample thickness was much greater, bubble coarsening and large increases in void volume fraction were observed with increasing time at temperature. This may be seen by comparing samples T-C and T-D (SPAR 2, 74-10/2, ~85 sec above 660°C) with samples T-A and T-B (SPAR 2, 74-10/3, ~160 sec above 660°C), see Figure 6.

The void volume fraction in these samples, measured in the areas indicated in Figure 7, were T-C = 4.4%, T-D = 4.1%, T-B = 15.5%, T-A = 9.8%. Note that, in general, the largest voids were not counted (except that one was counted in T-B, probably resulting in the high measured void fraction). This is because sufficiently large sample areas were not available to include many of these large voids, and therefore their influence on measured void volume fraction could not be determined accurately. Not counting these voids resulted in falsely low measures of void volume fraction.

Because of the occurrence of the large voids and because of the results of analysis of SPAR I samples, it was concluded that statistical analysis of void size distribution, volume fraction, etc. would not be meaningful.

If the equilibrium volume occupied by trapped Ar is calculated for an external pressure of one atmosphere and then adjusted for the additional energy required to create bubble surface area, well over 1 $cm^3$ of bubble volume would be expected to be generated from 1 $cm^3$ of as-sputtered Al, i.e. over 50 percent void volume fraction would be expected. This was not observed, however, probably because of the effects of the adherent oxide layer. This oxide layer

If analysis of the ground-based tests results had been possible before SPAR II, the extent of this oxide layer effect would have been better understood and samples of sufficient thickness would have been used exclusively for the SPAR III experiments so that more useful data would have been accumulated and a better understanding of the effects of gas content and time above the melting point (2 times) would have been gained.

There was no large systematic difference in microstructure resulting from increased time at temperature for thin specimens. This may be seen by comparing specimens 1-D and 1-J (SPAR 1, ~30 sec above 660°C) with specimen 1-E (SPAR 2, 74-10/3, ~160 sec above 660°C), see Figure 3, or specimen 2-C (SPAR 1, ~30 sec above 660°C) with specimen 2-H (SPAR 2, 74-10/2, ~85 sec above 660°C) and specimen 2-G (SPAR 2, 74-10/3, ~160 sec above 660°C), see Figure 4, or Specimen 3-C (SPAR 1, ~30 sec above 660°C) with specimen 3-H (SPAR 2, 74-10/2, ~85 sec above 660°C) and specimen 3-G (SPAR 2, 74-10/3, ~160 sec above 660°C), see Figure 5. However, when sample thickness was much greater, bubble coarsening and large increases in void volume fraction were observed with increasing time at temperature. This may be seen by comparing samples T-C and T-D (SPAR 2, 74-10/2, ~85 sec above 660°C) with samples T-A and T-B (SPAR 2, 74-10/3, ~160 sec above 660°C), see Figure 6.

The void volume fraction in these samples, measured in the areas indicated in Figure 7, were T-C = 4.4%, T-D = 4.1%, T-B = 15.5%, T-A = 9.8%. Note that, in general, the largest voids were not counted (except that one was counted in T-B, probably resulting in the high measured void fraction). This is because sufficiently large sample areas were not available to include many of these large voids, and therefore their influence on measured void volume fraction could not be determined accurately. Not counting these voids resulted in falsely low measures of void volume fraction.

Because of the occurrence of the large voids and because of the results of analysis of SPAR I samples, it was concluded that statistical analysis of void size distribution, volume fraction, etc. would not be meaningful.

If the equilibrium volume occupied by trapped Ar is calculated for an external pressure of one atmosphere and then adjusted for the additional energy required to create bubble surface area, well over 1 $cm^3$ of bubble volume would be expected to be generated from 1 $cm^3$ of as-sputtered Al, i.e. over 50 percent void volume fraction would be expected. This was not observed, however, probably because of the effects of the adherent oxide layer. This oxide layer

effect would be difficult to calculate because the energy required to expand the foam against the oxide restraint would be a function of layer thickness, oxide stoichiometry, degree of continuity (fracturing) of the layer, specimen surface area-to-volume ratio, etc.

The only one of these influences examined here was the effect of decreasing the sample surface area-to-volume ratio, which was accomplished by increasing sample thickness, see Tables 2 and 5. In the "T" samples, which were approximately twice as thick as the other samples, effects of increasing time above the melting point were noted, as previously mentioned.

# CHAPTER V

# THE DIRECT OBSERVATION OF DENDRITE REMELTING AND MACROSEGREGATION IN CASTING

## Experiment 74-21

By

M. H. Johnston and C. S. Griner

Marshall Space Flight Center

PRECEDING PAGE BLANK NOT FILMED

## INTRODUCTION

The solidification of ammonium chloride-water solution ($NH_4Cl$-$H_2O$) has been directly observed on Earth and at $3 \times 10^{-5}$ g's on a Space Processing Applications Rocket (SPAR I) suborbital flight. In the 1 g experiments, fluid flow resulted in substantial dendrite remelting leading to an equiaxed zone in the center of the casting. No remelting of fragmentation of dendrite were observed in the low-g environment in the SPAR I experiment. Instead a completely columnar ingot was produced (reference Space Processing Applications Rocket Project, SPAR I Final Report, NASA TM X-3458). The second flight of this experiment on SPAR II was an attempt to expand the understanding gained from the previous experiment.

## EXPERIMENT OBJECTIVES

The objectives of the experiment are: 1) observe the influence of near zero g on the solidification process, 2) eliminate density driven flow as a factor in the formation of equiaxed zone in castings, 3) observe the growth of dendrites in the columnar solidification region and determine the influence of gravity driven fluid flow on dendrite remelting, 4) determine if macrosegregation is controlled by solidification contractions, 5) provide insight into the formation of the equiaxed zone in the Skylab welding experiments, and 6) increase knowledge of the formation of casting structures on Earth.

## EXPERIMENT RESULTS

Experiment 74-21 failed to solidify on SPAR II, thus prompting a post-flight thermal analysis of the 74-21 cuvette assemblies. The results are as follows:

a. 74-21/2. Figure 1 presents transient ground based test (GBT) and flight temperatures. The flight temperatures show a larger delta-T between the thermistors than in GBT which had been predicted before the flight due to the absence of gravitational forces acting on the fluid during flight. A thermal model of 74-21/2 assembly was constructed, and the results verified that the

measured delta-T's were possible during flight. As the curves indicate, the cuvette temperature at location No. 1 was well within the expected solidification range, but solidification did not occur.

Figures 2 and 3 present vertical test at White Sands Missile Range (WSMR) and post-flight test No. 1, respectively. These data show the same temperature trends, indicating that this experiment assembly operated properly.

b. 74-21/3. Figure 4 presents the transient GBT and flight temperatures of the 74-21/3 assembly. The flight temperature profile indicates a significant temperature increase at location No. 7, beginning at 70 sec and continuing throughout the flight. Also, the temperature profiles for locations Nos. 4 and 5 show a change in slope at 70 sec. However, the temperatures at locations Nos. 4 and 5 continue to decrease to a level where some solidification should have occurred before completion of this experiment. A thermal model of 74-21/3 assembly was constructed and matched to GBT temperature profiles. Using this thermal model, an attempt was made to produce the actual flight profile by considering all possible heat inputs to the cuvette except the thermoelectrics (i.e., radiation and/or convection from the heat sink to the base of the cuvette, conduction through thermistor No. 7 wires to the base of the cuvette, and convection to the internal environment of the payload). None of the heat sources were sufficient to produce the flight profile. Each condition only slightly influenced the cooling rate, and in each case the cuvette temperatures at location No. 7 reached 0°C or less in the proper timeframe. The temperature increase noted during flight at location No. 7 was also evident in the vertical test at WSMR (Fig. 5) and in post-flight tests (Figs. 6 and 7). Post-flight test No. 2 (Fig. 7) follows the flight profile very closely and shows a temperature increase at location No. 5 at 280 sec, much the same as in flight. The backup flight unit temperature profile from post-flight test No. 4 (Fig. 8) does not show this adverse temperature trend. It appears that the only way the measurements at locations Nos. 4 and 5 could have been influenced as they were during flight is due to inadequate heat dissipation across the thermoelectrics.

Based on evidence of shattered thermoelectric junctions during disassembly of the 74-21/3 flight assembly, it was determined that a cracked or loose junction would cause an increase in the Joule heating effect of the module. This would influence the experiment as seen in flight. A cracked junction is very possible in this type assembly due to the epoxy bond restraining the thermoelectrics on both sides. Also, this failure mode could be erratic or exhibit an

on/off effect. From these flight data, it appears that the anomaly occurred 70 sec into flight. The thermal model of 74-21/3 was run with increased Joule heating beginning at 70 sec (Fig. 9). The close correlation of the model to the actual flight temperature history indicates that increased Joule heating across the thermoelectrics, due to a loose or cracked junction, was the cause of the anomalous behavior of Experiment 74-21/3 thermistors. However, even considering this failure, the thermal model shows that the actual sample temperatures are approximately 10°C at 250 sec.

## CONCLUSIONS

The absence of sample solidification during the low-g period of flight precluded achieving the experiment objectives. A detail review of the engineering evaluation of the flight anomaly is provided in the SPAR II Engineering chapter of this SPAR II Final Report. A relight of the experiment is scheduled for a later SPAR mission.

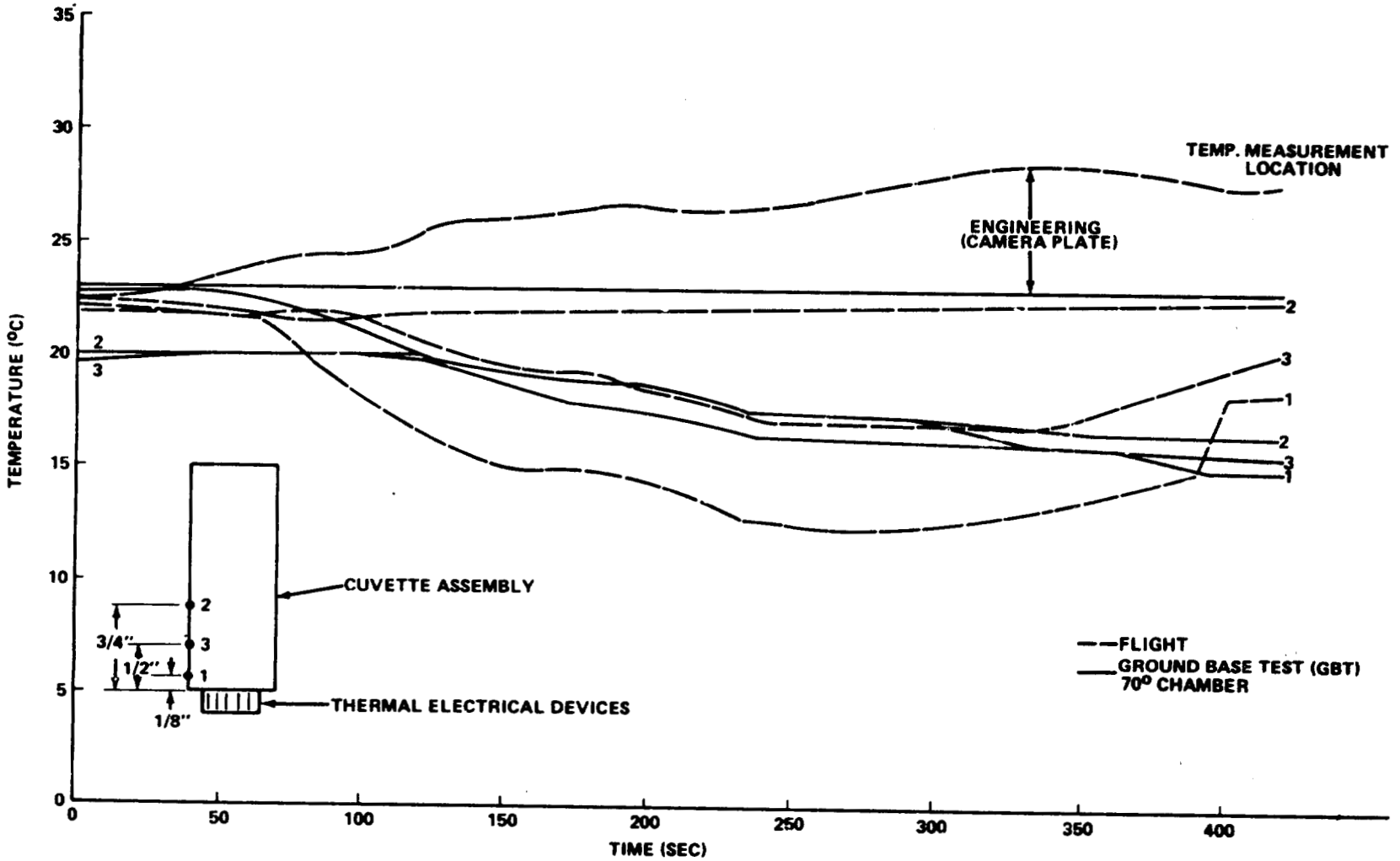


Figure 1. 74-21/2 flight and GBT.

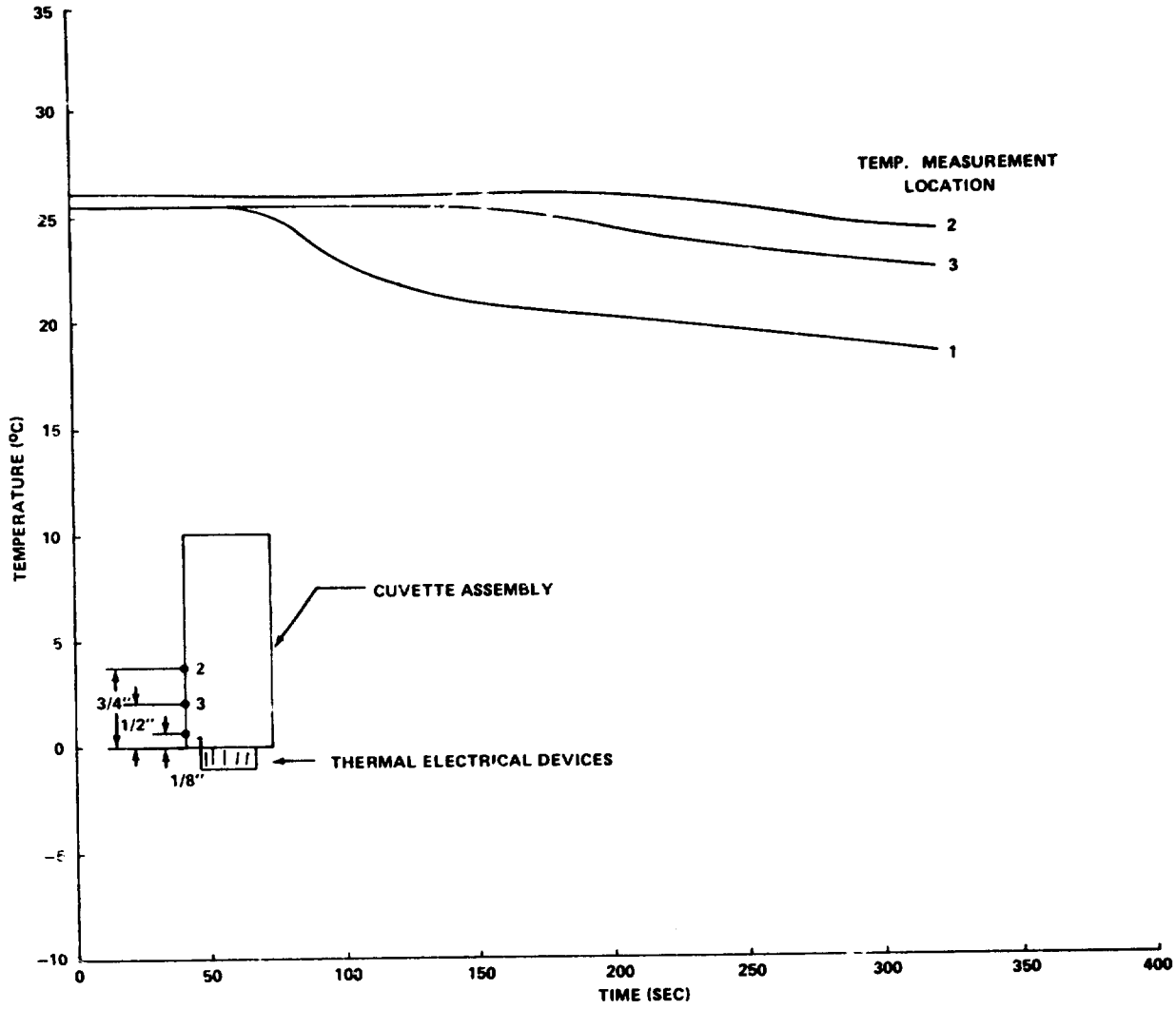


Figure 2. 74-21/2 vertical test at WSMR.

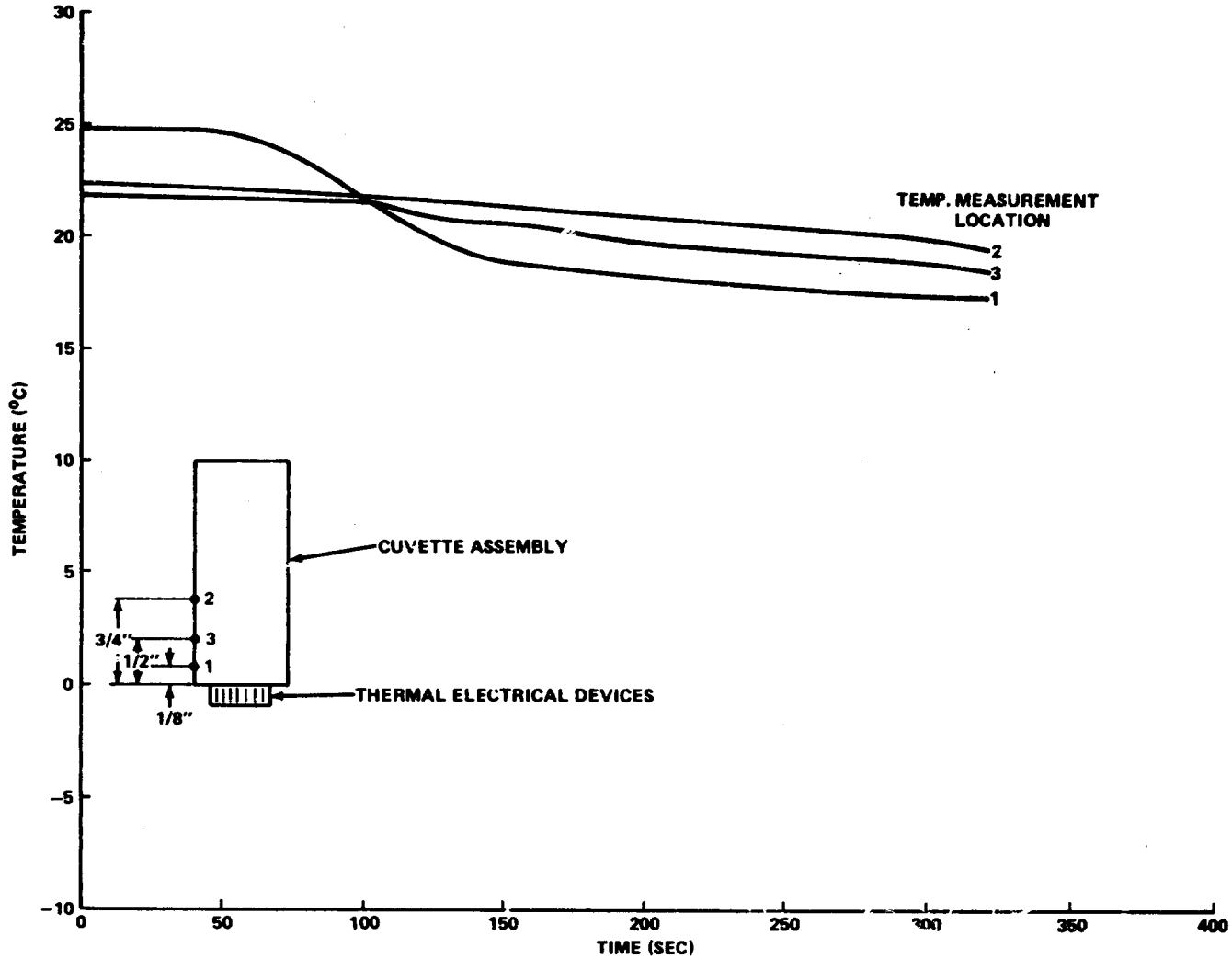


Figure 3. 74-21/2 post flight test No. 1.

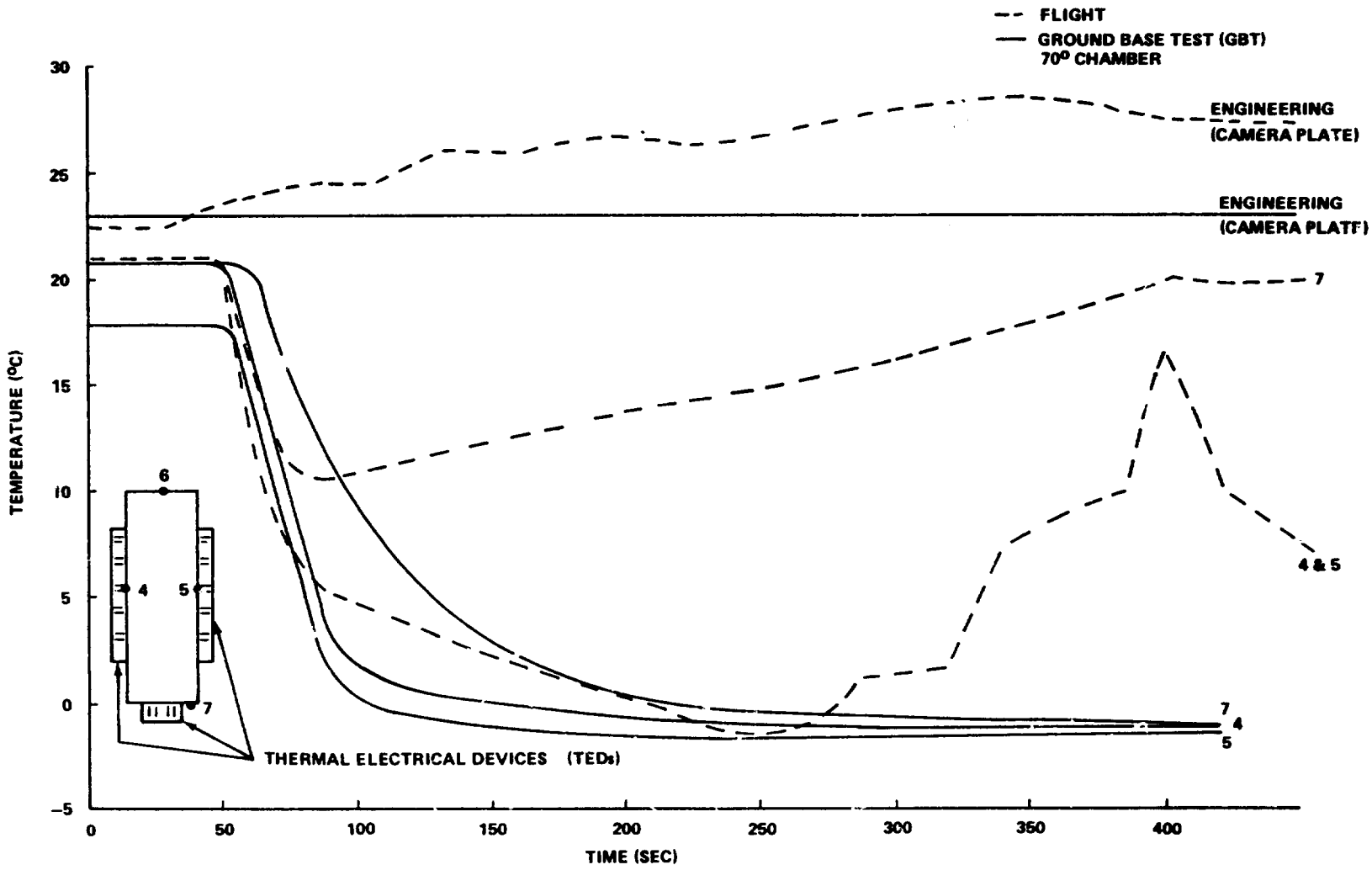


Figure 4. 74-21/3 flight and GBT.

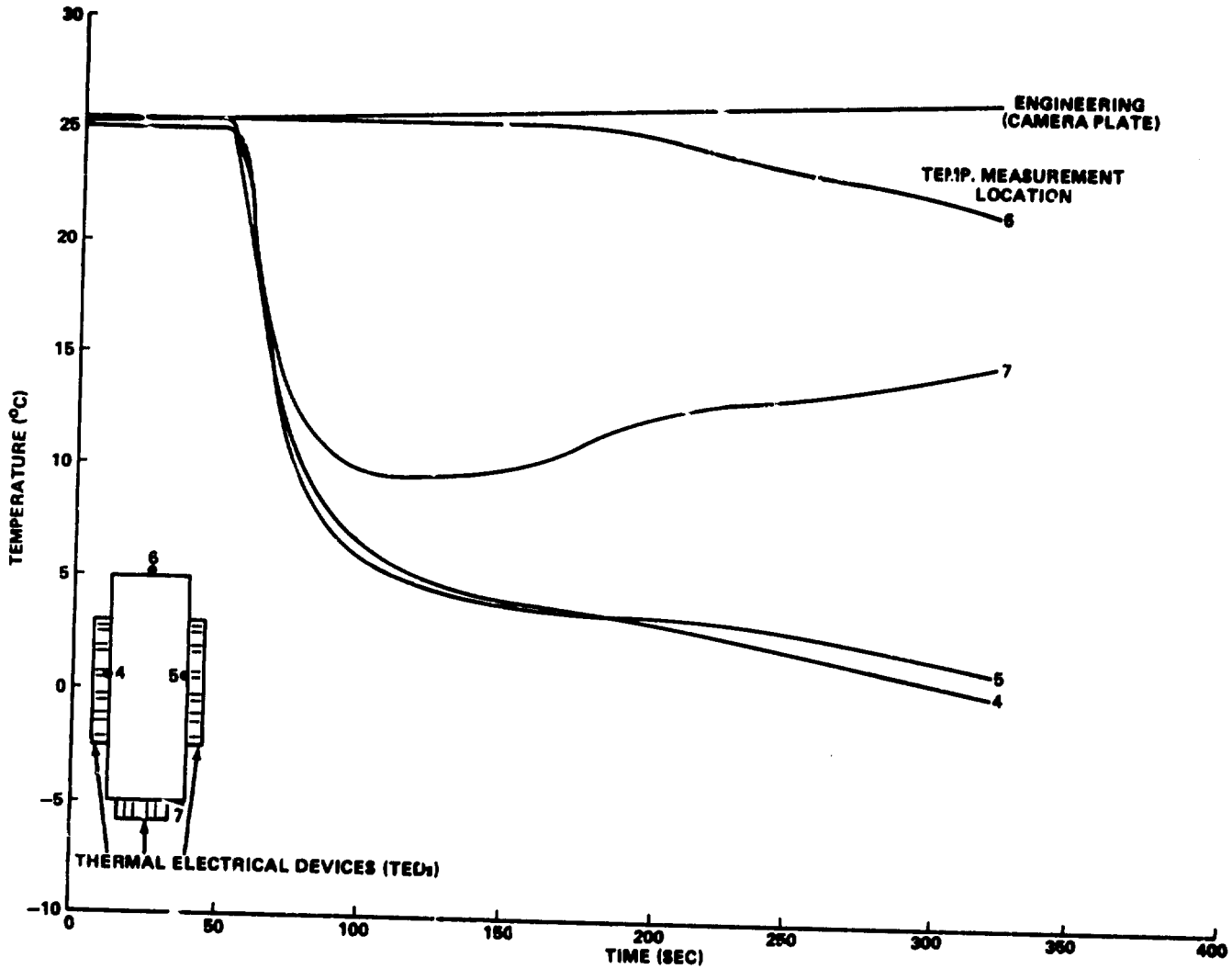


Figure 5. 74-21/3 vertical test at WSMR.

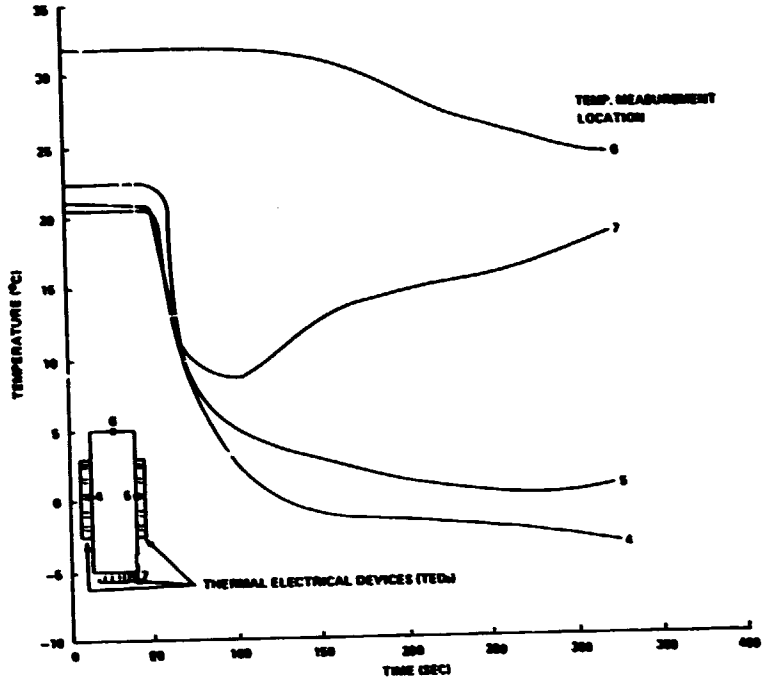


Figure 6. 74-21/3 post flight test No. 1.

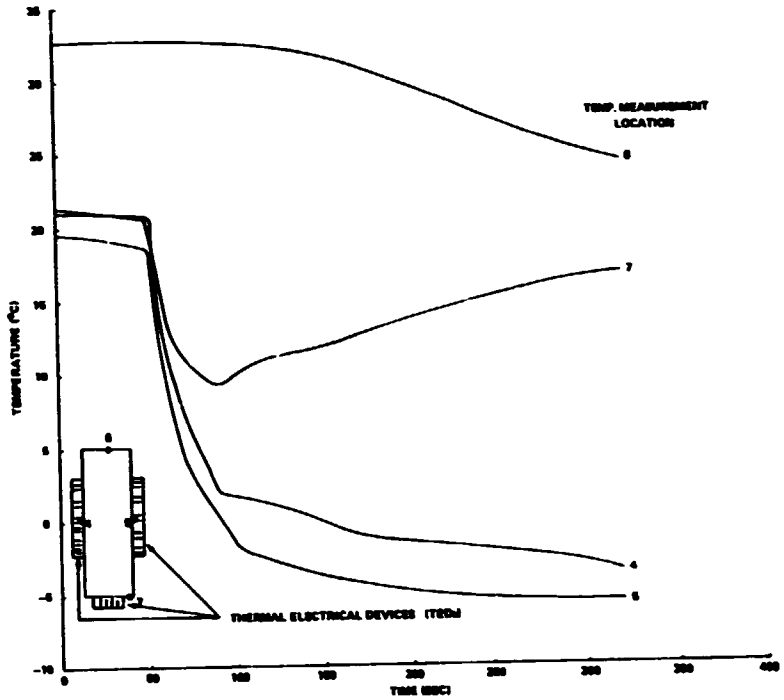


Figure 7. 74-21/3 post flight test No. 2.

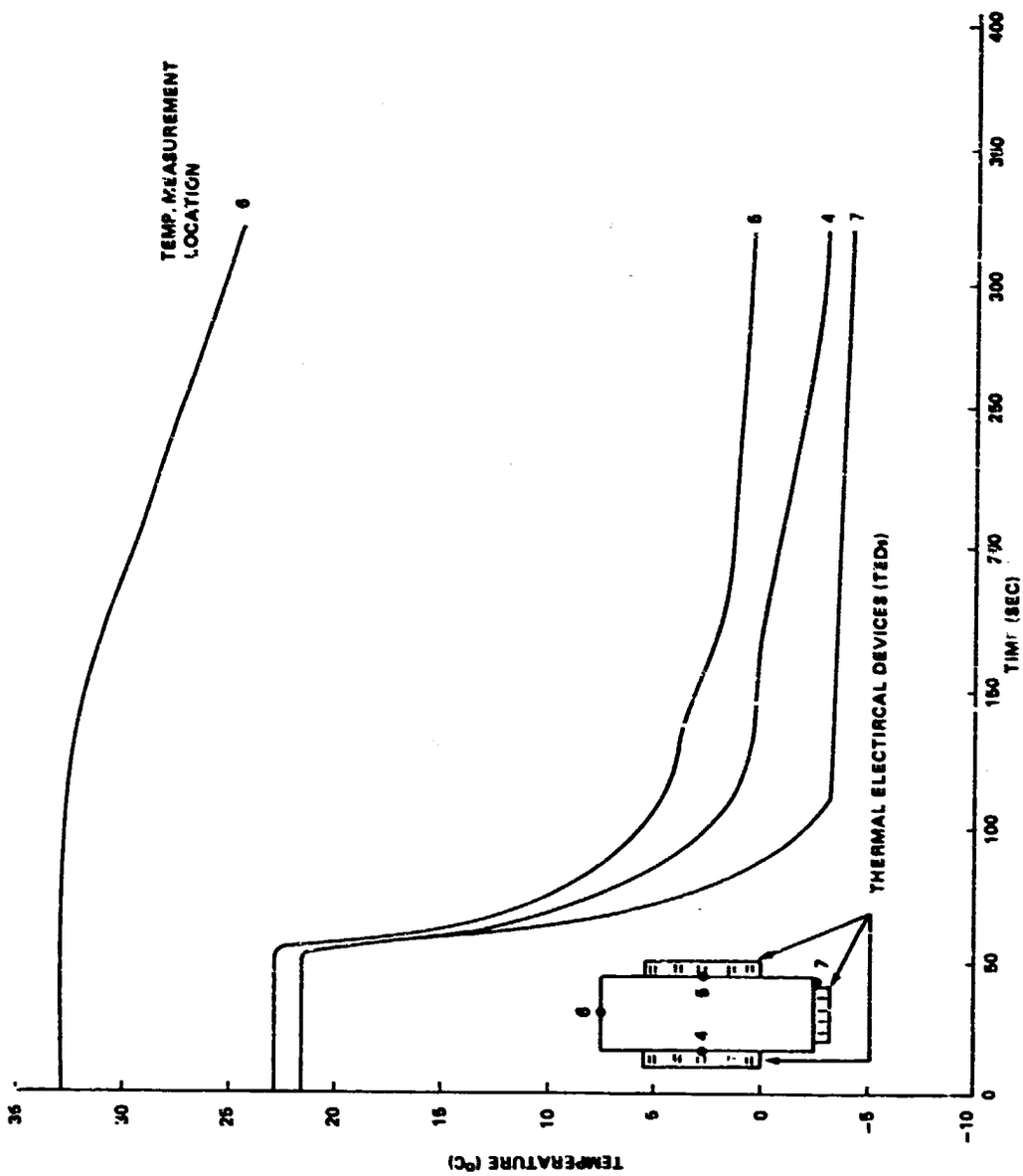


Figure 8. 74-21/3 post flight test No. 1.

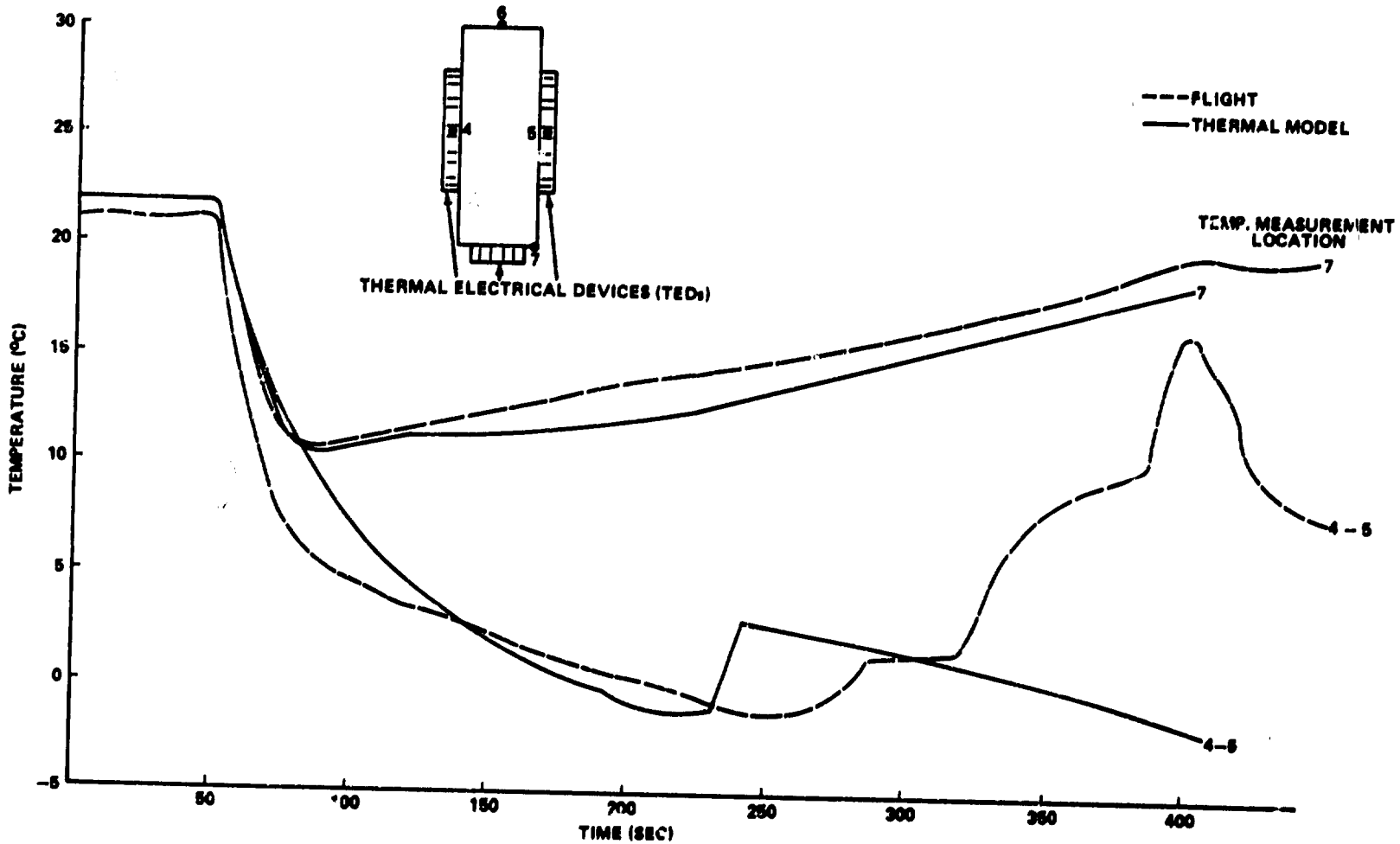


Figure 9. Failure mode of experiment 74-21/3.

# CHAPTER VI

# AGGLOMERATION IN IMMISCIBLE LIQUIDS

## Experiment 74-30

By

S. H. Gelles and A. J. Markworth

Battelle

## ABSTRACT

As part of a study to understand the influence of gravity, cooling rate, and composition on the structure of liquid phase immiscible materials, two alloys (Al-40 weight percent In and Al-70 weight percent In) were thermally treated on the SPAR II rocket flight. The treatments involved homogenization at a temperature above the miscibility gap and then rapid cooling through the miscibility gap followed by complete solidification. The last two steps were performed while acceleration levels were $<4 \times 10^{-5}$ g. Ground base samples similarly treated were used as a reference.

The results of radiographic and metallographic analysis showed the expected separation at 1 g of the ground base alloys into indium-rich and aluminum-rich layers. The flight alloys produced unexpected results. Instead of the fine uniform structures expected, they consisted of a macroscopically sized aluminum-rich central region surrounded by indium-rich metal. It was reasoned from past results on configurations formed by gas-liquid mixtures at low g that the observed structure corresponded to that with minimum surface and interfacial energies.

Since fluid motion at micro-g was necessary to achieve the final configuration, a number of different flow mechanisms were analyzed. Of those analyzed thus far, convection due to density differences, thermocapillary convection, and capillary effects all appear to be possibilities. Further analytical and experimental work is needed to differentiate among these possibilities and others.

## INTRODUCTION AND SUMMARY

### Background and Justification

Immiscible materials in the general context of the term make up a sizeable class of useful materials. In the broadest definition, they include any multiphase system, whether produced by solid or liquid phase reactions or by mechanically mixing. They include most common alloys and all composites. The multiphase nature of these materials may lead to enhanced mechanical and physical properties.

Liquid phase immiscibles make up a special class of materials which have gained renewed interest as a result of space processing activities. These systems contain a "miscibility gap," i.e., a field in the binary-phase diagram which represents the equilibrium between two liquids of different compositions. At a sufficiently high temperature, the two-phase equilibrium is usually replaced by a single-phase liquid field. An example of such a system is the Al-In binary-phase diagram presented in Figure 1 (1,2). The miscibility gap exists above 639°C and between the compositions 17.5 and 96.8 weight percent In. By choosing alloys of composition near the extremities of this range, it is possible to obtain mixtures of In droplets in an Al-rich host or Al-rich droplets in an In-rich host. By selecting a composition near the center of the miscibility gap, it should be possible to get an intimate mixture of the two phases in approximately equal proportions or a modulated structure produced by spinodal decomposition (3). Evidence for spinodal decomposition in liquid systems has recently been presented (4).

There are many examples of liquid-phase immiscible materials. For example, in a study for NASA, Reger (5) has listed over 500 systems which contain or were suspected of containing a miscibility gap. Some liquid-phase immiscible systems are presently being used in such applications as electrical contacts, permanent magnets, or bearings. There are many other potential applications, for example, in superconductors, superplastic materials, and catalysts. These applications have been explored in recent studies at Battelle's Columbus Laboratories for NASA-MSFC (6,7).

The link between liquid-phase immiscibles and space processing evolved from a desire to produce nonsegregated immiscible materials. Although this is an important aspect of the relationship between the two, a more important

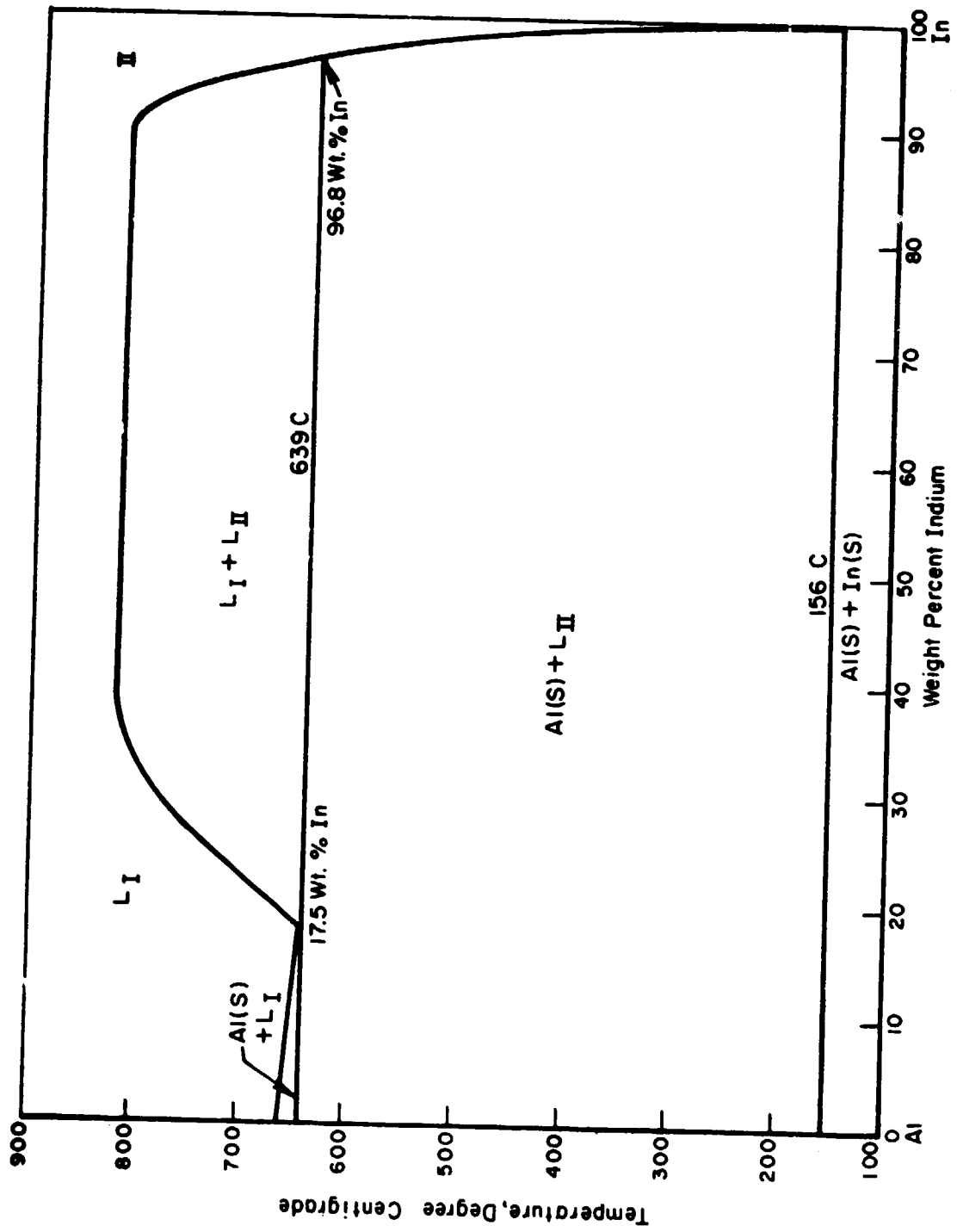


Figure 1. Al-In equilibrium diagram (1,2,3).

one was not realized until fairly recently, namely, that by processing liquid-phase immiscible materials in a low g environment. Not only is the second-phase dispersant expected to be more uniformly distributed, but it is also expected to be much finer.

This conclusion is based on a previous Battelle study (6,8) in which computer simulation was used to model the agglomeration of liquid droplets in a host liquid. From this study, it was concluded that some major mechanisms causing droplet coalescence are not active at zero g. These mechanisms depend on gravity-driven collision processes which result from differences in droplet velocity and are created in basically two ways:

1. Stokes flow — The settling or rising of droplets of one density in a host fluid of another density.

2. Gravity-driven convection currents — Velocity gradients which cause droplet collisions result from gravity-driven convection currents. The latter originate from density differences in the host fluid due to composition or thermal gradients.

The finer microstructures anticipated as a result of the computer-simulation studies have been observed in liquid-phase immiscibles by Reger and Yates (9). In addition, some unexpected results have been obtained in the form of unexplained and unidentified phases (9), unusual electrical properties (10), and an unusual dependence of the structural fineness on the cooling rate (11). This last observation has been made in the bismuth-gallium system after processing at zero g. In this case, it has been found that a sample which had been slowly cooled exhibited a finer microstructure than one cooled more rapidly. A possible explanation for this behavior has been suggested in terms of convection currents induced by the quenching operation producing droplet collisions and coalescence in the more rapidly cooled sample.

The discovery of unidentified X-ray diffraction lines in gold-germanium and lead-zinc-antimony alloys processed at low g offers the possibility that metastable alloys possessing unusual properties may be obtained in the bulk by space processing. However, a recent attempt to confirm the presence of metastable phases in these alloys was not successful (12). This effect must, therefore, be discounted until further evidence is obtained.

Although our understanding of the coalescence processes in liquid-phase immiscibles has increased significantly in the last two years, we are just

beginning the initial stages of a quantitative understanding of the effect of gravity and other system properties on the structure of liquid-phase immiscibles. For example, it is only recently that the first kinetic measurements of droplet size distributions have been obtained in a system with a miscibility gap (Al-40 weight percent In alloys cooled through the miscibility gap at two different rates at 1 g) (6). As would be predicted from the computer-simulation studies, the population of fine droplets decreased, and the concentration of coarse droplets increased as the cooling rate decreased.

In the overall current study, a portion of which includes the SPAR II rocket experiment, we intend to obtain a quantitative understanding of the effect of gravity, cooling rate, and composition on the structure of liquid-phase immiscible Al-In alloys.

Some of the questions to be answered in this study are as follows:

1. How fine can liquid-phase immiscible materials be made when processed at low g?

2. What effect does cooling rate have on the fineness of the structure?

3. Is there a critical cooling rate beyond which convection currents are induced in the liquid so that agglomeration and a coarser structure result?

4. What effect does composition have on the distribution of the immiscible phases and the fineness of the structure?

5. Does spinodal decomposition occur in the liquid phase immiscible system Al-In?

6. Is metastability in space-processed liquid-phase immiscible alloys a real effect?

The justification for the present work can thus be summarized in the following way:

1. Liquid-phase immiscibles are a useful class of materials whose application may be further increased.

2. Processing of such materials at zero g could lead to unique microstructures not obtainable in the bulk in terrestrially processed materials.

3. There is a need to determine quantitative relations between the structure and processing variables, such as composition, cooling rate, and the presence or absence of net gravitational forces. This information will allow us to make predictions about the type of structures achievable, their properties, and potential applications.

## Objective

The overall objective of this study is to gain an understanding of the influence of gravity, cooling rate, and composition on the structure of liquid-phase immiscible systems. The specific objective of SPAR II Experiment 74-30 was to determine the effect of gravity on the structure of the alloys, Al-40 weight percent In (13.55 atomic weight percent In) and Al-70 weight percent In (35.42 atomic weight percent In) when cooled through the miscibility gap at a controlled cooling rate (~15°C/sec). A future rocket experiment was originally planned to study the same alloys processed at a somewhat slower cooling rate. As will be seen in what follows, these plans have been at least temporarily altered pending further analyses of the present experiment.

## Experiment Description

### Experimental Configuration

SPAR II Rocket Experiment 74-30 was conducted in one cavity of the General Purpose Rocket Furnace (GPRF). A standard stainless steel capsule modified to accept a thermocouple for sensing the internal melt temperature contained the two alloys studied, Al-40 weight percent In and Al-70 weight percent In. The alloy components in proper proportion were contained in separate aluminum oxide crucibles especially machined for a close fit with the internal dimensions of the stainless steel cartridge. The samples were carefully prepared by initially melting the components in high vacuum and then by sealing the pure components in the cartridge under a partial pressure of helium. The helium pressure level was chosen so that the cartridge contained slightly less than 1 atm of pressure at the maximum temperature, 970°C. Eight capsules were prepared for ground base tests, flight tests, and backup.

## Flight Procedure

The stainless steel cartridge containing the two alloys was heated to approximately 950°C in the rocket for 15 min before launch. This temperature corresponds to positions in the Al-In equilibrium diagram within the homogeneous single phase liquid field above the miscibility gap (Fig. 1). The alloys were allowed to remain at this temperature during launch and for approximately 154 sec after launch. Accelerations were reduced to micro-g levels approximately 91 sec after launch so that a time period of approximately 63 sec was available for damping of any residual fluid motion in the specimen. At the end of this stabilization period, the samples were rapdily cooled by means of helium gas which was allowed to flow around the periphery of the stainless steel cartridge. A complete cooling curve was successfully telemetered from the rocket and indicated that the average cooling rate through the miscibility gap was 14.7°C/sec. A thermal arrest of approximately 9 sec duration corresponding to the monotectic transformation was clearly visible on the cooling curve. Complete solidification at approximately 156°C as indicated by the internal temperature of the alloy took place well within the micro-g time frame. The experiment appears to have been conducted successfully and according to the original plan.

Prior to the flight, which took place May 17, 1976, two ground base samples had been processed in the GPRF for the purpose of obtaining terrestrial standards for comparison with the flight samples. One of the samples was run in exactly the same way as the flight sample and had an average cooling rate through the miscibility gap of 17.9°C/sec which is very close to that of the flight sample. The other ground base sample which is to be considered a secondary standard was actually subjected to the thermal cycle twice and in an orientation antiparallel to that of the other two samples. Average cooling rates through the miscibility for the two cycles conducted on this sample were 12.2° and 12.9°C/sec.

The flight and ground base samples were examined by x-radiography, macroexamination, and by metallographic analysis.

## Results

As was delineated in the Background section of this report, we expected that the Al-40 weight percent In alloy flight sample would produce a fine dispersion of In-rich droplets within an Al-rich matrix. The expected structure

of the Al-70 weight percent In alloy flight sample was not as clearly defined. One possibility imagined was an interlacing network of Al-rich and In-rich phases on a microscopic level. Alternatively, the expected structure of this alloy might be that resulting from the spinodal decomposition of the homogeneous liquid. If this latter structure was retained during solidification, the sample should have a modulated structure consisting of composition fluctuations having a wavelength on the order of 0.01 to 0.1 $\mu$.

The expected macro- and microstructures were not observed on the flight sample. Moreover, the unusual and unexpected configurations encountered have proven the necessity for further analysis which is still under way. It is extremely important that the mechanisms leading to these unusual structures be understood so as to avoid their interference in these types of experiments. It is also important from the standpoint of providing a better understanding of materials behavior in the space environment.

X-radiography and macroexamination have confirmed the expected layering of the In-rich and Al-rich materials in the alloys processed terrestrially. However, the structure of the space processed alloys consisted of an Al-rich core surrounded by In-rich metal. For the Al-70 weight percent In alloy, the Al-rich core was approximately spherical; whereas, in the Al-40 weight percent alloy, the Al-rich core occupied a larger fraction of the container volume and was roughly the shape of the container. There was a great tendency for the In-rich material to wet the aluminum oxide container walls.

The microstructural features of all the samples were similar and consisted of the following phases:

- In-rich droplets
- Al-rich spheres showing evidence of the monotectic transformation
- Al-rich dendrites
- An Al-rich matrix
- An In-rich matrix.

A great difference in the distribution of the dispersed phases was seen between the samples processed at 1 g and those processed at the micro-g level. In the 1 g processed samples, the effect of gravity could be easily seen by the settling of the In-rich droplets in the Al-rich matrix and by the floating of the Al-rich spheres and dendrites in the In-rich matrix. The same type of droplets were seen in the flight sample and although they were relatively coarse, their distribution was much more uniform than it was in the samples processed on Earth.

The unusual distribution of phases in the flight sample appears to have resulted from two causes:

1. The tendency to form the configuration which has the lowest combination of surface and interfacial energies

2. Fluid flow mechanisms that provide the means to achieve the low energy configurations.

Analyses have been carried out of the configurations that are expected at low g for mixtures of molten Al and In as a function of the volume fraction of Al and where the two materials are of spherical geometry and are in a containerless configuration.

For this case, it has been shown that there is an overwhelming tendency for the molten In to surround a liquid Al sphere, when the interfacial energy between the Al- and In-rich materials is relatively low as expected. This tendency is replaced by one in which separate spheres of Al and [illegible] if the interfacial energy and Al content are sufficiently high. There is a threshold interfacial energy level below which the In-surrounding-Al configuration is stable even at the higher Al concentrations.

Insight into the case in which a container is involved has been obtained from published analyses and experiments conducted on liquid-gas mixtures at low g (13,14). Based on these results, the observed macrostructure of a wetting In-rich material surrounding an Al-rich core is expected.

A number of mechanisms leading to fluid-flow at the micro-g acceleration levels have been suggested as possibilities leading to the observed structure of the SPAR II flight sample:

- Residual motion from the rocket spin
- Conventional convection
- Marangoni effect
- Capillary flow.

The first three of these mechanisms have been analyzed with the following results.

The calculations dealing with residual motion from the rocket spin have shown that the time available at micro-g levels before the quenching operation (94 sec) is sufficiently long compared to the time needed to damp the residual motion to a very small level (30 sec for the Al-40 weight percent In alloy, 55 sec for the Al-70 weight percent In alloy) so that this source of potential fluid motion can be neglected.

The calculations dealing with convection flows arising from density differences in the liquid alloy show that fluid velocities on the order of 0.1 cm/sec are possible. In the 10 sec period between initial phase-separation and monotectic solidification, fairly sizeable fluid flows are possible. Thus, this mechanism is probably a contributor to the observed motion.

Calculation of the Marangoni numbers for the flight alloys (Ma = 229 for Al-40 weight percent In, Ma = 500 for Al-70 weight percent In) at the relatively high cooling rate of 15°C/sec shows that fluid motions caused by thermo-capillary effects are likely.

Fluid motion caused by capillary effects such as the spreading of droplets onto a solid surface has as yet not been analyzed. Droplet spreading and the surface dominated motion of liquids wetting a surface are usually rapid events and could also play a major role in the evolution of the observed structure of the flight samples.

## Recommendations

Since the physical observations and fluid flow analyses have only been partially completed, it is recommended that work be continued to further characterize the ground base and flight samples and that further fluid flow analyses be

carried out with the objective of understanding the mechanisms involved so that interference by undesired fluid flow in future experiments be avoided.

Further flight studies need to be carried out with the objective of performing the original experiment without the presence of unwanted fluid motion.

Two experiments should bring us closer to that goal:

1. Perform a flight experiment which eliminates the free surface and thus eliminates this source of thermocapillary motion

2. Perform low g experiments with a transparent immiscible system analagous to the present one to study the motions and configurations in these materials.

## DETAILED PROGRAM DESCRIPTION

### Cartridge Design

The experimental samples were designed to fit into a standard cartridge employed for the GPRF. Experiment 74-30 occupied one of the three chambers in this furnace.

The cartridge design is shown in Figure 2. The pure components for the Al-70 weight percent In and -40 weight percent In alloys are placed in separate aluminum oxide containers which have been carefully ground to fit the internal dimensions of the stainless steel capsule. The alloy components have been prepared from high purity Al and In and have been individually vacuum melted at approximately $10^{-3}$ Pa ($10^{-5}$ torr) to ensure that there would be no outgassing during the experiment. Pure components were used in this experiment rather than alloys because greater control of the final alloy composition could be effected in this manner with a system highly prone to macrosegregation.

The dimensions of the alloy components were carefully chosen to ensure that there would be no possibility of crucible breakage as a result of thermal expansion of the metal components during heating. In addition, the volume of the components was chosen to almost, but not completely, fill the crucibles at

ORIGINAL PAGE IS
OF POOR QUALITY

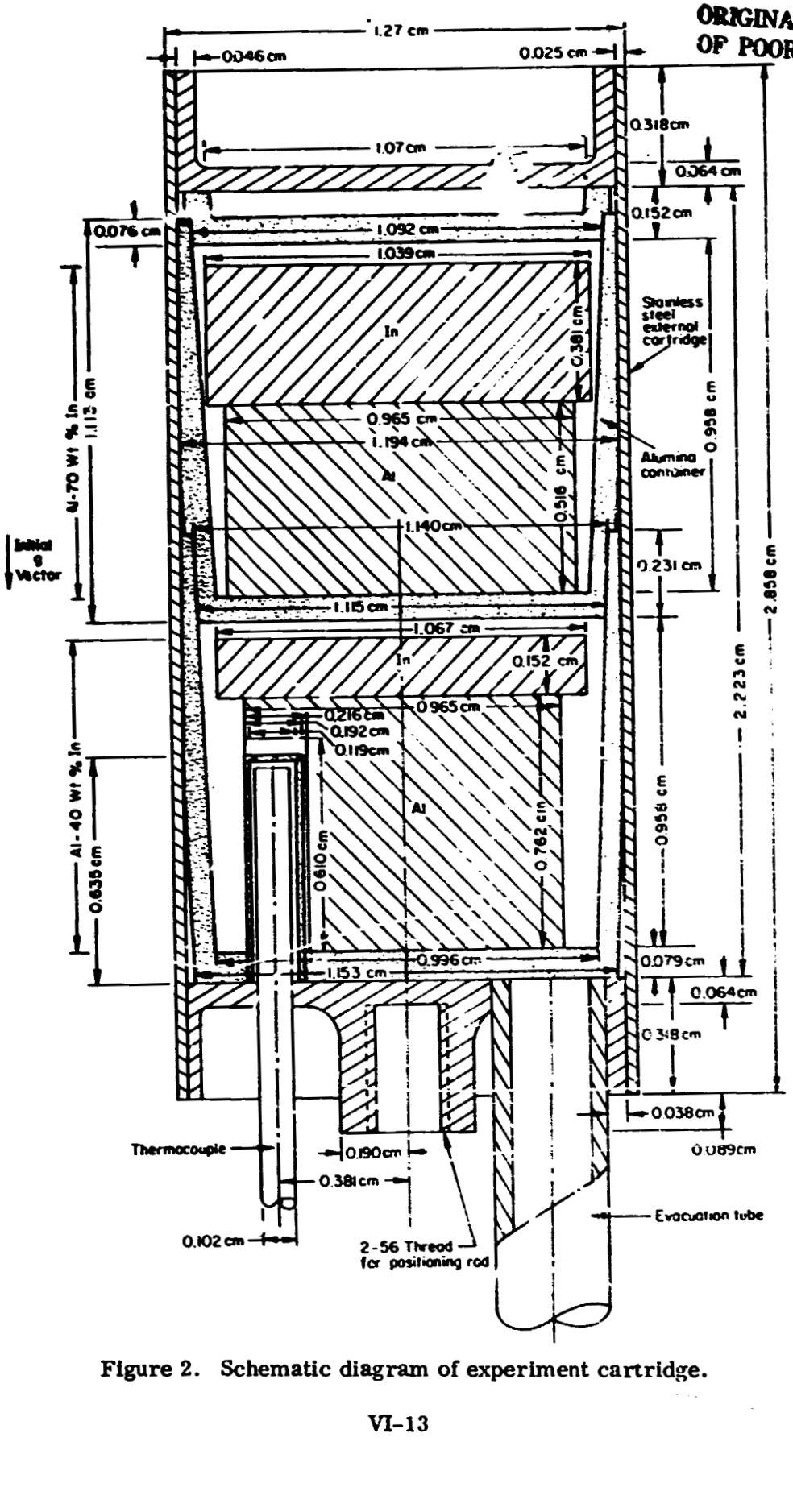


Figure 2. Schematic diagram of experiment cartridge.

the highest temperature of the experiment (970°C). This design minimized the tendency for excessive stresses to build up within the crucibles and thus avoided crucible breakage and molten metal leakage.

Another important feature of the cartridge design was the provision for a thermocouple within the Al-40 weight percent In alloy (lower alloy in Fig. 2). The thermocouple (approximately 1 mm OD) is chromel-alumel sheathed in Inconel and is brazed into the stainless steel cartridge with a nickel-base alloy. It is protected from the molten metal by an aluminum oxide tube sealed at one end. A tube approximately 3.2 mm OD × 2.2 mm ID is also provided at the lower end of the capsule for evacuation and backfilling with inert gas.

## Cartridge Construction

Each set of nesting alumina containers was fabricated from three commercially available crucibles. The two crucibles which were used to contain the alloy components were ground on the outside diameter to fit the stainless steel cartridge. A hole was drilled in the bottom of the lower container so that the closed end alumina tube to be used for the thermocouple well could be installed. The tube which was open-ended was cut to size and closed on one end by sealing with a slurry made from super-ground alumina powder and a 50 volume percent aqueous phosphoric acid solution. The tube was carefully cemented into the hole provided in the container with the same slurry while being axially aligned with a specifically designed jig. The exterior lateral surface of the upper container was tapered at its base by grinding so that it nested into the bottom container. The top lid was fabricated from the base of a third crucible. All the alumina components were fired in air at 1200°C for cleaning purposes and to harden the slurry.

The Al components were prepared from the vacuum melted high purity Al by machining, whereas the In components were fabricated from the vacuum melted rod by slicing a suitable length from the rod, die-pressing to expand the sample in diameter, and finally sizing with a suitable diameter cork borer. Final cleaning and adjustment of weights to control the exact composition of the alloy were effected in the case of the Al components by etching in a 20 weight percent aqueous solution of NaOH and in the case of the In components by etching in concentrated HCl. Table 1 summarizes the weights of the Al and In components and the calculated compositions of the alloys for the two ground base capsules (74-30-14 and 74-30-18 and the one flight sample 74-30-21) in addition

TABLE 1. SUMMARY OF GROUND BASE AND FLIGHT CAPSULES FOR SPAR II

| | Al-40 Wt % In | | | | Al-70 Wt % In | | | | |
|---|---|---|---|---|---|---|---|---|---|
| Capsule No. | Wt Al, g | Wt In, g | Composition Wt % | | Wt Al, g | Wt In, g | Composition Wt % | | Remarks |
| 74-30-15 | 1.3688 | 0.9121 | 39.99 | | 0.9852 | 2.2991 | 70.00 | | Successful test at BCL. |
| 74-30-16 | 1.3806 | 0.9206 | 40.01 | | 0.9640 | 2.2489 | 70.00 | | " " " |
| 74-30-13 | 1.3709 | 0.9139 | 40.00 | | 0.9549 | 2.2278 | 70.00 | | Successfully cycled at MSFC to establish furnace parameters. |
| 74-30-14 | 1.3955 | 0.9300 | 39.99 | | 0.9735 | 2.2700 | 69.99 | | Successfully cycled at MSFC. |
| 74-30-18 | 1.3378 | 0.8907 | 39.97 | | 0.8564 | 2.0020 | 70.04 | | " " " |
| 74-30-19 | 1.4200 | 0.9466 | 40.00 | | 0.9960 | 2.3739 | 70.00 | | Shipped to MSFC as spare. |
| 74-30-21 | 1.3802 | 0.9201 | 40.00 | | 0.7992 | 1.8644 | 70.00 | | Flight sample. |
| 74-30-22 | 1.3840 | 0.9228 | 40.00 | | 0.9215 | 2.1510 | 70.01 | | Back-up capsule. |

to the other capsules used in support of the SPAR II experiment. In all cases, the compositions were within 0.04 percent of the composition goal.

The stainless steel cartridges were received with the bottom end closure containing the evacuation tube and positioning boss already welded in place (Fig. 2). The first operation in the assembly of the cartridge consisted of drilling a hole into the bottom end closure to accommodate the thermocouple and then subsequently vacuum brazing the thermocouple into the stainless steel cartridge. The thermocouple was aligned through use of a tool which slipped over it and forced it to be parallel to the cartridge axis. This ensured that a proper fit could be made with the alumina tube cemented into the bottom crucible. After the brazing operation, the cartridges were leak checked and the thermocouple performance was tested in boiling water.

The alloy components in proper proportion were then assembled in their respective crucibles and the top alumina lid set in place. The assembly of nested crucibles was then carefully fit into the stainless steel capsule with care taken to ensure that the thermocouple was aligned with the well in the bottom crucible. The top stainless steel end cap was then welded in place while the capsule was surrounded with a copper chill designed to prevent melting of the In components. The cartridges were leak checked once again and were found to be leak tight within the sensitivity of the helium leak detector used (approximately $4 \times 10^{-10}$ $cm^3$ of helium second at STP).

The capsules were then individually evacuated through the tube provided to approximately $3.1 \times 10^{-3}$ Pa (approximately $3 \times 10^{-5}$ torr), backfilled with approximately 0.1 MPA of helium and reevacuated to approximately $2.1 \times 10^{-3}$ Pa (approximately $2 \times 10^{-5}$ torr). Backfilling again with 0.1 MPa of helium was followed by evacuation to approximately $1.1 \times 10^{-3}$ Pa (approximately $1 \times 10^{-5}$ torr). Final backfilling to $1.5 \times 10^{-2}$ MPa of helium was followed by sealing of the evacuation tube by a resistance spot welding technique. Consistent seals were obtained on the resistance spot welder with a load of 4450 N (1000 lb) applied to electrodes having 0.64 cm (1/4 in.) diameter bosses. Leak detection was conducted by placing the entire capsule in a pyrex tube and evacuating the latter with the helium leak detector. No external source of helium was used and the discovery of leaks depended on detection of helium escaping from the sealed cartridge. No leaks within the sensitivity of the detector were found.

## Ground Base Tests

A total of five cartridges were subjected to ground base tests to test the capsule design, to determine the proper settings for the GPRF, to provide the desired heating and cooling conditions, and to produce a reference material with which to compare the micro- and macrostructure of the flight sample.

Capsules 74-30-15 and -16 were used to test the design at BCL. They were individually heated to approximately 1000°C under a blanket of argon, held for approximately 15 min, and allowed to furnace cool to below the monotectic temperature (630°C) at which point they were rapidly cooled. A check of the cartridge dimensions after the thermal cycle showed no measurable change in cartridge diameters. Inspection of the interior components after removal from the stainless steel cartridges revealed that all components had performed well. This was in contrast with cartridges of a previous design in which graphite crucibles were used, and with which gross swelling of the stainless steel cartridge had been encountered.

Capsules 74-30-13, -14, and -18 were used at MSFC to determine the proper furnace settings for the desired thermal conditions. Initially, capsule 74-30-13 was successfully cycled a few times to determine the gross furnace settings. Capsule 74-30-14 was then cycled twice in an orientation antiparallel to that used in the flight sample. The first cycle simulated a 15-min ground hold at 970°C and was followed by helium quench which produced an average cooling rate to monotectic temperature of approximately 12°C/sec. The cooling rate was sufficiently fast to produce complete solidification in the required time period. The second thermal cycle conducted in the same orientation included a 30 min simulated ground hold and was also followed by a helium quench (approximately 13°C/sec to the monotectic temperature). In this case, although nearly complete solidification occurred in the time equivalent to the estimated duration of micro-g, a small fraction of the alloy still remained molten at the end of the period. It was thus determined that a holding time of 30 min would be too long and must be avoided for the flight sample. Some macroscopic observations have been made on polished sections of this sample.

The final ground base test was carried out on cartridge 74-30-18 in the same orientation as used in the flight sample. A 15 min hold time at 960°C was used and the helium quench resulted in a cooling rate of 17.9°C/sec to the monotectic temperature. At this cooling rate, the sample was completely solidified well within the required time period.

Since cartridge 74-30-18 closely simulated the thermal conditions used in the flight sample, this sample was considered to be the primary ground base sample and was subjected to the same macro- and microstructural analyses as the flight sample.

## Flight Parameters

Capsule 74-30-21 was flown in the GPRF on SPAR II on May 17, 1976. Pertinent data concerning the flight were telemetered to Earth and supplied to the principal investigator in the form of computer processed tabulations and graphs. The information supplied included data on the thermal conditions in and around the capsule, acceleration levels in three orthogonal directions, helium quench tank pressures, etc. The important flight data are summarized graphically in Figures 3 and 4 and are detailed in Table 2.

The sample was brought to an estimated temperature of 950°C, 15 min before launch, and held at this temperature through launch and for an additional 154 sec into the flight at which time it was rapidly cooled by means of a helium gas quench. The temperature data telemetered to Earth clearly show evidence of the monotectic transformation as noted by the plateau on the cooling curve in Figure 3 and as denoted in Table 2. The average cooling rate from the 950°C hold temperature to the monotectic temperature was 14.7°C/ sec, close to that of the ground base reference sample 74-30-18. No thermal effect corresponding to the solidification of In was noted from the data owing to the slowing of the cooling rate at the lower temperatures. However, the indicated temperature fell below 155°C, the equilibrium solidification temperature of In, at 269 sec. It is thus believed that solidification was completed at approximately this time.

Figures 3 and 4 and Table 2 also show that the micro-g level of acceleration ($<4 \times 10^{-5}$ g) was established 91 sec into the flight and continued to approximately 348 sec. Cooling of the sample thus took place approximately 63 sec after the micro-g level was established, and this level of acceleration lasted approximately 79 sec after solidification had been completed.

Another aspect of the flight worth noting is that at launch the rocket begins to spin about its axis until it reaches a maximum spin rate of 240 rpm at 30 sec. At 60 sec, the rocket is rapidly despun and approximately 94 sec later, cooling of the sample commences. This despinning action and its effect on the molten alloy will be discussed further in a later section of the report.

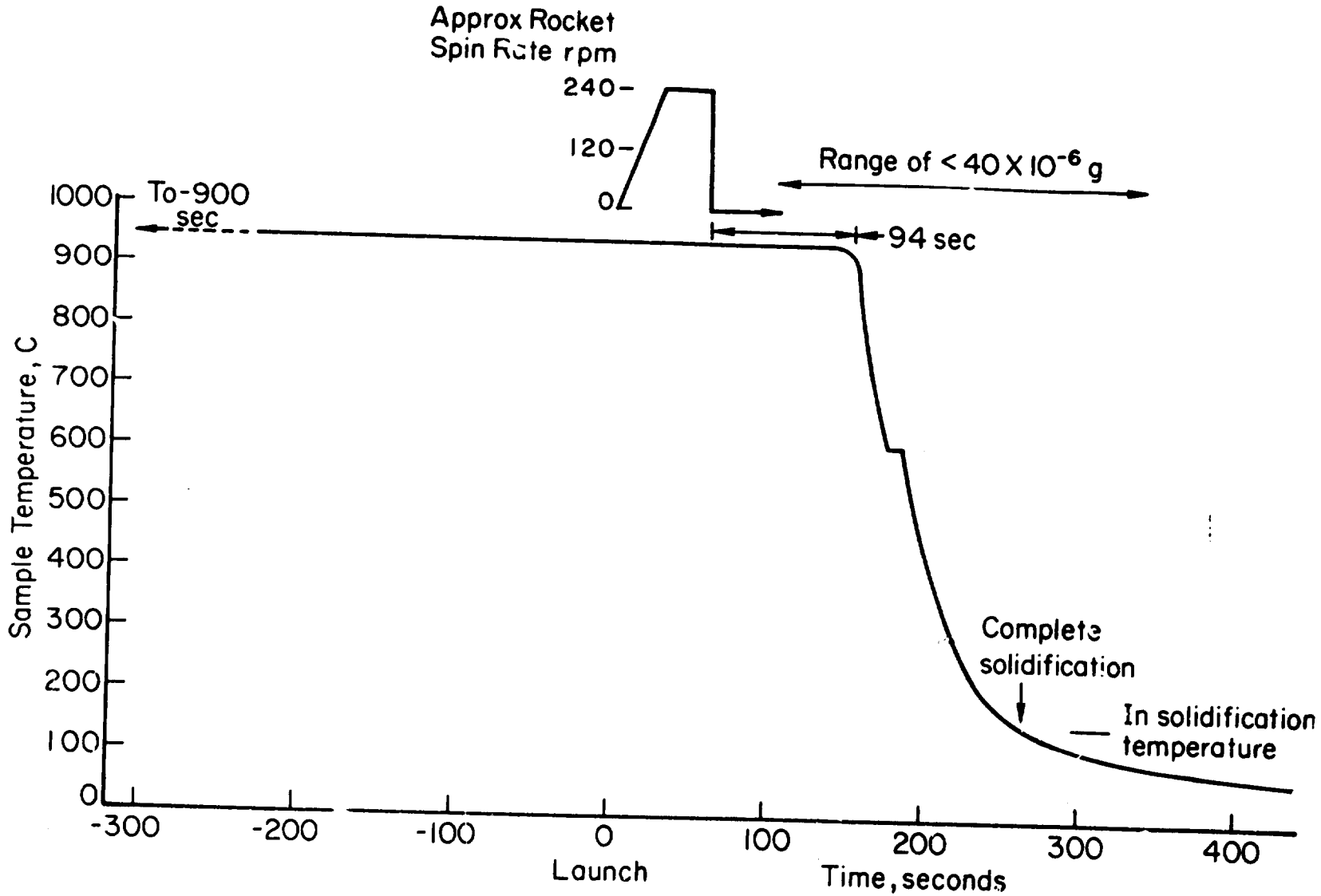


Figure 3. Thermal history, SPAR II Experiment 74-30.

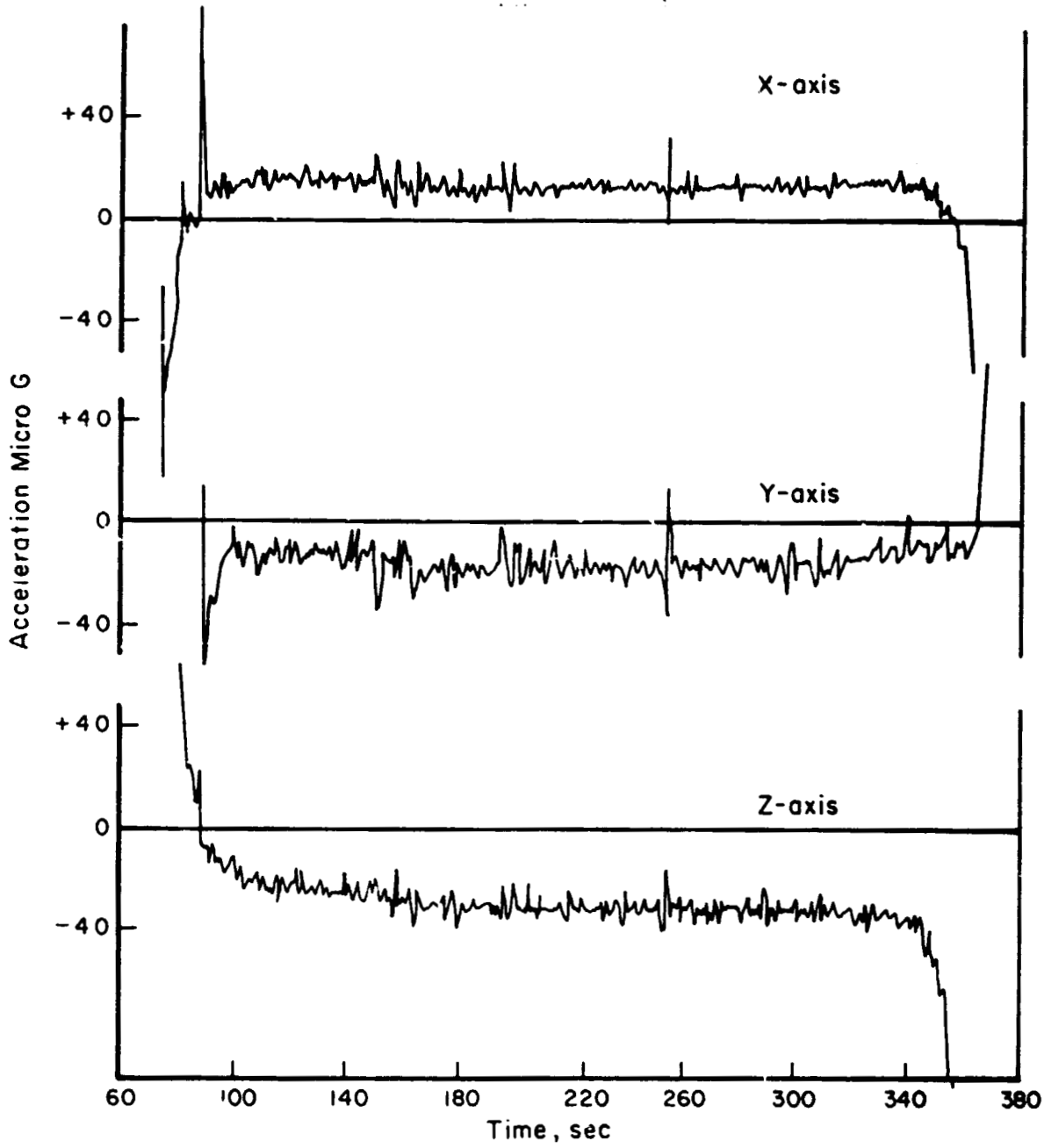


Figure 4. Accelerometer data from SPAR II flight.

TABLE 2. THERMAL HISTORY OF SPECIMEN 74-30-21 AND SPECIAL EVENTS IN THE SPAR II FLIGHT

| Time, sec | Sample Temperature, C | Remarks |
|---|---|---|
| -900 | 950 (Est) | Start of preflight temperature soak |
| -220 | 949 | First temperature data recorded |
| -200 | 948 | |
| -150 | 952 | |
| -100 | 950 | |
| - 50 | 954 | |
| - 25 | 953 | |
| 0 | 954 | Launch |
| + 25 | 954 | |
| + 50 | 943 | |
| + 60 | - | Rocket despun, maximum acceleration $3 \times 10^{-2}$g |
| + 75 | 947 | |
| + 91 | - | Start of low g period; acceleration <40μ-g |
| +125 | 949 | |
| +150 | 942 | |
| +153.7 | - | Start of sample cool-down |
| +176-+185 | 614 | Monotectic arrest |
| +~269 | <155 C | Solidification completed |
| +~348 | - | End of low g period of acceleration <40μ-g |

An overview of the flight details suggests that with a minor exception the flight plan was closely adhered to. A somewhat lower initial hold temperature (approximately 950°C versus 970°C) was the only discrepancy noted. This is not considered to be important because the equilibration kinetics are expected to be similar for the two temperatures and because the 950°C temperature is still well above the miscibility gap (Fig. 1).

## Examination of Ground Base and Flight Samples

### Radiography

Radiographic examination of the flight sample, 74-30-21, and the ground base sample, 74-30-18, was carried out at different voltage levels and at various sample orientations. This procedure allowed different features of the cartridge and samples to be distinguished. The images were recorded on Type M film with lead screens at a 132 cm specimen to film distance.

Figure 5 shows contact prints of some of the radiographs. The samples are positioned so that the alloy on top is Al-70 weight percent In and that on the bottom is Al-40 weight percent In. Radiographs 5a and b have been taken with the stainless steel cartridge in place, while radiographs 5c through f have been exposed after the removal of the stainless steel capsule. For the ground base sample, the crucibles containing the two alloys have been separated and radiographs taken in this condition (Figs. 5e and 5f).

The light vertical line in the bottom alloy of Figures 5c through f corresponds to the position of the thermocouple well.

The radiographs of the flight sample show some rather unusual features. Note the unusual shape of the alloy relative to the crucible in Figure 5a. Another unusual feature of the flight sample may be seen in the top alloy (Al-70 weight percent In). A central lower density region which is roughly spherical in shape is surrounded by a higher density region (Figs. 5b — 5d). Lastly, it may be noted in Figures 5c and 5d that near the top central high density region of the lower alloy there is a curl of lower density material that has a wave-like appearance and juts into the higher density material.

The radiographs of the ground base samples, Figures 5e and 5f, show the layered structure expected in this system. Here the high density region on the bottom of the alloys corresponds to an In-rich alloy, whereas the lower density region on the top of the alloys corresponds to the Al-rich region.

### Macroexamination

After radiography, the samples were examined macroscopically. Initial examination consisted of viewing the external surfaces of the alumina crucibles from the flight sample, 74-30-21, and ground base sample, 74-30-18. The macroviews of these samples are shown in Figure 6 and in general confirm the integrity of the samples after processing.

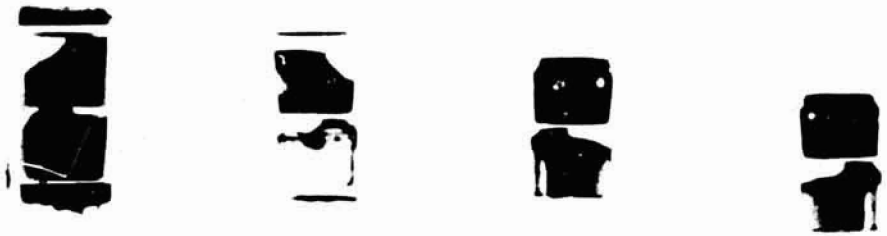

74-30-21

Flight Sample

(a) 80KVP (b) 240KVP (c) 200KVP (d) 200KVP

74-30-18

Ground-Base Sample

(e) 200KVP (f) 200KVP

Note: The top alloy is Al-70 weight percent In; bottom alloy is Al-40 weight percent In. (a) and (b) were taken in the stainless steel cartridge. Cartridge steel removed for (c) through (f).

Figure 5. Radiographs of flight sample 74-30-21 and ground-base sample 74-30-18 taken in various orientations and at various kilovoltages.

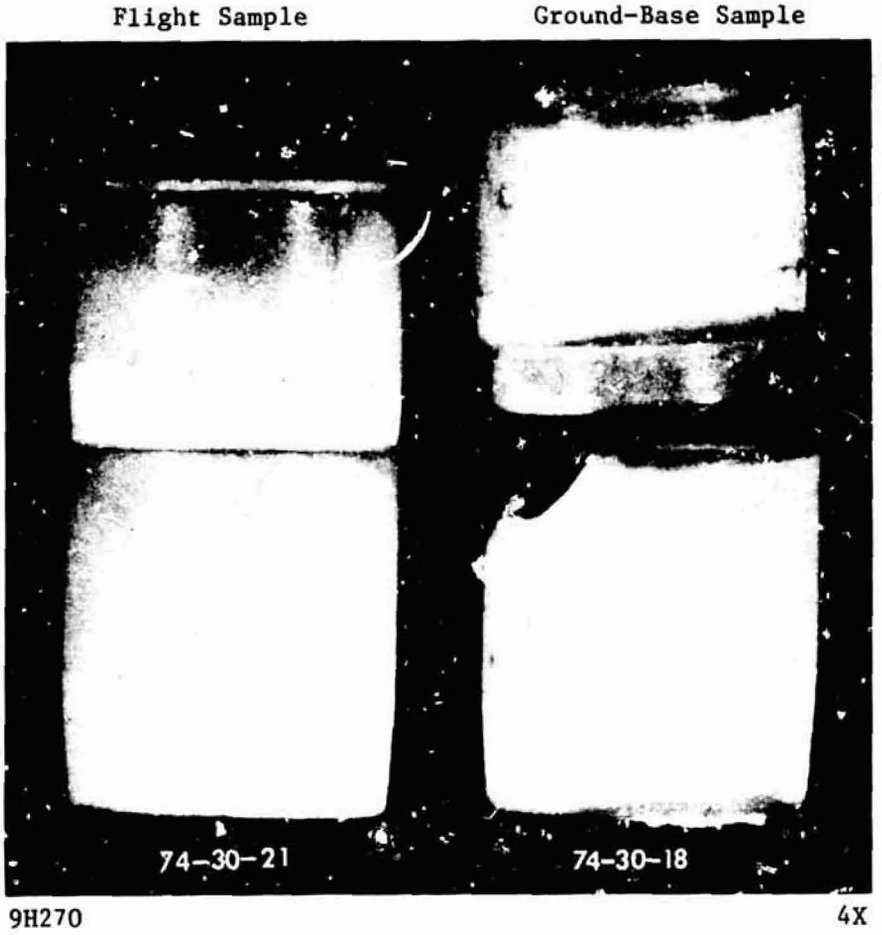


Figure 6. Macroviews of alumina containers from cartridges 74-30-21 (flight sample) and 74-30-18 (ground-base sample).

As previously mentioned, the two nesting crucibles in the ground base sample had been intentionally separated to view the alloy surfaces. During the separation, a small piece of the lower crucible fractured. The surface of the ground base Al-40 weight percent In alloy appeared clean and shiny, except for a small region which showed some evidence of dross. It was also evident that a portion of this alloy when molten had been in contact with the bottom of the top crucible and had adhered to it in the contact region. The entire exposed surface of the Al-70 weight percent In alloy consisted of a series of dull grain-like features separated by semicontinuous shiny boundaries.

After initial examination, the flight and ground base samples were split longitudinally by means of a SiC water cooled cut-off wheel approximately 1.25 mm thick. One of the longitudinal samples from each alloy was then polished metallographically and photographed at 4X. These macroviews are shown in Figures 7 and 8.

Since sample polishing was made somewhat difficult by the presence of the aluminum oxide crucibles, the mating section of each sample was also prepared for macroscopic and microscopic examination after the careful removal of the aluminum oxide crucible. In spite of the care taken, however, some pieces of the alloy, mainly from the In-rich portion were removed. Higher magnification (9.5X) macroviews of these sections are shown in Figures 9 and 10.

The ground base alloys (Figs. 8 and 10) show the typical layered structures that are expected in terrestrially processed liquid phase immiscible alloys. The lighter regions on the top parts of the alloys are Al-rich, while the darker regions are In-rich. The relative thickness of the layers is seen to vary in the expected way with composition. Careful examination of the macrostructure of the terrestrially processed sample reveals a relatively high concentration of particulate matter in the neighborhood of the layer interface and on both sides of it. As will be shown in the next section, the particles in the Al-rich layer correspond to In-rich droplets which have settled during the cooling process while those in the In-rich layer correspond to Al-rich droplets and dendrites which tend to float in the heavier In-rich host fluid. It should also be noted that the interface between these layers is not exactly planar, but shows some evidence of wave-like perturbations (see bottom alloy in Fig. 8 and top alloy in Fig. 10). Lastly, it should be noted that there is a great tendency for the In-rich liquid in the ground base sample, 74-30-18, to form a low contact angle with the crucible. This appears to be especially true in the top alloy, Al-70 weight percent In, and is clearly visible in Figure 10 where the In-rich material has climbed fairly completely up the side of the crucible wall.

The macrostructure of the flight alloys was significantly different from those of the ground base samples and also did not conform to the structure anticipated. Instead of the expected fine uniform structure composed of In-rich particles in an Al-rich matrix, the Al-40 weight percent In alloy (bottom alloys in Figs. 7 and 9) was made up of two distinct macroregions, an annular In-rich layer and an Al-rich core. The interface between the Al-rich and In-rich phases shows some wave-like characteristics, especially in the curl form clearly seen in Figure 7 and previously noted in the radiographs of Figures 5c and 5d.

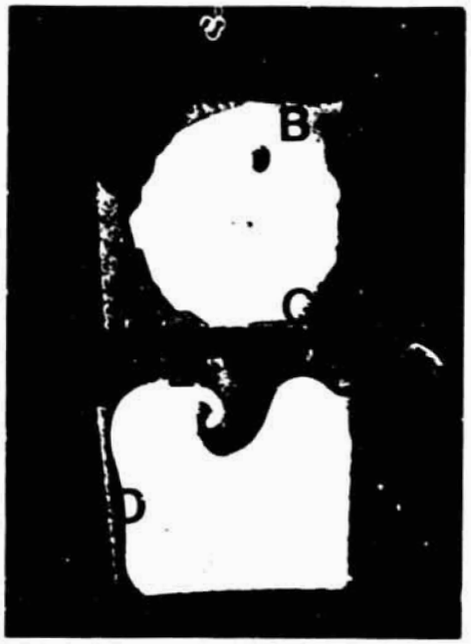


Figure 7. Macroview of central polished longitudinal section of flight sample 74-30-21.

Figure 8. Macroview of central polished longitudinal section of ground-base sample 47-30-18.

ORIGINAL PAGE IS

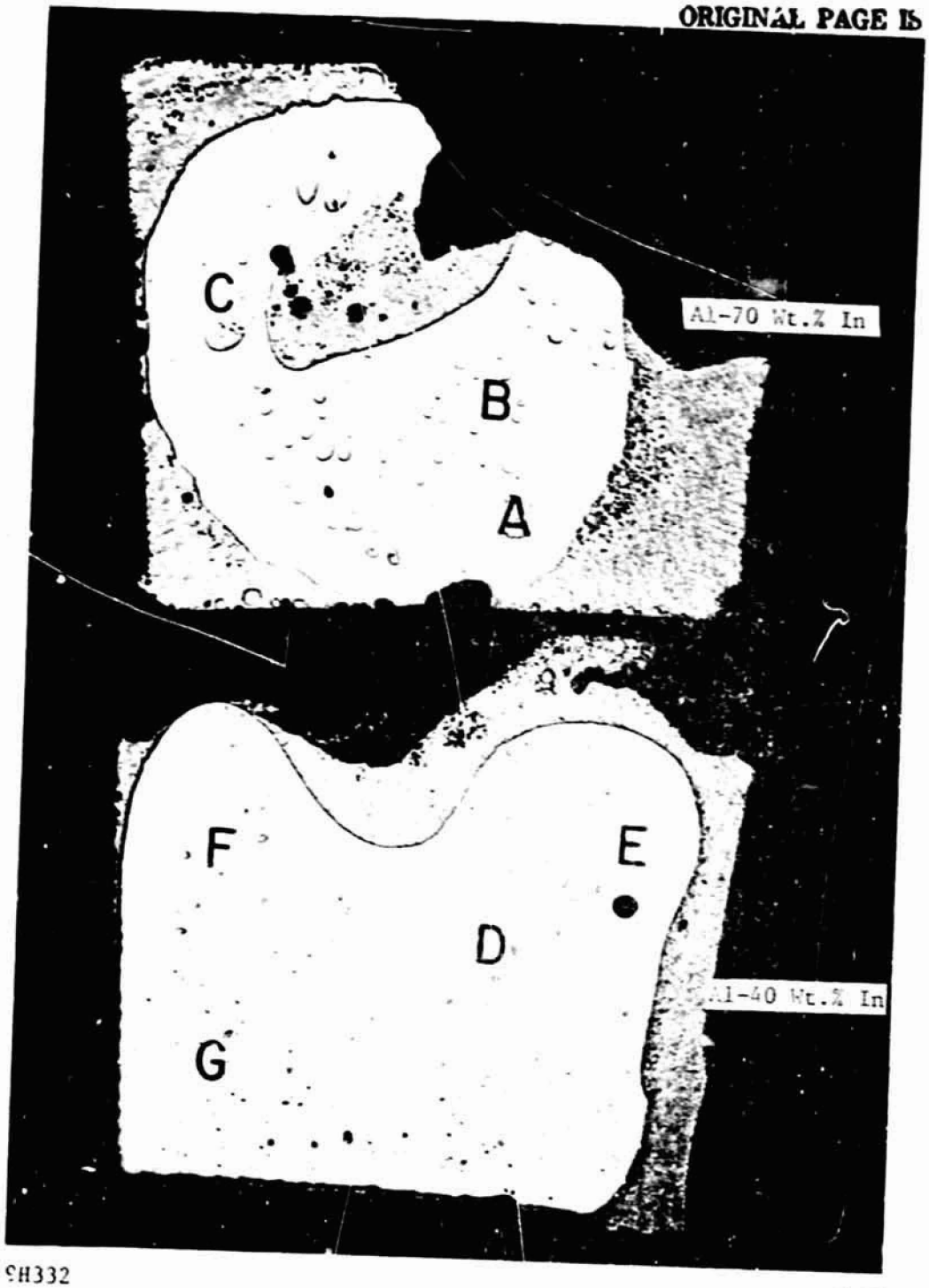


9H332

9.5X

Figure 9. Macroview of central polished longitudinal section of flight sample 74-30-21 after removal of alumina container.

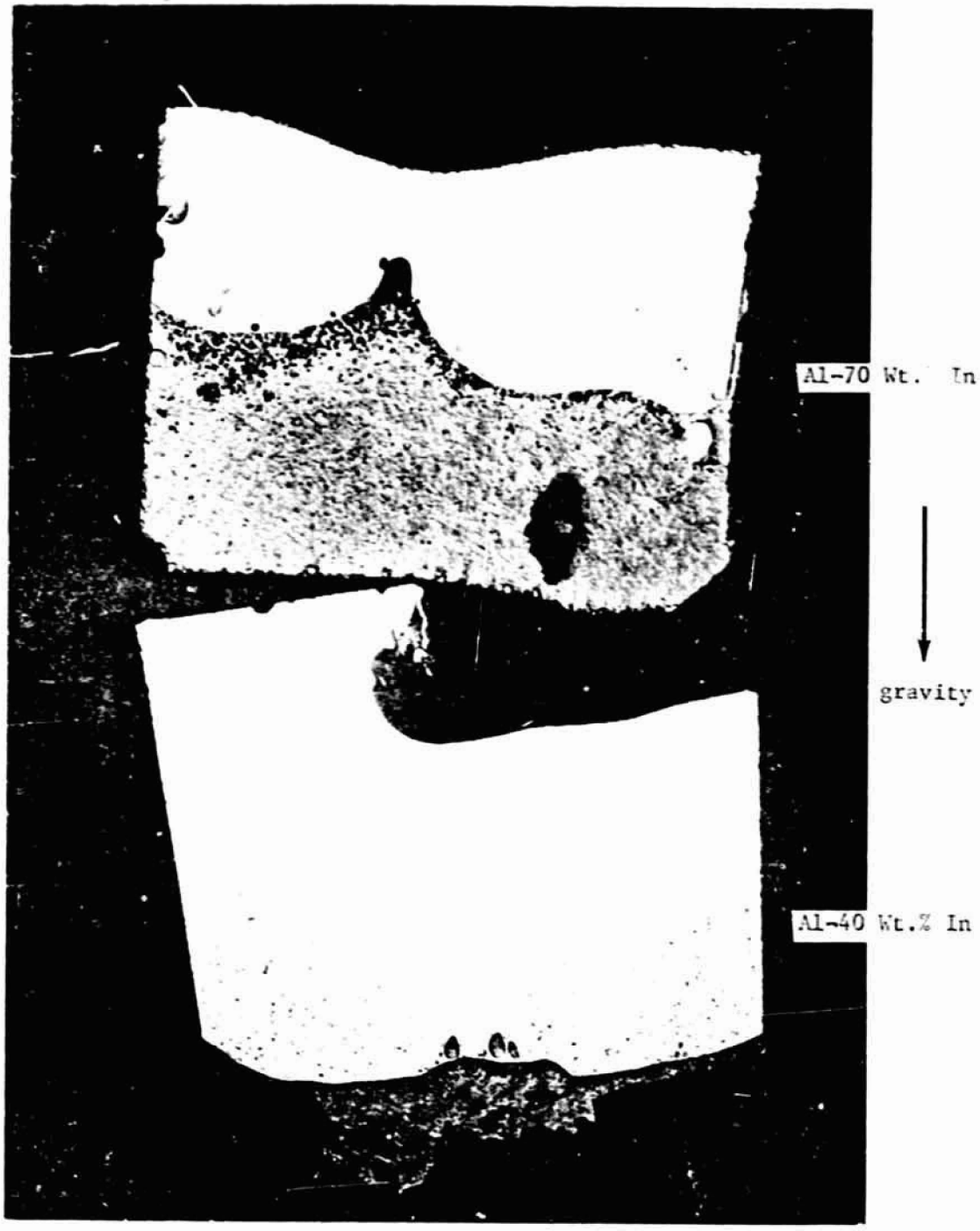


Figure 10. Macroview of central polished longitudinal section of ground-base sample 74-30-18 after removal of alumina container.

The same type of macrostructure is also seen in the Al-70 weight percent In alloy (top of Figs. 7 and 9). Here the effect is even more dramatic. The central region of the alloy is occupied by an Al-rich phase which takes on a roughly spherical form and is again completely surrounded by an In-rich layer.

The second phase particles within the Al-rich portions of the flight alloys appear to be fairly uniformly distributed in space but are relatively large in size. The large In particle at Region "C" in the Al-rich phase at the top of Figure 9 is believed to be an intrusion into the Al-rich core by the surrounding In-rich region.

The distribution of second phase particles in the In-rich regions is not quite as uniform. The Al-rich second phase particles have concentrated in a number of areas, such as the top surfaces and the interfacial regions near the bottom of both alloys (Fig. 9).

Microscopic Examination

The longitudinal sections shown in Figures 7 through 10 were also examined on a microscopic scale. Photomicrographs of the ground base samples are shown in Figures 11 through 14. The Al-rich region of the Al-70 weight percent In alloy from ground base sample 74-30-18 is shown in Figure 11. The photomicrographs in this figure represent regions at various distances from the interface between the Al-rich and In-rich layers. They clearly show the tendency for the In-rich particles which precipitate during cooling through the miscibility gap to settle out in the Earth's gravitational field. The same effect is shown in Figure 13 where photomicrographs of the Al-rich region of the Al-40 weight percent In ground base sample are shown. The particles seen in Figures 11a and 13a probably largely result from the monotectic decomposition of $L_I$ (Fig. 1), although some may still correspond to fine droplets precipitated in the miscibility gap.

The In-rich regions of the Al-70 weight percent In and Al-40 weight percent In alloys from ground base sample 74-30-18, shown in Figures 12 and 14, again demonstrate the tendency for Stokes migration in the gravity field. Here Al-rich spherical particles which precipitate in the miscibility gap have a tendency to float upward in the heavier In-rich liquid. The particles concentrate in the interfacial region between the Al-rich and In-rich layers.

ORIGINAL PAGE IS
OF POOR QUALITY

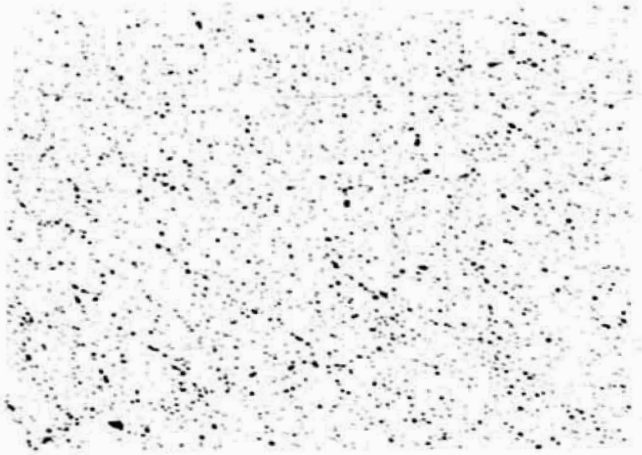

9H392 (a) 100X

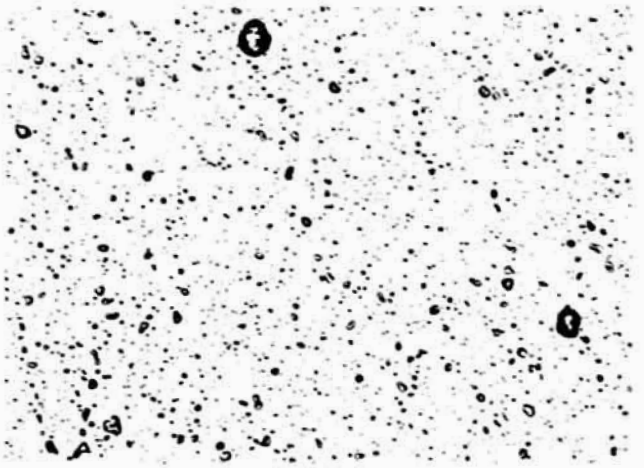

9H391 (b) 100X

1g

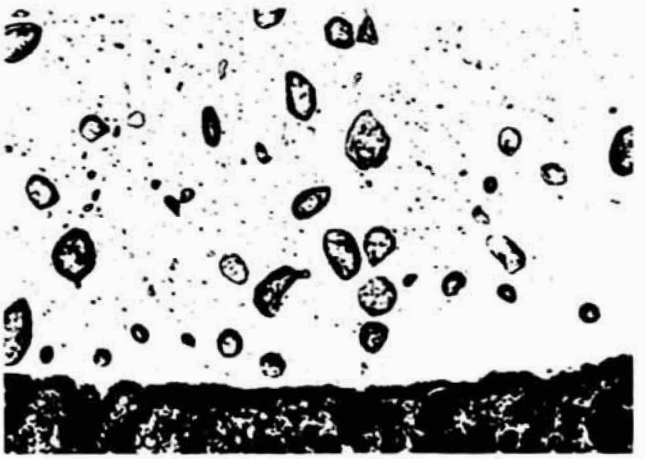

9H390 (c) 100X

(a) 3 mm above interface between Al-rich and In-rich layers,
(b) 1.5 mm above this interface, (c) at interface.

Figure 11. Photomicrographs of the Al-rich portion of the Al-70 weight percent In alloy ground base sample 74-30-18.

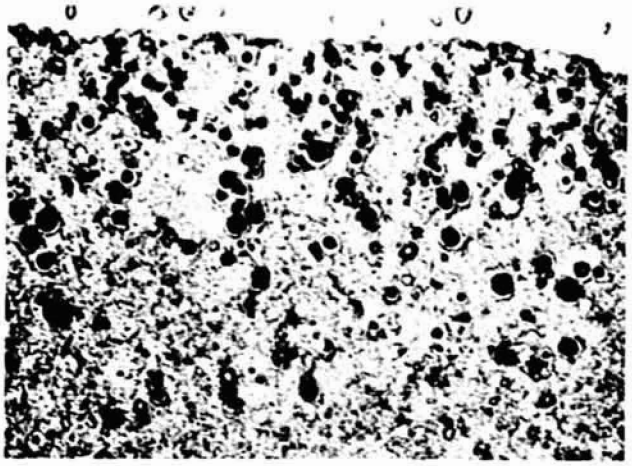

9H560 (a) 100X

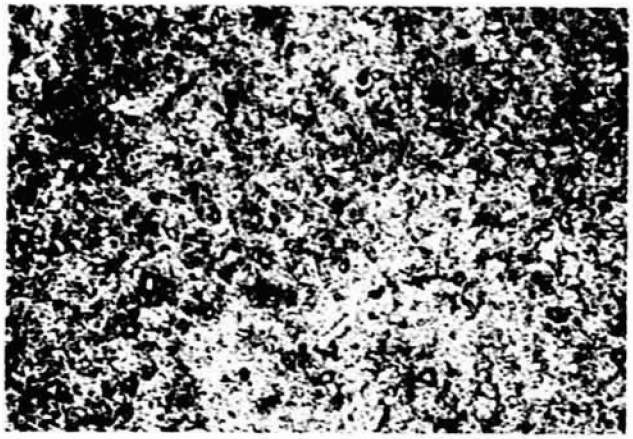

1g

9H561 (b) 100X

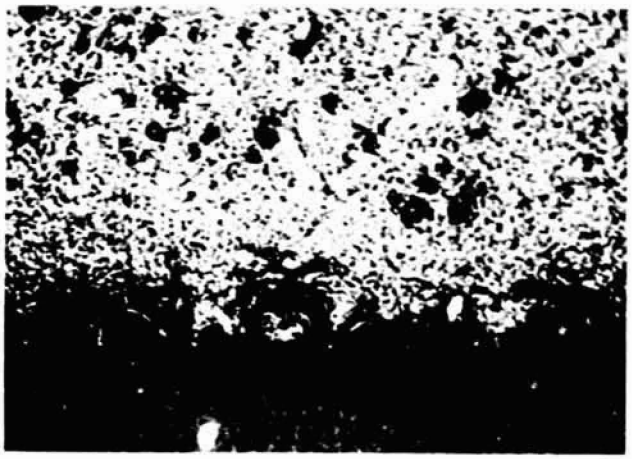

9H562 (c) 100X

(a) at interface between Al-rich and In-rich layers
(b) displaced 1 mm into In-rich layer
(c) at bottom alumina surface (reference Fig. 8)

**Figure 12.** Photomicrographs of In-rich portion of the Al-70 weight percent In alloy ground base sample 74-30-18.

ORIGINAL PAGE IS
OF POOR QUALITY

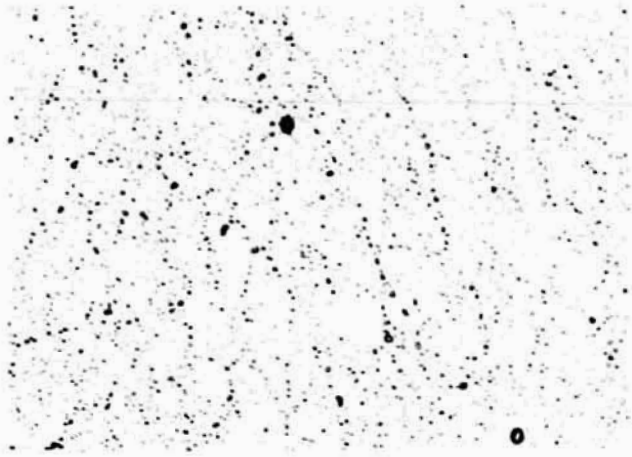

9H395 (a) 100X

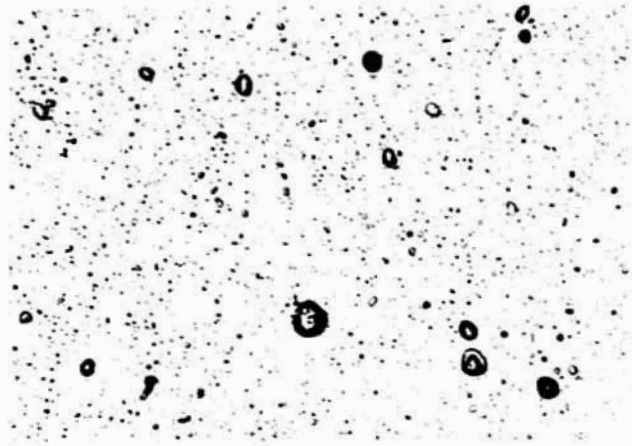

1g

9H394 (b) 100X

9H393 (c) 100X

(a) 3 mm above interface between Al-rich and In-rich layers
(b) 1.5 mm above interface
(c) at interface

Figure 13. Photomicrographs of Al-rich portion of the Al-40 weight percent In alloy ground base sample 74-30-18.

The structure of these spherical particles consists of an outer light colored (Al-rich) layer surrounding a darker (In-rich) core. This structure presumably results from the monotectic decomposition of the $L_I$ liquid droplets.

Al-rich dendrites are also present in the In-rich layers of the ground base alloys. The dendrites are generally located at a region further displaced from the interface between the layers and often appear to have nucleated at the Al-rich portion of the spherical particles. They are thought to arise in a portion of the In-rich layer which is relatively low in Al content and at a temperature below the monotectic transition.

Two other features of the In-rich layers present in the ground base samples are to be noted. First of all, angular particles, approximately 20 $\mu$ in size, are also present in the microstructure. They are thought to originate from the SiC cut-off wheel used to section the samples or from the polishing papers. Hard particles from one or both of these sources become embedded in the soft In-rich portion of the alloys. Another feature to be noted is the presence of relatively large Al-rich spheres along the alloy/aluminum oxide interface (Fig. 12c) and along the large cavity (presumably a gas pocket) seen at the bottom of Figure 14. These interfaces appear to be a source of entrapment for the precipitating Al spheres.

Photomicrographs of the Al- and In-rich portions of the flight alloys are shown in Figures 15 through 18. The positions at which the photomicrographs have been taken are referenced in the macroviews of Figures 7 and 9; the Al-rich portions shown in Figures 15 and 17 are referenced in Figure 9; whereas the In-rich portions shown in Figures 16 and 18 are referenced in Figure 7.

In general, the microstructural features are similar to those in the ground base samples. However, the second phase particles are generally more uniformly distributed. The Al-rich portion of the Al-70 weight percent In and Al-40 weight percent In flight samples (Figs. 15 and 17) show In-rich particles in an Al-rich matrix. The larger of these particles are roughly spherical in shape and have formed during cooling through the miscibility gap. However, some of the very large In-rich particles appear to have Al-rich dendrites or spherical droplets precipitated within them (Figs. 15a and 15c). These larger particles have structures which are more similar to the bulk In-rich phase and may indeed be part of this phase.

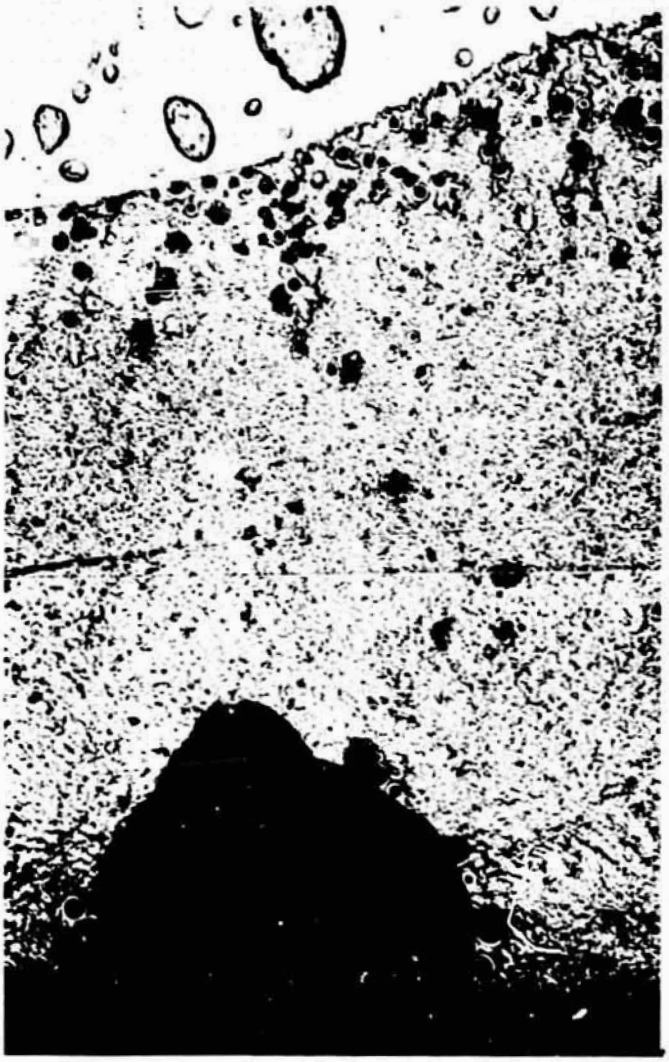


9H563/4 100X

Figure 14. Composite photomicrograph of the In-rich layer of the Al-40 weight percent In alloy ground base sample 74-30-18.

9H399 (a) 100X

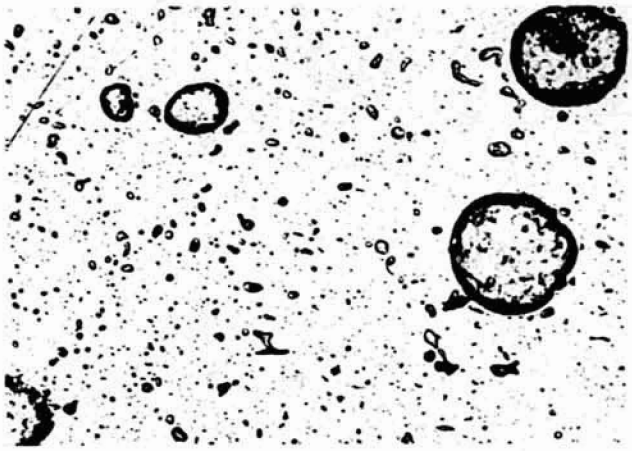

9H398 (b) 100X

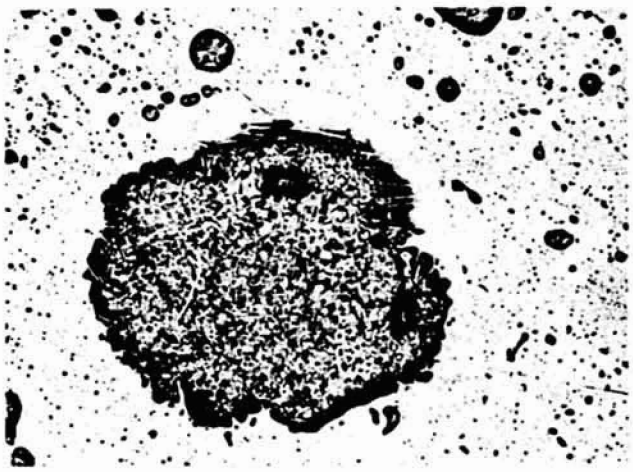

9H397 (c) 100X

(a) Region C of Figure 9
(b) Region B of Figure 9
(c) Region A of Figure 9

Figure 15. Photomicrographs of Al-rich portion of Al-70 weight percent In alloy flight sample 74-30-21.

ORIGINAL PAGE IS
OF POOR QUALITY

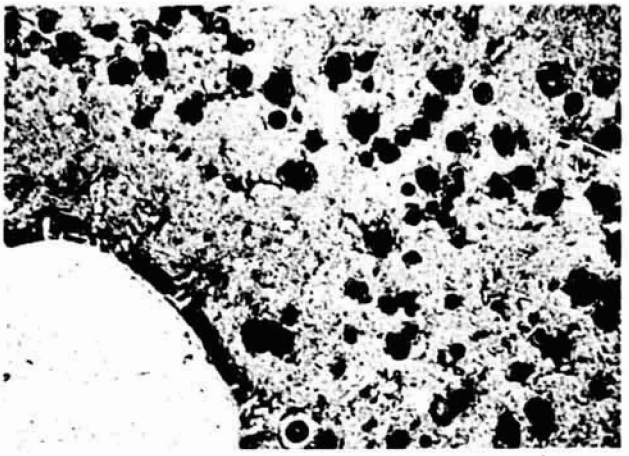

9H567 (a) 100X

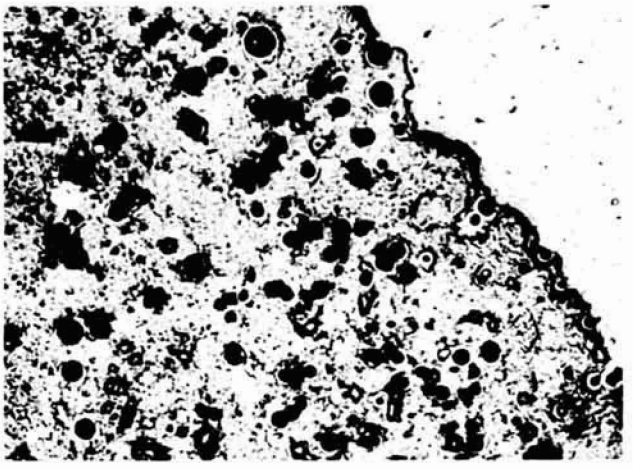

9H566 (b) 100X

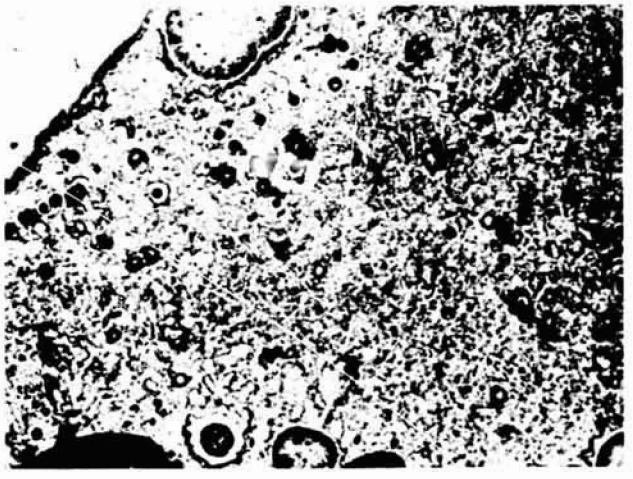

9H568 (c) 100X

(a) Region B of Figure 8
(b) Region A of Figure 8
(c) Region C of Figure 8

ORIGINAL PAGE IS
OF POOR QUALITY

Figure 16. Photomicrographs of In-rich portion of Al-70 weight percent In alloy flight sample 74-30-21.

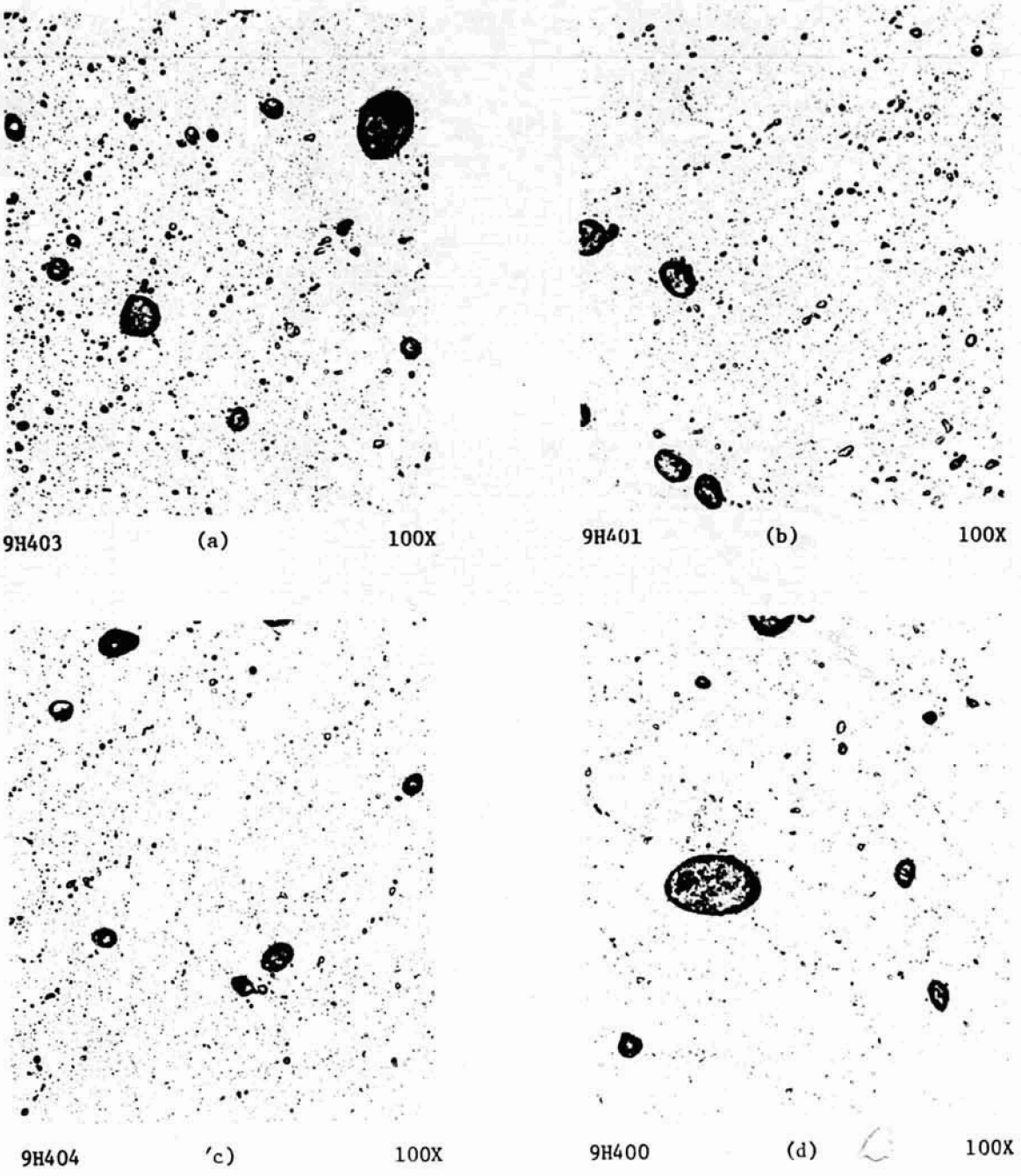


(a) Region F of Figure 9
(b) Region E of Figure 9
(c) Region G of Figure 9
(d) Region D of Figure 9

Figure 17. Photomicrographs of Al-rich portion of Al-40 weight percent In alloy flight sample 74-30-21.



ORIGINAL PAGE IS
OF POOR QUALITY

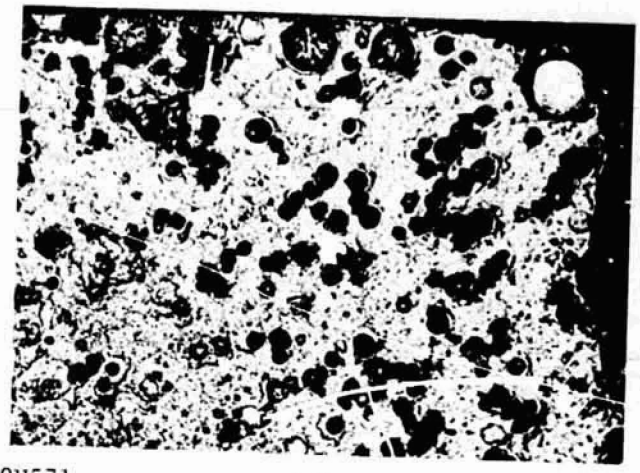

9H571 (a) 100X

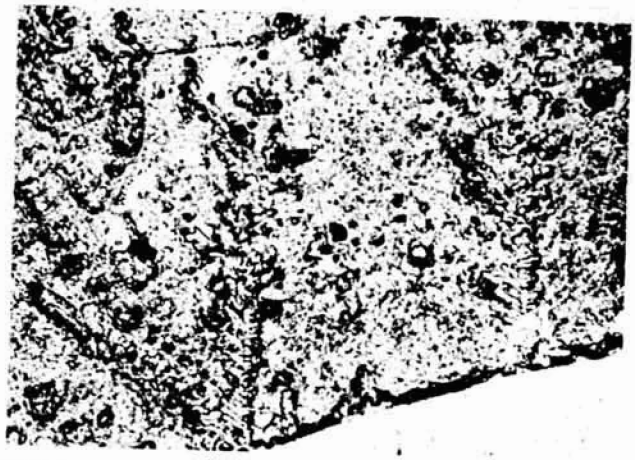

9H569 (b) 100X

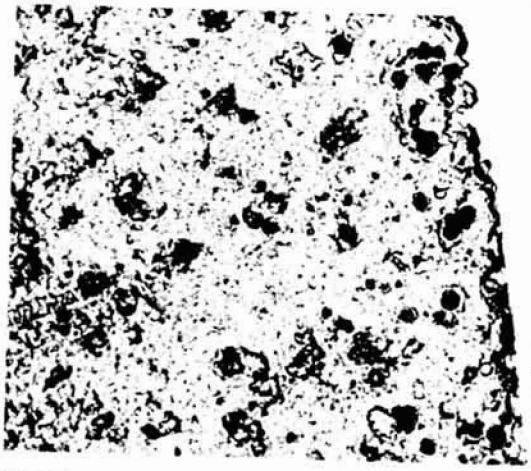

9F570 (c) 100X

(a) Region F of Figure 7
(b) Region E of Figure 7
(c) Region D of Figure 7

Figure 18. Photomicrographs of In-rich portion of Al-40 weight percent In alloy flight sample 74-30-21.

The In-rich portions of the Al-70 weight percent In and Al-40 weight percent In alloy flight samples are shown respectively in Figures 16 and 18. The phases present in these samples are very similar to those in the ground base sample, but their distribution is much more random and uniform. Here again, Al-rich spheres and dendrites are present, but now the dendrites not only nucleate at the spherical particles but are also seen to nucleate at the bulk Al-rich phase (Figs. 16a and 18b). As in the ground base samples, larger Al-rich spheres appear to be associated with the surface or indium/aluminum oxide interface. Also, angular particles attributable to the cut-off wheel or polishing abrasive should be noted and dismissed as artifacts.

## Interpretation of Results

### General Interpretation

Although the results have not been completely analyzed at this time, it is clear that the behavior of the ground base samples was close to that expected, whereas that of the flight sample was totally unexpected.

Ground Base Sample 74-30-18. The evaluation of the Al-40 weight percent In alloy ground base sample is consistent with the following model. The alloy starts out as a homogeneous liquid at 970°C from which temperature it is rapidly cooled. At 810°C (Fig. 1) a fairly large number of In-rich droplets suddenly precipitate and begin settling rapidly, agglomerating and partially forming an In-rich layer. This process essentially divides the alloy into two alloys, an Al-rich one and an In-rich one. Further cooling leads to precipitation of Al-rich spherically shaped liquid droplets in the In-rich layer. The Al-rich spheres float upward in the heavier In-rich liquid and concentrate at the region of the interface between the alloy layers. When the alloy reaches the monotectic temperature, approximately 639°C, the Al-rich host fluid in the upper alloy undergoes the monotectic reaction producing solid Al and fine In liquid droplets. The Al-rich liquid droplets in the bottom portion of the alloy also transform monotectically and thereby produce particles consisting of a solid Al annulus and an In-rich core. Further cooling of the alloy leads to precipitation of Al dendrites in the In-rich liquid. Finally, at a temperature of approximately 155°C, the In solidifies.

This description of the observed microstructure is based on the assumption that mechanical separation by means of Stokes migration at 1 g is a rapid process compared to diffusional processes. This seems reasonable in view of

the fact that within approximately 10 sec that the alloy is within the miscibility gap, particles >10 $\mu$ can move completely through the alloys.

The same type of description could also fit the microstructure of the Al-70 weight percent In ground base alloy. In this alloy, however, it is not clear whether In-rich droplets initially precipitate in an Al-rich host fluid or whether the reverse is true. In either event, the droplets will migrate under the influence of gravity and produce a separation into Al- and In-rich layers. Events subsequent to the layering action should be similar to those delineated for the Al-40 weight percent In alloy.

Rocket Flight Samples. The observation of massive segregation in the SPAR II Rocket Flight Sample and the relative coarseness of microstructural features indicate that large fluid flows have occurred at the micro-g acceleration levels encountered in these experiments. Possible causes of this fluid flow are as follows:

- Rocket spin
- Density differences
- Thermocapillary forces (Marangoni effect)
- Phase changes
- Capillary forces.

A number of these possibilities have been analyzed as detailed below. This work is by no means complete and is presented merely as a progress report.

All of these fluid flow driving forces will tend to produce a mixture of phases having the lowest configurational energy Some effort has been expended, therefore, at calculating some of the configurational energies.

Effect of Rocket Despin on Fluid Motion

Analysis of residual motion caused by the rapid despin of the rocket from 240 to 0 rpm at 60 sec has been treated by L. L. Lacy (15). Lacy performed terrestrial experiments to determine the effect of viscosity, container geometry, position of the spin axis, and fluid wetting characteristics on the damping time, T. The latter was defined as the total time to reach an angular velocity of

0.1 rad/sec (corresponding to a tangential velocity of 0.05 cm/sec in our case) and was found to vary according to the empirical relationship:

$$T = 0.074\, d^2 \nu^{-1} \qquad (1)$$

where d is the container diameter and $\nu$ is the kinematic viscosity. Lacy also assumed that the velocity decayed exponentially. Hence, for a tangential velocity an order of magnitude slower (0.005 cm/sec), the constant of proportionality increases from 0.074 to 0.105. For this latter case, the damping time for the Al–40 weight percent In alloy liquid at 1000°C ($\nu = 2.8 \times 10^{-3}$ cm$^2$/sec) in a 1 cm diameter container would be approximately 38 sec. For the liquid Al–70 weight percent In alloy under the same conditions ($\nu = 1.9 \times 10^{-3}$ cm$^2$/sec), the damping time would be 55 sec. This calculation is based on the published values of the viscosity of pure Al and pure In and assumes that the viscosity of the alloy is a linear function of the atomic percent of In.

The SPAR II flight sample was allowed a damping period of 94 sec between rocket despin and the start of the cooling period (Table 2). When this time is compared with the calculated damping times, the time period appears to be sufficient to damp the motion to very small velocities. This is especially true for the Al-40 weight percent In alloy in which the presence of a thermocouple should further decrease the damping time.

Thermocapillary Flow (Marangoni Effect)

The fact that the surface tension is generally temperature-dependent implies that temperature gradients existing within a liquid bounded by a free surface may result in convection currents. The Marangoni number (Ma), which is a dimensionless quantity, can be used to estimate the relative degree to which this phenomenon can be expected to contribute in a given situation; it is given by:

$$Ma = \frac{S(\Delta T)d}{\alpha \eta} \qquad (2)$$

Where S is the temperature coefficient of surface tension, $\Delta T$ is the temperature difference existing across the fluid layer, d is the depth of the layer, $\alpha$ is the thermal diffusivity of the fluid (equal to K, $\rho$C where K is its thermal conductivity, $\rho$ its density and C its specific heat), and $\eta$ is the viscosity of the fluid.

Let us consider the special case of pure liquid Al, taking $\rho = 2.27$ gm/cm$^3$, C = 0.26 cal/gm-°C, S = 0.15 dynes/cm-°C, $\eta = 9 \times 10^{-3}$ poise, and K = 90 W/m-deg.

$\Delta T$ was estimated from the rate of heat rejection from the liquid as deduced from the measured cooling rate of approximately 15°C/sec. On this basis, the calculated heat rejection rate of approximately 4.4 cal/cm$^2$-sec would correspond to an average temperature gradient of approximately 10°C/cm. Since the distance over which the gradient acts is approximately 0.5 cm, $\Delta T$ should be approximately 5°C. Insertion of the values of the material parameters into equation (2) yields a Marangoni number of 114.

The Marangoni number has also been calculated for the Al-40 weight percent In and Al-70 weight percent In alloys on the assumption that the only material constants that differ from those of pure liquid Al are the densities and viscosities.

The calculations resulted in the following values for the Marangoni number at 800°C:

Ma (Al-40 weight percent In) = 229

Ma (Al-70 weight percent In) = 500 .

All of these Marangoni numbers are substantial and would be expected to lead to large fluid velocities. More accurate calculations must await the availability of accurate values of thermal conductivity, surface tension, viscosity, and density as a function of temperature and alloy composition.

Convection Currents Induced by Density Variations

We have analyzed the extreme condition where density differences as large as $\Delta\rho = \rho_{In} - \rho_{Al}$ might exist in an alloy host fluid of average den o and might lead to conventional convection (16). The flow velocity, U, is governed by the Grashof number Gr:

$$Gr = \frac{g\Delta\rho d^3}{\rho\nu^2}$$

where d and $\nu$ are defined as before and g is the acceleration level.

Values of Gr calculated for the Al-40 weight percent In and Al-70 weight percent In are listed in Table 3. Since these values are large, U, the fluid velocity can be estimated (16) from:

$$U = \sqrt{Gr\ \nu/d} \quad .$$

The equation for fluid velocity can also be expressed in terms of system geometry and material parameters as follows:

$$U = \sqrt{\frac{g\Delta\rho d}{\rho}} \quad .$$

This equation can be used as a guide for the design of a system which avoids fluid flow arising from conventional convection. By minimizing g, $\Delta\rho/\rho$ and d, the fluid velocities associated with buoyancy driven convection currents can be minimized.

Bond Number Calculations

The relative importance of surface tension and acceleration forces can be estimated from the Bond number, $B_o$, given by:

$$B_o = \rho g d^2/\sigma$$

where $\rho$, g, and d are as previously defined and $\sigma$ is the surface tension (13).

Table 4 presents material characteristics for pure liquid Al and pure liquid In as well as the liquid alloys, Al-40 weight percent In and Al-70 weight percent In. The Bond numbers at 1 g and $10^{-5}$ g are also presented in this table for a value of d = 1 cm and show that surface tension effects are very important at $10^{-5}$ g and of some importance at 1 g.

Equilibrium Configurations

To determine the most stable geometric configurations for mixtures of Al and In, the total sum of the surface and interfacial energies in a crucibless

TABLE 3. CALCULATIONS OF GRASHOF NUMBER AND PREDICTED FLOW VELOCITIES AT 800°C FOR d = 1 cm

| Alloy | $\Delta\rho$[a] gm cm$^{-3}$ | $\rho$ gm cm$^{-3}$ | $\nu$[b] cm$^2$ sec$^{-1}$ | Gr at 1 g | Gr at $10^{-5}$ g | U cm sec$^{-1}$ at $10^{-5}$ g |
|---|---|---|---|---|---|---|
| Al-40 wt % In | 4.16 | 3.16 | $3.26 \times 10^{-3}$ | $1.2 \times 10^{8}$ | $1.2 \times 10^{3}$ | 0.113 |
| Al-70 wt % In | 4.16 | 4.25 | $2.1 \times 10^{-3}$ | $2.1 \times 10^{8}$ | $2.1 \times 10^{3}$ | 0.098 |

a. $\rho_{In} - \rho_{Al}$

b. Assumes linear relationship with composition expressed in atomic weight percent.

TABLE 4. BOND NUMBER CALCULATIONS FOR LIQUID Al, In, AND Al-In ALLOYS, 1000°C

| | $\rho$[a] gm cm$^{-3}$ | $\sigma$[b] dyne cm$^{-1}$ | $B_o$ at 1 g | $B_o$ at $10^{-5}$ g |
|---|---|---|---|---|
| Al | 2.27 | 822 | 2.7 | $2.7 \times 10^{-5}$ |
| Al-40 wt % In | 3.06 | 676 | 4.4 | $4.4 \times 10^{-5}$ |
| Al-70 wt % In | 4.13 | 567 | 7.1 | $7.1 \times 10^{-5}$ |
| In | 6.36 | 457 | 13.6 | $13.6 \times 10^{-5}$ |

a. Values for the alloys were calculated on the basis of an assumed linear relation between specific volume and composition expressed in weight percent.
b. Values for the alloys were calculated on the basis of an assumed linear relation between $\sigma$ and weight percent In.

configuration has been calculated as a function of the volume fraction of Al. Three configurations have been considered, all in spherical form:

1. An In annulus surrounding an Al sphere

2. An Al annulus surrounding an In sphere

3. Two spheres — one Al and one In.

The total surface and interfacial energies as a function of the volume fraction of Al, $V_{Al}$, for the three configurations are as follows:

Al surrounding In

$$4\pi \left(\frac{3}{4}\right)^{2/3} \gamma_{Al} + 4\pi \left(\frac{3}{4\pi}\{1 - V_{Al}\}\right)^{2/3} \gamma_{Al\text{-}In}$$

In surrounding Al

$$4\pi\left(\frac{3}{4\pi}\right)^{2/3}\gamma_{In} + 4\pi\left(\frac{3}{4\pi}V_{Al}\right)^{2/3}\gamma_{Al\text{-}In}$$

Separate spheres

$$4\pi\left(\frac{3}{4\pi}V_{Al}\right)^{2/3}\gamma_{Al} + 4\pi\left\{\frac{3}{4\pi}(1 - V_{Al})\right\}^{2/3}\gamma_{In} \quad ,$$

where $\gamma_{Al}$, $\gamma_{In}$, and $\gamma_{Al\text{-}In}$ are respectively the surface energies of Al and In and the interfacial energy of the Al-In boundary.

The calculations were performed for an assumed temperature of 800°C where the surface energy of pure Al, $\gamma_{Al}$, is 850 ergs/cm$^2$ and $\gamma_{In}$ is 490 ergs/cm$^2$. The value of the interfacial energy between liquid Al and liquid In, $\gamma_{Al\text{-}In}$, is unknown. If its value is similar to those in other comparable liquid phase immiscible systems, it should be approximately 100 ergs/cm$^2$ or less (17).

The sum of the surface and interfacial energies is plotted in Figure 19 as a function of $V_{Al}$ for the three configurations and for two assumed levels of the interfacial energy $\gamma_{Al\text{-}In}$, 200, and 500 ergs/cm$^2$.

The curves of Figure 19 show that the lowest energy configuration should be the one with the In annulus surrounding an Al sphere over all values of $V_{Al}$ if $\gamma_{Al\text{-}In} < \sim 360$ ergs/cm$^2$. If $\gamma_{Al\text{-}In} = 500$ ergs/cm$^2$, the In-surrounding-Al configuration is stable up to a volume fraction of aluminum, $V_{Al} = 0.72$. For Al contents higher than this value, a configuration consisting of separate Al and In spheres has the lowest surface energy of the three possibilities considered.

Based on the previous discussion, it is not surprising that the configuration having In around an Al sphere is approximately the configuration observed in the Lohberg and Ahlborn SPAR II experiment (18) as well as in the present experiments. Since in the former experiment there was a nonwetting condition between metal and container, the experimental conditions more closely meet the assumptions of the calculations. Similar configurations have been encountered in drop tower samples of the alloy, Al-68.8 weight percent In (6,19). These samples were much smaller (4.2 mm diameter by 1.4 cm long) and were processed in graphite containers under nonwetting conditions. Again, there was a clear tendency for the In-rich metal to surround an Al-rich core.

The tendency for one of the materials to surround the remainder of the alloy has also been noted in Pb-Zn alloys processed on ASTP (20) and terrestrially in the Bi-Se system (21). Although it is not clear whether the conditions were wetting or nonwetting, in both cases the material with the lower surface energy surrounded the higher surface energy portion of the alloy (17).

The conditions encountered in the present experiment in which the alloy wets the crucible is much more complicated than in the nonwetting situation since two liquids, a gas, and a solid are involved. This situation has not been analyzed as yet but some insight can be gained from analyses and experiments reported in the literature dealing with contained gas-liquid mixtures at low g (13,14). In these cases, the configurations depend on the shape of the container, the amount of liquid, and the degree to which the liquid wets the container. However, if there is complete wetting, the liquid will, in most cases, surround the gas phase. The configuration observed in the flight sample probably can be explained in a similar way. . the present experiment, the In-rich liquid wets the alumina crucible (i.e., forms a low energy interface) and thus tends to surround the Al-rich liquid.

In summary, it is possible to produce the observed configuration in which In-rich metal surrounds an Al-rich core in a nonwetting and wetting situation. In the former case, this results from the lower surface energy of the In-rich liquid relative to the Al-rich liquid and the low interfacial energy between them, and in the latter case it results from the relatively low energy of the In-rich liquid/alumina boundary.

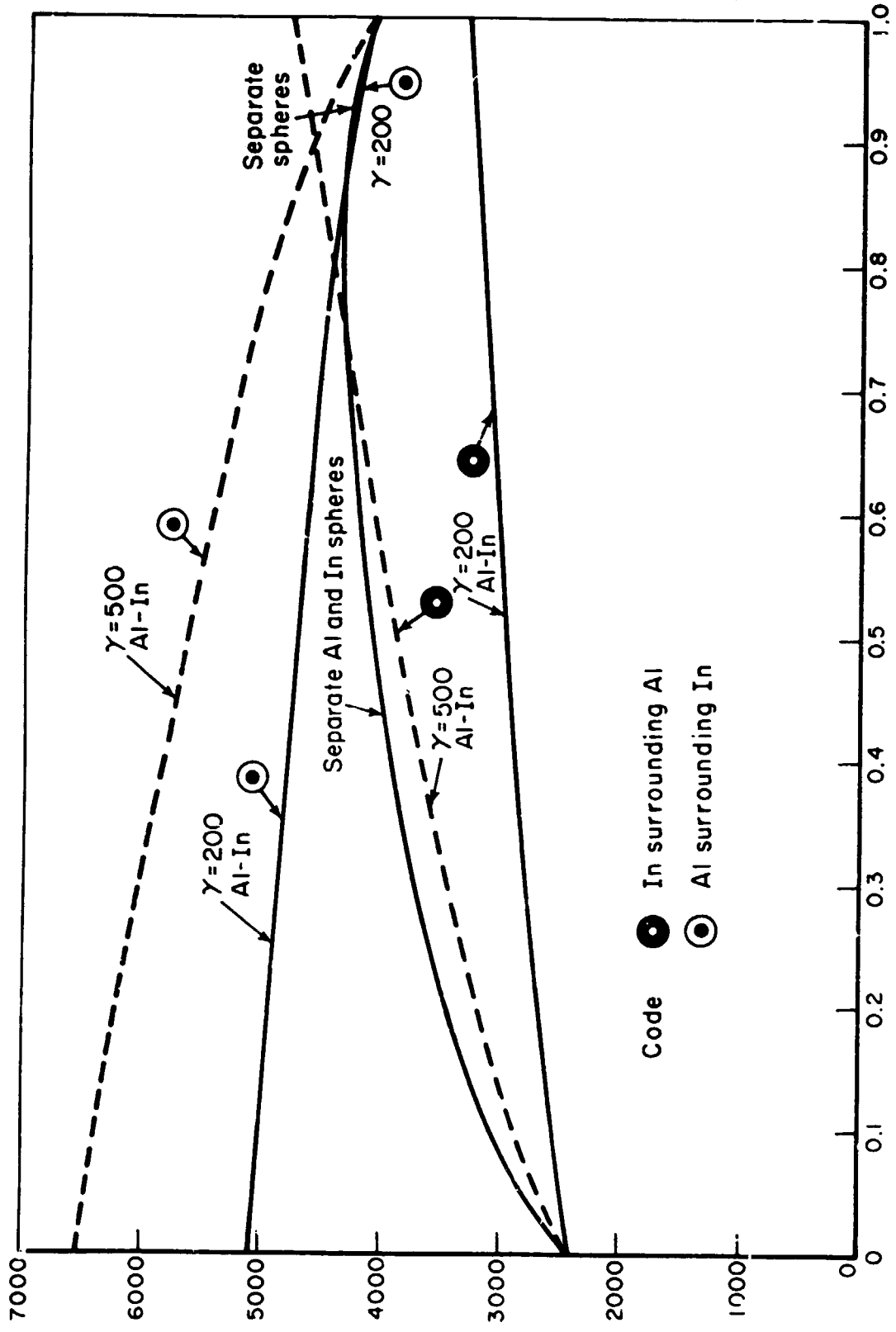


Figure 19. Total surface and interfacial energy for various Al and In configurations.

## Capillary Effects

Liquid droplet spreading on a solid surface is a possible mechanism by which the In-rich layer is formed at the container walls from a dispersion of droplets. We have just started to analyze this problem and have determined that droplet spreading is extremely rapid ($10^{-7}$ sec) when there is no constraining fluid around the droplet. Somewhat slower spreading times are anticipated in the latter case. The spreading action can cause local fluid flow which may bring other droplets in contact with the solid wall or with a liquid film at the wall; therefore, further coalescence may proceed by this action.

A somewhat related case involves the rearrangement of the fluid phase in contained gas-liquid mixtures when gravitational forces are largely eliminated. The capillary dominated motion in these cases depends on the size of the container but even for relatively large containers (10 cm) the time involved is approximately 1 sec and decreases for smaller containers (13).

It thus appears that the time-scale for such flows is consistent with the present experiment and that capillary flows may be a very important mechanism leading to the observed configurations. Further analysis is clearly required.

## Conclusions and Recommendations

On the basis of the analyses carried out to date, the following conclusions can be made:

1. Results from processing Al-40 weight percent In and Al-70 weight percent In samples terrestrially are qualitatively in agreement with those anticipated.

2. A model to explain the macro- and microstructure of the ground base samples has been presented.

3. The processing of the rocket flight sample proceeded according to plan except for a somewhat lower initial hold temperature.

4. The presence of a thermocouple within the melt allowed unambiguous determination of cooling rates and solidification temperatures.

5. The type of macrostructure resulting from processing the Al-40 weight percent In and Al-70 weight percent In samples in space was unexpected. The morphological evolution has been interpreted in terms of fluid flow occurring in the micro-g environment.

6. Fluid flow in the micro-g region can arise from numerous sources. Of the sources analyzed, thermocapillary convection and conventional convection are probably active. Capillary flow has as yet not been analyzed but probably is important. Residual fluid motion due to ricket spin does not appear to make an important contribution.

7. The equilibrium configuration of the Al and In in the micro-g environment has been calculated on the basis of known surface energies of the components and assumed values of the interfacial energy based on those of similar systems. A configuration consisting of an annular ring of In surrounding an Al-rich core is predicted and agrees closely with the observations in the present system as well as with some past results.

8. Bond number calculations support the observation that surface tension forces in this alloy system are dominant in the micro-g environment.

On the basis of this SPAR experiment and the analyses conducted thus far, the following recommendations can be made:

1. Ground base analyses should be continued in the following areas:

a. Additional ground base and flight sample sections should be analyzed metallographically to increase the observational statistics.

b. SEM and/or electron microbeam analyses should be used to determine the overall composition distribution to uncover further evidence for understanding fluid flow mechanisms. The local microstructure should be related to local chemistry.

c. Further experiments relating microstructure to cooling rate and composition should be conducted.

d. Further analyses of possible sources of fluid-flow at micro-g should be performed.

Rocket experiments should be designed to eliminate the sources of low g fluid flow and/or to learn what they are.

a. Conduct experiments without the liquid-gas interface to eliminate Marangoni effect from this source.

b. Conduct experiments with transparent systems analogous to the metal ones containing a miscibility gap to directly view the onset and pattern of fluid flow and to determine the effect of geometrical and material parameters on the flow.

NOTE: Reflight of the experiment is planned for SPAR VI.

## REFERENCES


(1) S. H. Gelles, "The Aluminum-Indium Liquid Phase Immiscibility Gap", submitted for publication October, 1976.

(2) Metals Handbook, Volume 8, Metallography, Structures and Phase Diagrams, American Society for Metals, Metals Park, Ohio (1973)

(3) John W. Cahn, "Spinodal Decomposition", Transactions of the Metallurgical Society of AIME, Volume 242, p 166 (1968).

(4) A. J. Schwartz, W. I. Goldburg, and J. S. Huang, "Spinodal Decomposition in a Binary Liquid Mixture Near Critical Point", Journal of Chemical Physica, Volume 62, p 1847 (1975).

(5) J. L. Reger, "Study of Processing Immiscible Materials at Zero-G", Interim Report to NASA-MSFC, Contract NAS8-28267 (May, 1973).

(6) A. J. Markworth, W. Oldfield, J. Duga, and S. H. Gelles, "Investigation of Immiscible Systems and Potential Applications", Final Report to NASA-MSFC, Contract NAS8-20748 (April, 1975).

(7) S. H. Gelles, E. W. Collings, W. H. Abbott, and R. E. Maringer, "Analytical Study of Space Processing of Immiscible Materials for Superconductors and Electrical Contacts", Final Report to NASA-MSFC, Contract No. NAS8-31445 (September, 1976).

(8) A. J. Markworth, S. H. Gelles, J. J. Duga, and W. Oldfield, "Immiscible Materials and Alloys", in Proceedings of the Third Space Processing Symposium, NASA Report No. 74-5, p 1003 (June, 1974).

(9) J. L. Reger and I. C. Yates, Jr., "Preparation and Metallurgical Properties of Low Gravity Processed Immiscible Materials", AIAA Paper No. 74-207, presented at AIAA 12th Aerospace Sciences Meeting, Washington, D. C. (January 30 - February 1, 1974).

(10) L. L. Lacy and G. H. Otto, "The Electrical Properties of Zero-Gravity Processed Immiscibles", AIAA Paper 74-208 presented at AIAA 12th Aerospace Sciences Meeting, Washington, D. C. (January 30 - February 1, 1974).

(11) J. L. Reger, "Experimental Development of Processes to Produce Homogenized Alloys of Immiscible Metals", Final Report to NASA-MSFC, Contract NAS8-27805 (December, 1972).

(12) W. T. Anderson, "Post Skylab Investigations, Experiment M-557, Immiscible Metal Alloys", Supplemental Report to NASA-MSFC, Contract NAS8-28309 (November, 1975).

(13) E. W. Otto, "Static and Dynamic Behavior of the Liquid-Vapor Interface During Weightlessness", Aerospace Chemical Engineering, Volume 62, p 158 (1966).

(14) J. T. Neu and Robert J. Good, "Equilibrium Behavior of Fluids in Containers at Zero Gravity", AIAA Journal, Volume 1, p 814 (1963).

(15) L. L. Lacy, Personal Communication (July, 1976).

(16) Simon Ostrach, "Convection Phenomena at Reduced Gravity of Importance from Materials Processing", Paper presented at 19th Plenary Meeting, COSPAR, Philadelphia, Pennsylvania (June 8-19, 1976).

(17) Lawrence E. Murr, Interfacial Phenomena in Metals and Alloys, Addison Wesley Publishing Company, Reading Massachusetts, pp 101-106, (1975).

(18) K. Löhberg and H. Ahlborn, "Preliminary Report on the Results of the SOLUOG-Experiment SPAR II: Solidification Behavior of Aluminum-Indium Alloys Under Zero Gravity Conditions" (July, 1976).

(19) S. H. Gelles and A. J. Markworth, "Rocket Experiment 74-30: Agglomeration in Immiscible Liquids at Low-G", Monthly Progress Report to NASA-MSFC, Contract No. NAS8-31543 (August 18, 1976).

(20) C. Y. Ang and L. L. Lacy, "Monotectic and Syntectic Alloys, Experiment MA-044", Apollo-Soyuz Test Project Preliminary Science Report, NASA Document [illegible]8171 (February, 1976).

(21) P. J. Knight, Che-Yu Li, and C. W. Spencer, "Monotectic Reaction in the Bi-Se System", Transactions of the Metallurgical Society of AIME, Volume 227, pp 18-22 (1963).

# CHAPTER VII

# CASTING DISPERSION-STRENGTHENED COMPOSITES AT ZERO GRAVITY

## Experiment 74-34

By

L. Raymond and Choh-Yi Ang

The Aerospace Corporation

## ABSTRACT

The space processing Experiment 74-34, Casting Dispersion-Strengthened Composites, has been completed after the successful SPAR II flight of the second experiment in the series. The SPAR I experiment, which involved the intentional addition of dispersoids as thoria particles in magnesium, produced encouraging results proving the beneficial effects of low-g on the dispersion of heavy second phase in a light metal matrix. Experimental observations of SPAR I were utilized to modify some process parameters for the SPAR II experiment, which differed from SPAR I in that a dispersion of thoria particles was achieved by the gettering of oxygen from magnesia by the added thorium metal.

As predicted, the gettering-dispersion was achieved in SPAR II, and the flight-cast sample was microstructurally sound with very uniform hardness. In comparison, the ground-processed sample showed a high degree of segregation of the dispersoids and contained numerous internal pores. The hardness of the low-g sample is twice that of pure magnesium, and 30 percent greater than its 1-g counterpart and the commercial high-strength Mg-Th-Zr alloy, HK31A, processed under identical experimental conditions.

The beneficial effects of low-g were examined and mechansims were postulated for the observed microstructural features and dispersion hardening. Certain observations from the SPAR II experiment also led to a modification of the interim conclusion of SPAR I relative to the occurrence of dispersion-depleted layers. Analysis of the results of this experiment series was also used to generate the recommendations of continuing low-g experimentation in the field of particle-strengthened metal composites, and of the tyoe of theoretical study and ground-based laboratory research to support the flight experiments.

## INTRODUCTION

This is the final report of the Space Processing Applications Rocket (SPAR) Experiment 74-34, Casting Dispersion-Strengthened Composites at Zero Gravity. This investigation, which was initiated on 3 June 1975, involved a series of two rocket furnace experiments representing a stepped plan to study the phenomena and establish the feasibility of synthesizing metal composites which contain uniform dispersions of matrix-strengthening particles. The low-g levels attainable during short duration rocket flights were utilized to investigate a composite system in which the matrix and the dispersoids differ widely in density. The metal and the dispersoids were selected on the basis of metallurgical and thermodynamic considerations for optimum dispersion-strengthening. Feasibility of sample preparation, possibility of application spin-offs, usefulness of data for guiding future dispersion-strengthening experiments in space, and compatibility with the performance characteristics of NASA-provided apparatus were all important factors in planning the experiment series.

The SPAR I flight experiment, which was successfully flown on 11 December 1975, was the low-g melting and solidification of a hot-pressed magnesium (Mg) compact containing two volume-percent thoria ($ThO_2$) particles. The data and phenomenological observations of the first flight experiment provided a basis not only for explaining some results of the second flight experiment, but also for the introduction of necessary changes of the latter's experiment plan. The SPAR II experiment, successfully flown on 17 May 1976, involved the same composite system except that the dispersoid $ThO_2$ was formed during the melting and solidification of Mg compacts containing magnesia (MgO) and thorium metal (Th). The ability of the Th to getter oxygen from MgO and to precipitate out as heavy inert $ThO_2$ particles in a light Mg matrix is considered important in future space processing of dispersion-strengthened, high strength-to-weight ratio metals or alloys which contain difficult-to-remove oxygen impurity.

The SPAR I Preliminary Post-Flight Technical Report [1] contained detailed descriptions of sample preparation and cartridge construction. Results of the SPAR I flight experiment and the bulk of comparative characterization of flight and ground-base tested (GBT) samples were discussed in the SPAR I Post-Flight Technical Report [2]. In this final report, although the emphasis is on reporting SPAR II results, certain pertinent data and observations presented in the first two reports are reintroduced and discussed in conjunction with the SPAR II findings. While SPAR I results helped explain many SPAR II

observations, the latter in turn have led to modification of certain interpretations of the former. On the basis of this series of two experiments, conclusions and recommendations are made to help develop pre-Spacelab fundamental understanding and experimental techniques in this important technology of dispersion-strengthening at low-g.

## OBJECTIVES

The ultimate purpose of the SPAR Experiment 74-34 is to gain an understanding of low-g effects on the dispersion of particles in a metal matrix and to develop techniques and establish the feasibility of casting in space dispersion-strengthened useful metal composites that are difficult if not impractical to achieve on Earth because of large differences in density of the constituents. The specific goals of the two flight experiments are: (1) to observe the phenomena associated with dispersing Th particles in the molten Mg matrix at low-g; (2) to establish the feasibility of reaction-precipitation of $ThO_2$ dispersion via the gettering mechanism under low-g conditions; and (3) to determine low-g effects on Mg matrix strengthening by comparing flight and ground-based samples processed under identical thermal conditions.

## BACKGROUND INFORMATION

### Dispersion Strengthening

The strengthening of a metal, especially at elevated temperatures by the dispersion of fine particles in the matrix is a well known phenomenon [3,4]. It is generally believed that fine particles less than 0.1 $\mu$m in size and interparticle spacings in the neighborhood of 0.5 $\mu$m will lead to optimum strengthening with a density of dispersoids from 1 to 10 volume-percent. This generalized observation has been based on the SAP (sintered aluminum products) process and some internal oxidation investigations involving Cu and $Al_2O_3$. Other studies [5,6] have shown that strengthening can also be achieved with dispersoid sizes as large as 5 $\mu$m. Obviously, the applicable method of introducing or forming the dispersed particles and the dominant mechanism of strengthening (such as dislocation pinning, particle shear, etc.) for the composite system in question will influence the experimental results.

In our experiment series with Mg and $ThO_2$, we first arbitrarily chose a 2 v/o dispersion as the criterion and used the finest available $ThO_2$ powder (average size 0.8 $\mu$m) in the SPAR I experiment. For the SPAR II experiment, we attempted to form the same amount of $ThO_2$ in the Mg matrix by making use of the gettering tendency of Th metal (see comparison of free energies of oxides formation in Table 1). The fact that Th metal up to 40 weight-percent (Fig. 1) will be dissolved in molten Mg makes it feasible to conduct the second experiment within the temperature capability (~1100°C) of the furnace system. Since we could not control the oxygen content as an impurity in Mg, we decided to introduce MgO powder into the Mg + Th mix as the starting material, with a calculated reaction product of 2 v/o $ThO_2$.

TABLE 1. COMPARISON OF FREE ENERGIES OF SOME METAL OXIDES AT HIGH TEMPERATURES

| Metal (m.p. in °C) | Solid Oxide (m.p. in °C) | $\Delta F_T$ of Oxide Formation, Kcal T = 1273°C | T = 2273°C |
|---|---|---|---|
| Mg (651) | MgO (2800) | -117.8 | --- |
| Th (1845) | $ThO_2$ (3050) | -245.4 | -208.2 |
| Ti (1668) | TiO (1750) | -101.0 | - 75.5 |
| | $Ti_2O_3$ | -296.7 | -237.2 |
| | $Ti_3O_5$ | -480.3 | -317.7 |
| | $TiO_2$ (1640) | -182.1 | -141.6 |
| Li (186) | $Li_2O$ (> 1700) | -109.3 | --- |
| Al (660) | $Al_2O_3$ (2050) | -324.5 | --- |
| Zr (1857) | $ZrO_2$ (2700) | -216.0 | -174.4 |

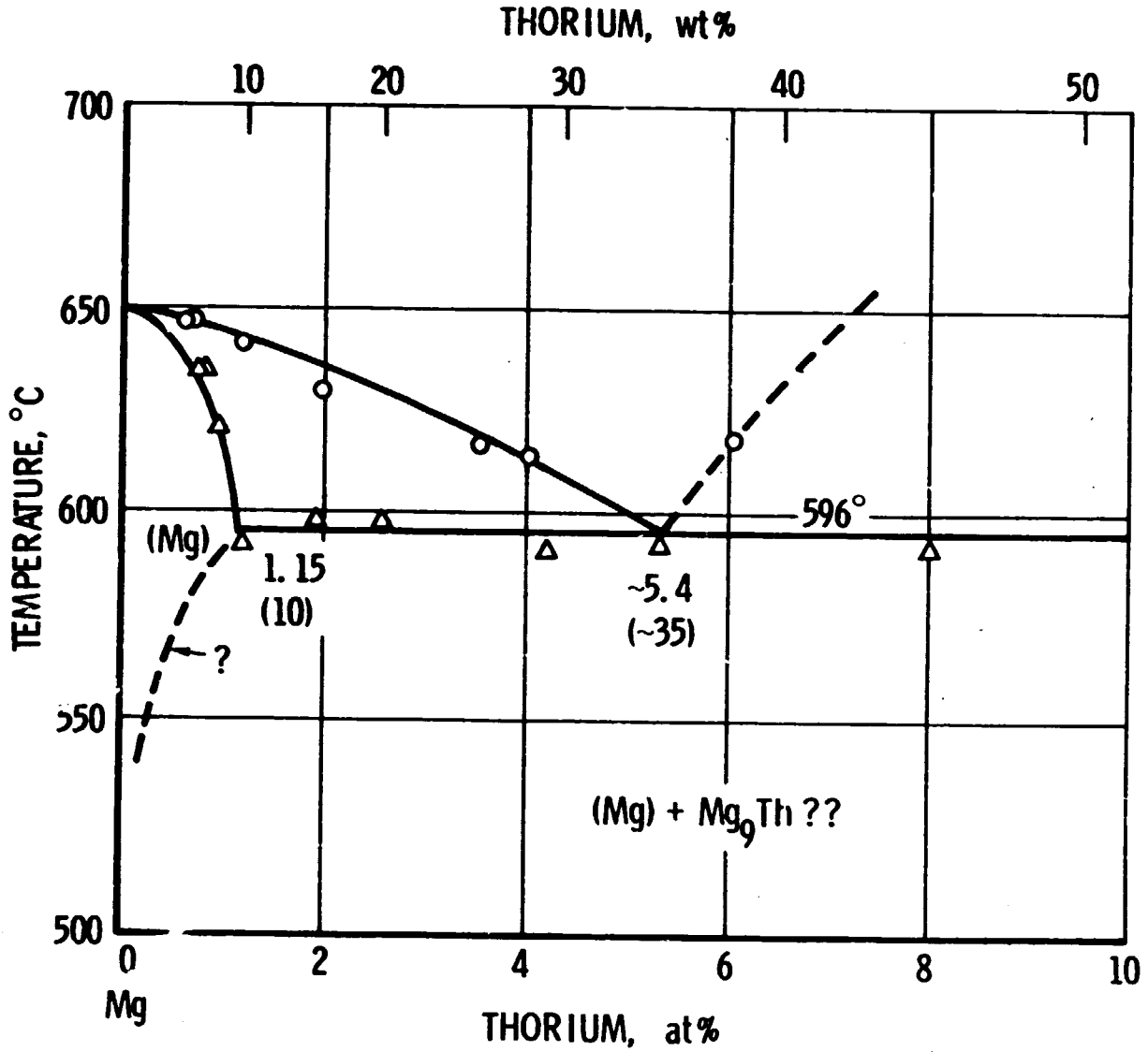


Figure 1. Mg-Th phase diagram.

It must be remembered that the experiment was intended to compare low-g and 1-g samples processed under identical conditions except for the g-level. The experiment was not an in-depth dispersion-strengthening research for achieving optimum properties of the Mg-$ThO_2$ composite system.

## Sample Preparation

In the two rocket experiments, the starting materials were 99.9+ percent purity powders of Mg, MgO, $ThO_2$, and Th. The $ThO_2$ powder had an average particle size of approximately 0.8 μm; the others were all -200 mesh (~74 μm). Scanning Electron Microscope (SEM) photographs of the Th, $ThO_2$, and MgO powders are shown in Figure 2. No attempt was made to break up the powder clusters for taking the SEM photographs.

To insure uniform distribution of constituents, 50- to 100-g batches of the two mixes were ball-milled 2 hours under an atmosphere of ultrapurity argon. While the SPAR I composition was as originally planned, the SPAR II experiment, with the availability of two furnace cavities for processing, had undergone several perturbations with regard to compositions of the two samples. Because of the difference in "soak" time between the two SPAR II furnaces, it was finally decided to process duplicate samples of the same composition. Therefore, the SPAR I and SPAR II experimental compositions, in terms of weight percent, are as follows:

SPAR I 89.5 Mg - 10.5 $ThO_2$ (2 v/o $ThO_2$)

SPAR II 87.6 Mg - 9.2 Th - 3.2 MgO (2 v/o $ThO_2$ after gettering).

Several powder sample preparation methods, such as isostatic pressing (with and without sintering), cold-press and sinter, and hot pressing, were considered for achieving samples with minimum internal porosity and capable of retaining as-introduced distribution of constituents until melting occurred. With a lead time of less than 2 months to delivery of the first group of samples, hot-pressing at 250°C under argon atmosphere was selected as the method of sample preparation. The justification for using the method of hot pressing was three-fold:

1. High degree of densification
2. Minimum residual stresses (slow heating and cooling) in the compact
3. Simple tooling.

ORIGINAL PAGE IS
OF POOR QUALITY

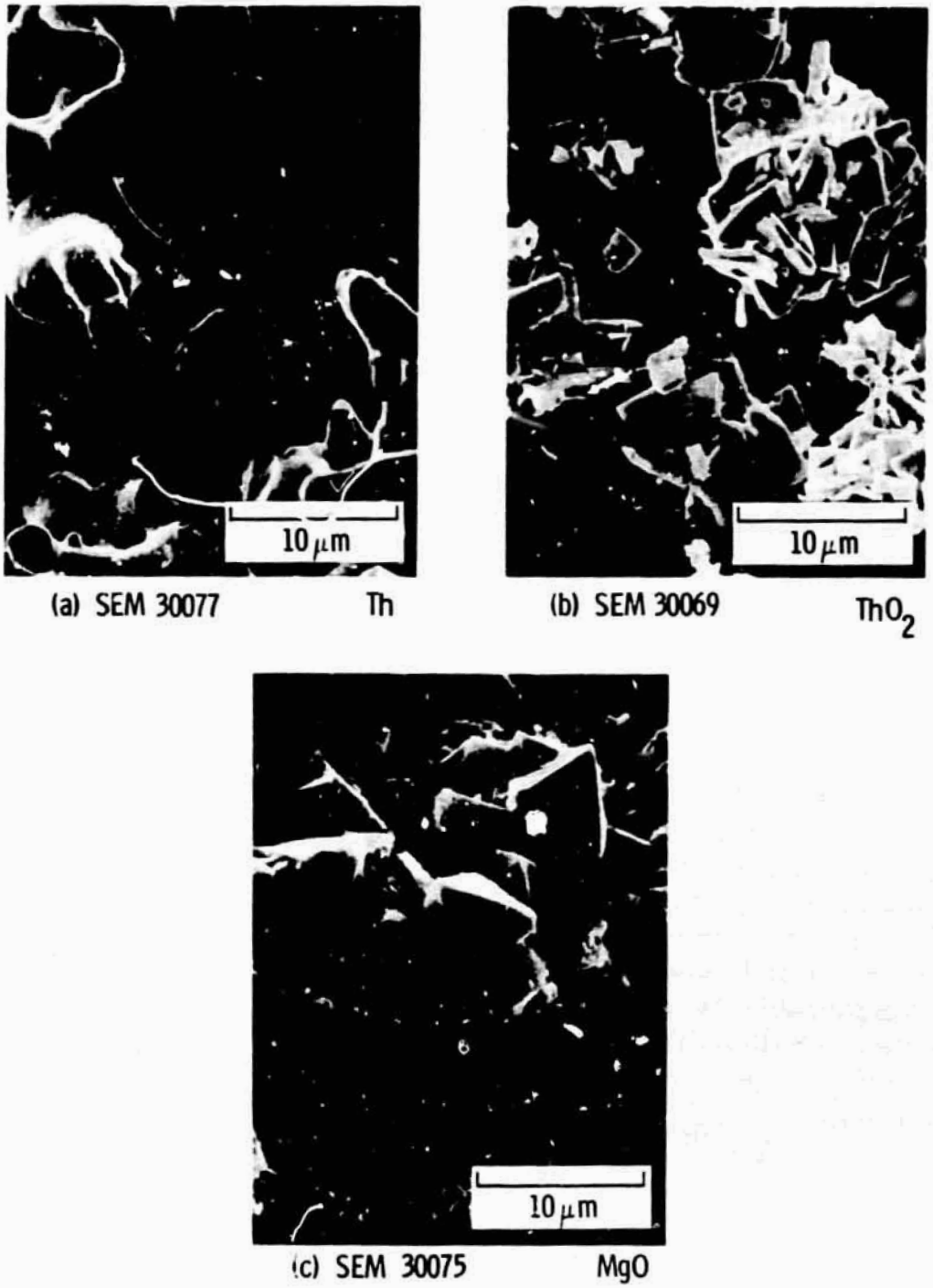


Figure 2. Structure of Th, $ThO_2$, and MgC powder particles.

The experience gained in conducting the Apollo-Soyuz Test Project (ASTP) Experiment MA-044, Monotectic and Syntectic Alloys [7], was utilized in the encapsulation of hot-pressed samples. Figure 3 is a schematic of the ampoule and cartridge assembly. Briefly stated, the >95 percent dense compact was loaded in a POCO graphite crucible with a threaded cap. Graphite cement was used to seal the cap. The loaded ampoule was then encapsulated in a stainless steel cartridge which was designed by NASA for proper interface with the furnace system. All sample preparation and ampoule loading operations were carried out in a vacuum glove box under an atmosphere of argon. The final e-beam welding of the stainless steel cartridges was carried out in a vacuum of approximately $10^{-6}$ torr.

The POCO DPF-3-2 high purity dense graphite crucible was used because molten Mg does not wet it. Since the rocket furnace system could not be used to perform containerless melting experiments, the nonwettability between crucible and the melt was considered essential in minimizing wall effects which can be physical and chemical in nature.

The use of inert argon atmosphere instead of vacuum was justified on the following bases:

1. Mg has a high vapor pressure, e.g., 1 torr at 625°C (25°C below the melting point), $10^{-3}$ torr at 383°C, and $10^{-5}$ torr at 287°C. Therefore, an evacuated environment within the cartridge or ampoule was considered detrimental in terms of excessive metal evaporation before melting and unpredictable melt agitation and vapor condensation during soaking and cool-down.

2. To minimize the oxidation of Mg powder during sample preparation, working under one atmosphere of inert gas inside a vacuum glove box is an established practical laboratory procedure. The low level of alpha radioactivity associated with small quantities of $ThO_2$ and Th could also be brought under control in a glove box.

3. The casting of Mg on Earth is carried under the protection of a flux. Therefore, from a practical standpoint, any spin-off from the SPAR experiments that might lead to a new Earth process for casting dispersion-strengthened Mg alloys should probably not involve vacuum.

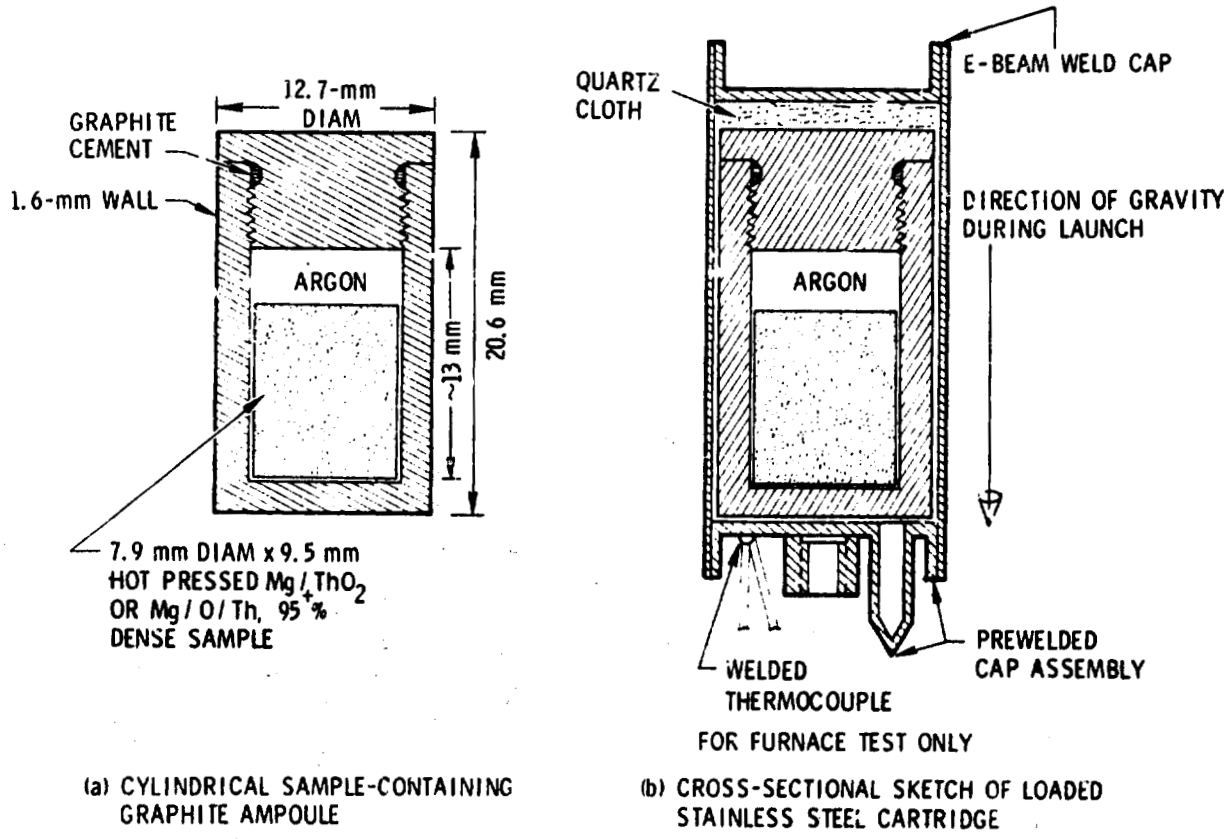


(a) CYLINDRICAL SAMPLE-CONTAINING GRAPHITE AMPOULE

(b) CROSS-SECTIONAL SKETCH OF LOADED STAINLESS STEEL CARTRIDGE

**Figure 3. Sample/ampoule/cartridge assembly.**

## Process Parameters

The low g period, i.e., g-levels $\leq 1 \times 10^{-4}$ g, during the coasting phase of the two SPAR flights was estimated to be approximately 4 min. A high heat-up rate up to 10°C/sec was deemed necessary to heat the sample to ≥ 800°C as the rocket entered its coasting phase. A rapid gas quench (>10°C/sec) was also required to insure the solidification of a melted sample before encountering reentry g forces. Another critical requirement was that the melting point (651°C) of Mg must not be reached when g-levels were greater than $1 \times 10^{-3}$ during the ascend phase. Presoaking the cartridge before launch at some temperatures below 600°C was considered permissible.

The exact thermal profiles were determined by a series of furnace tests conducted at MSFC. It was determined that during heat-up, the temperature of the cartridge wall would lag behind the furnace control temperature by as much as 150°C, and the sample inside the cartridge should lag behind the cartridge temperature by only a few degrees. At soak, the cartridge (and the sample) would be approximately 50°C colder than the indicated furnace control temperature. The formal ground-based tests would use thermal profiles identical to those for the flight tests and would use identically designed furnaces. In conjunction with several phenomenological considerations, the specified experiment requirements of process parameters were as follows:

1. SPAR I One Mg + $ThO_2$ Sample

   Low-g sample soak temperature: 800°-950°C

   Low-g soak time: ≥ 180 sec

   Prelaunch soak: ~300°C

   Heat-up rate: ≥ 10°C/sec

   Quench rate: ≥ 10°C/sec

2. SPAR II Two Mg + Th = MgO Samples

| | Forward Furnace | Aft Furnace |
|---|---|---|
| Low-g sample soak temperature: | 800°-950°C | 800°-950°C |
| Low-g soak time: | ~60 sec | ≥ 180 sec |

| | Forward Furnace | Aft Furnace |
|---|---|---|
| Prelaunch soak: | ~500°C | ~500°C (600°C max) |
| Heat-up rate: | <10°C/sec | <10°C/sec |
| Quench rate: | ≥10°C/sec | ≥10°C/sec |

## Phenomenlogical Considerations

### Density-Induced Sedimentation and Segregation

The well known Stokes Law [8] is applicable under "ideal" conditions for the describing sedimentation velocities of dilute concentration of small particles in a liquid matrix. Assuming sphericity of particles and absence of wall effects and convection-induced currents, the terminal settling velocity ($V_t$) of a particle of size d in a gravity field ($g$) in a liquid with a viscosity $\eta$ in poise can be related to the particle/liquid density difference ($\Delta\rho$) by the expression:

$$V_t = d^2 g \Delta\rho / 18\,\eta \ (\mathrm{cm/sec}) \quad . \qquad (1)$$

Figure 4 is a plot of $V_t$ versus g-level for the sedimentation of $ThO_2$ dispersoids in molten Mg. Under ideal conditions and the influence of 1-g, "spherical" Th particles 0.8 $\mu$m in diameter should settle in molten Mg for a distance of approximately 0.4 mm in 180 sec, while larger (2 $\mu$m) particles may move 4 mm downwards. At a g-level of $1 \times 10^{-4}$ g, the small settling distances would be difficult to measure.

In our experiment the crucible wall effects and concentration- and $\Delta$T-induced convection currents, coupled with the nonsphericity of particle shape (Fig. 2), would preclude the exact description of sedimentation by the Stokes Law. Nevertheless, we did expect to see within a range of a few hundred $\mu$m the phenomena of layered sedimentation, dense clustering of particles, and nonuniform distribution of clusters under 1-g conditions. In space, however, we expected to see very little disturbance of the distribution of $ThO_2$ particles or agglomerates as originally introduced in the starting compact in the case of SPAR I, and of MgO sites, where the gettering reaction would be taking place, in the case of SPAR II. What the effects of natural or nongravity related convection currents would have on the dispersion was one question to be answered by this experiment.

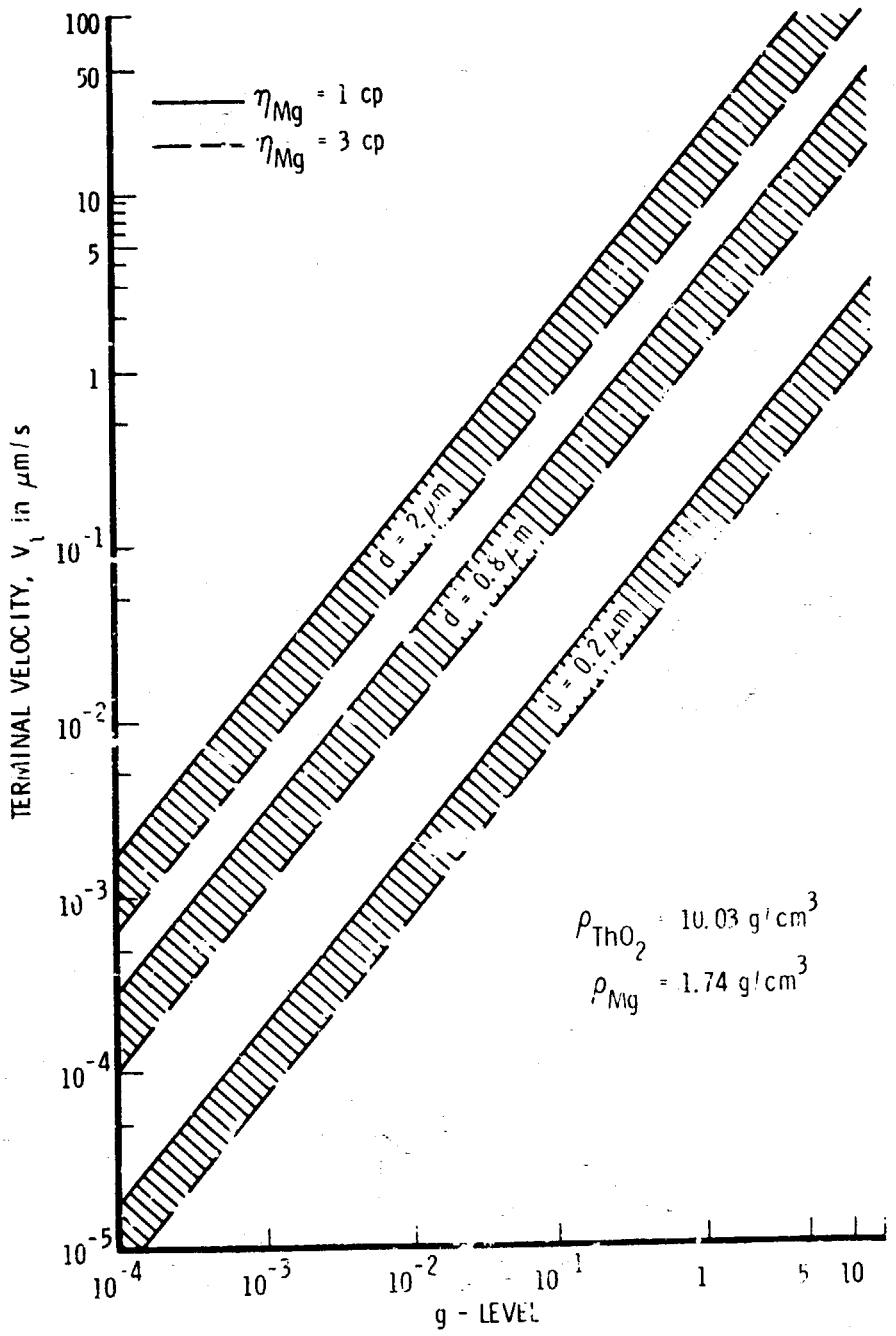


Figure 4. Sedimentation velocity for $ThO_2$ dispersoids in molten Mg.

## Diffusion and Gettering Mechanisms

As mentioned previously, Th metal would dissolve in molten Mg and react with solid MgO to form $ThO_2$. This reaction could proceed at high velocity if molten Th in Mg made many points of contact with MgO particles. Without knowing the "activities" of the reactants and other thermochemical parameters, it is not possible to calculate the reaction velocity; but, we expected that the slower process of liquid Th diffusion to be the determining factor.

In liquid metal diffusion, the values of diffusion coefficient D for most miscible binary systems fall within the range of $10^{-5}$ to $10^{-4}$ $cm^2/sec$. In place of the Fick's Law for solid state diffusion, the liquid metal diffusion may be approximated by the relationship

$$D \simeq \frac{\overline{x^2}}{2t} \qquad (2)$$

where $\overline{x^2}$ is the rms distance covered by the random, long-range motion of atoms in the liquid state. If it is assumed that the maximum distance for one Th atom to travel to the MgO is 74 $\mu$m (average size of Mg powder particle before melting) and a D of $1 \times 10^{-4}$ $cm^2/sec$, the time involved would be less than 1 sec. Consequently, it is our belief that in the SPAR II Experiment, the two different soak times of 60 and 180 sec would give us the opportunity to observe the kinetics of the gettering mechanism if large agglomerates of MgO were present and larger distances were involved in Th diffusion.

The size of precipitated $ThO_2$ particles from the gettering reaction was expected to be small. However, the growth rate of the precipitate and the starting size of the nuclei were unknown parameters.

## Convection Effects and Gas-Liquid Movement

Under the influence of 1 g, any argon gas trapped below the sample or even inside the highly densified compact should eventually float to the top. Heating the sample to $\geq 800°C$ will cause the gas to expand and, within a confined space, the gas will develop a pressure $\geq 3$ atm depending on equilibrium conditions, and "gas voids" of various sizes should exist throughout the 1-g castings. Filling of voids by the molten metal either during cooling or via other processes such as diffusion or surface tension-induced Marangoni motion might also be observed.

Even at low g, there still exist many possible natural convection-induced effects [9] and the phenomenon of gas movement associated with the nonwettability between the container wall and the liquid.

The experimental observations at low-g by Reynolds [10] concerning the tendency of a nonwetting fluid to "bounce" off the wall leaving the gas in contact with wall could provide the necessary driving force to eliminate internal gas voids in our low-g samples. As previously mentioned, molten Mg does not wet the POCO graphite. However, some mechanical locking would be expected because of the presence of machining grooves and surface porosity on the ID of the graphite crucible which will trap molten Mg.

The complex and interrelated process parameters associated with a short-duration rocket flight test made if difficult to identify beforehand the possible natural convection effects that could play a major role during melting and solidification of the samples. For example, we did not know if a heat-up rate of 10°C/sec would induce thermoacoustic effects [11]. The consequences of these effects which would cause rapid movement of the liquid and gas could not be predicted because the experiment was not designed to provide critical boundary conditions for a quantitative analysis.

The gravity-driven convection velocity, $V_c$ in cm/sec, however, can be estimated by using the following expression [12]:

$$V_c = \frac{\Delta T}{L} \frac{\rho \beta g L^3}{12 \eta} \left[ \left( \frac{X}{L} \right)^3 - \frac{X}{L} \right] \quad . \tag{3}$$

The convection velocity reaches its maximum value at a point $x = 2L/3$ where L is half way between the cartridge wall and the center of the molten metal. Figure 5 is a plot of $V_c$ versus g-level for various $\Delta T/2L$ or $\Delta T/0.4$ cm, using the values of 1.74 g/cm$^3$ for $\rho$, $1 \times 10^{-5}$/°C for $\beta$ (the volumetric coefficient) and $1 \times 10^{-2}$ P for the viscosity $\eta$. It should be noted that we did expect the $\Delta T/2L$ to be less than 10°C on the basis of the furnace tests.

Irrespective of the g-level, before the melt attains an equilibrium soaking temperature, the thermal lag ($\Delta T$) between the externally heated cartridge wall and the center of the molten sample will be an important influence on the motion of small suspended particles. One can empirically analyze the situation by using appropriate values and taking the ratio of equations (3) and (1) to arrive at the expression:

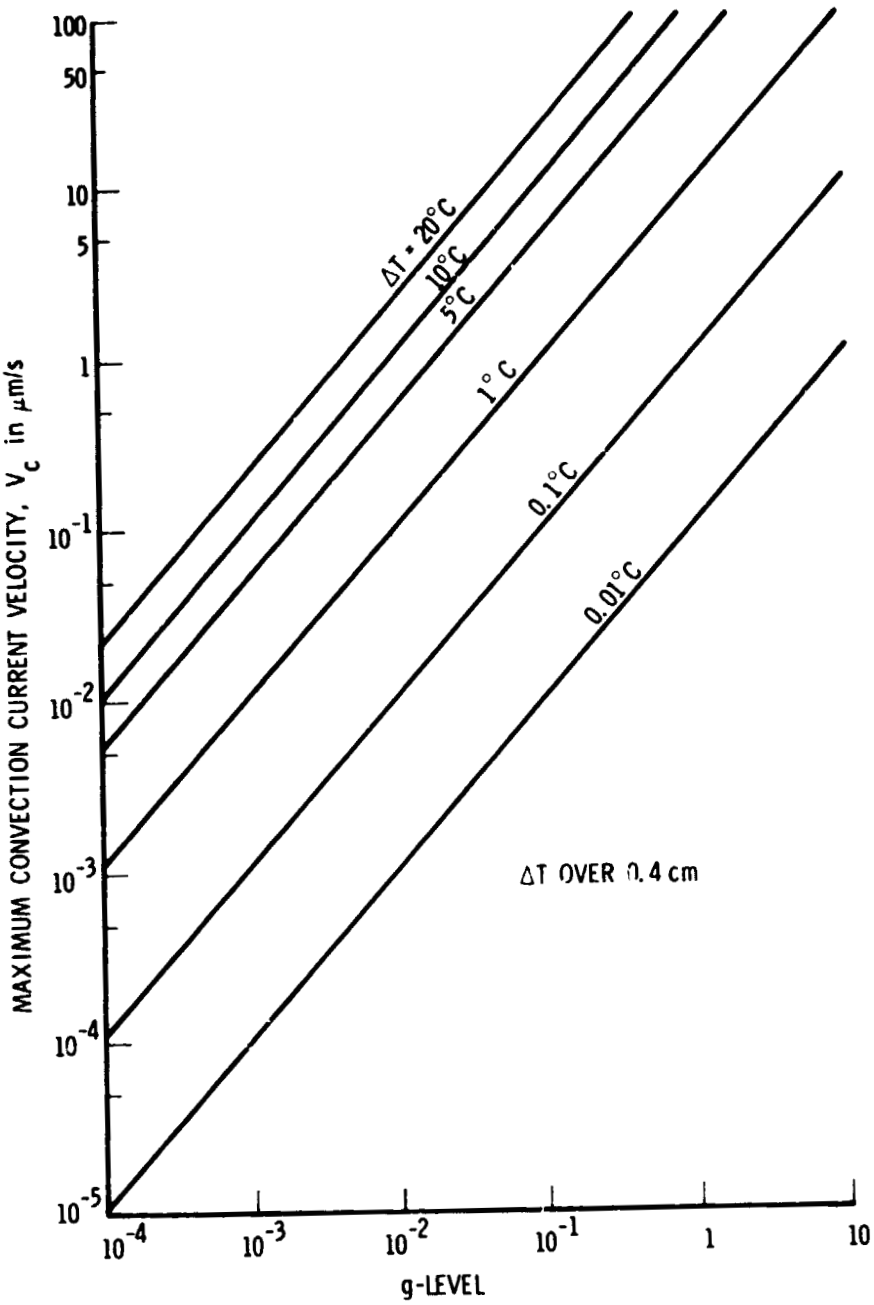


Figure 5. Convection velocity versus g-level and temperature gradient.

$$V_c / V_t \simeq 8 \times 10^{-8} \Delta T / d^2 \quad . \qquad (4)$$

In our experiment, with its given sample/cartridge configuration, any gravity pull on particles $1 \times 10^{-4}$ cm or smaller would not be able to overcome the agitation caused by convection currents when the $\Delta T$ is greater than 1°C. It was therefore important that $\Delta T$ must be minimized. The prelaunch temperature soak and the high thermal conductivity of Mg would favor the attainment of small $\Delta T$.

If $\Delta T$-induced convection currents could be controlled, they could become a means of dispersing small particles in a melt in space. This experiment, however, was not designed to provide a controlled convection.

Directional Solidification and Particle Rejection

The rapid quenching system would provide a direct contact between the cartridge wall and the cold gas; i.e., the sample/cartridge should cool down even more rapidly than the furnace. It was our estimate that during cooling through the solidification temperature, the directional growth rate of grains from the crucible wall inwards would be much higher than the commonly observed [13] critical velocity of approximately 20 $\mu$m/sec for the rejection particles >100 $\mu$m in size. It was our belief that any segregation of dispersoids observed in either the flight or GBT samples would not be caused by the mechanism of particle rejection or trapping during the advancement of solidifying fronts.

## EXPECTED RESULTS

Based on the foregoing discussions on anticipated phenomena and their dependence on sample characteristics and experimental constraints, we expected to make the following observations with the SPAR I and SPAR II flight and GBT samples.

### SPAR I

1. Retention of original macroscopic distribution of Th dispersoids in the flight sample.

2. Segregation and denser packing of Th clusters, especially towards the "bottom" of the 1-g GBT samples.

3. Flight sample should have less internal gas voids than the GBT samples and should not have shrinkage cavities commonly observed in Earth castings.

4. Identification of microstructural features that may lead to understanding of low-g effects on metallic melts.

5. Development of appropriate characterization techniques and identification of process anomalies that may lead to either refinement or modification of SPAR II experiment plan.

## SPAR II

1. Formation of $ThO_2$ particles from the gettering reaction in flight and GBT samples, especially the ones processed for a longer soak time.

2. Dispersion of precipitated $ThO_2$ dispersoids should retain the original macroscopic distribution of MgO particles as the reaction sites in the flight samples.

3. More segregation and sedimentation of precipitated Th particles in the 1-g GBT samples than in the flight samples.

4. In comparison with the GBT samples, the flight ingots should have less internal gas voids and exhibit more uniform microstructure and hardness.

5. Identification of microstructures and microanalysis of constituents that will help understand the gravity-induced effects on dispersion strengthening and the time-dependent kinetics of the gettering process.

## SAMPLE EVALUATION PLAN

The original plan for the proposed investigation was quite extensive; it included the detailed comparison of SPAR samples with the commercial magnesium alloy HK31A (Mg-3Th-1Zr). Because of funding and scheduling

constraints, the scope was reduced and laboratory samples, which were not considered critical in the final experiment plan for the two SPAR flights, were not processed to completion. Nevertheless, it should be mentioned that a total of over 40 samples were prepared, which included the Mg-$ThO_2$ (SPAR I), pure Mg, alloy HK31A, and two compositions of Mg-Th-MgO (SPAR II).

In the case of SPAR II compositions, because of incompatibility with the programmed thermal cycles of other experiments in one of the two flight furnaces (each furnace had three cavities), it was decided to process two samples of the same composition,

$$Mg + Th + MgO \rightarrow (2\ v/o\ ThO_2 + Mg) \quad ,$$

and make use of the difference in soak time to study the kinetics of reaction-dispersion. Therefore, all encapsulated samples, except the ones for process development and control purposes, of the second composition which would have provided a 0.7 v/o $ThO_2$ dispersion, were not processed further for formal characterization.

Nineteen samples were encapsulated and delivered to MSFC for various GBT and SPAR I and SPAR II flight tests. Table 2 identifies the samples and their disposition. From this table, it can be seen that for SPAR I there was one flight (G1) and one GBT (G2) processed sample, and for SPAR II, a total of four samples for the flight and GBT with short (D3, C1) and long (D5, C5) soak times. As will be discussed in more detail later, only the long-soaked SPAR II samples were extensively characterized. The short-soaked flight sample D3 did not reach the soak temperature as planned; consequently, its GBT counterpart was also not extensively characterized.

The characterization plan for all samples is shown in Figure 6. Because of limitation of sample materials, step 6b, chemical analysis of tested samples, was not carried out. Otherwise, all formal experiment cartridges and samples were characterized according to the plan, from leak testing and radiography to microstructural analysis and microhardness testing. The supplementary laboratory samples, however, were only characterized to the extent that data obtained could contribute to the understanding of observed microstructures and analytical results of the formal flight and GBT samples.

TABLE 2. IDENTIFICATION AND DISPOSITION OF ENCAPSULATED SAMPLES DELIVERED TO NASA/ MSFC

| Sample No. | Composition | Type Test Intended | Type Test Conducted | Remarks |
|---|---|---|---|---|
| | | SPAR I | | |
| H1 | Mg-$ThO_2$ | Furnace Test | Fce. Test | |
| H2 | Mg-$ThO_2$ | Furnace Test | Fce. Test | |
| H3 | Mg-$ThO_2$ | Furnace Test | Fce. Test | |
| H4 | Mg-$ThO_2$ | GBT | GBT | Improperly tested |
| H5 | Mg-$ThO_2$ | GBT | GBT | Improperly tested |
| H6 | Mg-$ThO_2$ | GBT | GBT | Improperly tested |
| G1 | Mg-$ThO_2$ | Flight Test | Flight Test | For characterization |
| G2 | Mg-$ThO_2$ | Flight Back-up | GBT | For characterization |
| | | SPAR II | | |
| C2 | (A)* | Fce. Test | Fce. Test/GBT | Unsuited as GBT |
| C4 | (A) | Fce. Test | Fce. Test/GBT | Unsuited as GBT |
| C3 | (B)* | Fce. Test | Fce. Test | |
| T5 | HK31A alloy | Fce. Test | Unknown | |
| C1 | (A) | Fce. Test | GBT (S)** | For characterization |
| C5 | (A) | GBT | GBT (L)** | For characterization |
| C6 | (B) | GBT | --- | Shelved |
| D5 | (A) | Flight Test | Flight Test (L) | For characterization |
| D6 | (B) | Flight Test | --- | Shelved |
| D3 | (A) | Flight Back-up | Flight Test (S) | For characterization |
| D4 | (B) | Flight Back-up | --- | Shelved |

* Composition (A) Mg + Th + MgO → Mg + 2 v/o $ThO_2$,
(B) Mg + Th + MgO → Mg + 0.7 v/o $ThO_2$

** (S) Short soak in Forward Furnace, (L) long soak in Aft Furnace.

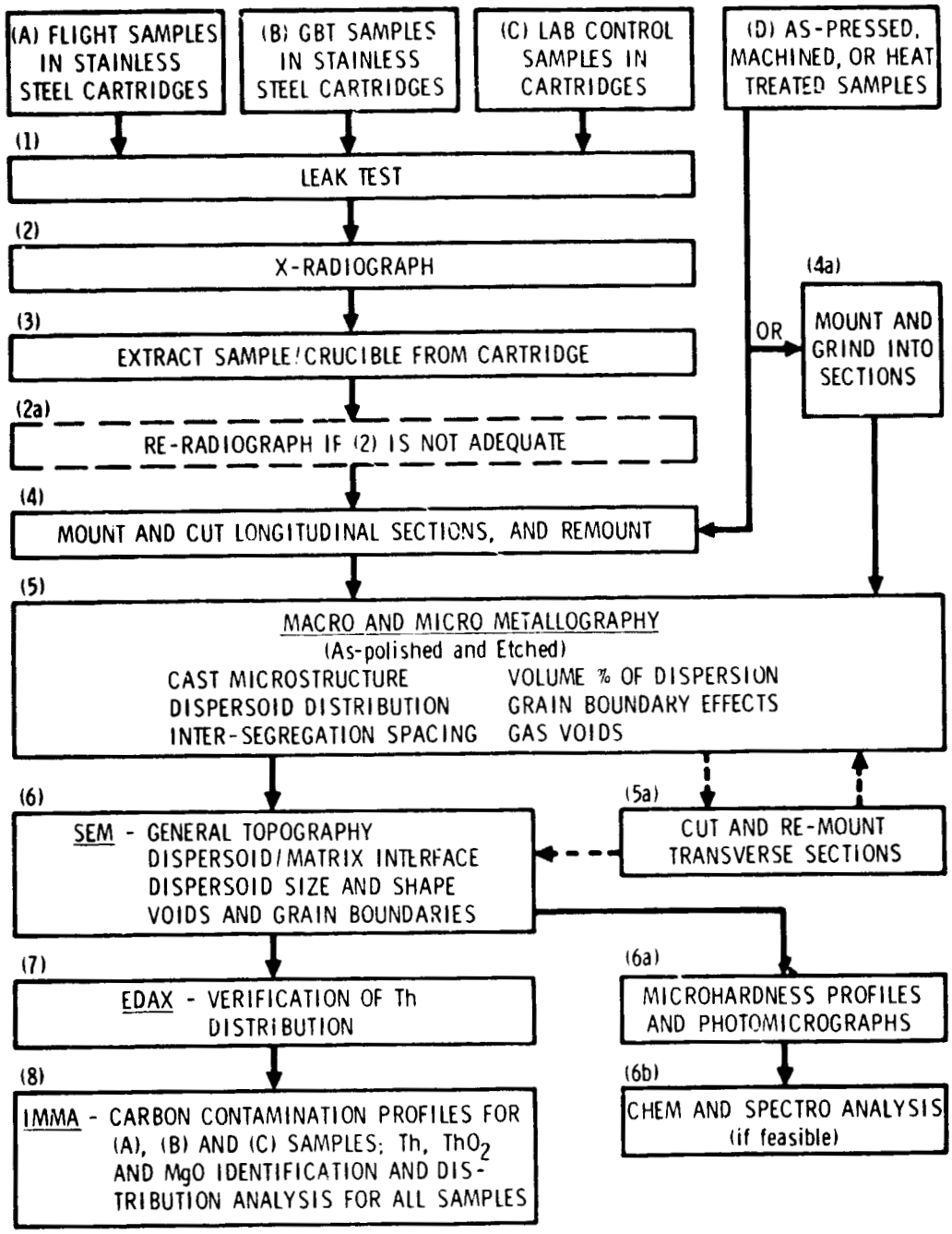


Figure 6. Sample characterization flow chart.

## FLIGHT AND GROUND BASED TEST DATA

For SPAR I and SPAR II tests, the thermal profiles were determined by a series of furnace tests and GBT tests. In the beginning of SPAR I furnace tests, separate runs with thermocouples inserted inside the ampoule and spot-welded to the outside cartridge wall indicated that cartridge and sample temperatures during heat-up and cool-down were within a few degrees C of each other. The thermal lag between cartridge and furnace control temperature during heat-up could be more than 50°C depending on the heating rate. During the cool-down, the cartridge temperature was actually decreasing at a higher rate than the furnace temperature because of immediate contact with the quenching helium gas.

Figure 7 is a plot of SPAR I flight test thermal and g-level profiles. References 1 and 2 had discussed in detail these profiles and their possible effects on the expected and unexpected microstructural features of the flight and three original GBT samples. Several significant observations relative to the profiles are summarized as follows:

- The thermal lag between cartridge (and therefore, sample) and furnace during heat-up was quite large; i.e., >100°C during the initial stage when the heat-up rate was approximately 10°C/sec.

- During quenched cool-down, the "interpolated" cartridge temperatures appeared to decrease ahead of furnace temperatures by as much as 10 sec.

- Post-flight analysis of the accelerometer data indicated g-level profile was indeed as plotted in the figure and g-levels $< 1 \times 10^{-3}$ g was maintained after Mg melted and before solidification started.

- Ground-based tests either using a separate furnace or the same flight furnace (after recovery) had essentially identical thermal profiles as the flight profile.

There were two furnaces in the SPAR II flight experiment assembly. The Aft Furnace was the SPAR I furnace, and its cavity No. 1 contained our test sample D-5 for the long soak ($\geq$180 sec). The second flight sample D-3 was contained in the cavity No. 3 of the Forward Furnace which had a designed temperature capability (to 1200°C) higher than the Aft Furnace. This second

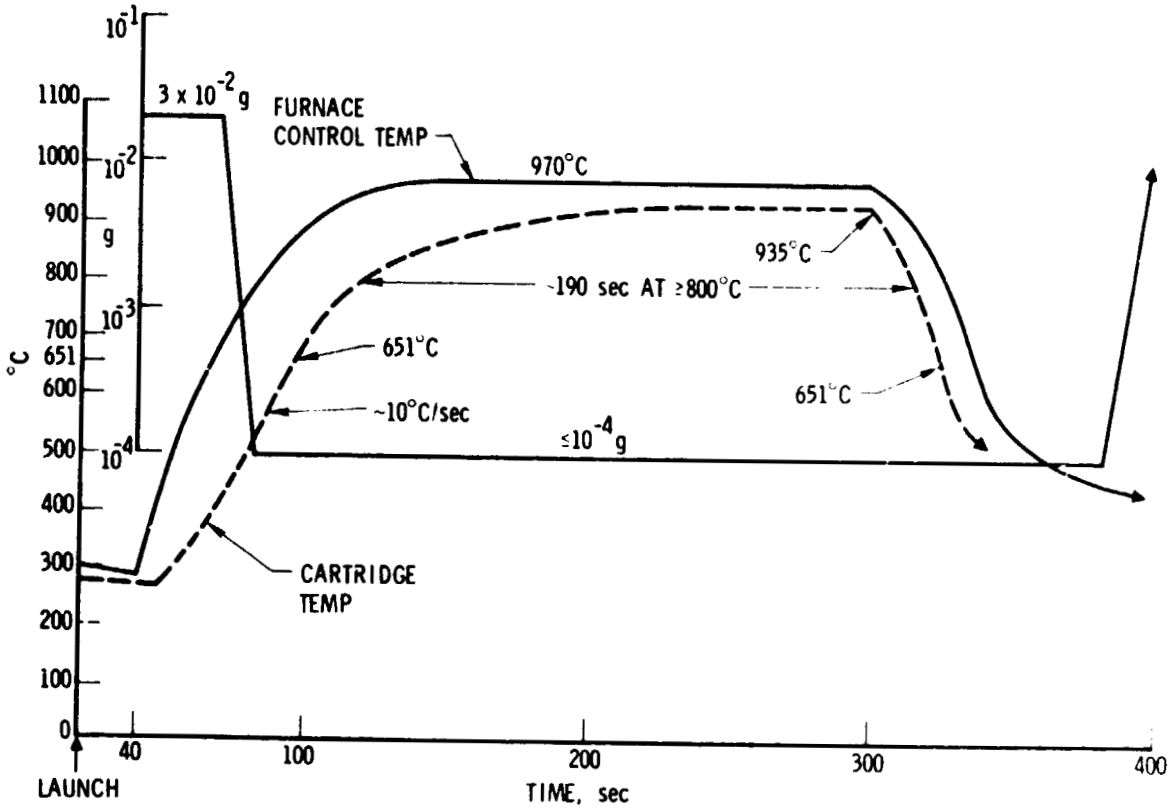


Figure 7. SPAR I flight test g-level and thermal profiles.

sample was to be soaked for approximately 60 sec at ≥ 800°C. Due to decreased output from the power source, the SPAR II Forward Furnace did not heat our sample to temperatures greater than 800°C (Fig. 8) in which the GBT thermal files were included for comparison. The Aft Furnace profiles for flight and GBT tests are respectively presented in Figures 9 and 10. As will be discussed later, the prelaunch temperature soak for SPAR II had been raised from approximately 300°C to 500°-600°C to yield a lower heat-up rate.

The g-level data for SPAR II flight test showed that our samples did not experience g-level $>1 \times 10^{-4}$ g between melting and solidification. For clarity reasons, the g-level profiles are not plotted in Figures 9 and 10.

The pertinent data of the SPAR II thermal profiles are summarized in Table 3. Important features of the profiles that will be significant items for later discussions are as follows:

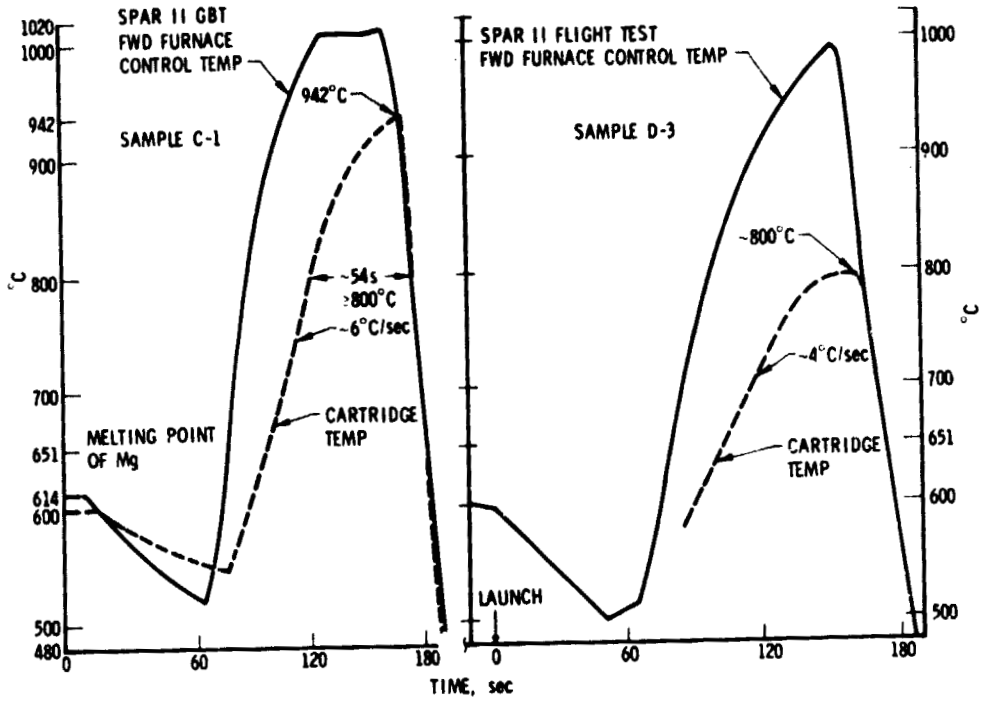


Figure 8. Comparison of short-soak SPAR II GBT and flight test thermal profiles.

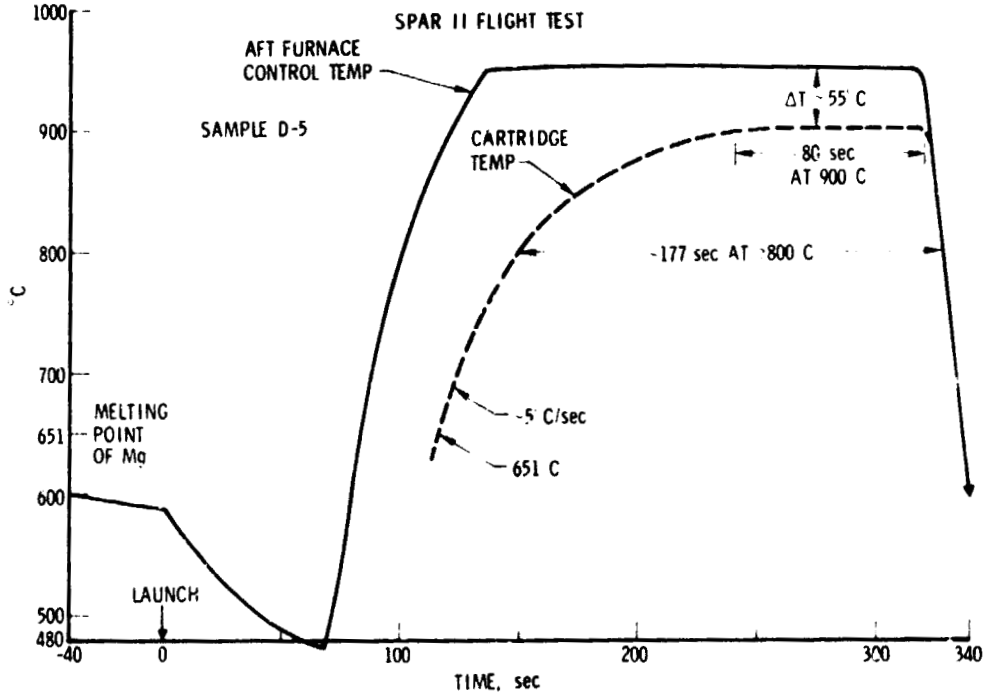


Figure 9. Long-soak SPAR II flight test furnace and cartridge thermal profiles.

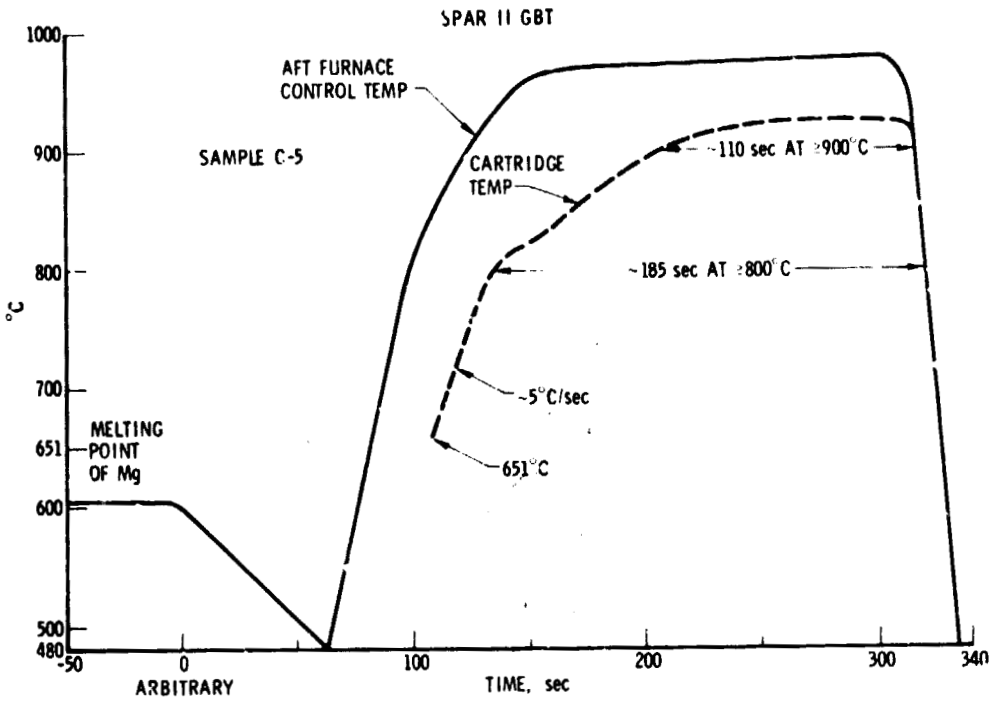


Figure 10. Long-soak SPAR II GBT furnace and cartridge thermal profiles.

TABLE 3. SUMMARY OF PERTINENT SPAR II THERMAL DATA

| | | Planned | Actual | |
|---|---|---|---|---|
| | | | GBT | Flight |
| Forward Furnace (Short-Soak) | Soak Duration at ≥ 800°C | ~60s | 54s | 0 |
| | Heat-up Rate | < 10°C/s | ~6°C/s | ~4°C/s |
| | Max. Cartridge Temp. During Soak | 900-950°C | 942°C | ~800°C |
| | Quench Rate | > 10°C/s | ~20°C/s | ~20°C/s |
| Aft Furnace (Long-Soak) | Soak Duration at ≥ 800°C | > 180s | ~185s | ~177s |
| | Heat-up Rate | < 10°C/s | ~5°C/s | ~5°C/s |
| | Max. Cartridge Temp. During Soak | 900-950°C | ~930°C | 900°C |
| | Quench Rate | > 10°C/s | ~20°C/s | ~20°C/s |

- In the flight and GBT tests, the short and long soak periods were shorter than originally programmed.
- The prelaunch temperature soaks were carried out as planned.
- The heat-up rates were significantly reduced as planned.
- The short-soak flight test in the Forward Furnace appeared to have failed, because the interpolated cartridge temperature had barely reached 800°C when quenching was initiated.

## EXPERIMENTAL RESULTS AND DISCUSSION

The results of characterizing SPAR II samples and the discussion and analysis of experimental findings, using certain specific SPAR I results for support, are the emphasis of this report.

Aside from the acquisition of actual experimental data, all observations and experience gained in the conduct of the first SPAR test by the investigators and the program management and engineering personnel had contributed significantly to the implementation of SPAR II test plans. Scheduling problems did arise because of unavoidable delays of the SPAR I flight, which resulted in the impossibility of making all the desired changes of SPAR II experiment parameters. Nevertheless, some changes recommended and executed did lead to favorable SPAR II results.

### Summary of SPAR I Results

The SPAR I experiment was intended to test the feasibility of low-g dispersion of physically introduced $ThO_2$ particles in a Mg matrix. The experimental results and analysis of the findings after the conclusion of the post-flight GBT test may be summarized as follows:

1. The low-g flight Sample G-1 (Fig. 11a) has no detectable internal porosity. All gas voids had been displaced by the melt and appeared as cavities along the graphite crucible walls. This phenomenon is considered as a beneficial effect of low-g when a liquid does not wet the wall.

ORIGINAL PAGE IS
OF POOR QUALITY

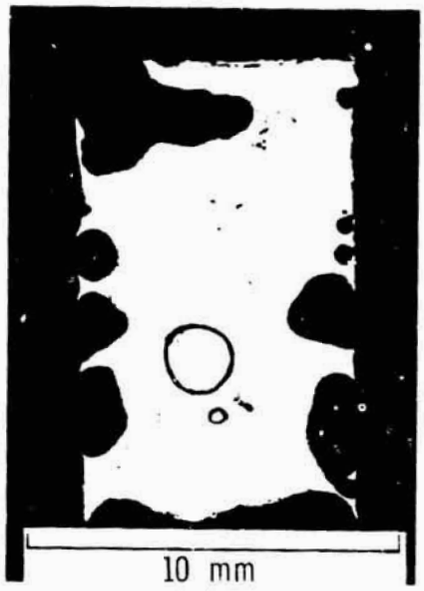


(a) SPAR I, FLIGHT G-1

(b) SPAR I, GBT G-2

(c) SPAR I, GBT H-6

Figure 11. Macrostructures of SPAR I flight and GBT sample sections.

2. The 1-g GBT Sample G-2 (Fig. 11b) retained the large shrinkage cavity and contained many small internal gas voids.

3. One GBT Sample (H-6) which was inadvertently cycled three times (Fig. 11c), and with the original argon-filled space (Fig. 3) on the bottom, showed evidence of excessive thermal agitation and the phenomena of gas voids staying within the melt.

4. The nonuniformly distributed layers of dispersion-depleted areas in all the 1-g samples were considered as gravity-induced sedimentation interrupted and agitated by convection currents and gas motions.

5. The presence of a few dispersion-depleted layers in the low-g sample was attributed to the possibility of g-levels greater than $1 \times 10^{-2}$ g during the initial stages of heat-up but after the sample had melted. (This postulate was later invalidated by careful analysis of the flight data.)

6. The large, near-spherical dispersion-depleted areas in the low-g sample, which were similar in outline to the gas voids in the 1-g sample H-6, were probably first caused by the thermoacoustic effects during rapid heat-up resulting in expanded gas pockets in the melt when it entered the quiescent soak stage. During soak, the gas was replaced by the molten Mg due to the latter's nonwettability with graphite wall. Filling of the gas voids was accelerated by surface tension-induced motion and was probably assisted by condensation of Mg vapor during cool-down. There was no microstructural evidence of directional solidification resulting in particle rejection or entrapment.

7. The $ThO_2$ particles in the low-g sample were more dispersed than in the 1-g sample, as shown by Figures 12a and 12b.

8. The dispersion-depleted areas in the low-g sample also contained $ThO_2$ particles outlining the small recrystallized Mg grains, as shown in Figure 12c. The dispersoids were identified as $ThO_2$ by ion microprobe mass analysis (IMMA). Figure 12d is the IMMA $ThO_2$ map covering both the dispersion-depleted and dense dispersion areas.

9. Particle size and distribution measurements made on the low-g sample G-2 yielded an average size of 0.76 $\mu$m and an average interparticle spacing of 1.44 $\mu$m.

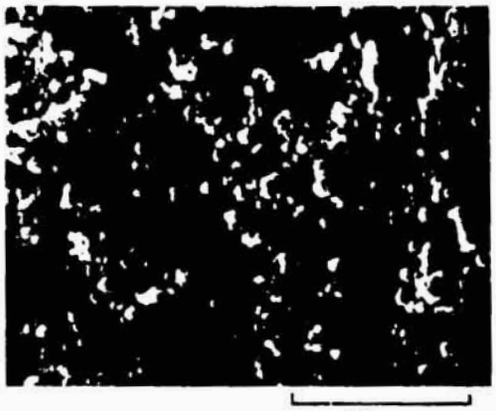


(a) LOW-g G-1 SHOWING DISPERSION OF $ThO_2$ PARTICLES

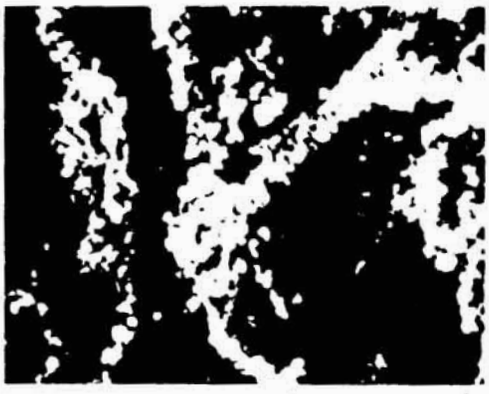


(b) ONE-g G-2 SHOWING SEGREGATED DISPERSION CLUSTERS

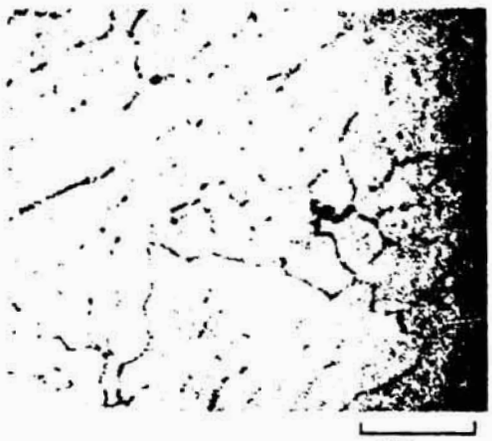


(c) LOW-g G-1 SHOWING $ThO_2$ PARTICLES IN DISPERSION-DEPLETED AREA

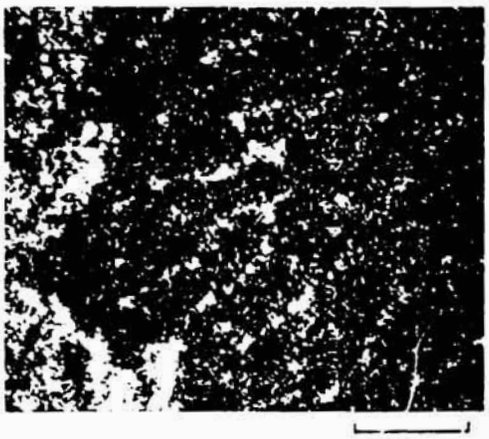


(d) IMMA $ThO_2$ MAP OF DENSE AND DISPERSION-DEPLETED AREA IN LOW-g G-1

Figure 12. Microstructures of SPAR I flight and GBT samples showing effects of gravity on dispersion and IMMA identification of dispersoids.

10. During the characterization of SPAR I samples, techniques of metallography, SEM, energy dispersive x-ray analysis (EDAX) and IMMA were refined. A modified microhardness measurement scheme was also developed, in which a 1.6-mm Brinell steel ball indentor was used with a 1000-g load in a Tukon $\mu$-hardness tester.

After analyzing the SPAR I results, specific recommendations were made for the SPAR II test. These first recommendations were later modified after compatibility with other furnace experiments were determined and the characteristics of the second furnace (Forward Furnace) were identified by a series of furnace tests. The final recommendations for SPAR II were represented by the planned thermal parameters in Table 3 and the requirement of low g levels ($\leq 1 \times 10^{-4}$) after melting and before solidification. These recommendations were intended to accomplish the following:

1. Higher prelaunch soak temperatures to insure a heat-up rate less than 10°C/ sec which in turn should minimize the thermoacoustic effects.

2. Avoid the occurrence of layered sedimentation in the flight sample by making sure that g-levels during the initial periods would be less than $1 \times 10^{-4}$ g.

3. Complete melting of the metal matrix, even for the short-soak, by programming the thermal cycle for a soak temperature in the 900°-950°C range, so that kinetics associated with the gettering-dispersion mechanism could be investigated.

## Microstructural Analysis of SPAR II Samples

The characterization steps presented in Figure 6 were carried out. In contrast to SPAR I, the metallographic samples of SPAR II were studied more extensively by EDAX and IMMA because the gettering mechanism was involved in the melting and solidification process. Microhardness measurement was used not only to compare the SPAR II samples with pure Mg and the remelted commercial alloy HK31A, but also to reveal uniformity in hardness of the low-g and 1-g samples.

## Macrostructures of the Low-g and 1-g Samples

The macrostructures of the long-soaked low-g and 1-g samples (D-5 and C-5) are shown in Figures 13a and 13b. Although the soak periods for the flight and GBT tests were shorter than originally planned (Table 3), complete melting and dispersion (and segregation) of reaction products had taken place. Except for two spherical gas voids near one end and a couple of small voids near the other end, the low-g sample was very sound. The 1-g counterpart, however, had numerous small, spheroidized pores throughout the casting in addition to several large voids.

The low-g sample again contained some dispersion-depleted layers as was observed with the SPAR I low-g sample. However, unlike the SPAR I low-g sample, large spherical dispersion-depleted areas were absent in the SPAR II low-g sample. The dispersion-depleted layers in the 1-g sample were more numerous and their orientation appeared to have been influenced by the large gas voids. There were also layered separations (cracks) in the 1-g sample.

As discussed previously and shown by the thermal profiles (Fig. 8), the short-soaked SPAR II flight and GBT samples never completely melted. Their macrostructures are shown in Figures 14a and 14b. In fact, the low-g sample D-3 appeared to have melted only in some areas near one end, and the numerous layered separations appeared to be "pressure-cracks" commonly observed in powder compacts with high residual stresses caused by pressing strokes. The 1-g counterpart of the short-soak process had evidence of more advanced melting, but it retained some cracks and several partially Mg-filled separations.

## Microstructure and Identification of Constituents

The long-soaked low-g sample had a higher degree of dispersion of particles than the 1-g counterpart. The SEM photos in Figure 15 represent a comparison of the dispersion in the two samples. The absence of unreacted MgO in the longitudinal sections of both the low-g and 1-g samples soaked for 175 and 135 sec respectively at $\geq 800°C$ was confirmed by IMMA. The dispersoids in the microstructures of both samples were identified as Th-containing particles and then determined as $ThO_2$ by IMMA. Figure 16 typifies an IMMA mapping sequence applied to one area in the long-soak low-g sample D-5. It should be noted that the Mg map was scanned with reduced gas ion current, and the brighter spots were due to topographic enhancement effects (e.g., surface irregularities).

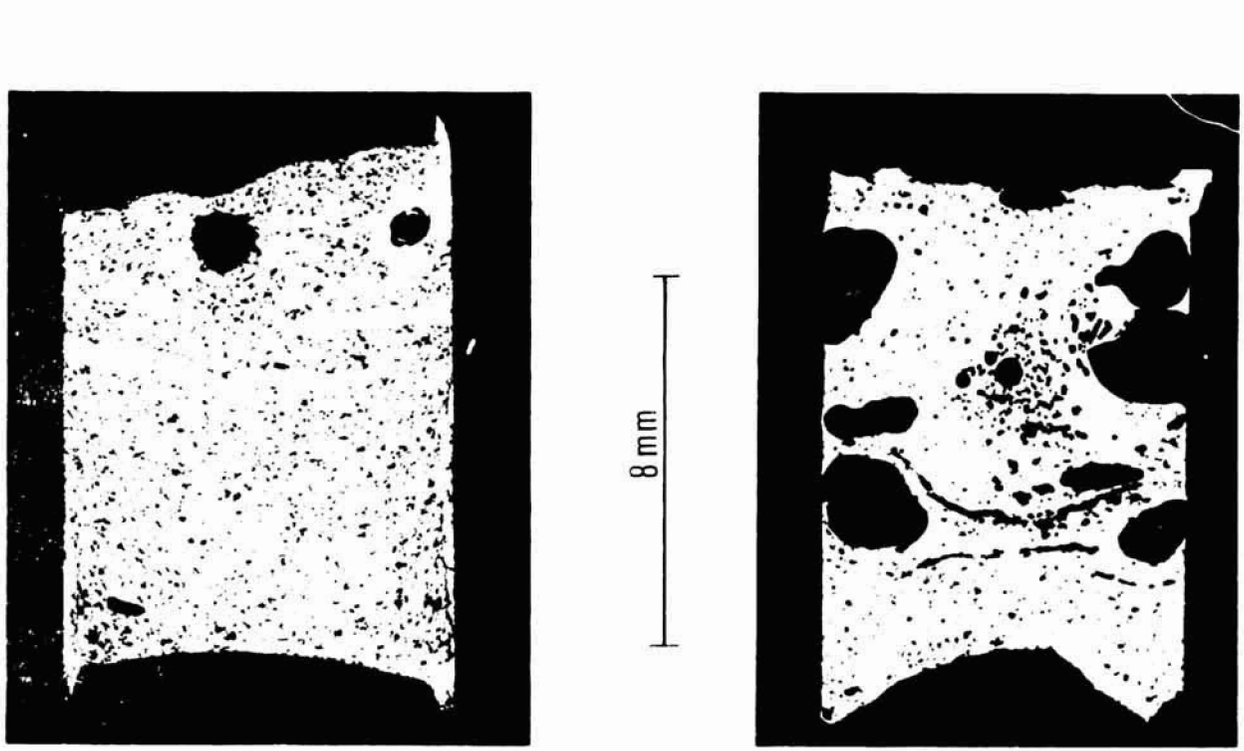


(a) LOW-g D-5, LONG-SOAK

(b) ONE-g C-5, LONG-SOAK

Figure 13. Comparison of macrostructures of SPAR II long-soak flight and GBT ingot sections.

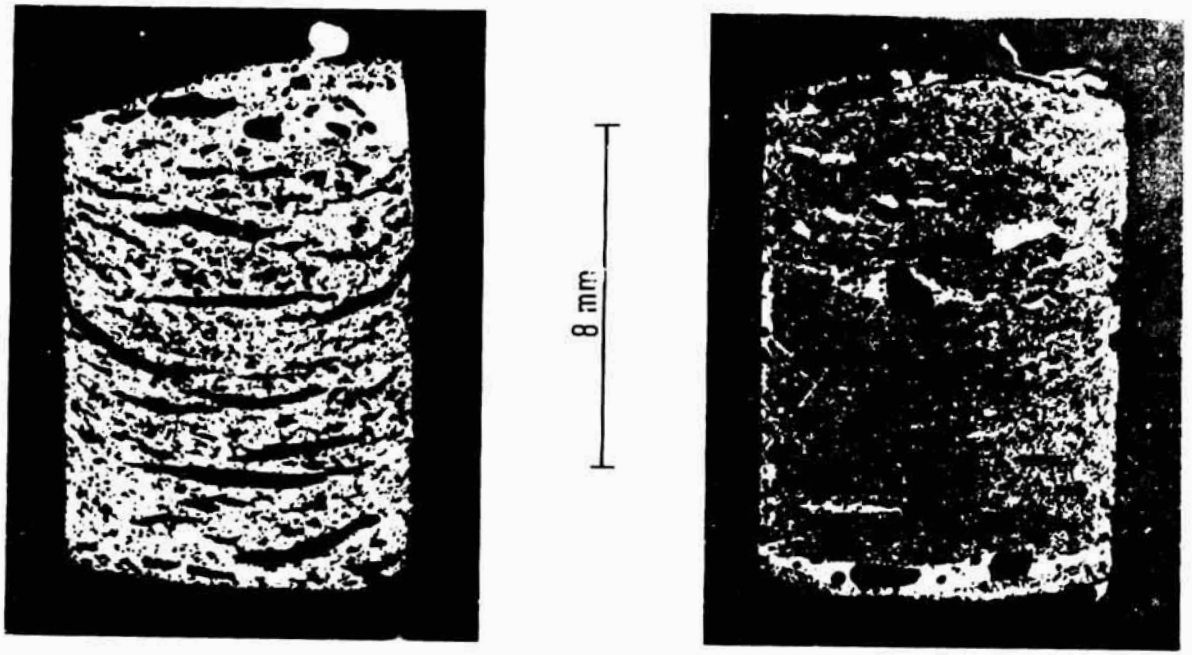


(a) UNDERHEATED LOW-g D-3, SHORT-SOAK

(b) ONE-g C-1, SHORT-SOAK

Figure 14. Macrostructures of SPAR II short-soak flight and GBT ingot sections showing partial melting and pressure cracks.



ORIGINAL PAGE IS
OF POOR QUALITY

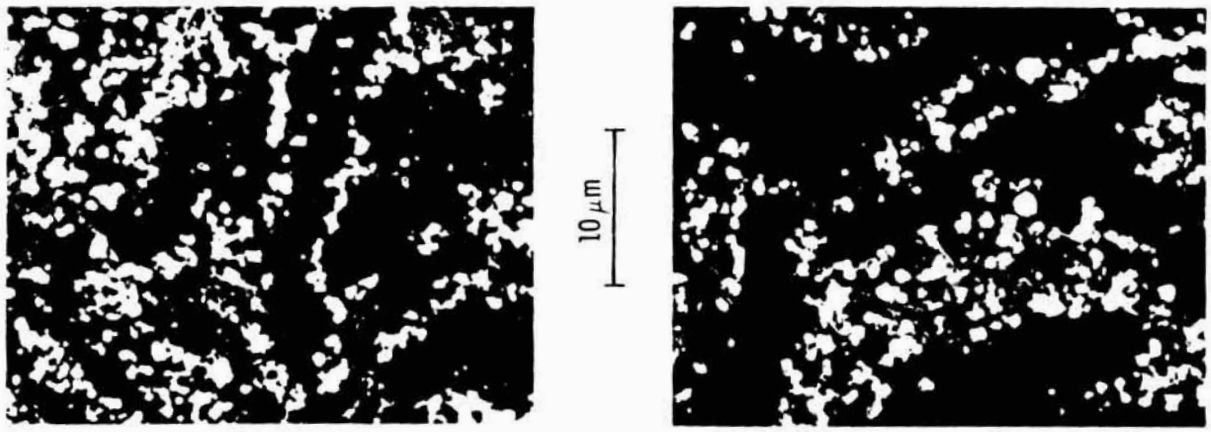


(a) LOW-g D-5 (b) ONE-g C-5

Figure 15. Microstructures of SPAR II long-soak flight and GBT samples showing distribution of dispersion.

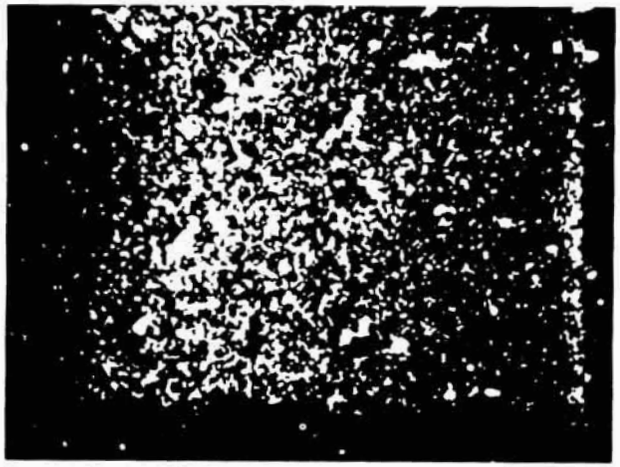

(a) Mg MAP 330X

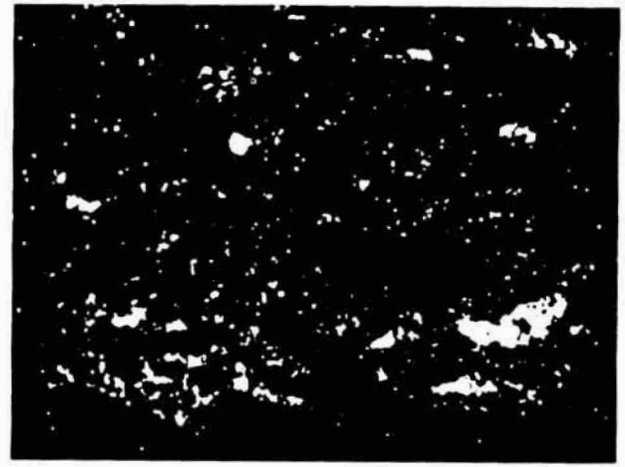

(b) Th MAP 330X

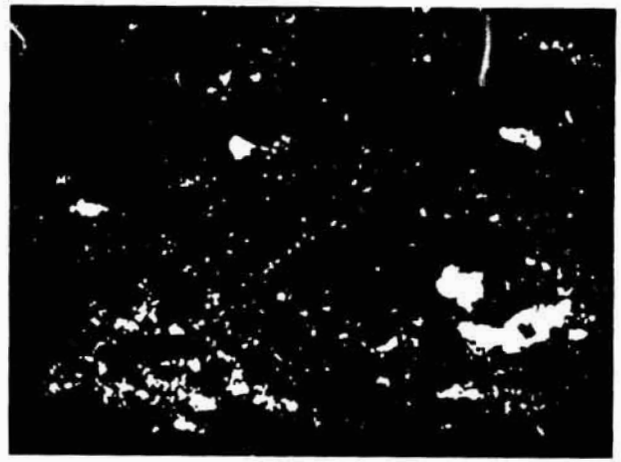

(c) $ThO_2$ MAP 330X

Figure 16. Identification of constituents in the microstructure of SPAR II long-soak sample D-5 by IMMA.



ORIGINAL PAGE IS
OF POOR QUALITY

The short-soak low-g sample D-3 which was heated only to 800°C had generally a microstructure not unlike that of the as-pressed compact [2] or some partially melted laboratory samples. Figure 17a shows the typical microstructure of D-3 which contained nonreacted MgO and Th particles or agglomerates, as well as voids and partially melted Mg grains. Figure 17b is an IMMA map for MgO. Figures 17c and 17d are respectively the SEM photograph and EDAX map showing an agglomerate of unreacted Th metal.

Because of higher soak temperature (800°-942°C), the short-soak 1-g sample C-1 showed evidence of achieving the gettering reaction. The segregation of partially reacted agglomerations was quite severe in the sample. Figure 18a is a 1000X SEM photo of the microstructure of C-1 showing segregations and evidence of reaction that had taken place at the MgO sites. Figure 18b is an IMMA map for the oxide of Th from an area similar to that of Figure 18a. It should be mentioned that IMMA spectrum and mapping indicated presence of $ThO_2$ and ThO. However, ThO could be the result of dissociation of $ThO_2$ in the plasma.

The presence of the reaction product $ThO_2$ was also verified by high magnification SEM. Figures 19a and 19b show the SEM photographs of the dispersoids in the low-g sample D-5 showing the crystal structure of $ThO_2$ precipitate similar to that of the $ThO_2$ powder particles in Figure 2. Th crystals were also found in the 1-g sample C-5, as shown in Figure 19c.

As observed in SPAR I, there was no evidence of particle rejection due to directional solidification. The freezing rate was too great for piling-up of dispersoids to occur during quenching.

Particle Size and Distribution in the Dispersion

Scanning electron photomicrographs at 1000X magnification of representative areas of the long-soak flight and GBT sample were used in the measurement of particle size and distribution. The typical frequency histograms for the counted particles in the two samples are shown in Figure 20. The average particle size and interparticle spacing for the low-g sample are respectively 0.58 $\mu$m and 2.7 $\mu$m, and for the 1-g sample, 0.57 $\mu$m and 2.2 $\mu$m. These values may be compared with those for the SPAR I flight sample, i.e., 0.76 $\mu$m and 1.44 $\mu$m.

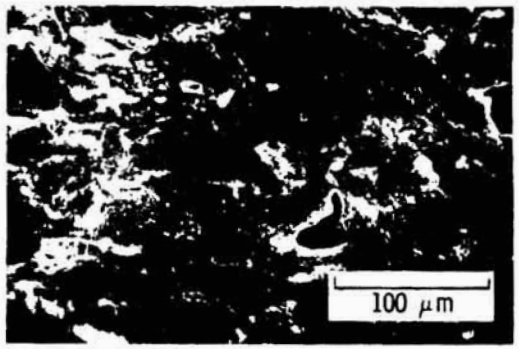


(a) LOW-g D-3,
UNDERHEATED MICROSTRUCTURE SHOWING VOIDS AND UNREACTED MgO AND Th

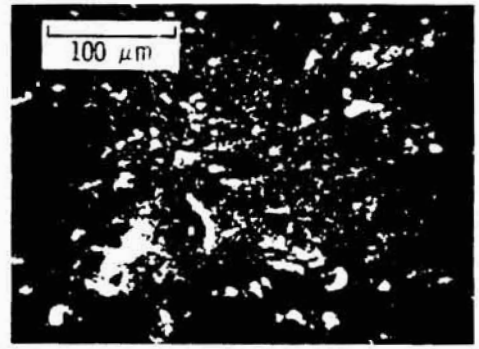


(b) IMMA MgO MAP,
IDENTIFICATION OF UNREACTED MgO IN THE UNDERHEATED LOW-q SAMPLE D-3

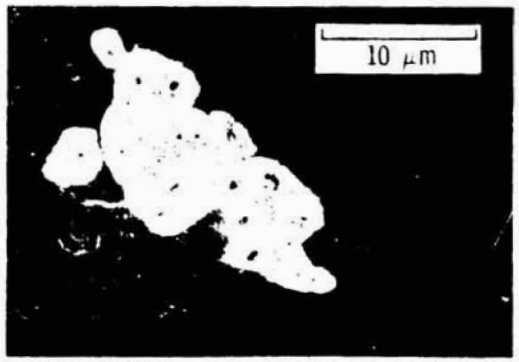


(c) UNREACTED Th PARTICLES IN UNDERHEATED D-3

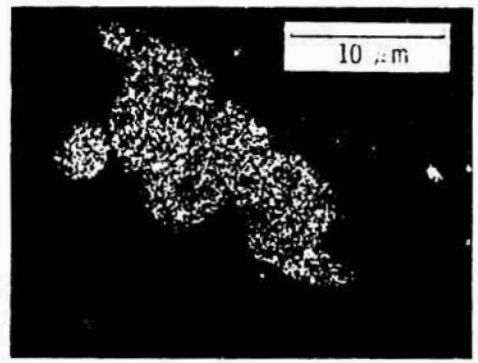


(d) SEM/EDAX MAP IDENTIFYING UNREACTED Th PARTICLES IN D-3

Figure 17. Microstructure of underheated short-soak SPAR II flight sample D-3 and identification of unreacted MgO and Th particles.



ORIGINAL PAGE IS
OF POOR QUALITY

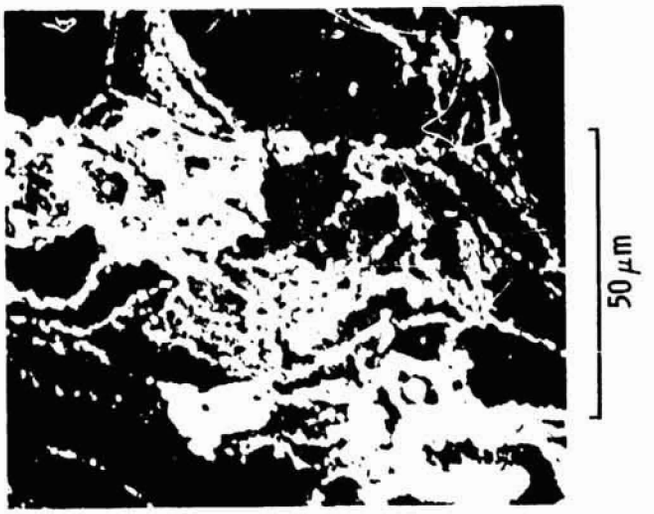


(a) MICROSTRUCTURE OF SHORT-SOAK GBT C-1 SHOWING INTERRUPTED GETTERING REACTION AT MgO SITES AND DISPERSION OF PRECIPITATES

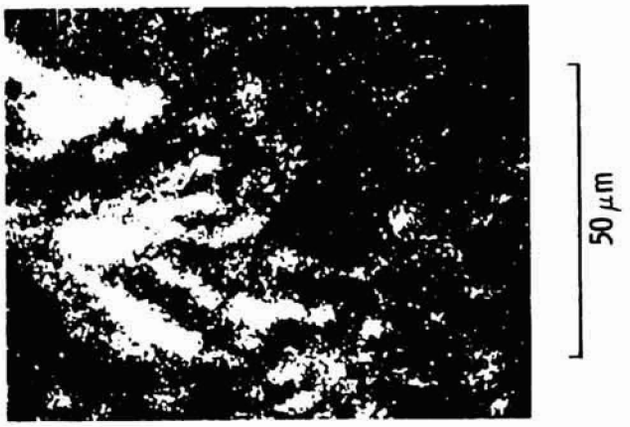


(b) IMMA MAP OF SHORT-SOAK GBT C-1 SHOWING SEGREGATION AND DISPERSION OF $ThO_2$ PARTICLES AFTER GETTERING

Figure 18. Microstructure and IMMA $ThO_2$ map of SPAR II short-soak GBT sample C-1.

ORIGINAL PAGE IS
OF POOR QUALITY

ORIGINAL PAGE IS
OF POOR QUALITY




Figure 19. Precipitated crystals within $ThO_2$ "particles" in SPAR II long-soak flight and GBT samples.

It is our belief that we were not measuring the true particle size of the reaction-precipitates. For example, Figure 19b shows an agglomerate at 30,000X, the overall size of which is approximately 1 $\mu$m. However, the agglomerate appears to be composed of several $ThO_2$ crystals some of which may be as small as 0.1 $\mu$m. This phenomenon of dispersion and segregation will be analyzed later.

If we were to disregard the inability to resolve crystallites within the small agglomerates and to count sizes smaller than 0.2 $\mu$m from the photomicrographs, the histograms in Figure 20 suggest a Gaussian-type of distribution which is to be expected of a reaction-precipitation process.

Microhardness and Uniformity in Dispersion Hardening

Since we had only a limited number of samples which were all small in size, the microhardness measurement was considered as the tool to use for the determination and comparison of gravity effects on dispersion strengthening. The modified technique of microhardness determination developed during SPAR I investigations was used extensively on various SPAR II samples. The commercial Mg-Th-Zr alloy HK31A and pure Mg were also measured for comparison. To have a valid comparison, the HK31A and pure Mg were also encapsulated and thermally cycled.

Microhardness readings were taken on polished longitudinal sections of the samples. Depending on the section size, a grid system with a point-to-point distance of 0.8 mm would provide more than 120 readings. Since the specimens were metallographically mounted, voids and cracks would produce a hardness reading of the cured epoxy which were softer than Mg and also easily distinguished optically. Figures 21A and 21B are respectively the microhardness topographs for the long-soak SPAR II flight sample D-5 and its 1-g counterpart C-5. The measurements plotted are the Filar units (or diameters of the indentations) which are inversely proportional to hardness. By including the voids in the plot, the comparison of these samples clearly shows the superiority of low-g samples in terms of soundness of the casting and uniformity in hardness.

Similar topographs for the short-soak SPAR II flight sample D-3 and GBT sample C-1 were also constructed and shown in Figures 22a and 22b. As previously mentioned, these two samples were at best only partially melted with the flight sample actually "under-heated." The two hardness topographs are presented for the purpose of demonstrating the use of this technique for visual representation of unsound castings.

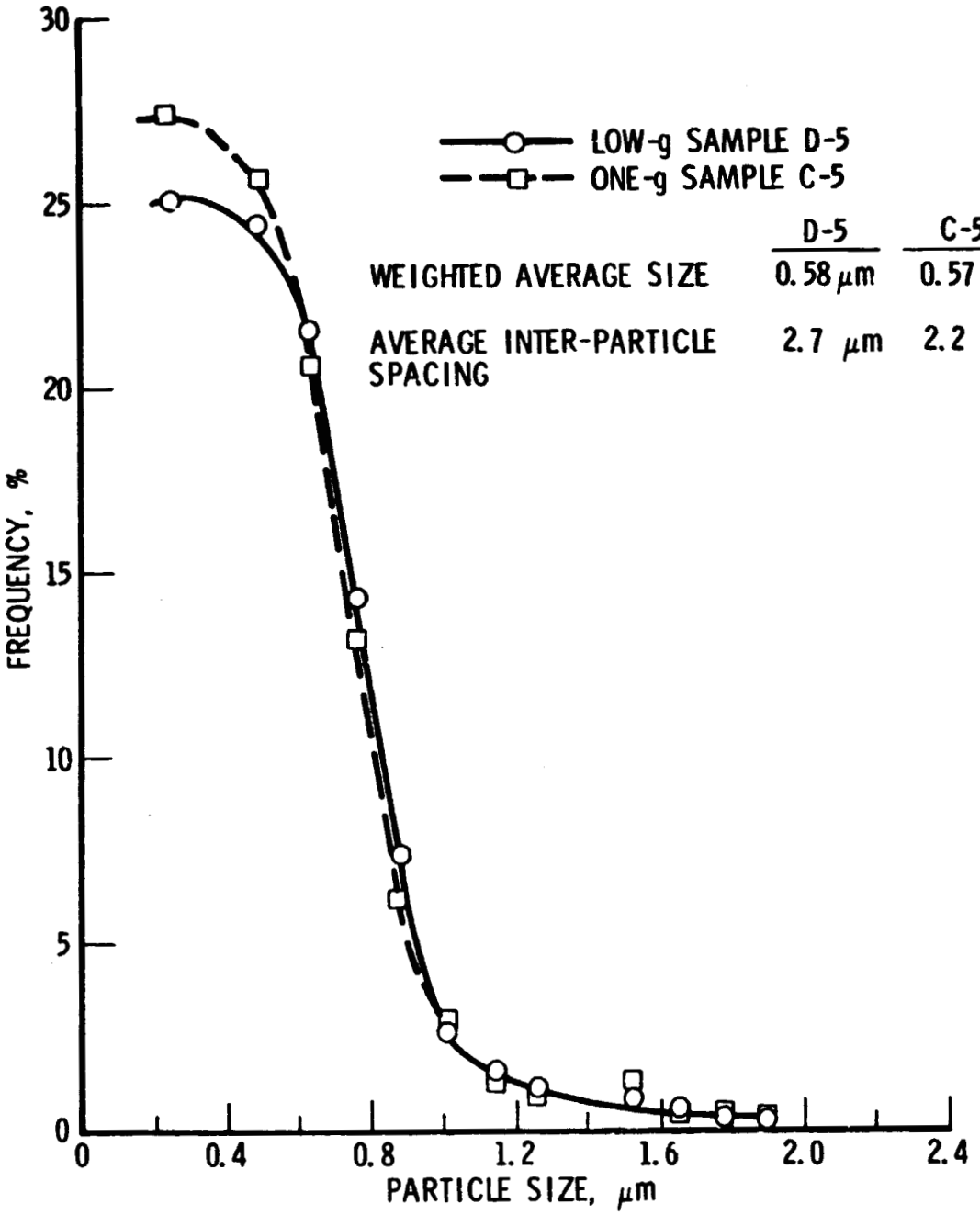


Figure 20. Histograms of particle size distribution in SPAR II long-soak flight and GBT samples.

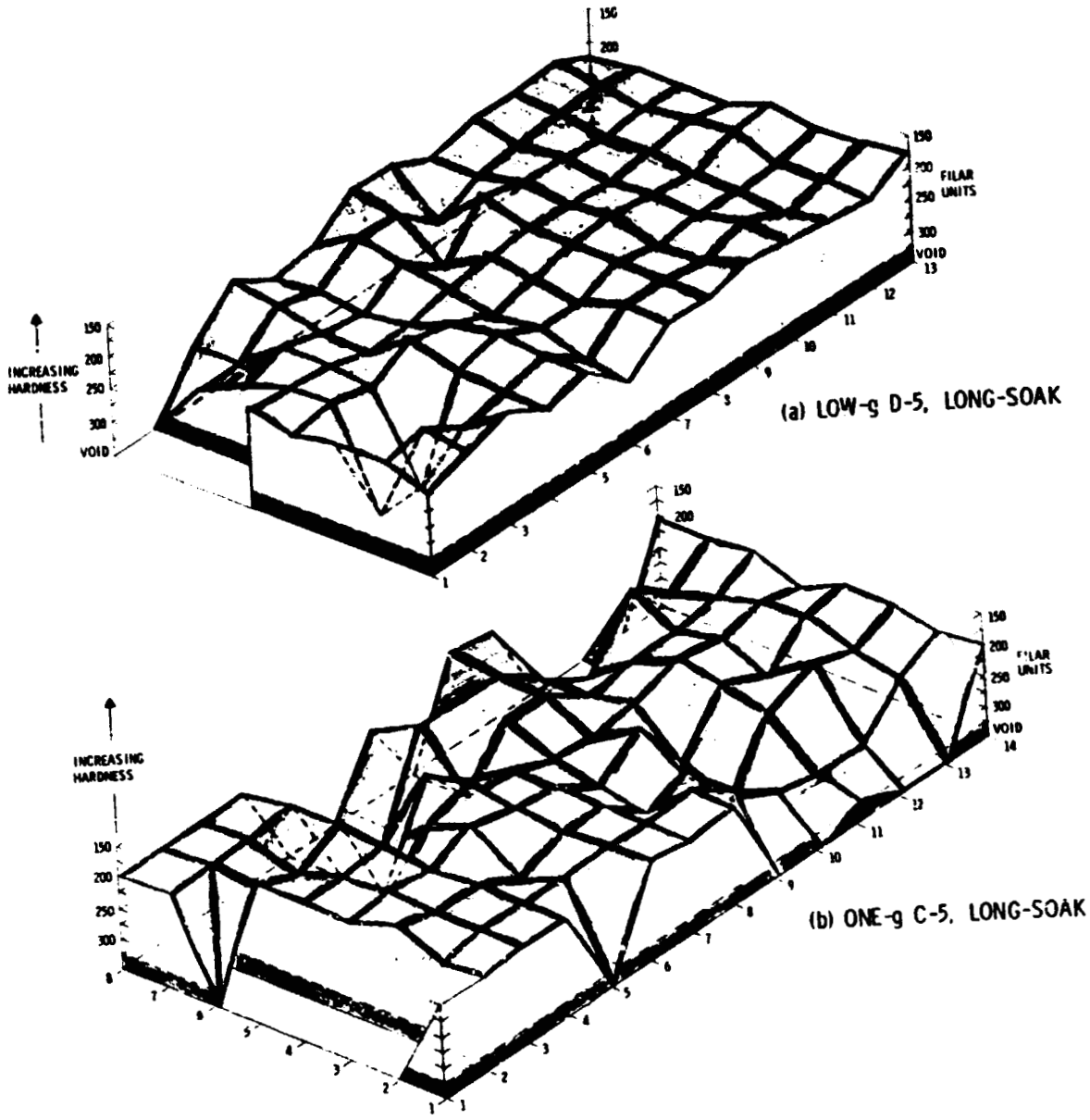


Figure 21. Microhardness topographs of long-soak SPAR II flight and GBT sample sections.

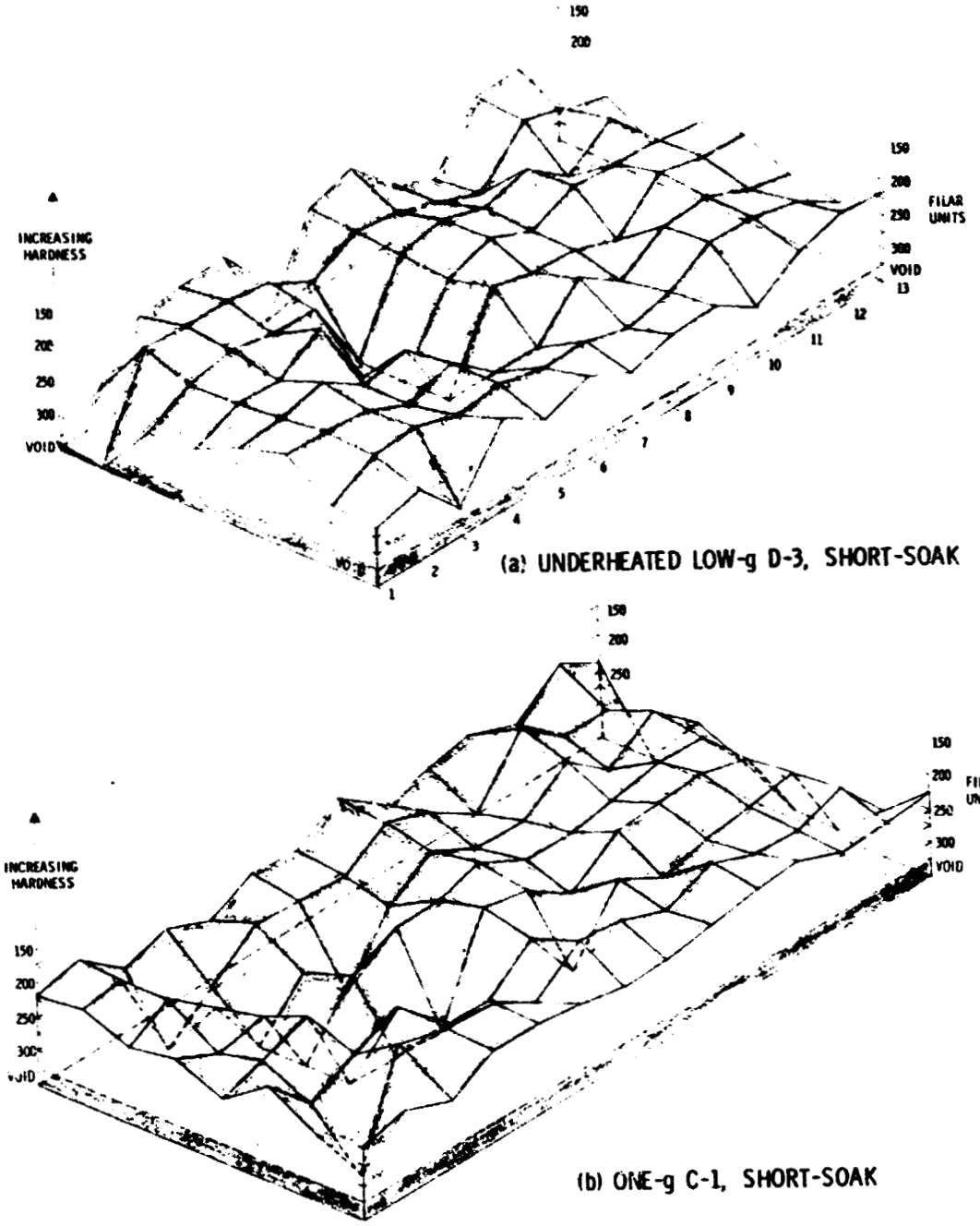


Figure 22. Microhardness topographs of underheated SPAR II flight and short-soak GBT sample sections.

The hardness readings for the epoxy-filled voids and cracks were disregarded in the comparison of hardness of four samples, namely low-g D-5, 1-g C-5, remelted HK31A alloy, and remelted pure Mg. In units of "modified Brinell" hardness, the measurements and the calculated standard deviations for the four samples are as follows.

SPAR II low-g sample (Mg + 2 v/o $ThO_2$): 31.1 ± 3.0

SPAR II 1-g sample (Mg + 2 v/o $ThO_2$): 21.0 ± 6.6

Commercial HK31A alloy (Mg + 3 Th + 1 Zr): 23.1 ± 2.9

Pure Mg: 13.7 ± 1.3

The above-listed values show that given identical thermal treatment, the low-g reaction-dispersion strengthened sample has higher hardness than either its 1-g counterpart or the commercial alloy. The lower hardness of the 1-g sample also represents nonuniformity in dispersion with segregation of dispersoids and higher percentage of dispersion-depleted areas. The commercial alloy HK31A can be further hardened by cold working. Unfortunately, a comparison of work-hardened materials could not be made because we did not have large enough experimental samples for mechanical and thermal treatments. It is also important to remember that retention of strength (or hardness) at elevated temperatures is what one looks for in the dispersion-strengthened metals, in addition to initial as-cast or wrought properties.

## Analysis of SPAR II Results

### The Gettering-Dispersion Mechanism

Experimental results have confirmed the postulated mechanism as expressed by the chemical reaction

$$2\,MgO + Th \rightarrow ThO_2 + Mg$$

and are consistent with the consideration based on calculated free energy values of the two oxides. There was also evidence that the particle size of the Th precipitates may be as small as 0.1 $\mu$m (Fig. 19). The particle size determination at a magnification of 1000X was only able to detect small agglomerates

of $ThO_2$ crystals. In low-g experiments involving oxygen as the "interstitials," such as $O_2$ in titanium, the formation of agglomerates of refractory oxide precipitates should not occur.

The previous discussion on the diffusion of Th in molten Mg to the MgO sites can be used to account for the formation of $ThO_2$ agglomerates. It appears that during the short-duration quiescent soak at low-g, the natural convection forces due to concentration gradients were not sufficient to break up the small agglomerates. At 1-g, although sedimentation on a macro scale was not observed, the segregation of the agglomerates was evident, as revealed by the microstructural study and the microhardness measurement.

The phenomenon of hardening (or strengthening) of Mg by particle dispersion has been observed in this experiment. Under identical processing conditions, the data show that the low-g sample has an average microhardness more than twice that of Mg and 35 percent higher than the precipitation-hardenable commercial Mg-Th-Zr alloy. The lower hardness of the low-g sample (approximately equivalent to the commercial alloy) has been attributed to gravity effects on the segregation of dispersoids with more dispersion-depleted areas. The most beneficial effect of low-g processing is the enhanced uniformity in hardening as illustrated by the hardness topography in Figure 21. Uniformity in property can also be deduced from the calculated standard deviations. With 20 measurement points (voids not included), the $\sigma$ value for the 1-g sample is more than twice that for the low-g sample.

The objective of studying the time dependency of the reaction-precipitation mechanism was not achieved. The 1-g and low-g samples for the short-soak had only undergone partial melting. Flight furnace data indicated that the low-g sample was not heated above 800°C an the IMMA analysis showed that MgO was not reacted. Nevertheless, these two short-soak samples, which contained numerous expanded pressure cracks, provided an explanation for the presence of dispersion-depleted layers in the SPAR I and SPAR II samples.

Low-g Effects on Soundness of Casting

In a contained gas/metal system when the molten metal does not wet the container wall, experimental evidence indicates that at low-g the diffusion of gas to the wall coupled with movement of the melt away from the wall can contribute to the soundness of the casting. At 1-g, gas will either be trapped or

float upwards, depending on the equilibrium attained at the instant of solidification of the casting, as evidenced by all the 1-g samples which showed numerous internal voids and shrinkage cavities.

The motion of expanded gasses at 1-g also contributed to uncontrollable segregation of the dispersoids. Large deviations from the Stokes Law for density-induced sedimentation can be expected because of the excessive agitation of the melt. We have observed this type of uncontrollable phenomenon with all the SPAR I and SPAR II GBT samples.

In future space processing and manufacturing, not all end-products can be produced under containerless conditions. Certain geometric controls must be applied to the metallurgical processes in space, so that materials produced in space will have sizes and shapes suitable for subsequent fabrication on Earth. High vapor pressures of the materials may also require a pressurized system in space processing. It is therefore our belief that investigations of low-g effects on gas/metal/container systems are warranted.

Dispersion-Depletion and Pore Filling

The observation of "pressure cracks" in the under-heated low-g and 1-g samples explains the presence of dispersion-depleted layers in other completely melted and solidified samples. However, it does not explain the dispersion-depleted spheres in the SPAR I low-g sample. The thermoacoustic effect was used to explain the "arrest" of expanded gas spheres prior to reaching the quiescent soak stage and subsequent pore filling by Mg. The previous discussion on thermoacoustic effects was intuitive in nature because the experiment was not designed to provide definable boundary conditions for analysis. Nevertheless, the effects due to rapid heating led to the reduction in heat-up rate from 10°C/sec to 5°C/sec for SPAR II. Although we had only one low-g sample for examination, the absence of dispersion-depleted spheres in the interior of the SPAR II low-g sample does suggest that our reasoning may be valid.

It should be mentioned that the longitudinal section of low-g sample D-5 shown in Figure 13a was repolished for microhardness testing. After the removal of some material, the larger spherical void near the "top" center of the sample opened up to the top surface. It is our belief that if given a longer soak time, this particular gas void would have disappeared completely via the mechanism of liquid/wall nonwettability previously discussed. The same mechanism would suggest the continued movement of the few smaller gas voids to the side wall with a longer soak time.

We have proposed for pore filling the mechanism of Mg diffusion and possible condensation of Mg vapors as the trapped gas diffuses to the walls at low-g or shrinks in volume during cooling at either low-g or 1-g. The fact that dispersion-depleted areas contained fine Th particles suggests a diffusion process involving comparatively lower-viscosity liquid replacing the escaping or shrinking gases. The surface tension variations (the Marangoni effect) could also contribute to the diffusion process; however, the condensation of Mg vapor during cooling cannot be ruled out as a contributing factor in pore filling. The rate of evaporation, $R_E$ in g/sec/cm$^2$, of a metal may be estimated by applying the Langmuir expression,

$$R_E = P(M/T)^{1/2}/17.14 \qquad (5)$$

where P is the vapor pressure in torr, M is the molecular weight of the species and T is temperature in K. If we consider one of the larger (~1.6 mm in diameter) dispersion-depleted spheres in the SPAR I low-g sample (Fig. 11a) and neglect the argon gas pressure at 900°C with an Mg vapor pressure of 100 torr, approximately 0.04 g of Mg will evaporate away from the surrounding molten metal in 100 sec. Therefore, with a continuous supply of Mg from the melt, condensation of vaporized Mg upon cooling will be theoretically sufficient to fill the cavity. The actual situation is quite complicated because within the crucible confinement, vaporization rate of Mg will be greatly reduced by the argon pressure until cooling starts.

Sample Preparation Considerations

The original contention that hot pressing would counter the tendency of forming pressure cracks was obviously in error in this case. In normal powder metallurgy practices, pressure cracks can "heal" during subsequent sintering in a flowing atmosphere or under vacuum. In our experiment, the argon atmosphere and sample were confined, the thermal cycle was short, and heat-up rates were high. Furthermore, crack healing and pore filling, as occurred in our samples, only contributed to the nonuniform distribution of dispersoids.

It is our belief that in experiments of this type, when the constituents must be introduced by powder metallurgy methods to insure having uniform starting materials before melting, the technique of isostatic compaction followed by vacuum presintering prior to sample encapsulation should be used.

The intentional introduction of MgO powder for this gettering-dispersion experiment was to control the amount of oxygen. Since the feasibility of casting dispersion-strengthening at low-g has now been established, future space experiments in which the constituents to be gettered can be introduced as dispersed phases (e.g. oxygen interstitials in titanium or nitrogen in columbium) should lead to optimum fine-particle strengthening.

## CONCLUSIONS

Table 4 is a tabulation of observed gravity effects as a comparison between low-g and 1-g SPAR II samples. The experimental results of this experiment series have led to the following conclusions:

1. Low-g melting and solidification of particle-dispersed metal matrices in a gas-filled encapsulated system is feasible. When the crucible is not wetted by the molten metal, sound ingots with no internal pores can be obtained.

2. The gettering-dispersion mechanism can be utilized to cast composites which are difficult to do on Earth. Segregation of dispersoids due to density differences can be reduced or avoided by processing in space.

3. On the basis of microhardness measurements, the SPAR II low-g processed Mg-$ThO_2$ sample is much more uniform in property than the 1-g counterpart. The average hardness of the low-g sample is twice that of pure Mg and is 30 percent greater than the 1-g sample and the commercial Mg-Th-Zr (HK31A) alloy similarly thermal-cycled.

4. The short-duration of low-g achievable in SPAR flights can be utilized to conduct furnace experiments at elevated temperatures, provided time-dependent mechanisms and rates of heating and cooling do not complicate the experimental observations.

5. Sample preparation techniques are of paramount importance, especially when apparatus constraints and the characteristics of interfacing between sample, container, and the furnace may present problems not normally encountered in an Earth laboratory.

TABLE 4. SUMMARY OF OBSERVED GRAVITY EFFECTS ON SPAR II SAMPLES

| | Low-g | One-g |
|---|---|---|
| Gettering Reaction | Complete | Complete |
| Ingot Soundness | Sound | Porous |
| Average Size of Dispersoids | 0.5 - 0.6μm | 0.5 - 0.6μm |
| Segregation of Dispersoids | Moderate | Severe |
| % Area with Sufficient Dispersion | ~90 | ~50 |
| Modified Brinell Microhardness | 31.1 ± 3.0 | 21.0 ± 6.6 |
| Uniformity in Hardness | Uniform | Highly Non-uniform |

6. Known principles or theories pertaining to physical and chemical phenomena, rate processes, or phase equilibria can only be used as a rough guide at this embryonic stage of space processing technology.

7. Past model space experiments involving nonreacting substances and oversimplified process parameters do not necessarily offer results or observations applicable to metallurgical experiments requiring high thermal energies. This experiment with Mg and $ThO_2$, in principle, approaches the meeting of requirements for a model experiment for future metallurgical experiments of dispersion-strengthening at low-g.

## RECOMMENDATIONS

On the basis of our experimental observations and from our points of view, the following recommendations are offered:

1. Particle-dispersion phenomena which are associated with immiscible material systems should be a metallurgical area for continuing space processing experimentation.

2. The next experiments involving the mechanism of gettering-dispersion should logically be the introduction of initially dispersed to-be-gettered constituents, such as oxygen and nitrogen, in the elemental or molecular form, the amount of which can be controlled.

3. Future space processing investigations should allow for sufficient lead time for adequate preparatory work and must have continuity with sufficient time for making use of results of the preceding experiment.

4. In the area of melting and solidification at low-g, reexamination of physical principles should be an important aspect of the space processing technology, but any theoretical or laboratory supporting research must embody premises derived from observations made by already completed space experiments.

## REFERENCES


1. Raymond, L. and Ang, C. Y., "Casting Dispersion-Strengthened Composites at Zero Gravity," Post-Flight No. 1 Preliminary Technical Report, NAS 8-3159, Aerospace Corporation, December 1975.

2. Raymond, L. and Ang, C. Y., "Casting Dispersion-Strengthened Composites at Zero Gravity," Post-Flight Te nical Report, NAS 8-31539, Aerospace Corporation, March 1976.

3. Bunshah, R. F. and Goetzel, C. G., "A Survey of Dispersion Strengthening of Metals and Alloys," WADC Technical Report 59-414, AD-237146 (1960).

4. Ansell, G. S., Cooper, T. D., and Lenel, F. V., editors, "Oxide Dispersion Strengthening," Vol. 47 of Metallurgical Society Conferences, Gordon and Breach, N. Y. (1968).

5. Grant, N. J., "A Look at Dispersion Strengthening by Powder Metallurgy Methods," Progress in Powder Metallurgy, Vol. 16, Proc. 16th Ann. Mtg. MPI, Chicago, April 1960.

6. Easterline, K. E., et al, "The Particle-to-Matrix Bond in Dispersion-Hardened Austenitic and Ferritic Iron Alloys," Powder Metallurgy, Vol. 16 (1973).

7. Ang, C. Y. and Lacy, L. L., "Monotectic and Syntectic Alloys," Apollo-Soyuz Test Project, Preliminary Science Report, NASA TM X-58173, February 1976.

8. Stokes, G. G., Mathematical and Physical Papers (1901).

9. Grodzka, P. G. and Barnnister, T. C., "Natural Convection in Low-g Environment," Paper No. 74-156, AIAA 12th Aerospace Sciences Mtg. (1974).

10. Reynolds, W. C., "Behavior of Liquids in Free Fall," J. of Aerospace Sciences, December 1959.

11. Spradley, L. W., "Thermoacoustic Convection of Fluids in Low Gravity," Paper No. 74-76, AIAA 12th Aerospace Sciences Mtg. (1974).

12. Bird, R. B., et al, Transport Phenomena, Chapter 10, John Wiley & Sons, N. Y. (1960).

13. Uhlmann, D. R., Chalmers, G. and Jackson, K. A., "Interaction Between Particles and a Solid-Liquid Interface," J. Applied Physics, Vol. 35, October 1964.

CHAPTER VIII

# SEGREGATION AND SOLIDIFICATION OF LIQUID ALUMINUM-INDIUM ALLOYS UNDER ZERO-GRAVITY CONDITIONS*

By

Dr. Karl Löhberg and V. Dietl

Institute for Metal Research/Metal Sciences
of the Technical University of Berlin

and

Dr. Hans Ahlborn

University of Hamburg

*Translated from German

## INTRODUCTION

Melts of an alloy system with miscibility gap in the liquid state, when homogeneous at high temperatures, should exhibit different separation mechanisms when entering the miscibility gap during the cooling process, depending on whether the separation starts within or outside the range of spinodal decomposition. Even alloys with a noncritical composition are capable of spinodal separation, if the binodal temperature is undercooled to the spinodal temperature. The spinodal separation is characterized by spontaneous decomposition of the melt without any nucleation leading to extremely fine and uniform dispersion of the two phases. Under zero-g conditions and at high cooling rates, there should be neither a segregation of the two phases nor an essential coalescence of the droplets of the two melts, and for this reason the experiment was expected to provide an answer to the question whether alloys of different compositions exhibit different structures depending on the separation mechanism.

The aluminum-indium (Al-In) alloys proposed for this experiment show marked differences in the density of the Al-rich and the In-rich melt. As a further advantage the critical temperature of the miscibility gap is approximately 830°C, which means that homogeneous melts can be produced in the furnace available aboard the Black Brant VC rocket.

Consistent with the objective of the experiment, two alloy compositions were chosen, i.e., an alloy with critical composition — called alloy 60/40 — and an alloy with 89 a/o aluminum and 11 a/o indium — called alloy 89/11. The alloy with critical composition (60/40) was selected to ensure spinodal decomposition even if there is no undercooling. In addition to the flight experiment, some laboratory experiments were conducted — some of them before and some after the rocket flight on 17 May 1976 — which will be dealt with first.

## PREFLIGHT TESTS AND ANALYTICAL EXPERIMENTS

The preflight tests were conducted to serve several objectives. First, it was to be checked whether the phase diagram published by Predel [1] is of sufficient accuracy concerning the critical temperature and the critical composition. Second, it was indispensable to determine the holding times for the molten alloys above the critical temperature which assured complete homogenization of the melts prior to their cooling. Furthermore, it had to be investigated which crucible material was sufficiently inert towards the Al-In melts and which



PRECEDING PAGE BLANK NOT FILMED

crucible sealing material was most suited. Finally, the metallographic examination methods (grinding, polishing, and etching) to be used had to be verified in preliminary tests to avoid unnecessary material losses due to the small mass of the samples treated in the rocket flight.

The analytical experiments after the rocket flight were intended primarily to acquire data for evaluating the significance of the interface energies between the crucible material and the different melts. Furthermore, some tests were performed dealing with the formation of Al-rich droplets of the In-rich melt.

## Phase Diagram of the Al-In Alloys

The phase diagram shown in Figure 1 which was established and also thermodynamically evaluated by B. Predel [1] was confronted with a later publication by A. N. Campbell and R. Wagemann [2]. The critical data given by the individual authors are presented in Table 1.

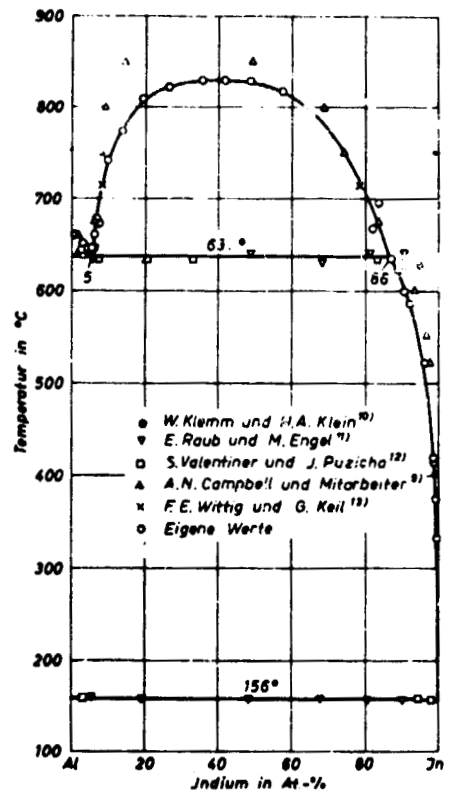


Figure 1. Phase diagram of the system Al-In [1].

TABLE 1. DATA OF THE CRITICAL POINT OF THE MISCIBILITY GAP ACCORDING TO DIFFERENT AUTHORS

| Author | a/o Al | a/o In | $T_{cr}$ (° C) |
|---|---|---|---|
| Predel [1] | 60 | 40 | 830 |
| Campbell [2] | 65.9 | 34.1 | 945 |
| Gelles [3] | ? | ? | 820 |

According to the data supplied by Gelles [3], it should be noted that a critical concentration cannot be read from the course of the binodal running horizontally between approximately 12.5 and 64.5 a/o In at 820°C. A strictly horizontal course of the binodal is impossible for thermodynamical reasons; a gentle decline extending from the maximum to both sides is more likely [1].

Measurements of the binodal temperatures of some alloys yielded the values listed in Table 2. They were determined by means of a differential thermoanalysis using a Mettler apparatus (sample mass: 2.6 gm) at different cooling rates.

TABLE 2. BINODAL TEMPERATURES OF SOME Al-In ALLOYS SUPERHEATED TO APPROXIMATELY 1000°C

| a/o Al | a/o In | T°C (8°/min) | T°C (4°/min) |
|---|---|---|---|
| 70 | 30 | 801.5 | 802 |
| 60 | 40 | 836 807 | 808 808 |
| 50 | 50 | 806 | 810 |

Conducting any further measurements was not necessary because: (1) the critical temperature at approximately 810°C is within the range of the data supplied by Predel and Gelles, (2) these binodal temperatures are expected to depend little on the cooling rate, and (3) more accurate measurements would have required more experimentation time than could be justified for the present purpose. Our measurements confirmed the flat course of the binodal in the vicinity of the critical point. Hence, the critical temperature should be at 820°C.

## Homogenization Behavior[1]

As an essential prerequisite for the success of the rocket experiment, the melt should be completely homogenized at temperatures above 825°C prior to launch. To avoid any damage to other rocket-borne equipment, the holding time at the homogenization temperature should be as short as possible; therefore, tests had to be performed to find out the shortest homogenization time.

For these tests, a silicon carbide tube furnace was placed in a vertical position and provided with a fixture which allowed samples heated to the homogenization temperature of 900°C to drop directly into water, thus cooling them abruptly. The very rapid cooling was required to avoid, as far as possible, the decomposition due to gravity-induced segregation. For this reason, samples with a diameter of only 3 mm had to be used, because it was found that samples with larger diameters could not be quenched with sufficient speed. The cylindrical samples were heated in a graphite crucible approximately 6 mm in diameter and quenched. The holding time at 900°C was changed and, in some cases, also the holding temperature (between 850°C to 1000°C). Total sample length was 40 mm (20 mm Al and 20 mm In).

The tests showed that only a holding temperature of at least 20 min assured a complete homogenization of these samples.

It should be noted that these samples had considerably less favorable geometrical dimensions for the mixing than the flight sample (approximately 10 mm $\phi$, 5 mm thick). For shorter homogenization times and decreasing holding times, increasingly coarse In particles were observed. These probably originated from the more rapid growth of incompletely dissolved nuclei or from incomplete dissolution of larger areas (possibly due to oxide layers). However, the structures of the samples homogenized for periods shorter than 20 min differed considerably and could not always be reproduced for the same lengths of time. Consequently, individual samples with very large homogeneous areas were obtained even after periods as short as 5 min. However, in spite of their favorable geometrical dimensions for the mixing, 30 min is proposed as the preheating time for the flight samples.

In addition to the previously given descriptions, the following should be noted:

---

1. Data taken from investigations conducted by H. Ahlborn and R. Rothe

1. The Hamburg results are in line with our observations and considerations. Since the samples already had to be molten before the rocket launch (in view of the required homogenization periods), it was decided to arrange the starting materials in the crucibles such that the Al with less specific weight was placed in a slice on the bottom, and the heavier In, also in the form of a slice, was put on top. As a result, the In melting at 156°C sinks to the bottom through the Al, dissolving part of the Al as it settles.

2. If mixing of the two components was by diffusion only, a diffusion time of approximately 20 min would have to be taken into account in the case of a mean diffusion coefficient of $D = 5 \times 10^{-5}$ cm $s^{-2}$ for a diffusion distance of 0.5 cm; applying a safety factor of 2, the time would be approximately 40 min. In our case, the sample arrangement in the crucible which supported convection should contribute to an accelerated mixing.

3. The initially requested holding time of 30 min at a homogenization temperature of 925°C [4] could not be assured by NASA due to technical reasons. Following repeated discussions, the experimenters finally agreed to a preflight holding time of 15 to 20 min at 925°C.

## Crucible Material

The low-priced Pythagoras crucibles (trade name of crucible manufactured by the Haldenwanger Company, Berlin primarily composed of 60 percent $Al_2O_3$, 35 percent $SiO_2$, with trace amounts of MgO, $Fe_2O_3$, $Na_2O$, among other components) used initially proved to be unsuited. After preparation of alloys composed only of pure Al and pure In, a non-negligible amount of silicon was found in the sample. At these high temperatures (above 900°C) and the holding times applied, silicon had been reduced out of the crucible material by the liquid Al and was dissolved by the melt. Since the use of graphite as crucible material (which due to its favorable heat conductivity would have offered advantages) was likely to entail reactions leading to the formation of aluminum carbide, Alsint (sintered alumina, Haldenwanger Company, Berlin) was chosen with a content of 99.7 percent $Al_2O_3$ (usable temperature up to 1900°C, density at 20°C: 3.9 gm $cm^{-3}$, thermal conductivity 75.24 J $h^{-1}$ $gm^{-1}$ $K^{-1}$, thermal expansion: $7.2 \times 10^{-6}$ mm $mm^{-1}$ $K^{-1}$ between 20 and 1000°C).

## Preliminary Tests on the Sealing of the Crucibles and Their Arrangement in the Cartridges

Initial sealing of the crucibles by means of Alsint lids as well as enveloping the crucibles in the cartridge with quartz wool (to avoid dangerous shock loading during acceleration) had not met the requirements during ground tests. Figure 2 is an X-ray photograph made by NASA of one of the first test samples (sample 74-62-70). It shows a marked bulge on the cartridge (Fig. 3), the crucibles placed on top of each other, and the alloy samples. Figures 2, 3, and 4 indicate that melt had escaped from the crucible. A reaction causing damage to the cartridge material has not been observed.

Figure 2. X-ray photograph of a ground-base sample (NASA).

Figure 3. Steel cartridge from ground-base sample (V - 2).

Figure 4. $Al_2O_3$ crucible from ground-base sample. Melt escape on lid (V ~ 6).

An examination of the sample yielded the following results:

1. The formation of the melt regulus 60/40 with the marked appearance at the interface of the two melts is very unusual and is seldom observed. The formation indicated the presence of oxide films; however, there presence could not be proven. After removal from the crucible, the two parts could be separated easily.

2. Contrary to the instructions of the investigators, the cartridges were inserted into the furnace rotated by 180 degrees. As a result, the melts were situated on the lids in each case. This favored the escape of molten material and also the penetration of gases into the crucibles. Regardless of the mistakes in the experimental procedure, a more reliable cement for the cover had to be found.

3. The droplet seen on the cartridge wall (Fig. 2) consisted of In.

4. The In and Al must have been mixed prior to the cooling process. Therefore, it could not be determined if a complete homogenization was achieved from the samples available.

5. The formation of the structure was as expected. As an example, Figure 5 shows the structure of the Al-rich layer near the interface in sample 60/40. From the figure it can be seen that the In droplets embedded in the

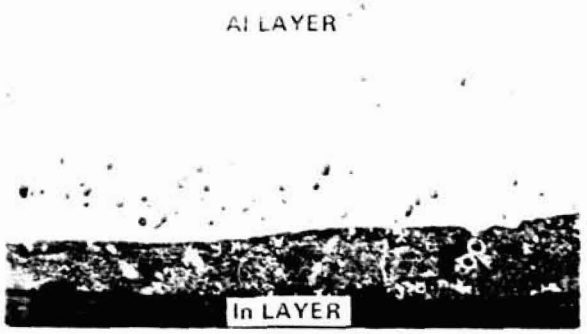


Figure 5. Structure of ground-base sample 60/40 at interface (V ~ 35).

Al matrix increase in size as they approach the interface. In addition, individual Al-rich droplets in the In-rich layer, characterized by aluminum surrounding an indium core, can also be seen. Such droplets usually occur near the interface. In this layer the Al precipitated partly dendritically (precipitated along the liquidus curve of the aluminum between 637 and 156°C) and partly in a very fine eutectic distribution (at 156°C) (Fig. 6). The distribution density of the Al dendrites decreases from the interface to the Al-rich layer towards the bottom, consistent with the gravity-induced segregation.

## Metallographic Analysis[2]

The melt reguli were cut by means of a jigsaw and immediately embedded into "Scaniaplast" (manufactured by the Scandia company). Microsections were produced by microtomy with a steel knife at a cutting depth of 1 to 3 $\mu$m and simultaneous cooling by alcohol. Following 15 min of prepolishing with a wool cloth, the sections were fine-polished on green fine-polishing cloth (Wirtz Company, Cloth E) under oil with "alumina 3." For electrolytic polishing an electrolyte of 700 ml alcohol, 100 ml butylcellosolve, and 200 ml perchloric acid at a bath voltage of 25 V and a treating duration of 40 s proved to be suited for Al. For In an electrolyte of 330 ml nitric acid and 670 ml methanol (95 percent at a bath voltage of 40 to 50 V and a treating duration of 1 to 2 min) were used.

2. Data taken from investigations by Renate Stienen.

ORIGINAL PAGE IS
OF POOR QUALITY

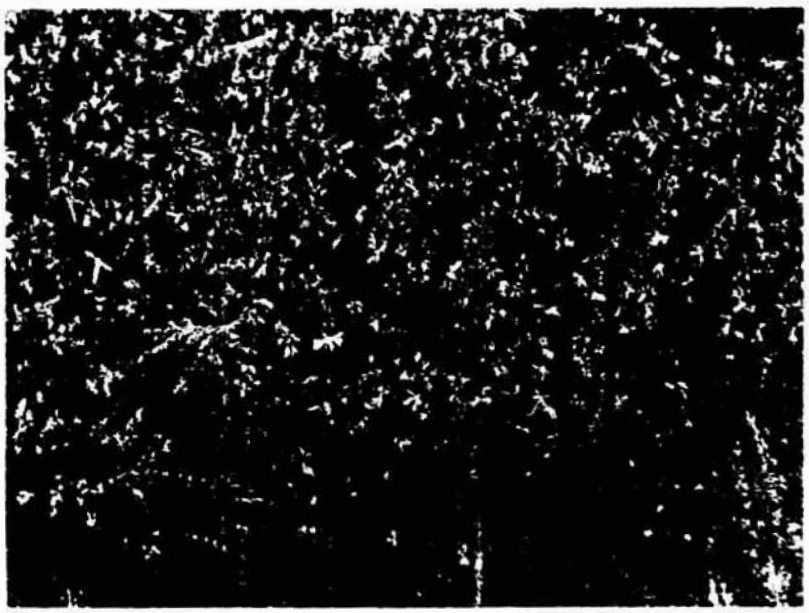

Figure 6. Al dendrites and eutectic matrix of the In-rich melt. Al content increasing from the regulus bottom to the regulus top (V ~ 100).

The microstructure was revealed by etching with the following etching solutions:

1. Indium —

   a. 100 ml ethyl alcohol
      5 ml hydrochloric acid (D = 1.19)
      1 gm picric acid
      etching duration: 5 s.

   b. 2 to 5 gm potassium bichromate dissolved in distilled water until saturation. To this solution was added 1 drop of hydrochloric acid. Etching duration: 10 to 20 s.

2. Aluminum —

   a. 1 percent aqueous sodium hydroxide.

   b. Anodic deep etching with 18 percent hydrofluoboric acid at 45 V and a treating duration of 1 min (preparing samples for scanning electron microscopy).

An etching procedure which can reveal the microstructure of both the In-rich and the Al-rich phases is not known.

## Interface Energies [5]

The wetting of $Al_2O_3$ crucible materials by liquid Al was measured by H. John.[3] The measurements showed that at temperatures near the Al melting point, $Al_2O_3$ is practically dry. The wetting angle $\theta$ is approximately 175 to 180 degrees. According to most recent data given in the literature [6],

$$\gamma_{l,g}^{Al} = 866 - 0.15\,(t - t_s) \qquad t_s = 660°C.$$

Measurements of wetting of $Al_2O_3$ by liquid In [5] produced the following wetting angle:

$$\theta_{273°C} = 158° \quad \text{and} \quad \theta_{568°C} = 149° \; .$$

With linear extrapolation,

$$\theta_{660°C} = 146° \; .$$

For $\gamma_{l,g}^{In}$ (given in Reference 6),

$$\gamma_{l,g}^{In} = 555 - 0.12\,(t - t_s) \qquad t_s = 156°C \; .$$

Calculated from this,

$$\gamma_{l,g}^{In,\ 660°C} = 495 \text{ erg cm}^{-2} \; .$$

Since the same matrix material $Al_2O_3$ was used for the measurements, the relationship

3. Data obtained through personal communication.

$$\gamma^{Al}_{l,\ Al_2O_3} - \gamma^{In}_{l,\ Al_2O_3} = 495 \times \cos 146° - 86 \times \cos 175°$$

and be employed to calculate the difference

$$\gamma^{Al}_{l,Al_2O_3} - \gamma^{In}_{l,Al_2O_3} = 586 \text{ erg cm}^{-2}$$

assuming that $\gamma^{Al}_{l,g}$ and $\gamma^{In}_{l,g}$ can be used in an invariable form.

The interface energy $\gamma^{l}_{Al-In}$ does not have to be taken into account, as the two liquid phases exist concurrently.

In the system under investigation, there is no concurrent existence of pure Al and pure In melts; however, there is a concurrent existence of In containing Al melt and an Al-containing In melt. Assuming in a first approximation a linear dependence of $\gamma_l$ on the concentration,

$$\gamma^{Al(In)}_{l,g} \sim 820 \text{ erg cm}^{-2}$$

and

$$\gamma^{In(Al)}_{l,g} \sim 555 \text{ erg cm}^{-2} \quad .$$

Using these values,

$$\gamma^{l}_{Al,\ Al_2O_3} - \gamma^{l}_{In,\ Al_2O_3} \sim 507 \text{ erg cm}^{-2} \quad .$$

Consequently, the interface energy of the system is at its lowest level when the In-rich melt touches the crucible wall.

In the event of free surfaces, it is expected that In accumulates near the surface, since, according to Lang [7], In reduces the surface energy of the liquid Al (indicating that it is surface-active).

## Spot Tests on the Influence of the Cooling Rate on the Formation of Structure

Alloys consisting of 60 a/o Al + 40 a/o In were melted in $Al_2O_3$-coated crucibles made of austenitic chromium-nickel steel (18/8). This crucible material was selected to assure a rapid transfer of heat during the cooling process. After being heated to 950°C, the melts were maintained at this temperature level for 30 min and then cooled under the following conditions:

1. Quenching in methanol from - 70°C.

2. Quenching in water from 0°C.

3. Quenching in water from 100°C.

4. Heated in the furnace to 660°C, then cooled in air.

5. Heated in the furnace to 660°C, maintained at this temperature for 1 h and then:

   a. Cooled in the furnace.

   b. Cooled in air.

6. Cooled from 950°C to room temperature in the furnace.

In all cases, the decomposition of the melt and separation into the Al-rich and In-rich layers had occurred. The observations may be summarized as follows:

1. When quenching from 950°C to low temperatures, the more abrupt the cooling process the more In-rich melt droplets that are found in the Al-rich layer. Hence, decomposition along the binodal occurred, the gravity-induced separation was, however, not completed. Near the interface, we find numerous In droplets enveloped by Al in the In-rich layer. Here, the Al crystallization is very fine, and is primarily the result of dendritic and eutectic reaction.

2. The samples cooled to 660°C in the furnace and subsequently solidified in air showed the same structure in the In-rich layer as the samples quenched from 950°C. This was independent of whether they were maintained at this temperature for a longer period of time or not. The only difference is that fewer In-rich droplets are found in the Al-rich layer.

3. The samples cooled to room temperature in the furnace no longer show any Al-rich melt droplets in the In-rich layer, but only Al dendrites. Sample 6, which was cooled from 950°C directly to room temperature, contained a larger amount of In-rich droplets in the Al-rich layer than sample 5a, where the holding time at 660°C led to a very large-scale gravity-induced separation.

As an example of the two extreme structure formations, Figures 7 and 8 show the structures of samples 1 and 5a. From the analytical results it is concluded that the decomposition of the alloy melts along the binodal apparently occurred very fast and that the slower the cooling rate, the larger-scale the gravity-induced separation. If the Al layer contains more In-rich droplets than the In layer contains Al-rich droplets, this is due to the fact that settling of the heavy In droplets is prevented by the crystallization of the Al at 637°C, because the light Al-rich droplets can rise from the In layer (liquid until 156°C) more completely at the lower the cooling rate. A reliable indication of slow cooling of the melts below 637°C is the development of coarse Al dendrites in the In-rich layer.

## EXPERIMENTAL ALLOYS, CRUCIBLES, CARTRIDGES

Detailed information referring to the work performed by ERNO-Bremen is contained in the "Experiment Implementation Plan for Soluog Experiment" of October 1975 and especially in its Annex of March 1976.

### Alloy Composition

To produce the alloys, starting materials of highest purity (zone-refined Al 99.9999 percent from Vereinigte Aluminiumwerke Bonn, and zone-refined In 99.995 percent from Preussag, Goslar) were used, which were inserted into the crucibles in the form of small plates. Table 3 gives data on alloy composition, weights (mass and volume), as well as the data used in the computations. Any volume expansions of the melts beyond the rule of mixing were not considered.

### Crucibles

Alsint was used as the crucible material. After filling the appropriate quantities of Al and In into the crucibles, whose clear volume was approximately 0.48 $cm^3$ at a clear diameter of approximately 0.9 cm, they were evacuated, closed with an Alsint lid, and sealed by means of the cementing material Thermostix 200. In each crucible, the Al was placed on the bottom, with the In on top.

ORIGINAL PAGE IS
OF POOR QUALITY

Figure 7. Lab sample 60/40; thermal treatment: 950°C - 30 min/in the furnace to 660°C/in air to room temperature ( V ~ 20).

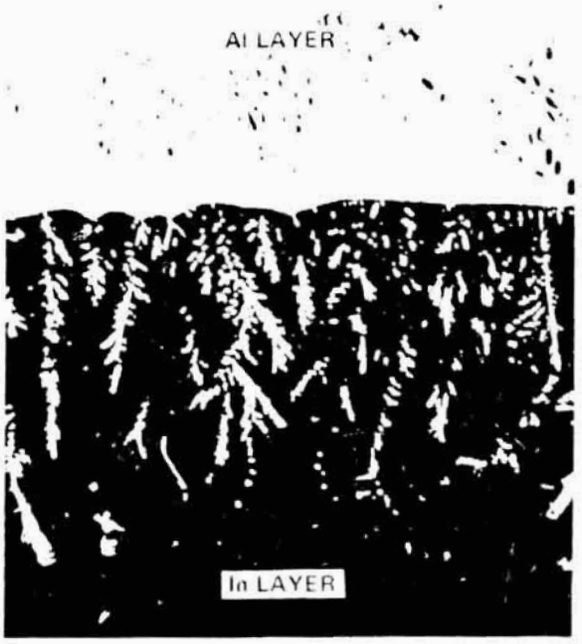


Figure 8. Lab sample 60/40; thermal treatment: 950°C - 30 min/ in the furnace to 660°C - 60 min/in the furnace to room temperature ( V ~ 20).

ORIGINAL PAGE IS
OF POOR QUALITY

Figure 7. Lab sample 60/40; thermal treatment: 950°C - 30 min/in the furnace to 660°C/in air to room temperature (V ~ 20).

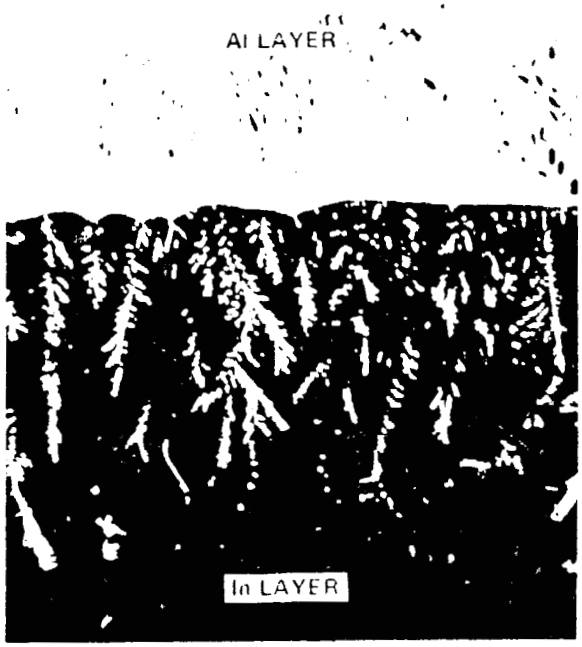


Figure 8. Lab sample 60/40; thermal treatment: 950°C - 30 min/ in the furnace to 660°C - 60 min/in the furnace to room temperature (V ~ 20).

TABLE 3. ALLOY COMPOSITION

| | Aluminum | Indium |
|---|---|---|
| Atomic Weight | 26.98 | 114.76 |
| Density (gm × $cm^{-3}$) at 20° | 2.70 | 7.31 |
| Density (gm × $cm^{-3}$) Fluid | 2.27 | 6.36 |
| Thermal Expansion (mm/mm × K) | $23.9 \times 10^{-6}$ | $30 \times 10^{-6}$ |
| Volume Expansion (%) s → 1 | 4.8 | 2.5 |
| Alloy 60/40 | | |
| a/o | 60 | 40 |
| m/o | 26.1 | 73.9 |
| v/o (20°) | 48.8 | 51.2 |
| Sample Weight: gr | 0.515 | 1.457 |
| $cm^3$ (20°) | 0.191 | 0.199 |
| $cm^3$ (fl)[a] | 0.227 | 0.229 |
| Alloy 89/11 | | |
| a/o | 89 | 11 |
| m/o | 65 | 35 |
| v/o | 83.5 | 16.5 |
| Sample Weight: gr | 0.878 | 0.474 |
| $cm^3$ (20°) | 0.325 | 0.065 |
| $cm^3$ (fl)[b] | 0.387 | 0.075 |

a. The total volume ($v_{Al} + v_{In}$) corresponds to that of a spherical radius of 0.48 cm, $v_{Al}$ to a spherical radius of 0.39 cm.

b. The total volume ($v_{Al} + v_{In}$) corresponds to a spherical radius of 0.48 cm, $v_{Al}$ to a spherical radius of 0.45 cm.

## Cartridges

The high-temperature resistant ferritic steel Thermax 4747 was chosen for use to keep the difference between the thermal expansion of the cartridge and the crucible materials to a minimum. The two crucibles were inserted such that the bottom compartment of the cartridge contained the alloy 89/11 and the top compartment contained the alloy 60/40; i.e., as seen in flight direction, the alloy 60/40 was "in front." The cartridges were evacuated and subsequently welded air-tight. These activities, as well as testing of the samples, were performed by ERNO, Bremen.

## DATA SUPPLIED BY NASA

### Temperature Measurements

Figure 9a shows the temperature profile shortly before liftoff of the rocket and during flight. The temperature of these samples was measured outside, but directly on the cartridge (dashed curve). Forty seconds before the launch the temperature was 980°C; after the launch it sank rapidly to 950°C. The temperature was maintained at this level for approximately 120 s. At 150 s after the launch, the cooling process was started by means of a helium flow. Approximately 300 s after liftoff, it decreased to 150°C with the following cooling rates:

| | |
|---|---|
| 950 to 600°C: | 17.5 K $sec^{-1}$ |
| 600 to 400°C: | 13.3 K $sec^{-1}$ |
| 400 to 300°C: | 5 K $sec^{-1}$ |
| 300 to 200°C: | 2.4 K $sec^{-1}$ |
| 200°C: | 1 K sec |

However, these measurements do not provide any information on the actual temperatures of the samples. In the same rocket flight, the alloys of the system Al-In investigated by Dr. Geiles were contained in the same furnace as the samples described in this report, but in an adjacent furnace chamber. In this case, a thermocouple had been inserted in the crucible in direct proximity of an alloy specimen. The related temperature-time curve is given in Figure 9a by a solid line. The environment of the holding point at approximately 620°C is given in Figure 9a on an enlarged scale. This temperature corresponds to that of the monotectic equilibrium temperature (637°C); i.e., the equilibrium appears to be undercooled by approximately 17°C, but the reaction is mainly isothermal.

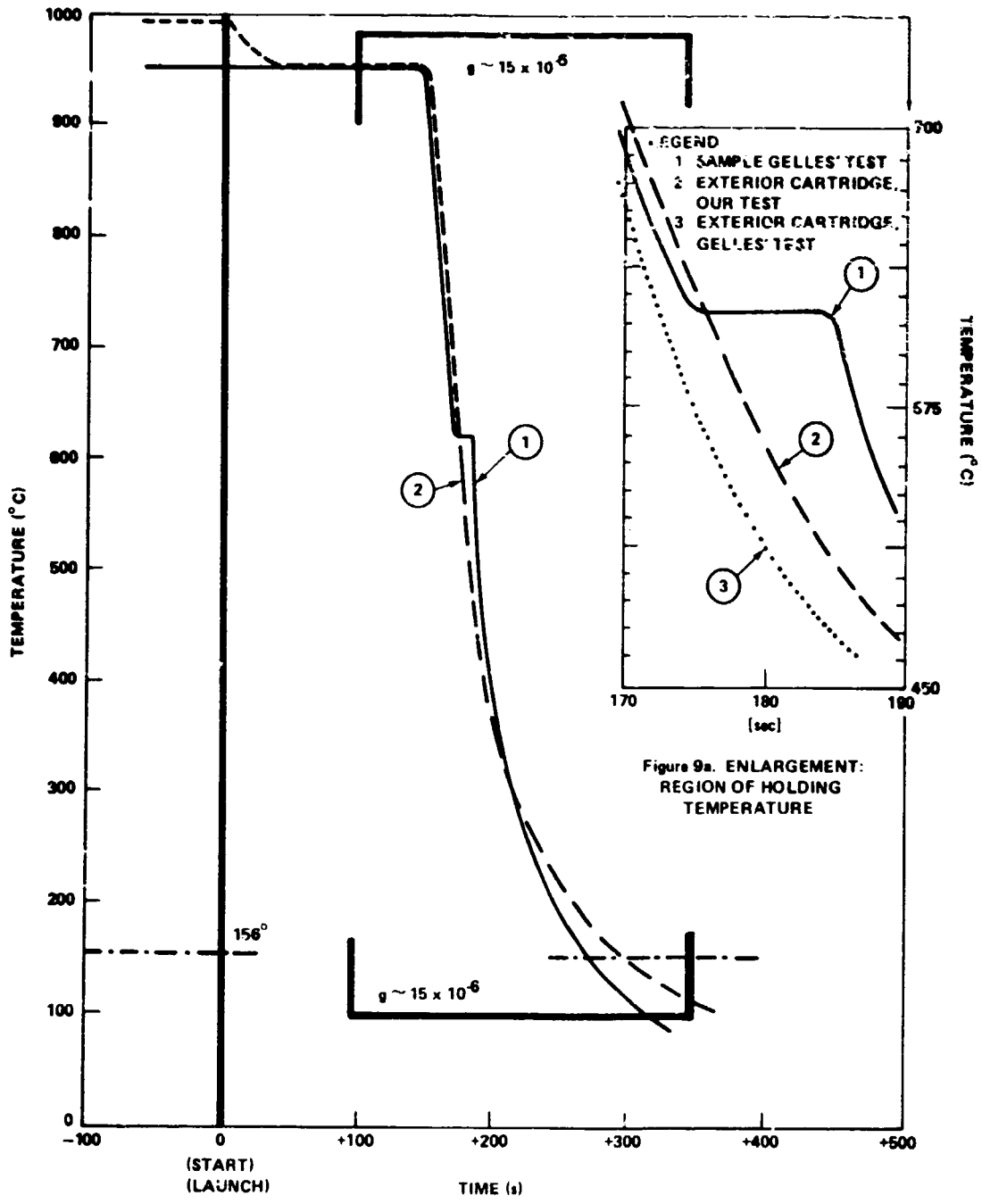


Figure 9. Time-temperature profile.

Because of the near identical thermal conditions for the US and the German samples, it is concluded that the monotectic reaction

$$^{1}_{Al(In)} \rightarrow {}^{s}_{(Al)} + {}^{1}_{In(Al)}$$

occurred isothermally.

## g - Measurements

Figure 10 contains the acceleration-time curve (compensating curve) measured in three coordinates during the period of low g-values. It can be seen that at approximately 90 to 100 s after the launch a constant value of an average 15 $\mu$g at approximately $15 \times 10^{-6}$ g is reached. As can be taken from the exact diagram, a value of $< 40 \times 10^{-6}$ g is reached.

Complete weightlessness was not achieved. The lowest g-values have thus prevailed in the period between approximately 100 and 345 s after liftoff. As is seen from Figure 9a, the melts had cooled to below 150°C during this time period. No information is available on the accuracy of the temperature measurements.

## X-ray Photographs of the Samples

Figure 11 shows the X-ray photographs taken by NASA of the sample 74-62-92 molten under $g < 4 \times 10^{-5}$ in the SPAR II flight. A detailed description of the appearance of the specimens will be given in the following section.

# METALLOGRAPHIC ANALYSIS OF THE MOLTEN SAMPLES

## Macroscopic Examination

First, some chips were removed with the microtome at both ends as well as on the lateral surfaces of the melt reguli. Then, the samples were cut in halves by means of a jigsaw, and the sectional areas were smoothed by means of the microtome. After examination of one of the halves, it was sliced further by the use of the microtome.

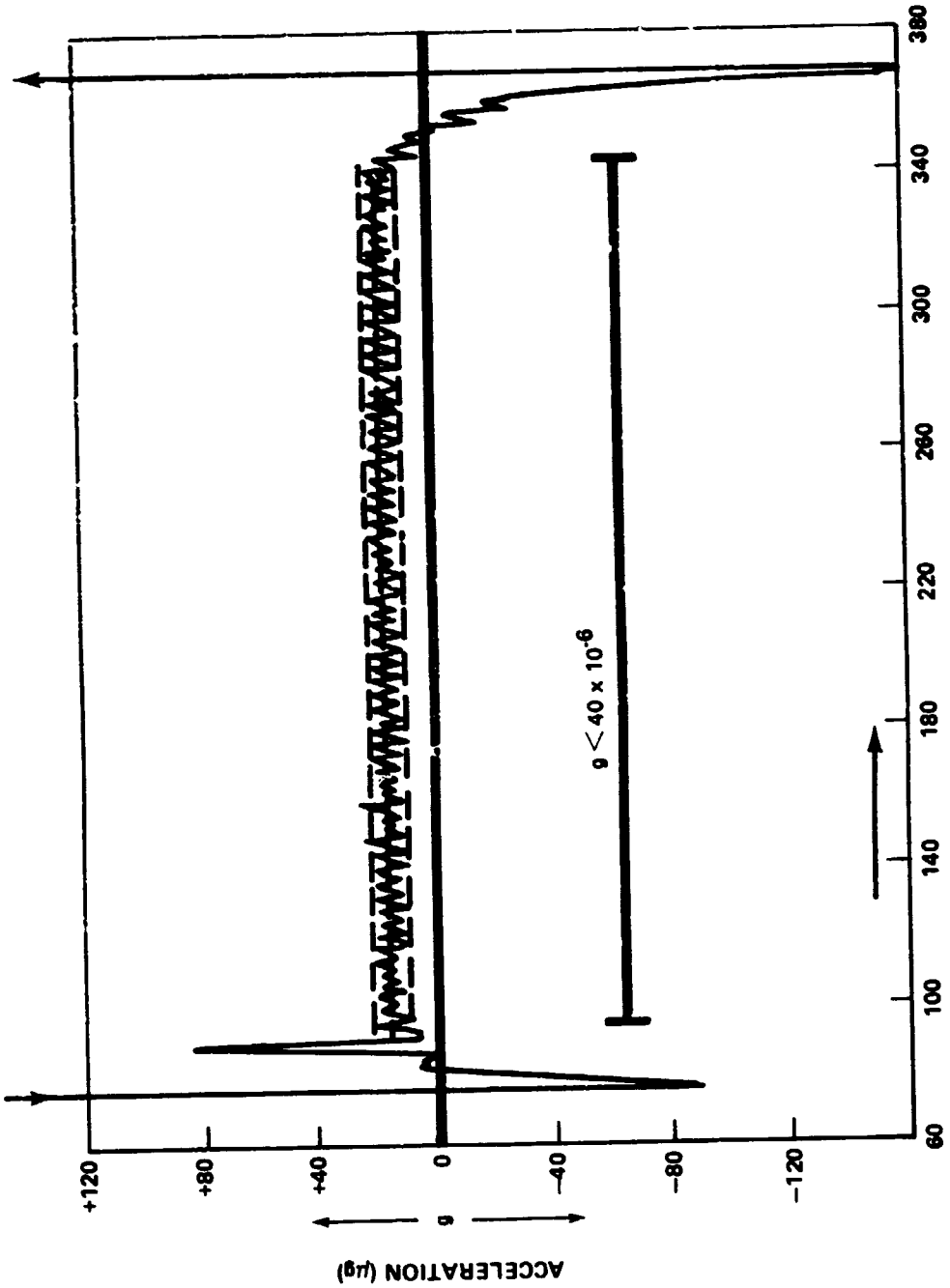


Figure 10. Detail from the time-acceleration curve in the region of minimum acceleration.

Figure 11. X-ray photograph of flight samples (NASA).

Alloy 89/11

Figure 12 shows the melt regulus of alloy 89/11. The barrel-like shape indicates a tendency towards formation of a microsurface; apparently, the liquid melt only randomly contacted the crucible wall. The regulus has on its top surface an indentation where numerous droplets with a diameter of approximately 100 $\mu$m (comparable to sweat globules) had accumulated (Fig. 13). The surface of the melt regulus had a greyish-greenish color. Figures 14a and 14b show longitudinal sections cut approximately through the center of the melt regulus. At the bottom side and the top side transverse sections had been made before, so these parts are missing in the photographs. The light part represents the Al-rich phase and the dark part the In-rich phase. The dark areas are not shrinkholes or pores.

Figure 12. Melt regulus of sample 89/11 (V ~ 6).

ORIGINAL PAGE IS
OF POOR QUALITY

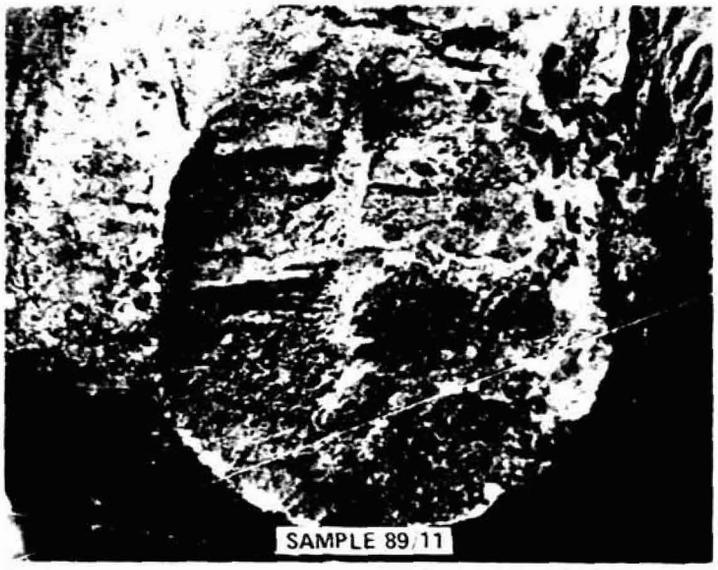


Figure 13. Indentation hole with melt droplets (V 10.5).

The regulus is barrel shaped and is determined by the Al phase, composed of small and large droplets, and coarse parts of the In-rich phase, whose size increases from the bottom of the regulus to the top of the regulus. The previously mentioned indentation is largely filled with In-rich phase, and it may well be that the large In droplets are somehow connected with each other. Near the bottom of the regulus only small In droplets are found. The entire circumference of the regulus is surrounded by In-rich melt droplets approximately 0.04 mm in size.

Alloy 60/40

Figure 15 shows a photograph of the melt regulus of the alloy 60/40. The darker surface was of a greyish-greenish color. The shape of the regulus has no rotational symmetry. On the left side, it appears to have been pushed to the crucible wall and bottom; otherwise the contact area between the regulus and the crucible wall is very small. Figures 16, 17, and 18 show transverse and longitudinal cuts through the regulus, which confirm the asymmetry shown in the X-ray photograph. The white surfaces represent the Al-rich portion with embedded In-rich phase. In the In-rich portion small Al crystals are observed. This surprising finding is described as follows.

An Al globule (Fig. 18) is completely surrounded by In-rich melt (Figs. 16, 17, and 18); the interior of the sphere also contains an In-rich phase, which is connected with the exterior In-rich part by an interconnection through the Al

a. Sectional area a (V ~ 10.5).

b. Sectional area b (V ~ 10.5).

Figure 14. Longitudinal section through sample center; sectional areas a and b separated by jigsaw.

ORIGINAL PAGE IS
OF POOR QUALITY

Figure 15. Melt regulus of sample 60/40 (V ~ 6).

Figure 16. Longitudinal section near jacket through sample 60/40: Al sphere with In shell (V ~ 6).

sphere (Fig. 19, upper left). The external surface of the Al sphere is not ideally spherical, however, the inner surface appears to be. Figure 19 also shows that the In-rich envelope is rather thin in the upper portion of the regulus and considerably thicker on the bottom.

From this regulus, transverse sections were taken from the bottom (only In-rich phase) and the top (prior to completing the longitudinal section) so that these parts are missing in Figures 17 and 18. The longitudinal section in Figure 16 was taken near the lateral surface parallel to the axis.

From Figure 18, it should be noted that the section was strongly etched for an examination by scanning electron microscopy. The inner In sphere became visible only after this etching treatment.

Figure 17. Longitudinal section cut through the center of sample 60/40, between the section shown in Figures 16 and 19 (V ~ 10.5).

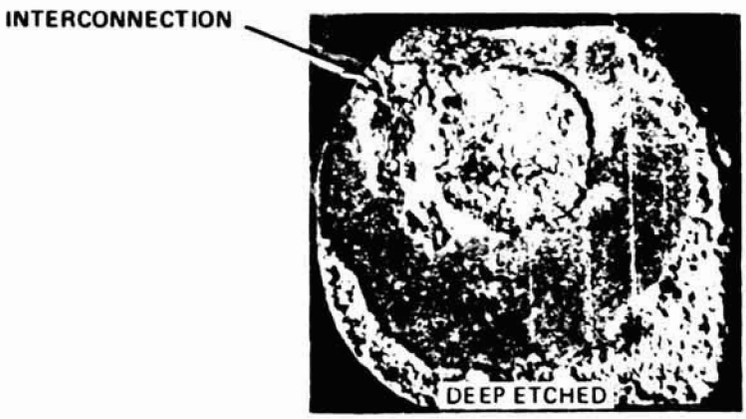


Figure 18. Longitudinal section through center of sample 60/40: In in Al globule surrounded by In (V ~ 6).

Figure 19. Transverse section through sample 60/40 at the level of interconnection in Figure 18 (V ~ 16).

Figure 19 shows a transverse cut through the upper part of the transverse cut depicted in Figure 18 (the missing sample half had been separated during preparation of the sections according to Figs. 16 and 18). Notice that the inner In sphere is not in a symmetric position to the axis of the regulus, which can also be seen from Figure 18. The interconnection through the Al sphere is in the left part. The figure confirms the spherical shapes which are, however, by no means ideal. A striking feature is the netlike arrangement of the In in the "Al finger" pointing downward in the vicinity of the interconnection (shown in Fig. 20 in an enlarged view). Another noteworthy feature is the aluminum's shape of a coastal beach belt and an island bow in one part of the section.

## Microscopic Examinations

### Alloy 89/11

Figures 21 and 22 show the structure of the Al-rich part in the lower portion of the melt regulus (Fig. 15, lower right). In droplets of different sizes are visible partly inside the Al crystals of a stem-like growth and partly in the form of larger droplets on the grain boundaries.

Figure 23 shows the In-rich droplets at the surface of the melt regulus and the considerably finer In-rich droplets in the Al matrix mentioned previously.

Figure 20. Detail from Figure 19 (left) in higher magnification (V ~ 43).

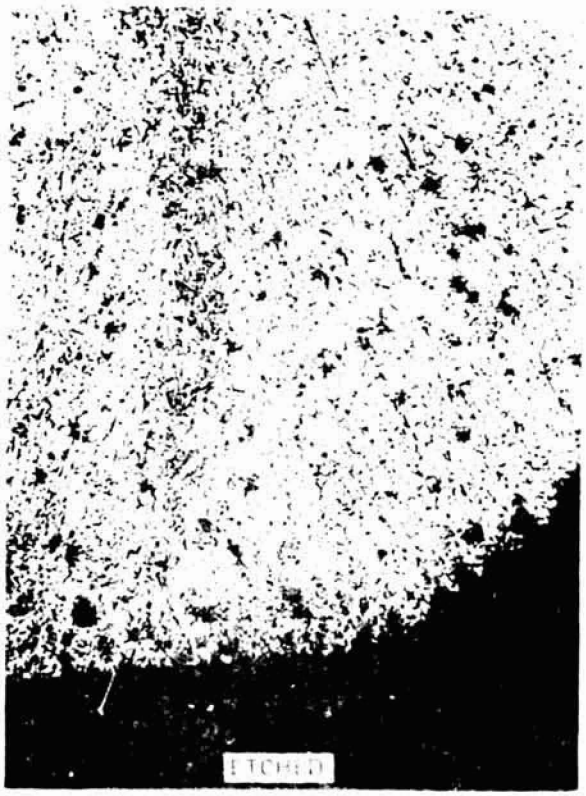

Figure 21. Sample 89/11: radial Al crystals grown from the cooling side (Fig. 15 lower right) (V ~ 60 : 1).

ORIGINAL PAGE IS
OF POOR QUALITY

Figure 22. Detail from Figure 22 in higher magnification (V ~ 500 : 1).

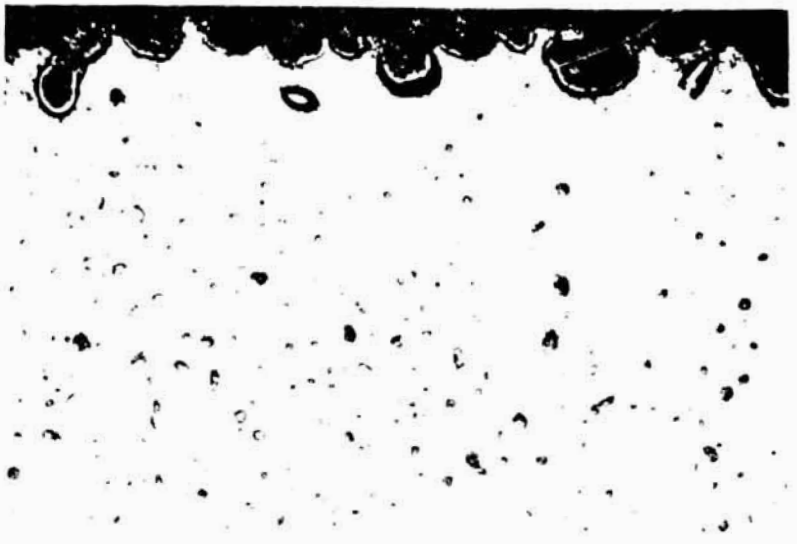

Figure 23. In-rich droplets in the surface of sample 89/11 (V ~ 300).

Alloy 60/40

Figure 24 shows a microsection of the structure of the Al sphere. Al appears to be equiaxially crystallized. Within these crystals and primarily on the grain boundaries In is found.

Figure 24. Al matrix in Al globule with In on grain boundaries (V ~ 300).

Figure 25 shows droplets in the In-rich matrix which are characterized by an Al envelope with an In core. Such droplets are also noticed in a similar manner in terrestrially molten samples in the In-rich matrix.

Figures 26 through 31 show structures in the vicinity of the interconnection. Figure 26 shows in higher magnification the surroundings of the "Al finger" (Fig. 19) in a parallel sectional plane. Most noticeable is the smooth limitation of this "finger" towards the crucible wall, and the less smooth limitation towards the interconnection with numerous detached Al crystals. In Figure 27 the fissured boundary between Al and In is even more pronounced. At this and other locations the detached small Al crystals appear in parallel arrangement to the boundary; i.e., they appear to be blown off.

In the In-rich area, in the vicinity of the interconnection outside the inner In sphere, strange scour-like round recesses partly surrounded by Al are observed (Figs. 18 and 29). It is definitely seen from the scanning electron



ORIGINAL PAGE IS
OF POOR QUALITY

ORIGINAL PAGE IS
OF POOR QUALITY

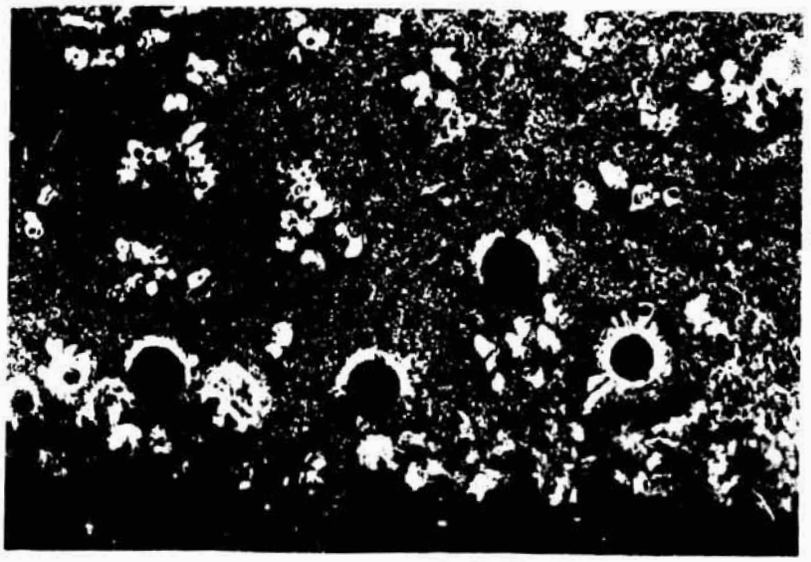

Figure 25. Structure of In sphere near the interface to Al globule (V ~ 300).

Figure 26. Al globule near interconnection (Figs. 18 and 19); separated Al crystals in In (V ~ 250).

Figure 27. Al globule near interconnection; separated Al layers and crystals (V ~ 250).

Figure 28. Al globule near interconnection; voids in the In inside the spherical shell (V ~ 50).

ORIGINAL PAGE IS
OF POOR QUALITY

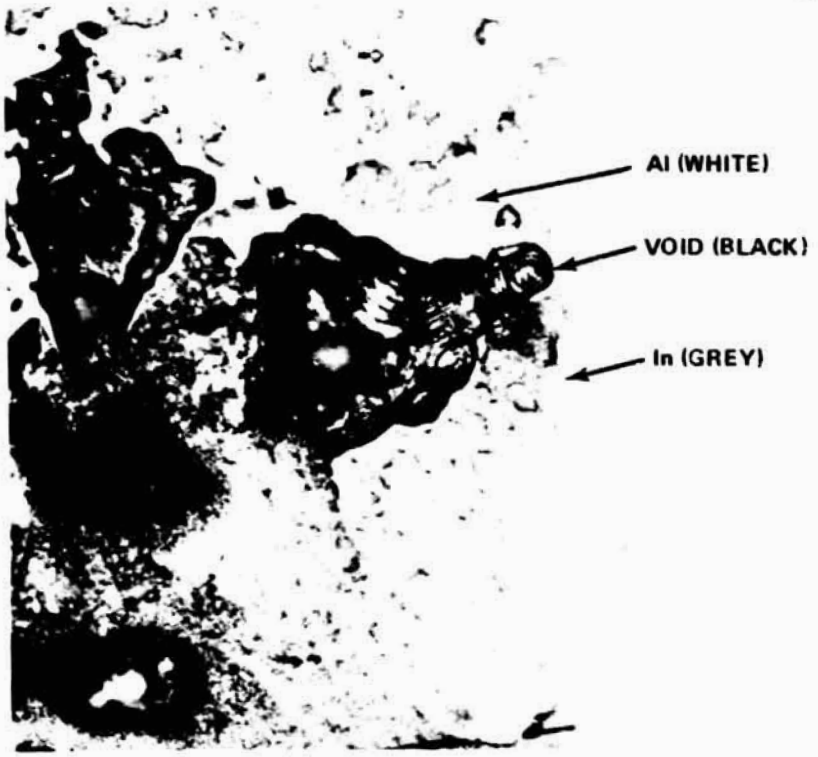


**Figure 29.** Enlargement of Al globule near interconnection; voids in the In inside the spherical shell (V ~ 100).

**Figure 30.** SEM micrograph of Al globule near interconnection; voids in the In inside the spherical shell (V ~ 115).

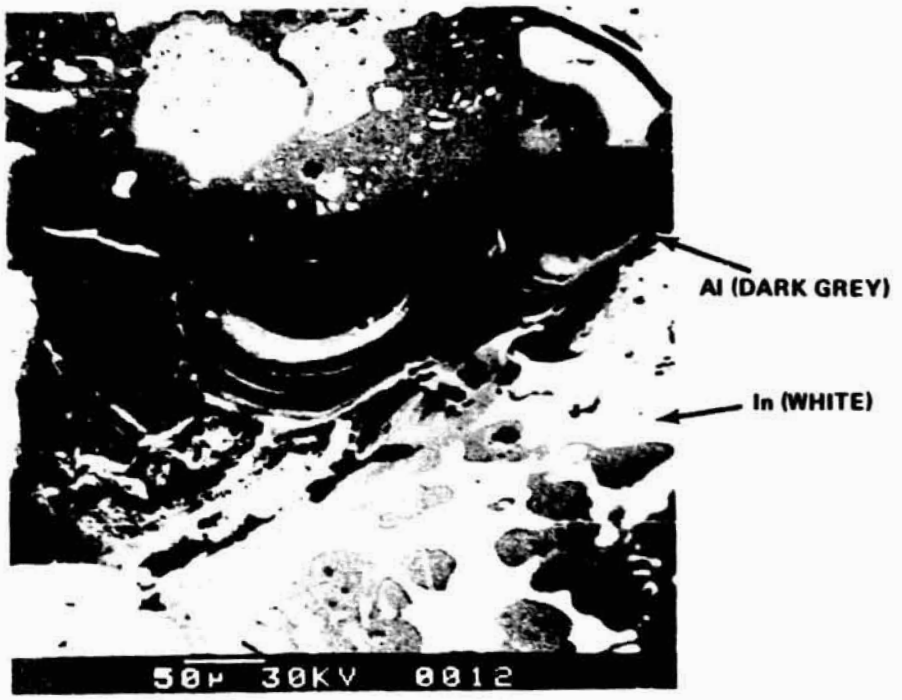


**Figure 31. SEM micrograph of Al globule near interconnection showing the contoured void vortices in In near the interface to Al (V ~ 240).**

micrographs that these are in fact scour-like structures (Figs. 30 and 31). In these micrographs (contrary to the light-optical structure photographs) the In-rich parts appear light and the Al-rich parts dark grey. When Figures 28 and 29 are compared with Figures 30 and 31, this can be readily seen. The scanning electron micrographs moreover show very clearly the very fine, netlike arrangement of the In phase in the Al, consistent with the structure formation in Figure 24.

Figure 32 shows the fine dendritic shape of Al in the In-rich sphere (Fig. 18) as it is formed upon rapid cooling between 637 and 156°C.

## DISCUSSION OF THE TEST RESULTS

First, it must be stated that examining flight samples 60/40 and 89/11 did by no means confirm the expectations described earlier in this report, nor did it provide any reliable information about the decomposition of the homogeneous

ORIGINAL PAGE IS
OF POOR QUALITY

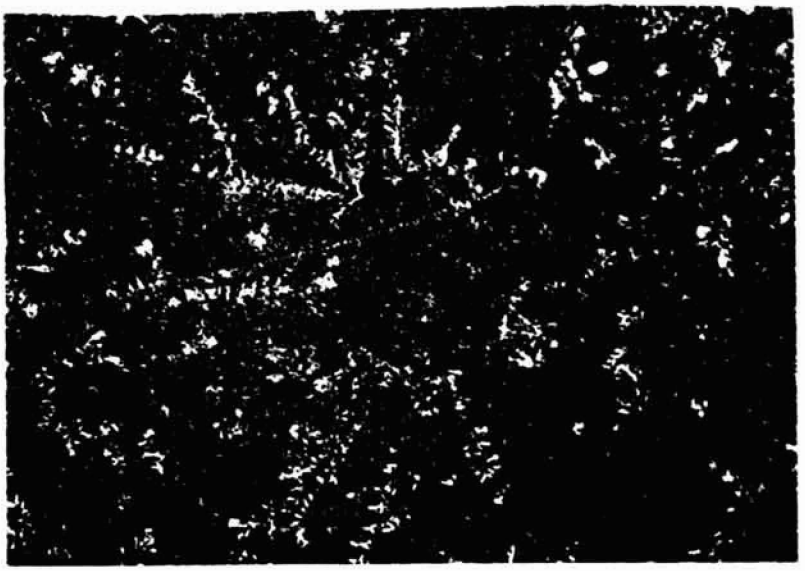

Figure 32. Structure of In sphere near the center:
Al dendrites and eutectic (V ~ 100).

melt into two immiscible melts. But then unexpected information was obtained about the process of separation of the two phases into an Al-rich and an In-rich region. As far as we know, such a separation process has not been observed with samples treated in the same way on Earth. Here the melts separate according to the specific weight with a more or less plane or undulated separation surface parallel to the Earth's surface.

In the following discussion, preference will be given to the examination result concerning sample 60/40. Here the situation seems to be somewhat clearer than in the case of the sample 89/11, although a similar separation process should have occurred. The following questions will be answered in an attempt to explain the previously mentioned occurrence:

1. What information can be provided concerning the homogeneity of the melts prior to the beginning of the cooling process?

2. Which accelerative forces could have favored the separation?

3. What could have been the role of interface energies?

4. How did the arrangement In-rich envelope/Al-rich globule/In-rich core zone develop in sample 60/40?

5. How could the In-rich melt break through the Al globule?

6. Were the samples completely solidified upon return into the Earth's gravitational field?

7. Which conclusions are drawn from the discussion of the previously mentioned questions for further tests?

## Ad 1

Before the beginning of the cooling process (approximately 150 s after liftoff), the temperature of the melts had been approximately 950°C for an unknown period of time. This temperature was more than 100°C above the critical temperature. Considering the components in the crucibles the conditions of homogenization were favorable. From the arrangement of the two structure constituents (Al with heterogeneously embedded In and In with heterogeneously embedded Al, especially in the sample 60/40), it is concluded that the melt has been homogeneous at 950°C. It cannot be said if a state of minimum free enthalpy was achieved or whether there was still a rest of viable In-rich clusters, in addition to viable Al-rich clusters, which could have favored the decomposition when passing through the binodal (or spinodal). It seems permitted to state that a minor deviation of melts 60/40 and 89/11 at 950°C from complete homogeneity might possibly have favored, but by no means caused, the separation process. It should be noted that these observations only provide information about the separation process of the two phases developed through decomposition.

## Ad 2

The temperature-time curves do not supply any information about the decomposition of the homogeneous melts, which should have started in sample 60/40 at the critical temperature (820°C), and in sample 89/11 at 720°C. However, apparently the decomposition and separation started before the monotectic temperature was reached (equilibrium: 637°C, as recorded in Gelles' sample: 614°C). This statement is derived from the following consideration and calculation, using conclusions drawn from the discussion of questions 4 and 5.

If the melt 60/40 had decomposed upon reaching the monotectic temperature, a more or less fine but uniform distribution of the two melts would have occurred at the monotectic temperature. The Al crystallizing at this temperature

would then have pushed the entire In-rich melt existing and developing at 637°C (resp. 614°C) ahead of it and enveloped it as a spherical shell. The ratio between the volumes of the Al spherical shell and the In core would then be

$$v_{Al} : v_{In} \sim 0.82 : 1 \quad ,$$

or the ratio of the radius r of the inner In sphere to the wall thickness $d = (R - r)$ of the Al spherical shell would be

$$d_{Al} : r_{In} = 0.25 : 1 \quad .$$

If, however, the two melts were already completely separated upon reaching the monotectic temperature, then the crystallizing Al would only push the developing In-rich melt ahead of it. The ratio between the volumes of the Al spherical shell and the In core would then be

$$v_{Al} : v_{In} = 12 : 1 \quad ,$$

or the ratio of the radius r of the inner In sphere to the wall thickness $d = (R - r)$ of the Al spherical shell would be

$$d_{Al} : r_{In} = 1.2 : 1 \quad .$$

From the metallographic cuts and sections (Figs. 18 and 19), the radius r of the inner In sphere is estimated to be 0.23 cm and the wall thickness of the Al spherical shell approximately 0.2 cm, i.e.,

$$d_{Al} : d_{In} \sim 1 : 1 \quad .$$

This confirms the second assumption, namely that the two melts were already separated when the monotectic temperature was reached.

Originally, it had been assumed [8] that the separation of the two melts could have been caused by the fact that the melt had not yet come to a complete rest after despin of the rocket, when the decomposition started. According to Lacy [9], the spin-down times for Al melts at 975°C are approximately 40 s, for In melts approximately 200 s.

According to Gelles and Markworth [3], however, the despin aftereffects in the melts should have largely disappeared by the beginning of the cooling process (150 s after liftoff). The same authors also discuss (on the basis of calculations and estimations) the effect of various parameters on the melts, temperature gradient (Marangoni effect), and they conclude that these could cause a motion (current, convection) of the melt favoring separation.

Ad 3

Recall the shape of the melt reguli (Figs. 11, 12, and 15) and their position in the crucible. For a better understanding of the following descriptions, the two reguli and the crucible boundary are shown in Fig. 33. In both samples, we can clearly see a tendency towards the formation of minimum surfaces and thus also towards the formation of minimum contact areas between the samples and the crucible. This finding can be explained by the fact that the surface energy of the melts towards the atmosphere (in the crucible) is smaller than the interface energy between the melts and the crucible material.

The more or less thick In-rich layer covering the entire regulus surface is a result of the low surface energy of the molten In as well as of its low interface energy towards the crucible material; this was previously described in this report and is mathematically supported by Gelles and Markworth [3].

Only the In-rich melt, which is formed by decomposition along the binodal, can move into the surface and into the interface. The state of minimum interface energy would be achieved if all In-rich melt droplets had agglomerated. The agglomeration may take place through gradual coalescence inside the Al-rich melt and by convective motion on its surface. In the short periods between beginning of the decomposition at the binodal temperature and reaching of the monotectic temperature, an agglomeration exclusively by diffusion is not possible.

These processes caused by interface energies explain the envelope of the Al-rich melt in the two alloys, but they do not explain the mutual, i.e., different, arrangement of the Al-rich and the In-rich melts in the samples 60/40 and 89/11.

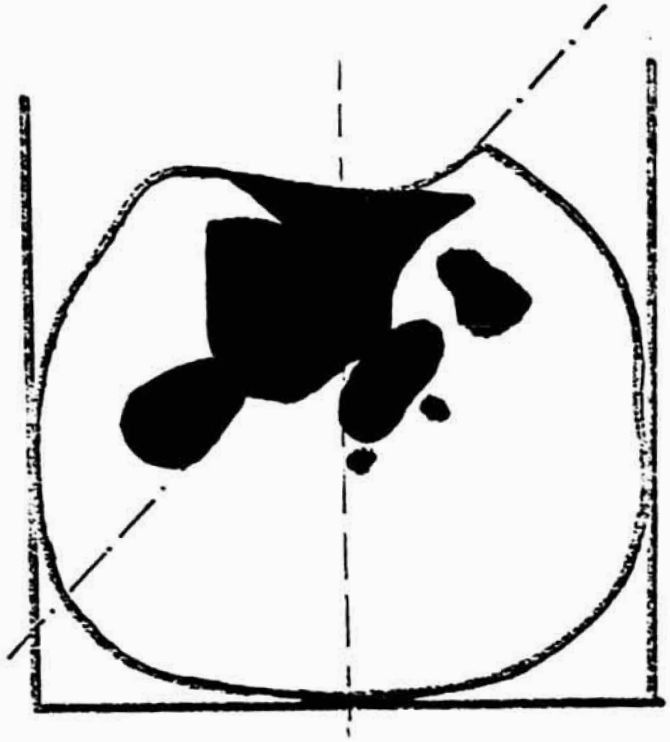

a. Sample 89/11: almost rotationally symmetrical.

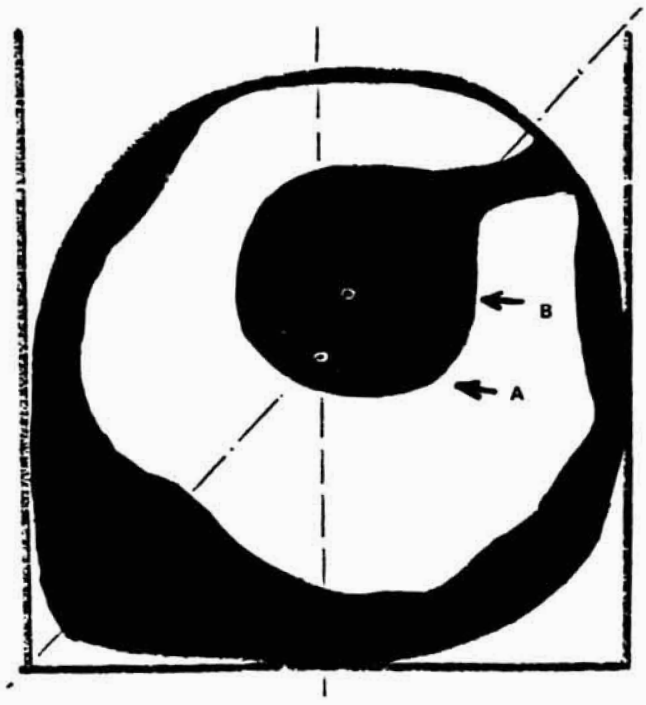


b. Sample 60/40: rotationally unsymmetrical.

Figure 33. Drawn sections through samples 89/11 and 60/40 (M ~ 10.5 × 1).

The shell, consisting of an Al-rich sphere around part of the In-rich melt, as observed in the sample 60/40, can by no means be the result of interfacial energy motions. The development of this striking arrangement may, however, be explained by the course of events occurring during the monotectic reaction, taking into account the arrangement of the two melts already present at this temperature. At the monotectic temperature (637°C, resp. 624°C as measured), the Al-rich melt decomposes according to

$$l_{Al} \rightarrow s_{Al} + l_{In}$$

with crystallization of Al. $l_{Al}$ with a $v_{l_{Al}} \sim 0.227$ cm$^3$ can form a sphere with R = 0.39 cm at the given crucible dimensions, this sphere being enveloped by In-rich melt at the beginning of this process. Dissipating latent heat can only go to the outside through this envelope. Since the process occurs fast and isothermally, the crystallization advances at the interface $l_{Al}/l_{In}$ into the interior of the sphere. The melt $l_{In}$ then formed is more and more separated from the outer melt $l_{In}$ by the growing Al shell and remains inside the sphere. The analysis according to Figure 18 and others indicates that a small amount of $l_{In}$ is overgrown or separated at the Al grain boundaries. The larger part is pushed into the interior of the sphere. The lack of shrinkage holes in the Al is understandable.

The accumulation of the In-rich melt in the "upper" part of the regulus 89/11 may have occurred in a comparable way. In this case, however, $v_{l_{Al}} \sim 0.39$ cm$^3$, to which corresponds a spherical radius of R ~ 0.45 cm. At the given crucible dimensions, the formation of a sphere is no longer possible. However, the volume percentage $l_{In}$ is considerably lower than in the case of the second alloy so that $l_{Al}$ is not enveloped regularly. Crystallization will thus start at the place of fastest heat dissipation, and this is, with the known location of the crucible in the cartridge, the crucible bottom which is in contact with the metal cartridge. The crystallization front advancing from the bottom to the top, during which (as shown in Figs. 14b, 21, and 22) radial crystals grow, partly encloses the developing melt $l_{In}$ and partly pushes it towards the top where it fills the indentation hole (shrinkage hole).

Towards the center (A) of the Al sphere of the sample 60/40 in the drawing (Fig. 33b), the In sphere (b) is shifted to the upper right, approximately in the direction of the diagonal drawn as dashed line, and the larger part of the In is found in the lower left of the figure. This In seems to have been pressed into this part of the crucible. If these shifts were a result of the interconnection, through which the In melt has obviously escaped to the upper right, then the associated reaction should have brought the Al shell with core into the opposite direction. The mutual position of the two structure constituents and primarily the accumulation of In at the bottom left indicate a movement of the still liquid In in the direction of flight when deceleration is started. (Recall that the interconnection previously discussed did not occur until decelerating forces became noticeable.)

## Ad 7 (Conclusions)

Several questions arise from the observations and their discussion:

1. Does the displacement of the In-rich melts depend on the velocity at which a crystallization front advances? Is there a critical velocity, below which heterogeneous particles (solid or liquid) present in the melt volume are overgrown? These questions should also be of significance for the production of composite materials made of liquid (metallic) and solid (ceramic) components (phases). To clarify this question, appropriate experiments (possibly by directional solidification) could be performed where the crystallization rate can be varied. This, however, cannot be achieved with a rocket-borne test.

2. It became obvious that the interfacial energy is of particular importance. Therefore, the question arises how the decomposition and solidification processes will take place if a crucible material (graphite?) is used which has the lowest interface energy among those possible in the system towards the primarily solidifying melt.

3. Can the containerless melting, where positioning offers difficulties, be replaced by melting in crucibles if a surface and interface active component, whose accumulation at the melt prevents a direct contact with the crucible wall, is added to the material of the part to be produced?

4. At what ratio between Al and In is the Al shell so strong that an interconnection does not occur? Such a test could be performed onboard a rocket. For this purpose, the alloys of different composition would have to be melted under the same thermal conditions, and these alloys would have to contain an absolute Al content allowing the formation of a sphere in the available crucibles.

5. Information on the importance of the mechanisms leading to the formation of a sphere, in particular on the role of the surface tension, could also be gained in tests where the sample shape differs from the length-to-diameter ratio (1/d ratio) of 1 used here. If the surface tension of Al is the predominant force to form a sphere, not a single sphere should be formed in samples with larger than 1/d ratios, but several spheres distributed over the length of the sample. If, however, other forces prevail, a coherent Al region differing from the spherical shape should be formed. These questions of importance for the solidification behavior of two-phased melts under zero-gravity will be answered in another rocket-borne test.

## SUMMARY

The objective of the experiment was to clarify the decomposition and crystallization behavior of two Al-In alloys characterized by a miscibility gap in the liquid state with a critical temperature of 810°C and a composition of 60 at. % Al + 40 at. % In. One alloy had this composition and should decompose spinodally; the other with 89 at. % Al and 11 at. % In should decompose by nucleation. In both case, a uniform dispersion of the In-rich and the Al-rich phases was expected, but with different size and arrangement.

In neither of the two cases was observed a phase arrangement meeting these expectations, nor a stratification as occurring in tests under g = 1. In the alloy 60/40, an Al-rich globule was observed, whose interior was filled with Al-containing In and which was enveloped by Al-containing In. The Al globule has an interconnection at one point. In the second sample the In-rich component accumulated in the upper part of the melt regulus, but not in a stratified manner. Here, too, is a narrow In-rich zone at the whole regulus surface. The Al crystallizing at the monotectic temperature (637°C) has an equiaxial form and the Al crystallizing below this temperature has a fine dendritic form.

In the Al-rich sample 89/11, a sphere could not be formed for geometrical reasons, but a tendency towards sphere formation is obvious. Consequently, the solidification occurred essentially towards the heat flow directed to the bottom, with the In-rich melt being displaced towards the top. In the sample 60/40, by contrast, the following process should have taken place. The spherical Al-rich melt was surrounded by an In-rich melt when the crystallization started at the monotectic temperature and advanced radially to the center against the heat flow going regularly into all directions. In this process, the larger amount of the separated In-rich melt was displaced into the interior of the sphere and was

subjected (because of the strong volume contraction during solidification of the aluminum) to a rising pressure which finally led to the Al sphere breaking through a weak point. The resulting current through the "channel" can still be traced in the solidified sample by "hollow vortices" existing only at this point.

The fact that the melt reguli are surrounded by In-rich melt may be understood from the different interface and surface energies of the In-rich and the Al-rich melts. Accumulation of In in the sample surfaces as well as in the interface between melt and aluminum oxide crucible may be the result of the lower surface and interface energies of the In-rich melt.

Although the observations do not correspond to the expectations, the test nevertheless allows important conclusions which should be founded with further experiments (in short-duration tests and also in long-duration tests under zero-gravity conditions):

1. Does the displacement of a second phase (In-rich melt) by the crystallizing phase (Al-melt) always occur or is there a critical growth rate, below which the second phase is overgrown (an important question also for the production of composite materials from melt) ? In such tests the crystallization rate would have to be varied.

2. What are the effects of different interface and surface energies of two liquid phases on the separation of decomposed phases and their crystallization behavior? In such tests the crucible material and/or the 1/d ratio of the samples would have to be varied.

## REFERENCES


1. Predel, B.: Zs. F. Metallkde, vol. 56, 1965, p. 791.

2. Campbell, A. N. and Wagemann, R.: Canad. Journ. of Chem., vol. 44, 1966, p. 637.

3. Gelles, S. H. and Markworth, A. J.: Final Post-Flight Report on SPAR II. NASA Exp. No. 74-30, December 1976.

4. Experiment Implementation Plan for SOLUOG-Experiment, ERNO, October 1975 (with an Appendix from March 1976).

5. Löhberg, K.: Material Sciences in Space. Proc. Sec. Europ. Symp. on Mat. Sci. in Space, Frascati, p. 375.

6. Lang, G. et al.: Zs. f. Metallkde, vol. 68, 1977, p. 113.

7. Lang, G.: Aluminum, vol. 49, 1973, p. 231.

8. Ahlborn, H. and Löhberg, K.: Preliminary Report on the Results of the SOLUOG-Experiment, July 1976.

9. Lacy, L. L.: Experimental Determination of Fluid Spin-Down Time for SPAR-Project, NASA ES 24, March 1975.

TECHNICAL REPORT STANDARD TITLE PAGE

| 1. REPORT NO. | 2. GOVERNMENT ACCESSION NO. | 3. RECIPIENT'S CATALOG NO. |
|---|---|---|
| NASA TM 78125 | | |

| 4. TITLE AND SUBTITLE | 5. REPORT DATE |
|---|---|
| Space Processing Applications Rocket Project<br>SPAR II Final Report | November 1977<br>6. PERFORMING ORGANIZATION CODE |
| 7. AUTHOR(S) | 8. PERFORMING ORGANIZATION REPORT # |
| | M-235 |
| 9. PERFORMING ORGANIZATION NAME AND ADDRESS | 10. WORK UNIT NO. |
| George C. Marshall Space Flight Center<br>Marshall Space Flight Center, Alabama 35812 | 11. CONTRACT OR GRANT NO. |
| | 13. TYPE OF REPORT & PERIOD COVERED |
| 12. SPONSORING AGENCY NAME AND ADDRESS | Technical Memorandum |
| National Aeronautics and Space Administration<br>Washington, D.C. 20546 | 14. SPONSORING AGENCY CODE |

15. SUPPLEMENTARY NOTES

This report was compiled by the Space Processing Applications Rocket Project Office, Special Projects

16. ABSTRACT

This document summarizes the experiment objectives, design/operational concepts, and final results of each of six materials science experiments conducted during the second Space Processing Applications Rocket (SPAR) mission flown by NASA May 17, 1976. The six individual SPAR experiments, covering a wide and varied range of materials processing objectives, were entitled:

1. Solidification of Pb-Sb Eutectic
2. Feasibility of Producing Closed-Cell Metal Foams
3. Direct Observation of Dendrite Remelting and Macrosegregation in Castings
4. Agglomeration in Immiscible Liquids
5. Casting Dispersion — Strengthened Composites at Zero Gravity
6. Solidification Behavior of Al-In Alloys under Zero-Gravity Conditions.

| 17. KEY WORDS | 18. DISTRIBUTION STATEMENT |
|---|---|
| | STAR Category 15 |

| 19. SECURITY CLASSIF. (of this report) | 20. SECURITY CLASSIF. (of this page) | 21. NO. OF PAGES | 22. PRICE |
|---|---|---|---|
| Unclassified | Unclassified | 291 | $9.25 |

* For sale by the National Technical Information Service, Springfield, Virginia 22161
*U.S. GOVERNMENT PRINTING OFFICE: 1977 - 735-078/55